

# **Molecular Layer Functionalized Neuroelectronic Interfaces:**

From Sub-Nanometer Molecular Surface Functionalization to  
Improved Mechanical and Electronic Cell-Chip Coupling

**Inauguraldissertation**

**zur Erlangung des Doktorgrades**

**der Mathematisch-Naturwissenschaftlichen Fakultät**

**der Universität zu Köln**

vorgelegt von

**Nikolaus R. Wolf**

**02.11.2020**

**Disputation**

**15.01.2021**



*Molecular Layer Functionalized Neuroelectronic Interfaces:  
From Sub-Nanometer Molecular Surface Functionalization to Improved Mechanical  
and Electronic Cell-Chip Coupling*

*Berichterstatter:* Prof. Dr. Roger Würdenweber  
Prof. Dr. Thomas Michely

*Tag der mündlichen Prüfung:* 15.01.2021

*Molecular Layer Functionalized Neuroelectronic Interfaces:  
From Sub-Nanometer Molecular Surface Functionalization to Improved Mechanical  
and Electronic Cell-Chip Coupling*

## Abstract

The interface between electronic components and biological objects plays a crucial role for the success of bioelectronic devices. Since the electronics typically include different elements such as an insulating substrate in combination with conducting electrodes, an important issue of bioelectronics involves tailoring and optimizing the interface for any envisioned application.

In this work, we present a method of functionalizing insulating substrates ( $\text{SiO}_2$ ) and metallic electrodes (Pt) simultaneously with a stable monolayer of organic molecules ((3-aminopropyl)triethoxysilane (APTES)). This monolayer is characterized by various techniques like atomic force microscope (AFM), ellipsometry, time-of-flight secondary ion mass spectrometry (ToF-SIMS), surface plasmon resonance (SPR), and streaming potential measurements. The molecule layers of APTES on both substrates, Pt and  $\text{SiO}_2$ , show a high molecule density, a coverage of  $\sim 50\%$ , a long-term stability (at least one year), a positive surface net charge, and the characteristics of a self-assembled monolayer (SAM).

In the electrical characterization of the functionalized Pt electrodes via impedance spectroscopy measurements, the static properties of the electronic double layer could be separated from the diffusive part using a specially developed model. It could be demonstrated that compared to cleaned Pt electrodes the double layer capacitance is increased by an APTES coating and the charge transfer resistance is reduced, which leads to a total increase of the electronic signal transfer of  $\sim 13\%$ .

In the final cell culture measurements, it could be shown that an APTES coating facilitates a conversion of bio-unfriendly Pt surfaces into biocompatible surfaces which allows cell growth (neurons) on both functionalized components ( $\text{SiO}_2$  and Pt) comparable to that of reference samples coated with poly-L-lysine. Furthermore, APTES coating leads to an improved mechanical coupling, which increases the sealing resistance and reduces losses. These increases were finally confirmed by electronic measurements on neurons, which showed action potential signals in the mV regime compared to signals of typically  $200 - 400\ \mu\text{V}$  obtained for reference measurements on PLL coated samples. Therefore, the functionalization with APTES molecules seems to be able to greatly improve the electronic cell-chip coupling (here by  $\sim 1500\%$ ).

This significant increase of the electronic and mechanical cell-chip coupling might represent an important step for the improvement of neuroelectronic sensor and actuator devices.

## Zusammenfassung

Die Schnittstelle zwischen elektronischen Komponenten und biologischen Objekten spielt eine entscheidende Rolle für den Erfolg bioelektronischer Geräte. Da die Elektronik typischerweise verschiedene Elemente, wie z.B. ein isolierendes Substrat in Kombination mit leitenden Elektroden, umfasst, stellt das Trimmen und Optimieren des Interfaces zwischen der Elektronik und dem biologischen Objekt eine der wichtigsten Herausforderungen der Bioelektronik dar.

In dieser Arbeit stellen wir eine Methode für die zeitgleiche Funktionalisierung von isolierenden Substraten ( $\text{SiO}_2$ ) mit integrierten metallischen Elektroden (Pt) mittels einer stabilen Monolage aus organischen Molekülen ((3-Aminopropyl)triethoxysilan (APTES)) vor. Diese Monolage wird durch unterschiedlichste Techniken wie Rasterkraftmikroskopie (AFM), Ellipsometrie, Flugzeit-Sekundärionenmassenspektrometrie (ToF-SIMS), Oberflächenplasmonenresonanz (SPR) und Strömungspotentialmessungen charakterisiert. Die Molekülschichten aus APTES weisen sowohl auf Pt als auch auf  $\text{SiO}_2$  eine hohe Moleküldichte, eine Bedeckung von  $\sim 50\%$ , Langzeitstabilität (mindestens ein Jahr), eine positive Oberflächen-Nettoladung und die Eigenschaften einer selbstorganisierten Monoschicht (SAM) auf.

Bei der elektrischen Charakterisierung mittels impedanzspektroskopischer Messungen konnten die statischen Eigenschaften der elektronischen Doppelschicht durch ein speziell entwickeltes Modell vom Diffusionsteil getrennt werden. Es konnte gezeigt werden, dass im Vergleich zu reinen Pt-Elektroden die Doppelschichtkapazität durch eine APTES-Beschichtung erhöht und der Ladungsübertragungswiderstand verringert wird, was zu einer Erhöhung des elektronischen Signaltransfers um  $\sim 13\%$  führt.

In den abschließenden Zellkulturmessungen konnte nachgewiesen werden, dass eine APTES-Beschichtung eine Umwandlung der ursprünglich biounfreundlichen Pt-Oberflächen in biokompatible Oberflächen ermöglicht, die ein Zellwachstum (Neuronen) auf beiden funktionalisierten Komponenten,  $\text{SiO}_2$  und Pt, ermöglicht, das mit dem von mit Poly-L-Lysin beschichteten Referenzproben vergleichbar ist. Darüber hinaus führt die APTES-Beschichtung zu einer verbesserten mechanischen Kopplung, die den elektronischen Dichtwiderstand zwischen Zellen und Chip erhöht und damit elektronische Verluste reduziert. Diese Erhöhungen wurden abschließend durch elektrische Messungen an Neuronen bestätigt, die Aktionspotentiale im mV-Regime zeigten, im Vergleich zu den üblichen Signalstärken von  $200 - 400 \mu\text{V}$  für konventionelle PLL-beschichtete Elektroden. Die Funktionalisierung mit APTES-Molekülen scheint somit die elektronische Zell-Chip-Kopplung signifikant zu verbessern, hier um  $\sim 1500\%$ .

Diese signifikante Verbesserung der mechanischen und elektronischen Zell-Chip-Kopplung könnte ein wichtiger Beitrag zur Verbesserung neuroelektronischer Sensor- und Aktuatorbauelemente darstellen.

## Contents

Abstract .....	I
Zusammenfassung .....	II
1. Introduction .....	1
2. Theoretical Background .....	4
2.1. Self-assembled molecular monolayer .....	4
2.1.1. Silanes .....	7
2.2. Surface potential .....	8
2.2.1. Electrical double layer .....	11
2.2.2. Electrokinetic potential .....	12
2.3. Electrochemical impedance spectroscopy .....	13
2.3.1. Representation of complex impedance .....	15
2.3.2. Physical electrochemistry and equivalent circuit elements .....	16
2.4. Cells as electronic components .....	18
2.4.1. Structure of neurons .....	20
2.4.2. Action potential .....	20
2.4.3. Cell adhesion .....	22
2.4.4. Neuroelectronic circuit .....	23
3. Experimental Methods .....	25
3.1. Choice of substrates, molecules, and sample preparation .....	25
3.1.1. Chemical cleaning .....	26
3.1.2. Lithography .....	26
3.1.3. Ozone cleaning and ozone activation .....	28
3.1.4. Molecular layer deposition .....	29
3.2. SAM characterization .....	31
3.2.1. Ellipsometry .....	31
3.2.2. Fluorescence Microscopy .....	32
3.2.3. Atomic force microscopy .....	33
3.2.4. Time of flight secondary ion mass spectrometry .....	34
3.2.5. Surface plasmon resonance spectroscopy .....	36
3.2.6. Streaming potential analysis .....	37
3.2.7. Impedance spectroscopy .....	38
3.3. Neuronal cells .....	40
3.3.1. Cell culture .....	40
3.3.2. Cell staining .....	42

*Molecular Layer Functionalized Neuroelectronic Interfaces:  
From Sub-Nanometer Molecular Surface Functionalization to Improved Mechanical  
and Electronic Cell-Chip Coupling*

3.3.3.	Cell-chip communication .....	42
4.	Results and Discussion .....	45
4.1.	SAM formations on electrodes .....	46
4.1.1.	Detection of monolayer .....	47
4.1.2.	APTES on SiO <sub>2</sub> .....	48
4.1.3.	APTES on Pt .....	49
4.1.4.	APTES monolayer properties .....	53
4.2.	Electronical characterization of the interface .....	61
4.2.1.	Chip design .....	62
4.2.2.	Electronic model for the interface .....	67
4.2.3.	Electrolyte resistance .....	74
4.2.4.	Double-layer capacitance .....	75
4.2.5.	Charge transfer resistance .....	78
4.2.6.	Impact of molecules .....	79
4.3.	Cell culture and cell-chip coupling on functionalized electrodes .....	85
4.3.1.	Bio affinity of SiO <sub>2</sub> and Pt surface .....	86
4.3.2.	Growth behavior and dynamic .....	91
4.3.3.	Mechanical cell chip coupling .....	95
4.3.4.	Electronic cell-chip coupling .....	97
5.	Conclusion and Outlook .....	99
I.	References .....	i
II.	Appendices .....	xii
	Figures .....	xii
	Script for impedance .....	xiv
III.	Acknowledgments .....	xx
	Erklärung .....	xxi
	<b>Lebenslauf</b> .....	xxii



## 1. Introduction

In today's world, the world of artificial intelligence, nanoelectronics, high-performance computers in the size of smartphones, one could conclude that with technology today, almost everything is possible. But considering seemingly simple things such as replacing an arm, as shown in science fiction movies (e.g. Star Wars or IRobot), we still face unsolved basic challenges. The arm alone (without hand) has already 7 degrees of freedom (R. Lioutikov, 2012), the hand adds another 27 degrees of freedom (ElKoura & Singh, 2003). Although, technologically we are already able to create almost the same degrees of freedom, nowadays prostheses are able to perform only 6 movements (Pylatiuk & Döderlein, 2006), which is far from what a real arm can do. Where does this big difference come from?

The fundamental challenges for a seamlessly integrated prosthesis are the information acquisition and information transfer, i.e. the reading and actuation of information, or simply, the communication between body and electronics.

In case of the arm prosthesis, only the muscles of the upper arm, shoulder, and chest can currently be used, which leads to a lack of information and thus a drastically reduced degree of freedom for the use of an artificial arm. Moreover, a feedback of the arm, e.g. any sensing, can not be coupled into the neuronal system this way. Therefore, these days, researchers and industries worldwide are working on reading and transferring information directly from or into the neuron system, the body's natural information highway. These approaches range from transplanting chips directly in the brain (Chaudhary et al., 2020; Fattahi et al., 2014; Fourneret, 2020; Loeb, 2018) to the electronics for neurons on-site (Fattahi et al., 2014; Loeb, 2018; Russell et al., 2019), i.e. in the case of the arm prosthesis, the neurons in the extant arm. These neurons transmit the information of the movements to the prosthesis, but also the sensor data of e.g. touching sense of the artificial arm to the brain.

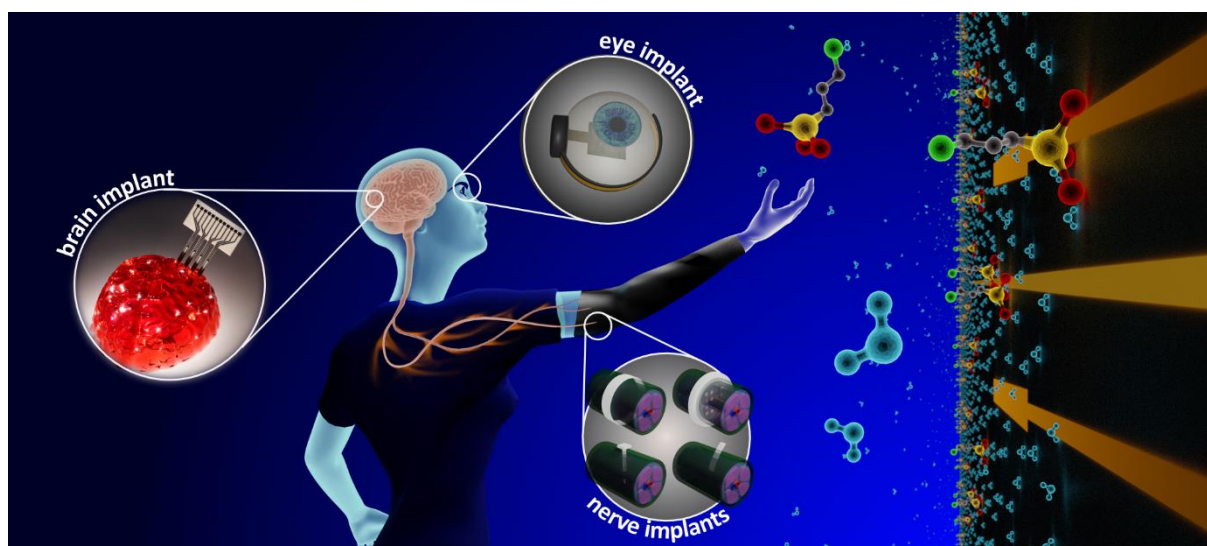


*Figure 1-1: Examples of different types of cell-chip communication used in prosthetics such as the brain chip communication (Lab Collection, n.d.), the eye implant (adapted from (Loeb, 2018)), and the measurement of nerve signals in the arm (adapted from (Russell et al., 2019)). All of these technologies are in the end based on the properties of the neuroelectronic interface, sketched on the right, including electrodes and electrolyte with molecules of various kinds.*

All suitable electronics (neuroelectronics), whether they are implanted in the brain, eye (Fattahi et al., 2014; Weiland & Humayun, 2014), or arm (Fattahi et al., 2014) are facing the same challenges due to the “rough” conditions in the body. The implanted electronics have to:

- operate stable for a long time (years),
- it should allow a perfect electronic coupling, i.e. low impedances, in order to be able to read smallest electrical signals,
- it must be biocompatible, i.e. it shouldn't provoke body reactions that could modify the neuroelectronic interface or even harm the cells,
- it should be flexible to mimic the dynamic and fragile nature of cells (Wu et al., 2020),
- and it should be of the size of individual neurons to be able to read single neuronal signals.

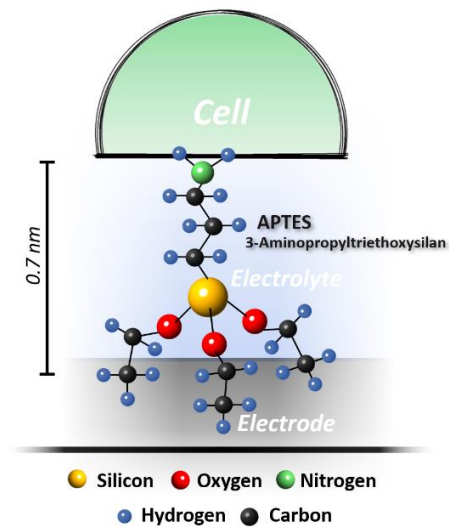


*Figure 1-2: Schematic of a neuroelectronic interface functionalized with APTES molecules.*

Since the electronics have to operate in body fluid during the whole operation time, the requirements on the neuroelectronics are harsh. Especially the interface formed by a thin film of water molecules on the electronic represents an important and largely unsolved problem in physics, chemistry, and biology. Thin water films can not only change the adhesive, lubricating, and reaction properties of surfaces, in biological processes they are decisive for the charge transport via ions (Teschke et al., 2001).

To address and solve these problems, researchers around the world tried different ideas, most of them come at the expense of other problems. For example, the use of relatively huge electrodes doesn't lead to cellular resolution, usually causes invasive damage, and still has problems to resolve small electrical pulses. Another approach to reduce the impedance is the use of 3D structured electrodes, such as planar electrodes with additional columns or mushroom-like extensions, which should increase the effective surface area (Kibler et al., 2012; J.-H. Kim et al., 2010; Petrossians et al., 2011; S. Weidlich et al., 2017; Wesche et al., 2012)). However, the desired effect turned out to be small, which is contrasted by the complicated, cost-intensive, and not very flexible production (Spanu et al., 2020). Flexible substrates (such as polydimethylsiloxanes (PDMS)) are also increasingly used to reduce invasive damage and to match the dynamics of the cells (Pennisi et al., 2010). In another approach, small microelectrodes coated with thin protein or peptide layers are used. These films make the electrodes biocompatible by mimicking the natural environment of neurons. However, this coating is still too thick (20 – 50 nm, (Colville et al., 2010)) to allow a good signal transfer. Furthermore, these coatings are only electrostatically bound to the electrode and substrate, and are easily removed by the cells (Y. H. Kim et al., 2011).

The question arises whether a thin organic monolayer could be used, which binds to the surface of the electronic and, at the same time, interacts with the bio-object. This approach is not

entirely new. Especially, self-assembled monolayers (SAM) made of alkanethiols have already been used to improve the interface between electrode and neurons mechanically (Bryant & Pemberton, 1991; Laibinis et al., 1991; Swalen et al., 1987). However, this doesn't include the binding of cells to the rest of the substrate. In order to promote adherence and binding of cells onto the complete chip (electrode and passivated areas), we have decided to use 3-Aminopropyltriethoxysilan (APTES) molecules as a coating for the neuroelectronic chip since:

- APTES has a silane head group which binds to all silicon-based substrates (e.g. SiO<sub>2</sub>, PDMS), which represents a standard carrier for neuroelectronics,
- APTES should cause little to no insulation due to its small size (~0.7 nm), and
- due to its amino group, APTES should be biofriendly and should provide a better mechanical coupling (Hao et al., 2016), which could even lead to a better clamping of the cells to the chip and, thus, an increased signal transfer (Metwally & Stachewicz, 2019).

The increase of the signal transfer has been observed in experiments with HL-1 cells by Markov et al. (Markov et al., 2018). However, it had neither been confirmed nor has the underlying mechanism been proven and analyzed yet. This will be the main task of this work.

Therefore, after introducing the theoretical background (chapter 2) and the experimental techniques and sample preparation (chapter 3), we will analyze and discuss the impact of APTES coating on the properties of neuroelectronic interfaces (chapter 4). We start with the investigation of the binding and stability of silanes on metallic surfaces (electrodes) like platinum in chapter 4.1. In chapter 4.2, we compare the electrical properties of chips without and with APTES coating in a simulated neuroelectronic environment using a measuring setup, which was specially developed to mimic cell-chip communication. In chapter 4.3, we analyze the mechanical and electrical cell-chip coupling of our APTES coated chips in direct contact with the cells. Finally, chapter 5 provides the conclusion and valuation of this work.

## 2. Theoretical Background

Due to their thinness, perfect arrangement, and the various functionalities, which can be achieved by the large variety of functional groups, self-assembled monolayers (SAMs) consisting of organic molecules represent ideal candidates for the modification of surfaces of substrates for many applications. They can even be used as essential components in simple as well as complex organic electronic devices. In the following, we will sketch the state of the art and provide a brief theoretical background on the usage of SAMs in interfaces between organics and electronics, which is separated in:

- (i) introduction and state of the art of *Self-assembled molecular monolayer* and the deposition of silanes on substrates and electrodes,
- (ii) the analysis and the meaning of the *Surface potential*,
- (iii) the state of the art of the *Electrochemical impedance spectroscopy* and its usage, and
- (iv) a brief description of cells and *Cells as electronic components*.

### 2.1. Self-assembled molecular monolayer

Studies on self-assembled monolayers (SAMs) date back to the 1940s (Sizov et al., 2019) and have become increasingly important since then. Nowadays, SAMs can be found in many applications, of which organic solar cells (Lee et al., 2013; Wang et al., 2014; Yip et al., 2008), organic light-emitting diodes (OLEDs) (An et al., 2019; Bardecker et al., 2008), organic field-effect transistors (OFETs) and biosensors (An et al., 2019; Bardecker et al., 2008) are presently the most common applications. But SAMs are also becoming more and more widespread in other areas such as batteries (Zettsu et al., 2016), fuel cells (C. Santoro et al., 2015; F. Y. Zhang et al., 2008), organic memory devices (Novembre et al., 2008), synaptors (Alibart et al., 2010) and RFID tags (Fiore et al., 2015). While in the latter cases, SAMs are still the subject of current research, SAMs have already reached the mass market in other areas (e.g. OLED displays).

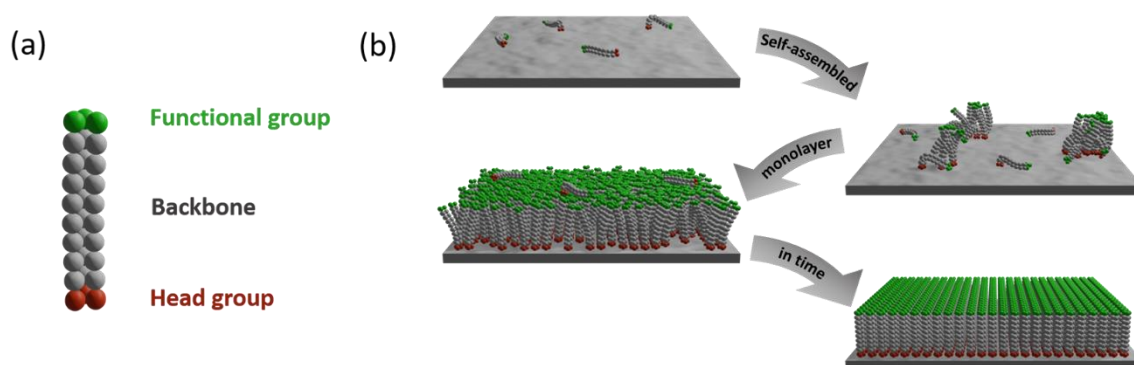


Figure 2-1: Formation of SAMs with (a) structural components of a typical organic molecule, and (b) SAM formation process in time (adapted from (Schmaltz et al., 2017)), starting with physisorption of molecules on the substrate, partially chemisorbed molecules, layer building process, to the final self-repairing dense monolayer.

**What are SAMs:** “Self-assembly being a unifying concept in nature” (S. Zhang, 2003) can be described as “autonomous organization of components into patterns or structures without human intervention” (Whitesides & Grzybowski, 2002). A SAM is a self-assembled monolayer

of organic surfactants. These surfactants have a specific structure. They typically consist of a head group, which binds to the substrate, a backbone, and a functional group (Figure 2-1 (a)). This amphiphilic structure allows a high packing density of the molecules standing upright on the substrate and thus can form a monolayer that is ordered in two dimensions. The choice of the functional group depends only on the application. Frequently used functional groups are methyl, hydroxyl, carboxyl, amino, or thiol (Table 1). The backbone consists of alkyl chains and acts as a kind of spacer. The choice of the backbone typically varies from C<sub>2</sub> to C<sub>12</sub> (Sizov et al., 2019). The head group is responsible for specific binding to the surface of the substrate and can be bound through either physical or chemical bonds. A few frequently used head group – substrate combinations are silanes on SiO<sub>2</sub>, thiols on Au, or phosphonic acids on Al<sub>2</sub>O<sub>3</sub> (Table 1). On one hand, the bonds between the molecules and the substrate have to be strong enough to obtain a stable layer and avoid distortion of molecules, on the other hand, they have to be weak enough to ensure certain mobility of the molecules on the surface. The latter is essential to maintain a high packing density since the mobility and van der Waals force between the molecules can lead to a correction of the packing defects (Schmaltz et al., 2017).

*Table 1: Table of typically used functional and head groups and applications (taken from (Alexey S. Sizov, 2019)). Notations are as follows: PEI is polyethyleneimine, TAA is triarylamine, PAA is polyacrylic acid, PEN is polyethylene naphthalate, PET is polyethylene terephthalate, and PI is polyimide.*

Precursor for SAMs		Substrate	Application
Functional group	Head group		
CH <sub>3</sub> , OH, SH, Ph, Imi	PO(OH) <sub>2</sub>	Al (AL <sub>2</sub> O <sub>3</sub> )	Multilayer dielectrics
NH <sub>2</sub> , SH, N <sub>2</sub>	PO(OH) <sub>2</sub> , SiCl <sub>3</sub> , Si(OAlk) <sub>3</sub>	Al (AL <sub>2</sub> O <sub>3</sub> ), Si (SiO <sub>2</sub> )	Adhesion promoters
NH <sub>2</sub> , CH, CH <sub>3</sub> , OH, SH, CF <sub>3</sub>	SiCl <sub>3</sub> , Si(OAlk) <sub>3</sub>	Si (SiO <sub>2</sub> )	Nanostructured surface
CH <sub>3</sub> , CF <sub>3</sub> , OH, PEI, TAA	Si(OAlk) <sub>3</sub> , PEI, PAA	PEN, PI, PET	Change of electrode workfunction
OOC-C <sub>6</sub> F <sub>6</sub> , COOH, OH, CH <sub>3</sub>	Si(OAlk) <sub>3</sub> , PEI, PAA	PEN, PI, PET	Biosensors

*SAM development:* To briefly sketch the process of SAM formation, let us look at Figure 2-1 (b). The process of self-assembly typically starts with single molecules absorbed on the surface. The more molecules are present, i.e. the higher the concentration of molecules on the surface, the more the molecules start to cluster in a disordered way caused by the van der Waals forces between the molecules. These clusters are fixed on the surface by the head group. This process continues, and the order improves until an ordered, stable monolayer has formed (Schmaltz et al., 2017). These layers can become extremely robust (Søndergaard et al., 2013) due to the high packing density, the strong bond to the substrate, and the forces between the molecules.

*Molecular Layer Functionalized Neuroelectronic Interfaces:  
From Sub-Nanometer Molecular Surface Functionalization to Improved Mechanical  
and Electronic Cell-Chip Coupling*

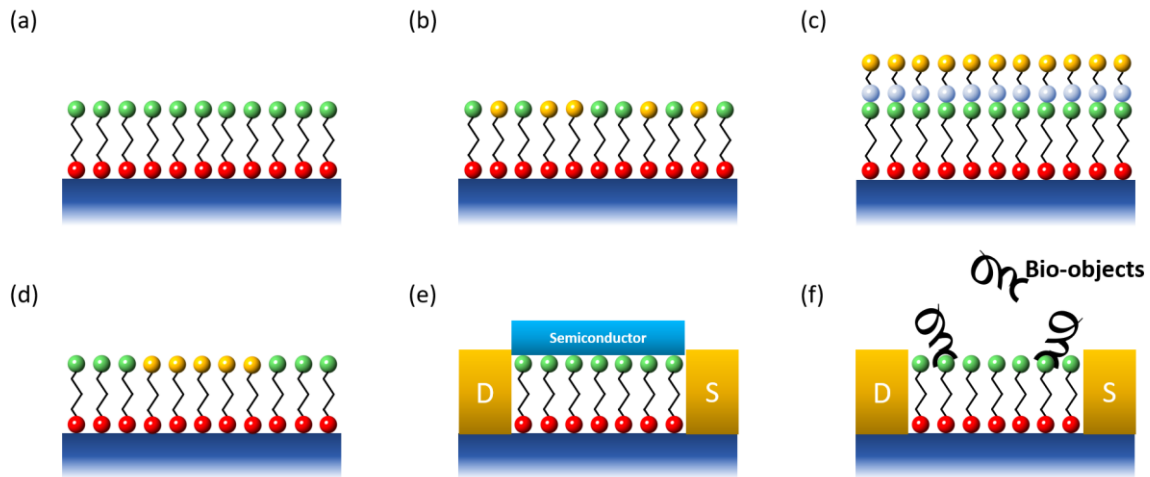


Figure 2-2: Different SAM constellations for different application fields, (a) non-local SAM, (b) mixed SAM, (c) multilayer SAM, (d) nanostructured SAM formations, (e) SAM used as dielectric/semiconductor interface in a FET and (f) SAM used as biosensors.

**Role of SAMs:** Even though SAMs are already used in industry, the production of reliable surface modifications with SAMs is still a major topic in current research. SAMs in organic electronics can fulfill various functions.

- The complete coverage of the substrate (Figure 2-2 (a)) is most common and mainly used to change the surface energy or act as an adhesion layer for further layers, nanoparticles, or bio-objects.
- To control the surface potential more precisely, a mixed SAM (Figure 2-2 (b)) can also be used (Markov et al., 2017), which allows to tailor the surface properties for specific conditions.
- Furthermore, SAMs can be stacked on top of each other forming well-defined multilayer and allowing a layer degree of flexibility (Figure 2-2 (c)) (Martin et al., 2017).
- Locally restricted SAMs (Figure 2-2 (d)) can be used to create nano- to microstructures for microelectronic components or structures for cells (Yuan et al., 2020).
- SAMs can also be used in combination with conventional electronic components, for example, to improve the electrical properties of FETs (Mathijssen et al., 2008) or to modify metal electrodes to change the working function or to enhance the injection of charge carriers in semiconductors (Figure 2-2 (e)) (Asadi et al., 2007).
- Finally, SAMs can be used as a linking layer in ultra-sensitive biosensors (Figure 2-2 (f)), where the functional group of the SAM binds to a target-specific receptor. For example, this enables the detection of picomolar concentrations of calcium in the salivary (Magar et al., 2020).

Definitely, the possible applications range of SAMs is far beyond the given examples.

### 2.1.1. Silanes

In this work, we will focus on the use of silanes as molecules for SAMs. Silanes have the advantage that they bind covalently to  $\text{SiO}_2$  – one of the most common substrates in electronics. Furthermore, we mainly focus on one silane, (3-Aminopropyl)triethoxysilane (APTES) (Figure 2-3 (a)), because

- (i) it is very small (sub-nanometer) and therefore can be deposited via gas-phase deposition (evaporation), and
- (ii) at the same time, the amino functional group of APTES is considered to be biocompatible, and in contact with an electrolyte, the amino group becomes positively charged, which makes it attractive for neuroelectronic applications.

To understand the binding of silanes to  $\text{SiO}_2$ , we first have to take a closer look at the standard substrate for the deposition of silane SAMs, i.e.  $\text{SiO}_2$ .

*SiO<sub>2</sub> Substrate:*  $\text{SiO}_2$  surfaces are typically obtained via temper processes from Si. It doesn't possess a perfect crystalline structure. In order to describe the  $\text{SiO}_2$  surface, a (111)  $\beta$ -cristobalite structure can be assumed (Figure 2-3 (b)), a diamond-like structure that behaves similar to amorphous  $\text{SiO}_2$  (M. Zhang et al., 2015). The lattice constants are  $a = b = c = 7.16 \text{ \AA}$  (M. Zhang et al., 2015) and in the top and side view, every second silicon has an OH group (Figure 2-3 (c)). The resulting distance  $x_{NN}$  of neighboring OH groups is:

$$x_{NN} = \frac{a\sqrt{2}}{2} = 5.06 \text{ \AA} .$$

Thus, each unit cell possesses three OH groups to which molecules can bind, and the maximum OH density would be  $4.55 \text{ nm}^{-2}$ , which agrees with the experimental data of  $4.9 \text{ nm}^{-2}$  (Pelmenschikov et al., 2000).

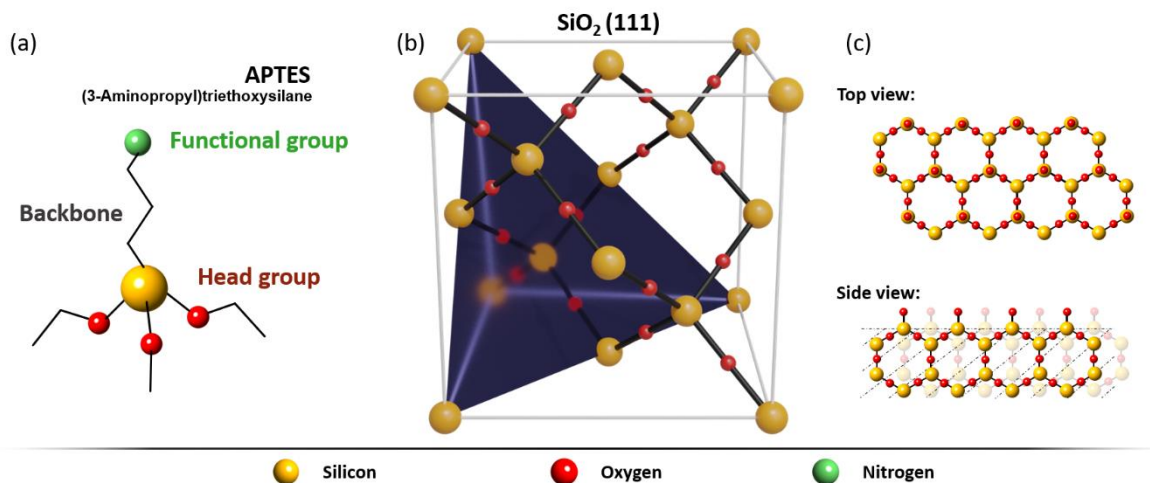


Figure 2-3: Schematic of (a) the molecule APTES, (b) the  $\beta$ -cristobalite structure of  $\text{SiO}_2$  with (111) cut, and (c) top and side view of the activated  $\text{SiO}_2$  surface with OH docking points for the covalent molecular binding of APTES.

*Molecules:* On contact with the surface, the methoxy group ( $\text{OC}_2\text{H}_5$  arms, Figure 2-3 (a)) of the molecule reacts with water molecules on the surface, and the molecules can bind to the OH groups on the surface. This reaction results in a covalent bond between the surface and the

molecule (Figure 2-4). With increasing density of bound molecules and due to the van der Waals interaction between their chains (backbones), the molecules finally stand upright (Schmaltz et al., 2017).

Due to geometric (steric) limitations, Si-O-Si links between the molecules or multiconnection to the substrate are not possible. The Si-O-Si group has a maximum length of 3.28 Å at an angle of 180° (Stevens, 1999) and thus is smaller than  $x_{NN}$ , the distance between possible docking points on the surface. Cross-links would only be possible for very unlikely geometries of the headgroup, which would automatically hamper the binding of adjacent molecules and the formation of stable and dense layers. Moreover, links between unbound and bound molecules are also unlikely due to the size limitations considering the backbone and its C-H bonds with a size of 1.08 Å and the van der Waals radii of 3.5 Å for H bound to C (Stevens, 1999). However, if the monolayer is not packed with maximum density, additional bonds between molecules and between molecule and surface are possible, e. g. molecules could be lying on the surface or building island polymerizations.

In conclusion, the formation of silane SAMs on SiO<sub>2</sub> surfaces is reasonably understood. Therefore, we will use this system, i.e. silane on SiO<sub>2</sub>, as reference in this work. However, the behavior of silanes and the possible formation of SAMs on other systems is less or not understood or even not examined up to now. Especially the SAM formation on metal surfaces, which is one of the major topics of this work, is not understood.

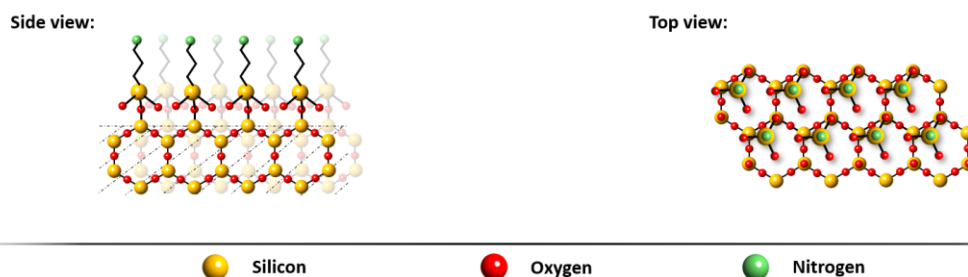


Figure 2-4: Sketched of bonded APTES molecules on SiO<sub>2</sub> substrate in the side (left) and top view (right).

## 2.2. Surface potential

The investigation of electrokinetic phenomena, i.e. the study of charges and their movement at interfaces in the form of space charges, is an old research direction that dates back to the 18th century (Wall, 2010). The understanding of the role of surface charge is essential for many areas like:

- colloidal dispersion (Barron et al., 1994; Byun et al., 2005), which is important for topics ranging from the effect, transport, and clustering of drugs to the production of paper,
- in the study of the fate, behavior, and toxicity of nanomaterials in ecological and biological systems (Lowry et al., 2016), and
- in the adhesion properties of bio-objects on surfaces (Kundu et al., 2016).



Also, other surface properties such as topology (Viswanathan et al., 2015), elasticity (Breuls et al., 2008; Sanz-Herrera & Reina-Romo, 2011), wettability (Dowling et al., 2011), and chemical composition (Tang et al., 2008) are often correlated to the surface potential.

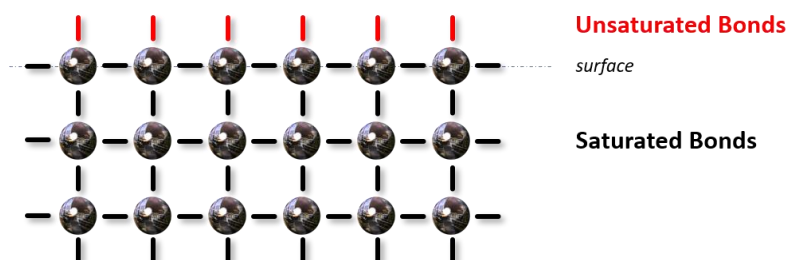


Figure 2-5: Schematic of a crystal structure with unsaturated bonds (red) at the surface (blue dashed line).

**What is a surface charge:** In general, a surface looks different from the rest of the crystal. On the surface, there are unsaturated bonds that interact with the environment (Figure 2-5). As a result, surface charges can form, leading to a 2D plane with a non-zero charge. For example, in a perfect conductor, all charges are located on the surface. In insulators, an electric field creates a polarization in bulk and binds charges at the surface. From a chemical point of view, there are different ways to create surface charges. According to Lyklema and Jacobasch (Jacobasch, 1989; Lyklema, 2011), there are five main reasons why surface charges appear (see also Figure 2-6):

- (i) dissociation of surface groups,
- (ii) preferential absorption of anions or cations,
- (iii) absorption of polyelectrolytes,
- (iv) isomorphous substitution of anions and cations, and
- (v) depletion or accumulation of electrons (e.g. by an applied potential).

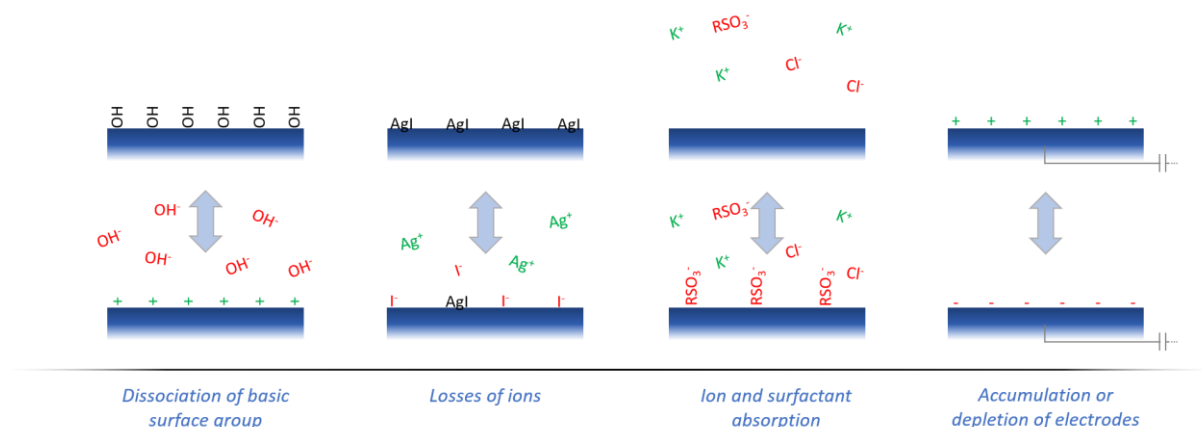


Figure 2-6: Sketches of different examples for the origins of surface charges starting from left to right with dissociation of basic surface groups, losses of ions, ion and surfactant absorption, and accumulation or depletion of electrodes (adapted from (Greben, 2015)). Always top and bottom schemes belong together.

Surface charges practically always occur when surfaces are in contact with liquids. This phenomenon is due to the anions and cations in liquids which interact with the surface. The exact determination of the surface charge is not possible with the current state of knowledge.

Still, there are various measuring methods that can analyze the electrical double layer (see *Electrical double layer*) and thus give an idea of the surface charge.

*Measurement methods:* There are different ways to investigate the surface charges at a solid/liquid interface (Figure 2-7) (Jacobasch, 1989). The choice depends mainly on the system to be investigated. For measurements of colloidal and nanoparticles, mainly electrophoretic or segmental measurements are used, whereas for planar surfaces or fixed particles, mostly streaming potential or electro-osmosis techniques are used. The principles are briefly described below.

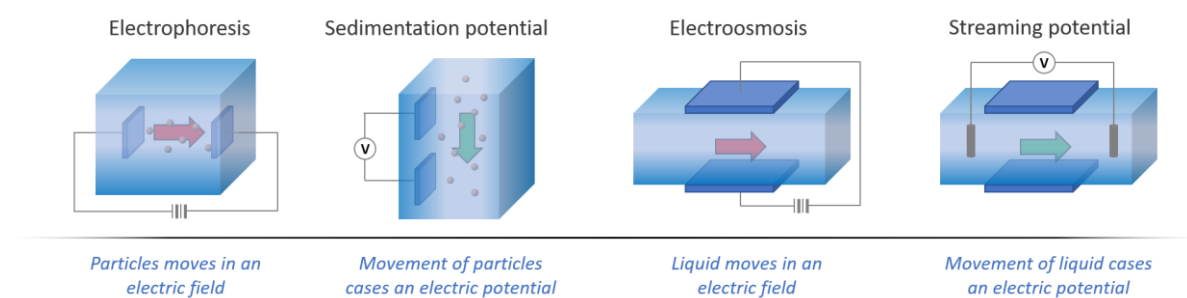


Figure 2-7: Measurement options of surface charges, starting from left to right with electrophoresis, sedimentation potential, electroosmosis, and streaming potential (adapted from (Geben, 2015)). The red arrow indicates the direction of particles/liquid flow forced by an electrical field, and the green arrow indicates the flow of the particles/liquid.

*Electrophoresis:* Electrophoresis describes the electric field-driven migration of charged particles in a medium. The electric field generates a shear force in the electric bilayer surrounding the particles. Only charged particles are set in motion in the electric field. The mobility of the particles in comparison to the resting medium allows conclusions on the surface charge.

*Sedimentation potential:* The sedimentation potential method is the opposite of electrophoresis. A particle moving in a gravitational field causes a potential at electrodes that allows to estimate the surface charges.

*Electroosmosis:* Electroosmosis is the oldest method to study surface charges. For this purpose, the flow of a liquid through a porous membrane is measured in a known electric field. The velocity of the electroosmotic flow is proportional to the interaction between the charges in the liquid and the external electric field. During electroosmosis, a pressure gradient develops due to the potential difference between the two electrodes, which influences the flow of the liquid.

*Streaming potential:* The streaming potential method is the opposite of electroosmosis. An electrical potential difference is created when an electrolyte flows under pressure through a channel with charged surfaces. This potential difference is caused by a displacement of the counter ions, which are deposited on the charged surface in the form of an electrical double layer and a mobile layer (see *Electrical double layer*). The pressure causes a potential shift in the so-called shear layer, which can be measured.

In order to understand the phenomena taking place at the surface, let's take a closer look at the so-called electrical double layer.

### 2.2.1. Electrical double layer

As mentioned above, as a consequence of ionization, almost all surfaces have a defined surface charge in a polar medium. The surface affects the arrangement of adjacent ions in the polar medium. Ions with the opposite charge are attracted and ions with the same charge are repelled from the surface (Figure 2-8 (a)). This attraction and repulsion are explained by the DLVO theory (Derjaguin, Landau, Verwey, Overbeek), which describes the impact of the different forces in front of the surface (Figure 2-8 (b)).

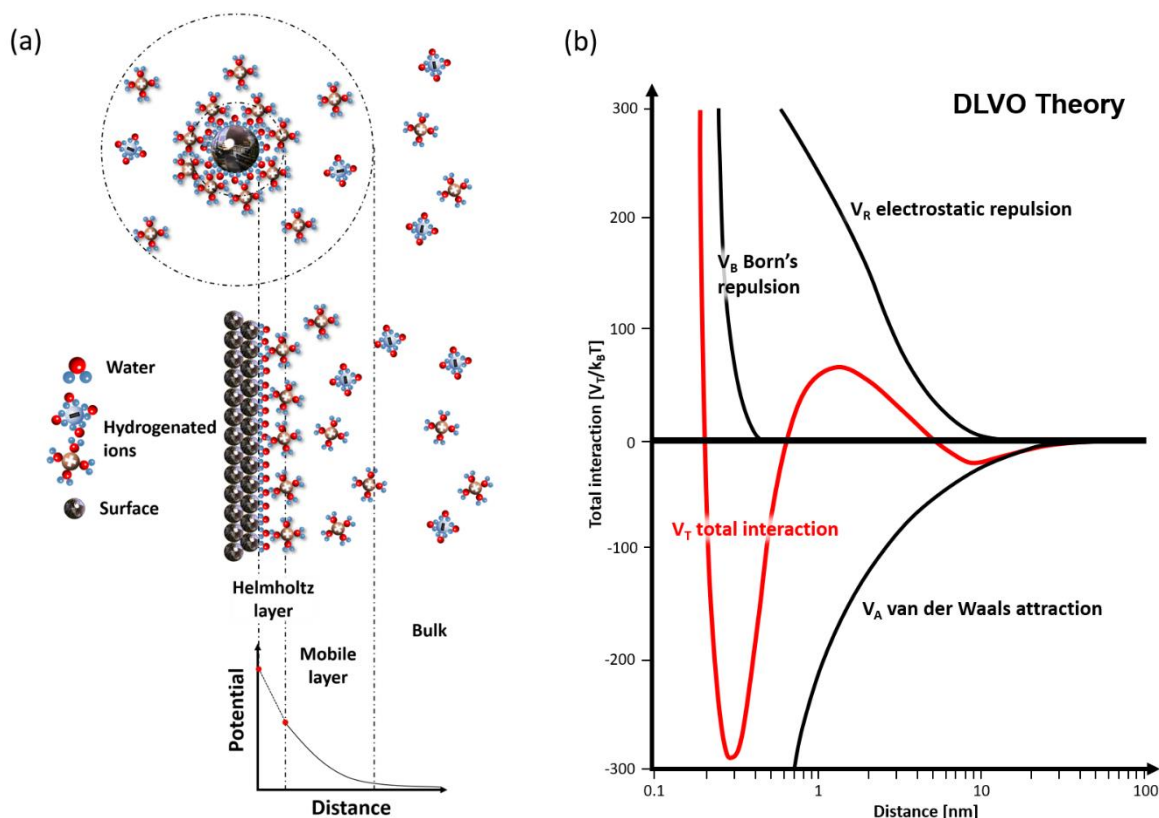


Figure 2-8: Schematics of the surface potential and the impact of different forces on the molecules in the electrolyte, with (a) a sketch of the electronic double layer of nanoparticles (top) and plane substrates (middle), and the resulting potential (adapted from (Lowry et al., 2016)) and (b) ion-surface interaction separated by the different forces according to DLVO theory (Derjaguin, Landau, Verwey, Overbeek).

The surface charges automatically form in a liquid (Figure 2-8):

- (i) a strongly bound physisorbed layer (Helmholtz layer),
- (ii) a weakly bound layer (mobile layer), and
- (iii) the neutral bulk of the electrolyte.

As a consequence of the different mobilities, the Helmholtz layer acts as a capacitor at the surface. The electrodes of this capacitor are formed by the surface and the ions in the Helmholtz layer separated by an insulating water layer. The thickness of the Helmholtz layer can be estimated by the size of 2 water molecules and half of the ion radius (Brown et al., 2016). The potential in the mobile layer drops off according to the Poisson equation using the Debye length and approaches zero in the neutral electrolyte of the bulk (Figure 2-8 (a) bottom).

*The role of molecules:* In order to modify (functionalize) the surface, for example, organic molecules, peptides, or proteins are placed on the surface to improve its properties in bio-applications. Different models for the impact of such a surface functionalization on the electrical double layer can be found in the literature. For example, it is suggested that the functional group of molecules represents a new surface and the electronic double layer is formed on this new surface (Dreier et al., 2018; Schweiss et al., 2001). Others claim that the effective surface is a mixture of the original surface and the surface defined by the molecules (Hotze et al., 2014; Jacobasch, 1989). The latter used will be discussed in chapter 4.1.

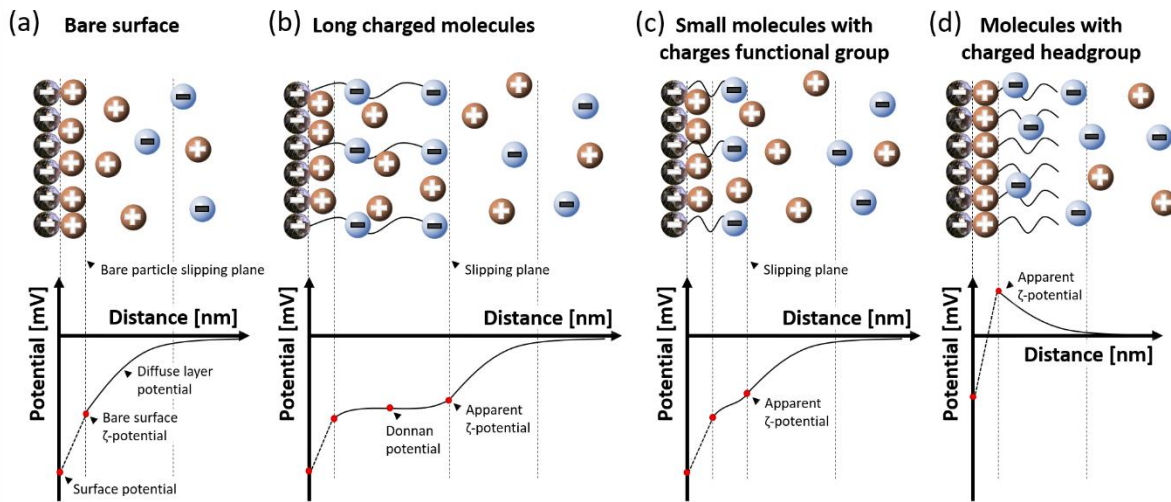


Figure 2-9: Surface charges and potential of different surfaces for the cases (a) no molecules, (b) large negatively charged molecules, (c) small molecules with negatively charged functional group, and (d) molecules with positively charged headgroups (according to (Lowry et al., 2016)).

Figure 2-9 illustrates four different cases of the electronic double layer on surfaces and the associated potentials in the electrolyte. The first case (Figure 2-9 (a)) shows the reference, i.e. a bare surface with adsorbed ions in an electrolyte. The second and third example (Figure 2-9 (b) and (c)) shows a negatively charged surface with long negatively charged molecules and short negatively charged molecules, respectively. The last example (Figure 2-9 (d)) shows a positively charged molecule on the negatively charged surface. The associated potential in the electrolyte is shown below each sketch. The molecules modify the potentials and the Debye length, in principle they extend the impact of the surface into the electrolyte. Especially interesting is the case of molecules with opposite charge on a surface (Figure 2-9 (d)), which applies for our case, i.e. APTES on a negatively charged surface. These molecules can lead to a charge reversal or charge overcompensation at the surface (Jacobasch, 1989; Plank & Sachsenhauser, 2006; Sachsenhauser, 2009, pp. 72, 117, 144).

### 2.2.2. Electrokinetic potential

As stated before, the surface charge cannot be measured directly. However, by measuring the electrokinetic potential ( $\zeta$ -potential), conclusions on the surface charges can be obtained. The  $\zeta$ -potential represents the potential at the shear plane, which is the plane between the stable Helmholtz layer and the mobile layer (Figure 2-10 (b)). It can be measured, for example, by streaming potential experiments. In this experiment, an electrolyte flow through a microchannel formed by two substrates with identical surfaces to be analyzed displaces the charged mobile

layer (Figure 2-10 (a)). By measuring the flow and the potential  $V_{str}$  or current  $I_{str}$ , the resulting  $\zeta$ -potential can be obtained via the Helmholtz-Smoluchowski equation (Hunter, 1981):

$$\zeta = \frac{dI}{dp} \cdot \frac{\eta L}{\epsilon \epsilon_0 A}, \quad (2-1)$$

where  $I$  is the resulting current flowing between the two electrodes,  $p$  is the pressure which is necessary to generate the laminar flow,  $\eta$  and  $\epsilon$  are viscosity and dielectric constant of the electrolyte, and  $L$  and  $A$  are the length and cross-section of the flow channel, respectively.

The  $\zeta$ -potential can be modified by coating the substrate with molecules, especially due to their functional group (Garcia et al., 2020). This allows us to tailor the surface for any application using especially the charge of the functional group and a given electrolyte (Hao et al., 2016; Metwally & Stachewicz, 2019).

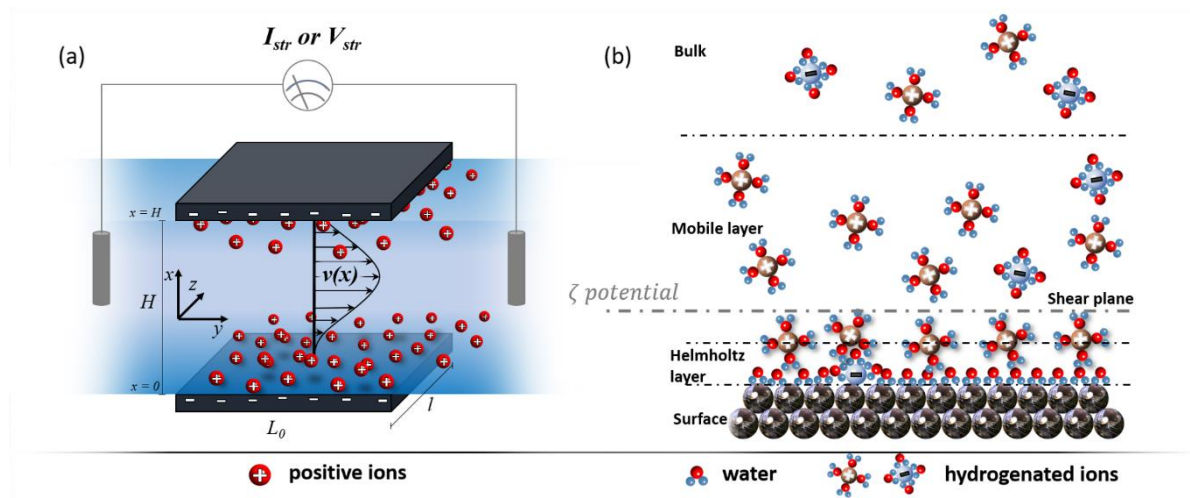


Figure 2-10: Schematics of the  $\zeta$ -potential, with (a) schematic of the streaming current channel for the measurement of the  $\zeta$ -potential (only counter ions of the electrolyte are shown) and (b) surface with the position of  $\zeta$ -potential.

### 2.3. Electrochemical impedance spectroscopy

Another way to characterize the electronic properties of the surface is the electrochemical impedance spectroscopy (EIS). In this technique, the charge transfer at the surface is analyzed. The idea of EIS is already more than one century old. The first concept was introduced by Oliver Heaviside (Lvovich, 2012, Chapter 1). Over the last century, it has become widely used mainly as an analysis tool in materials research. There exist many fields of application, which varied from corrosion investigation and control (Mansfeld, 1995; Scully, 2000; Sherif & Park, 2006b, 2006a), monitoring and synthesis of conducting polymer (Bardavid et al., 2008; Johnson & Park, 1996; Sarac et al., 2008), photoelectrochemistry, i.e. dye-sensitized solar cells and electron-transport properties (Han et al., 2004; He et al., 2009; Ku & Wu, 2007; Mahbuburrahman et al., 2015; Paulsson et al., 2006), batteries and fuel cells (Danzer & Hofer, 2009; Kato et al., 2004; Lu et al., 2007; Malevich et al., 2009; Piao, 1999), to, most important for this work, biosensors and bio-applications (Kulka, 2011; MacDonald, 2006; Park & Yoo, 2003; Randles, 1947). For example, Berggren et al. created a capacitive biosensor based on EIS for the detection of antibodies, antigens, proteins, DNA fragments, and heavy metal ions with

a detection limit down to femtomolar resolution by modifying electrode surfaces with SAMs (Berggren et al., 2001).

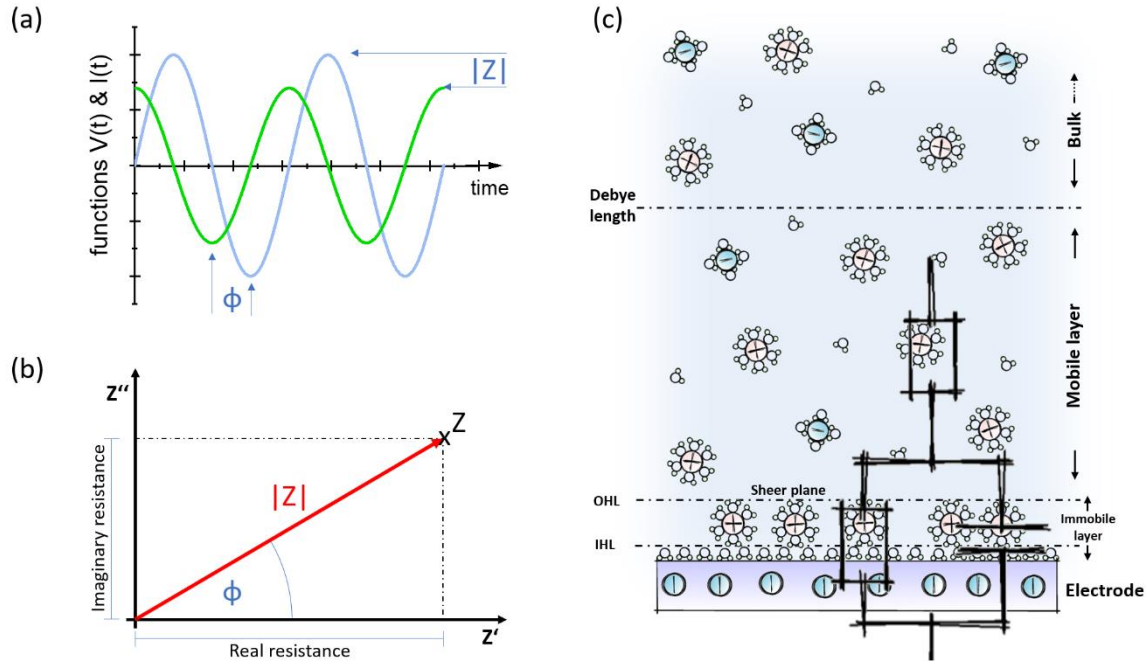


Figure 2-11: Sketches of the electrochemical impedance spectroscopy with (a) the alternating voltage and current visualizing phase shift and amplitude, (b) impedance  $Z$  in imaginary and real representation, and (c) sketch of the Helmholtz layer (inner Helmholtz layer (IHL) and outer Helmholtz layer (OHL)) and the corresponding electronic circuit given by a simple Randles circuit.

**What is impedance:** The impedance  $Z$  represents an extended concept of the resistive behavior in an alternating current circuit. The phase and amplitude of alternating current and voltage are observed in order to obtain the complex impedance (Figure 2-11 (a)). The complex voltage  $V$  and current  $I$  (Figure 2-11 (a)):

$$V = |V|e^{j(\omega t + \phi_V)}, \quad (2-2)$$

$$I = |I|e^{j(\omega t + \phi_I)}, \quad (2-3)$$

with imaginary number  $j$ , phase  $\Phi$ , and angular frequency  $\omega$ , allow to evaluate the impedance similar to Ohm's law:

$$Z = \frac{V}{I} = |Z|e^{j(\phi_V - \phi_I)}, \quad (2-4)$$

which can be represented in complex space (Figure 2-11 (b)) with  $\phi = \phi_V - \phi_I$  (Lvovich, 2012, p. 5). The absolute value of the impedance and the phase are given by:

$$\tan \Phi = \frac{Z''}{Z'}, \quad (2-5)$$

$$|Z| = \sqrt{Z'^2 + Z''^2}, \quad (2-6)$$

with  $Z'$  and  $Z''$  denoting the real part and imaginary part of the impedance, respectively.  $Z'$  is the real resistance (dissipation), whereas  $Z''$  represents the dispersive contribution of the impedance. Without phase shift ( $\Phi = 0^\circ$ ) the impedance corresponds to a perfect resistor, for  $\Phi = -90^\circ$  a perfect capacitive behavior, and for  $\Phi = 90^\circ$  a perfect inductive behavior is present. With this basic ansatz, models can be designed that describe a system to be measured in order to identify individual components of the system. These models can become quite complex.

Figure 2-11 (c) shows the typically used model to describe the Helmholtz layer (see *Electrical double layer*), which is the Randles equivalent circuit (Randles, 1947). With minor modifications, it is also the most commonly used model in EIS.

### 2.3.1. Representation of complex impedance

The most common representations of impedance spectra are the Bode diagram or the Nyquist diagram. Both diagrams are developed for the graphic representation of frequency-dependent functions with complex-valued values.

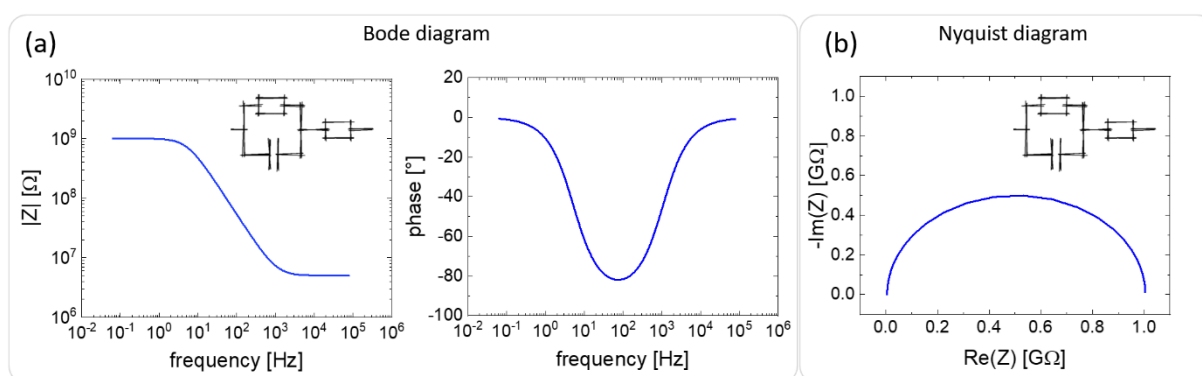


Figure 2-12: Representation of complex impedance from Randle circuit (inset) in form of a (a) Bode diagram (including the absolute impedance and the phase) and (b) Nyquist diagram. The chosen example values are for the parallel resistor  $1 \text{ G}\Omega$ , the parallel capacitor  $30 \text{ pF}$ , and the serial resistor  $5 \text{ M}\Omega$ .

**Bode diagram:** The Bode diagram, named after Hendrik Wade Bode (American electrical engineer, developed in the 1930s), is used to represent transfer ratios in dynamic systems. It is mainly used for the representation of linear and time-invariant systems in electronics, control engineering, and impedance spectroscopy. In the Bode diagram, the amplitude gain (absolute value of the impedance) and the phase are plotted separately against the frequency (Figure 2-12 (a)). Often, the absolute value of the impedance  $|Z|$  and the phase  $\Phi$  are plotted double-logarithmically and semi-logarithmically, respectively, as a function of frequency. This representation has the advantage that straight line segments can be used to approximate the course of the curves (Yarlagadda, 2010, p. 243) and thus identify the underlying model, i.e. equivalent electronic circuit.

**Nyquist diagram:** The Nyquist diagram, named after Harry Nyquist (Swedish-American electrical engineer) (Nyquist, 1932), is mainly used to control the stability of systems in signal processing. In contrast to the Bode diagram, it consists of only one diagram in which the complex-valued impedance is plotted as a real and imaginary part with frequency as a parameter (Figure 2-12 (b)). In contrast to the Bode diagram, it is not possible to obtain direct statements about characteristic frequencies, e.g., cut-off frequencies. Instead, the Nyquist diagram offers a more general statement about the system and its stability.

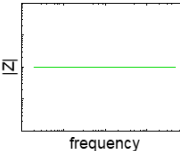
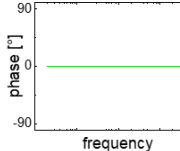
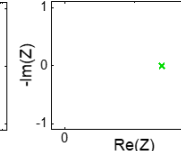
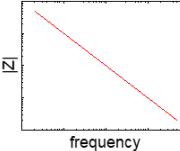
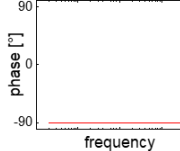
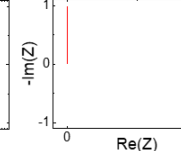
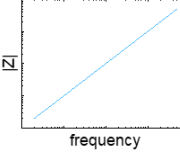
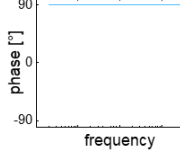
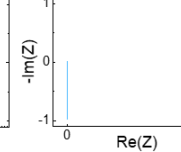
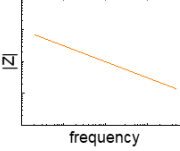
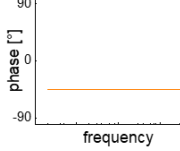
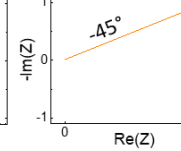
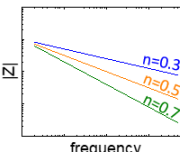
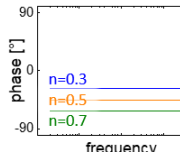
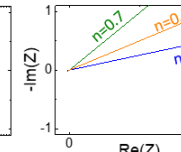
### 2.3.2. Physical electrochemistry and equivalent circuit elements

Each element in an electrical circuit has its impedance, which, similar to Kirchoff's rules (Kirchhoff, 1845), can be combined (in series or parallel) with other elements to obtain the total impedance finally:

Series combination:  $Z = Z_1 + Z_2 + \dots + Z_n$       Parallel combination:  $\frac{1}{Z} = \frac{1}{Z_1} + \frac{1}{Z_2} + \dots + \frac{1}{Z_n}$ .

Table 2 shows the most used conventional elements in graphical Bode and Nyquist representation (see *Representation of complex impedance*). In most models, interfacial structures are neglected, and just empirical circuit elements are used ('black box' principle with parameters which fit to the experimental data (Bazant, 2019). Especially notable is the constant phase element (CPE), which will be discussed in the following.

*Table 2: Ideal circuit elements (Lvovich, 2012, p. 38) used in models, including a graphical representation of the respective Bode and Nyquist diagram with frequency and  $|Z|$  in logarithmic form and phase,  $Z'$ , and  $Z''$  in linear form.*

Component	Equivalent Element	Impedance	Graphical representation		
Resistor	$R [\Omega]$	$R$			
Capacitor	$C$ [F or $\Omega^{-1}s$ ]	$\frac{1}{j\omega C}$			
Inductor	$L$ [H or $\Omega s$ ]	$j\omega L$			
Warburg diffusion	$Z_W [\Omega]$	$\frac{R_W}{\sqrt{j\omega}}$			
Constant phase element (CPE)	$Q$ or CPE [ $\Omega^{-1}s^n$ ]	$\frac{1}{Q(j\omega)^n}$			

*CPE*: Usually, in a real system, deviations from ideal elements behavior can be observed. These deviations are especially noticeable in the Nyquist representation when the center of the



characteristic semicircle doesn't lie on the x-axis (see Figure 2-13 (a)). A possible explanation for this is that due to unevenness or inhomogeneities of the electrode the resulting impedance has to be modeled by a large number of different capacitors and resistors connected in parallel or series (Figure 2-13 (b)). This situation is equivalent to different "filaments" on the electrode, which have a frequency-dependent effect on the impedance and can be mathematically described by the impedance of a constant phase element:

$$Z_{CPE} = \frac{1}{Q(j\omega)^n}, \quad (2-7)$$

with the fractional exponent  $n$  and the frequency-independent parameter  $Q$ . The name constant phase comes from its phase behavior, which is constant for this element (see Table 2). For  $n = 0$ , the impedance describes a perfect resistor, for  $n = 1$  an ideal capacitor, and  $n = -1$  a perfect inductor. In parallel with a resistor  $R_p$ , the CPE produces a slightly rotated semicircle in the Nyquist plot with a rotation angle of  $(n - 1) \cdot 90^\circ$  (Figure 2-13 (a)).

In the case of a perfect capacitor  $C_p$ , the capacitance can be calculated from the maximum angular frequency  $\omega_{max}$  in the semi circuit of the Nyquist plot using:

$$C_p = \frac{1}{R_p \omega_{max}}. \quad (2-8)$$

According to Hsu and Mansfeld (Hsu & Mansfeld, 2001), the effective capacitance  $C_{eff}$  for the case of a parallel arrangement of a constant phase element and a resistor can be calculated similarly (Figure 2-13 (a)):

$$C_{eff} = Q \frac{1}{(\omega_{max})^{1-n} \sin(n\pi/2)} \approx Q(\omega_{max})^{n-1}. \quad (2-9)$$

If the maximum angular frequency is not available because only parts of the semicircle have been measured, Brug (Brug et al., 1984; Hirschorn et al., 2010) demonstrated that the effective capacitance  $C_{eff}$  for a parallel resistance  $R_p$  and a parallel CPE (see Figure 2-13 (a)) can be calculated with the help of :

$$C_{eff} = \frac{(R_p Q)^{1/n}}{R_p}. \quad (2-10)$$

With an additional serial resistor  $R_s$  (Randel model) the equation (2-10) is modified to:

$$C_{eff} = \left[ \frac{QR_s R_p}{R_s + R_p} \right]^{1/n} \frac{R_s + R_p}{R_s R_p}. \quad (2-11)$$

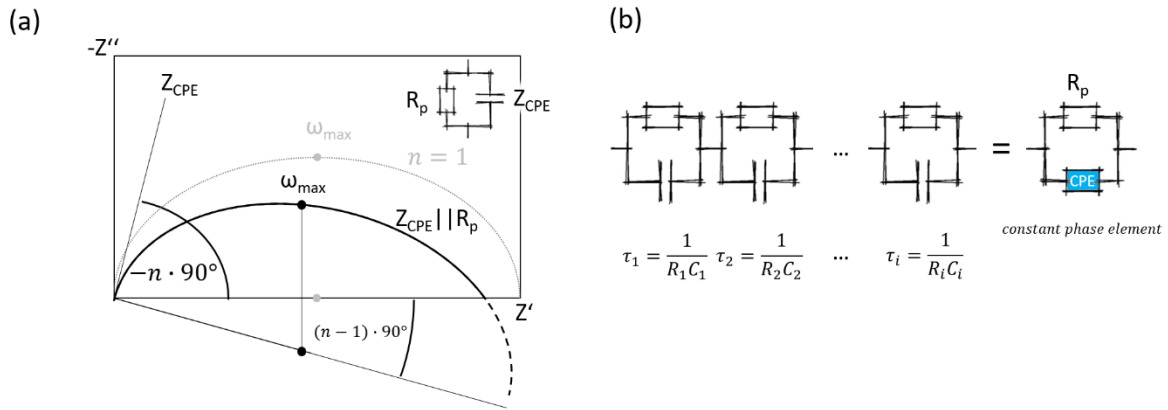


Figure 2-13: Sketch of the CPE behavior, with (a) the Nyquist plot of a CPE parallel to a resistor (inset) as depressed semicircle with  $n=1$  (gray) and  $n$  differs from 1 (black) for extracting the CPE (according to Lvovich, 2012, p. 40,41) and (b) the constellation of a CPE.

It should be noted that CPE elements often are used to fit any type of experimental impedance data by merely varying the  $n$ -parameter and thus do not help to unravel the underlying model of the electronic circuit. Therefore, the CPE just helps to analyze data if there already exists a physical model for the analyzed system.

Generally, the technic of analyzing an impedance spectrum hardly changed in the past century (Bazant, 2019). For different problems, different models are used. For example, the Butler-Volmer model is used for Faradaic reaction kinetics (Thomas-Alyea & Newman, 2012), the Frumkin-Temkin isotherm for ion absorption (Bockris, 1998), the Poisson-Boltzmann model for electrical double-layer structure, the Nernst-Planck model for ion transport (Thomas-Alyea & Newman, 2012), the Helmholtz-Smoluchowski model for electroosmosis (Thomas-Alyea & Newman, 2012), Maxwell-Wagner model for polarization effects at the interface between different components (Lvovich, 2012, p. 8), and the Randles circuit for interfacial impedance. The latter is the model we will use in this work.

## 2.4. Cells as electronic components

Until now, we mainly dealt with the interface between electrode and electrolyte. Ultimately, we want to achieve improved cell-chip coupling, not only to measure or stimulate neuronal activity but also to enable a mechanical stable and biocompatible bond between chips and cells. Besides, the basic research on neuronal cell systems, an “intimate” bond between neurons and electronics might be important for many biological and medical applications. This includes already existing applications of electronic stimulation such as cardiac pacemakers or deep brain stimulators for Parkinson's disease (Hejazi et al., 2020), but also developing areas such as electrical stimulation for epilepsy or type II diabetes (Loeb, 2018), and areas where signal recording is important, such as retina prosthetics (Weiland & Humayun, 2014), or brain-computer interfaces (BCI) for helping people suffering e.g. paralysis (Chaudhary et al., 2020; Fattahi et al., 2014; Thompson et al., 2016).

*Molecular Layer Functionalized Neuroelectronic Interfaces:  
From Sub-Nanometer Molecular Surface Functionalization to Improved Mechanical  
and Electronic Cell-Chip Coupling*

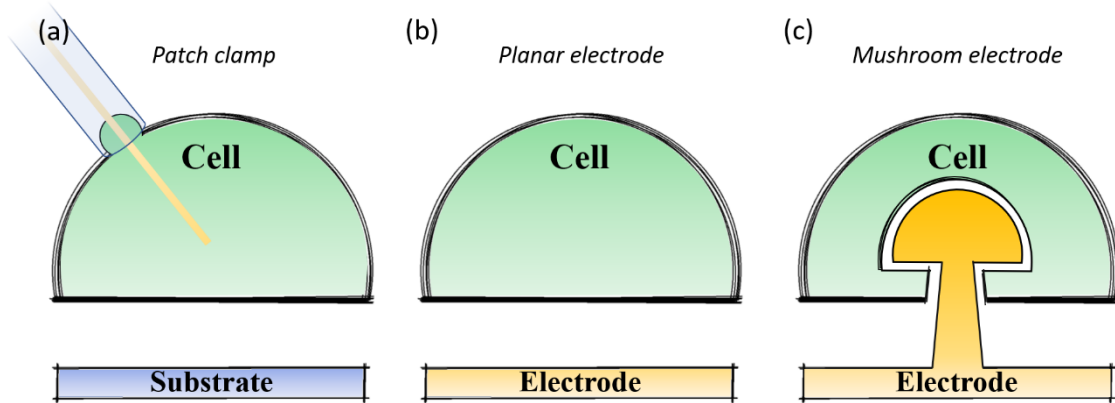


Figure 2-14: Examples of electrical cell signal measurements: (a) intracellular patch-clamp measurements, (b) planar electrode, and (c) 3D electrode (example mushroom-shaped electrode).

*How to measure a neuronal signal:* The biggest challenge, the development of long-life electrodes that are biocompatible, deliver high electrical signals, and cause little to no damage, hasn't been solved yet. However, the methods to approach this goal are manifold. Conventional tools, like intracellular micropipettes (e.g. patch clamps, see Figure 2-14 (a)), have a maximum signal yield but damage the cell within hours. Moreover, it is difficult to extend this method to multiple cell measurements (Wu et al., 2020). Approaches such as planar multi-electrode arrays (MEAs, see Figure 2-14 (b)) are non-invasive but suffer from low signal yield due to a weak electrode-membrane sealing (Wu et al., 2020). The combination of both approaches in the form of 3D electrodes (see Figure 2-14 (c)) is only slightly better than the planar MEAs (Heuschkel et al., 2002; Metz et al., 2001; Thiebaud et al., 1997). For example, mushroom-shaped electrodes increase the effective electrode surface and thus increase the gap resistance (S. Weidlich et al., 2017). However, the improvement is only small (400  $\mu\text{V}$  to 800  $\mu\text{V}$  are reported for recording of  $\sim 100$  mV action potentials) (S. D. Weidlich, 2017) given in the literature (up to 500  $\mu\text{V}$ ) (Spanu et al., 2020; Wu et al., 2020). Additionally, the production of 3D microelectrode arrays is usually associated with complicated and expensive preparation processes and little flexibility (Spanu et al., 2020).

Understanding the structure of neurons, their electronic signal and mechanism of adhesion is of major importance.

### 2.4.1. Structure of neurons

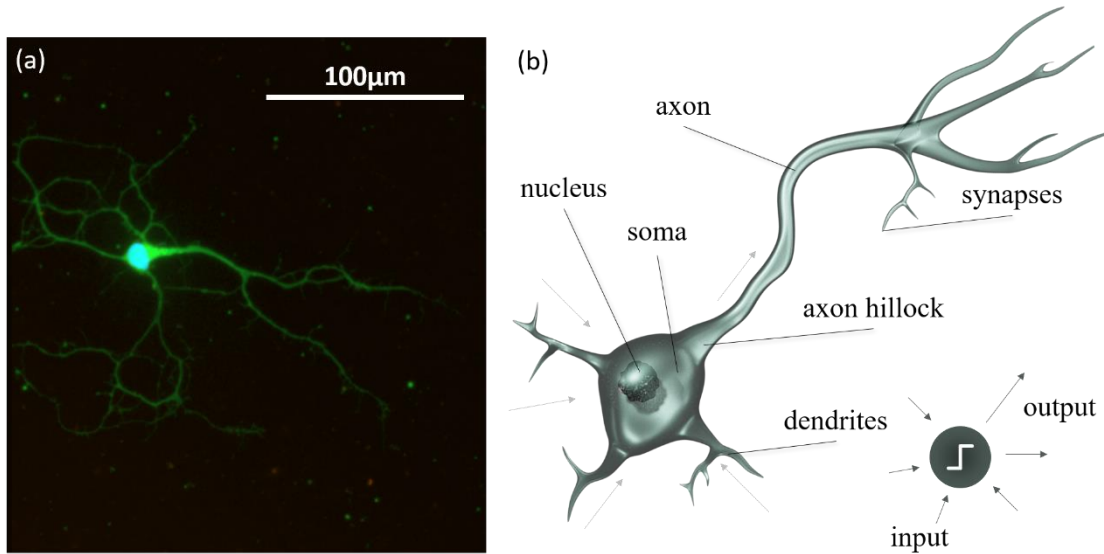


Figure 2-15: Cortical neuron cell with (a) a neuron cell stained in green (calcein) and nucleus stained in blue (DAPI DNA staining) (see Fluorescence Microscopy), (b) schematically sketch of a cortical neuron including the nucleus, soma, dendrites, axon hillock, axon synapses, and a schematic of information collection and transfer (marked by arrows) of a neuron.

Neurons represent the central units of the human nervous system. They are responsible for the information transfer in our bodies by receiving, integrating, and transmitting electrical signals. The general structure of a neuron cell is shown in a fluorescence microscope image in Figure 2-15 (a) and sketched in Figure 2-15 (b). It consists of a cell body, the so-called soma, dendrites, and an axon. The main machinery of the cell is the nucleus (blue-stained in Figure 2-15 (a)), in the soma. The dendrites are collecting the information (input), the axon hillock sums up all input signals and, if a threshold is reached, generates an action potential (AP), which is transmitted via the axon to the synapses where the signal is passed to the next neuron(s) (Figure 2-15 (b)). At the axon, terminal synapses connect electronically and chemically to a neighboring cell. The intracellular amplitude of an AP is ~100 mV (see *Action potential*).

### 2.4.2. Action potential

Neurons are enveloped by a membrane. This membrane consists of a bilayer of phospholipid molecules, it is approximately 5 nm thick and insulating (Kandel et al., 2000). Selective ion channels and pumps are penetrating the membrane to allow an exchange of ions between inside and outside of the cell (intra- and extracellular). The ion channels, special proteins, allow an ion-specific ion-exchange without significant energy consumption. Many factors can change the ion conductivity of the ion channel. The resulting intracellular ion concentration can lead to repolarization or depolarization of the membrane. For a specific ion X, the potential equilibrium  $\Phi_{X,eq}$  can be calculated by the Nernst equation:

$$\Phi_{X,eq} = \frac{RT}{zF} \cdot \ln \left( \frac{c_{X,ext}}{c_{X,int}} \right), \quad (2-12)$$

with gas constant R, temperature T, ions valence z, Faraday constant F, and internal and external ion-specific concentration  $c_X$ . The complete membrane potential  $\Phi_m$  can be obtained via the Goldman-Hodgkin-Katz equation:

$$\Phi_m = \frac{RT}{zF} \cdot \ln \left( \frac{P_{K^+} \cdot c_{K^+,ext} + P_{Na^+} \cdot c_{Na^+,ext} + P_{Cl^-} \cdot c_{Cl^-,ext}}{P_{K^+} \cdot c_{K^+,int} + P_{Na^+} \cdot c_{Na^+,int} + P_{Cl^-} \cdot c_{Cl^-,int}} \right) \quad (2-13)$$

with the ion-specific permeabilities  $P$ . Generally, the ion composition and concentration of the electrolyte inside and outside of the cell differ, which leads to a potential difference, the membrane potential (Dudel, 1998; Kandel et al., 2000). Due to reciprocal diffusion, leakage, and other interactions in the equilibrium state, a resting potential is established, which is typically  $\sim -70$  mV for neurons. If this potential is “depolarized” and reaches a threshold, an action potential (AP) is triggered. The AP can be separated into different phases (Figure 2-16 (a)):

- (i) It starts with a stimulus, which can be due to an external electronic or chemical stimulation or input signals from other cells. If the input signal is strong enough, i.e. higher than the threshold, which is usually at  $-50 \pm 5$  mV (Dudel, 1998; Kandel et al., 2000) (Figure 2-16 (a)), an action potential is triggered, otherwise the stimulus fails to generate an AP.
- (ii) After successful stimulation, the depolarization starts by opening the fast sodium channels. Due to the chemical gradient (at the resting potential, the extracellular  $Na^+$  density is larger than the intercellular  $Na^+$  density), the  $Na^+$  ions flow into the cell. This increases the positive ion concentration in the cell, and the membrane potential rises rapidly up to  $+(40 \pm 10)$  mV.
- (iii) When the sodium ion flow has reached its maximum, the potassium ion channels open and due to the chemical gradient (i.e. larger  $K^+$  density inside than outside the cell),  $K^+$  ions leave the cell (repolarization, Figure 2-16 (a)). The  $Na^+$  channels are successively closed at that time. Both depolarization and repolarization take typically 3 ms to a maximum of 20 ms.
- (iv) The continuous efflux of  $K^+$  ions results in hyperpolarization (a potential slightly below the resting potential of the membrane). The hyperpolarization is a result of the change of the membrane’s permeability and the resulting potassium dominance in the Goldman-Hodgkin-Katz equation (2-13). In this refractory period, no further AP can be created.
- (v) In the end, the membrane is again at its resting potential, and the process can start over again.

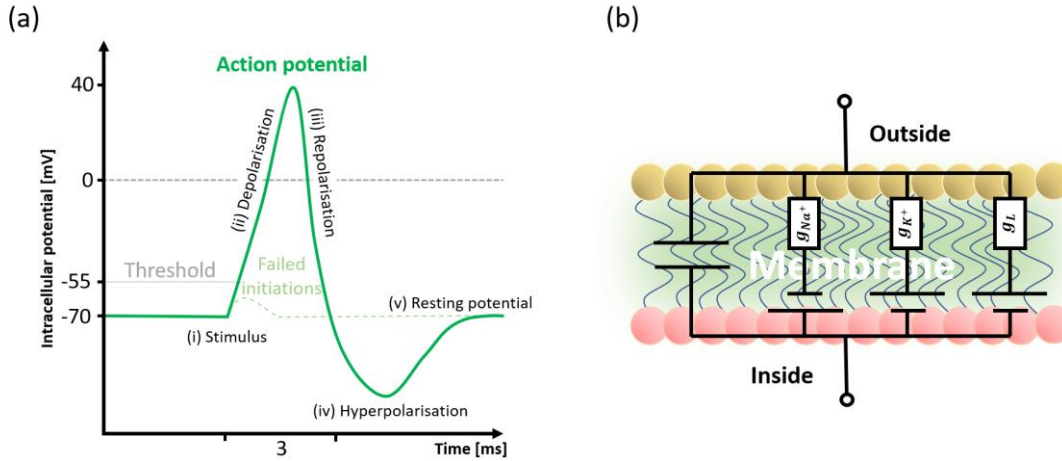


Figure 2-16: Sketches of action potential (a) and cell membrane (b). In (a) the different phases of the action potential and the threshold are shown. Depolarization and repolarization usually take 3 ms. In (b), the equivalent electronic circuit of a cell membrane, according to the Hodgkin-Huxley model, is shown.

Hodgkin and Huxley (Hodgkin & Huxley, 1952) introduced a model of the membrane with different ion conductance (Figure 2-16 (b)) equivalent to an electronic circuit consisting of the different conductance  $g_{Na^+}$  for sodium channels,  $g_{K^+}$  for potassium ions, and  $g_L$  for a leakage current which for instance describes the  $Cl^-$  ions. Parallel to the ion channels, the membrane capacitance has to be added. The resulting current contributions are:

$$\begin{aligned} I_{Na} &= g_{Na}(\Phi - \Phi_{Na,eq}), \\ I_K &= g_K(\Phi - \Phi_{K,eq}), \\ I_L &= g_L(\Phi - \Phi_{L,eq}), \end{aligned} \quad (2-14)$$

and the conductance  $g_K$  and  $g_{Na}$  vary in time with the membrane potential. The total current can then be specified as:

$$I_m = C_m \frac{dV}{dt} + I_{Na} + I_K + I_L, \quad (2-15)$$

where  $V$  represents the difference between resting potential and membrane potential and  $C_m$  is the membrane capacitance per unit area (Figure 2-16 (b)).

### 2.4.3. Cell adhesion

Another essential aspect of neuroelectronics is the cell adhesion to the electronics (typically the electrodes of an electronic). Generally, cell adhesion is their ability to attach to other cells or extracellular surfaces. This adhesion is of significant importance, not only for cell growth but also for cell communication (Metwally & Stachewicz, 2019). The cell adhesion to substrates can be separated into three phases (Table 3) (Hong et al., 2006; Khalili & Ahmad, 2015):

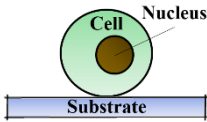
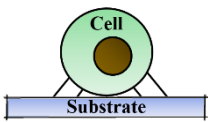
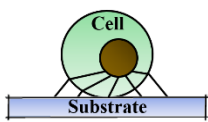
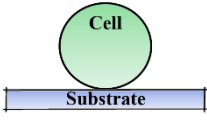
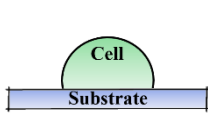
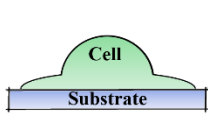
- I. The first phase describes the attachment of the cell body to the substrate. In this phase, cells and substrate interact via electrostatic interaction, which means the surface charge (see *Surface potential*) plays a dominant role in this phase (Metwally & Stachewicz, 2019).

II. Following the initial attachment, the cells continuously flatten and spread on the substrate. The spreading of the cells is the combination of an outgoing adhesion with a distribution and reorganization of the actin skeleton at the cell's body edge (Huang et al., 2003; Khalili & Ahmad, 2015).

III. In the last phase, the cell reaches the maximum area by spreading and organization of the actin skeleton with the formation of focal adhesion.

The bonds between substrate and cell get stronger the longer the cell adheres (Khalili & Ahmad, 2015). The adhesive bond is defined by the sum of all non-covalent (i.e. physical) bonds (e.g. hydrogen bonds, or van der Waals, dipole-dipole interaction) (McEver & Zhu, 2010).

*Table 3: The three stages of in vitro cell adhesion, starting with the electrostatic cell attachment to the substrate, the flattening and spreading of the cells to the formation of focal adhesion points (Adapted from (Khalili & Ahmad, 2015)).*

Cell Adhesion Phases	Phase I	Phase II	Phase III
Schematic diagram of cell adhesion			
Schematic diagram of the transformation of cell shape			
Cell adhesion mechanism	Electrostatic interaction	Integrin bonding	Focal adhesion
Adhesion stages	Sedimentation	Cell attachment	Cell spreading and stable adhesion

#### 2.4.4. Neuroelectronic circuit

In addition to Hodgkin and Huxley (Hodgkin & Huxley, 1952), who modeled the membrane in terms of an electrical circuit, Beer created an electrical model that describes the basic components of a neuroelectronic circuit (Beer, 1990). Figure 2-17 (a) shows all basic electronic elements of a neuron, the incoming and outgoing synaptic current and the intrinsic current, which mimics the complex electronic behavior of neurons and the interaction with other sensory neurons. The following R-C component represents the membrane impedance. Finally, there is the fire rate function, which does not represent every single action potential, but the overall rate of pulses at a given time.

If we add a simple electrode to this picture (Figure 2-17 (b)), then the model can be simplified using the point contact method (Fromherz et al., 1991; Ingebrandt et al., 2005), which facilitates the coupling between electrode and cell to a simple point contact. The model assumes that electrolyte penetrates into the gap between cell and electrode, which adds a seal resistance  $R_{\text{seal}}$ . The cell membrane is a simplified version of the Hodgkin and Huxley representation (Figure 2-16 (b)) with only one R-C circuit and divided into the free membrane area  $Z_f$ , (i.e. the area that is only connected to electrolyte) and the junction area  $Z_j$  which is located above the

*Molecular Layer Functionalized Neuroelectronic Interfaces:  
From Sub-Nanometer Molecular Surface Functionalization to Improved Mechanical  
and Electronic Cell-Chip Coupling*

electrode (Figure 2-17 (b)). This model allows us to describe the electronic properties of the cell-chip coupling in a simple and reasonable way.

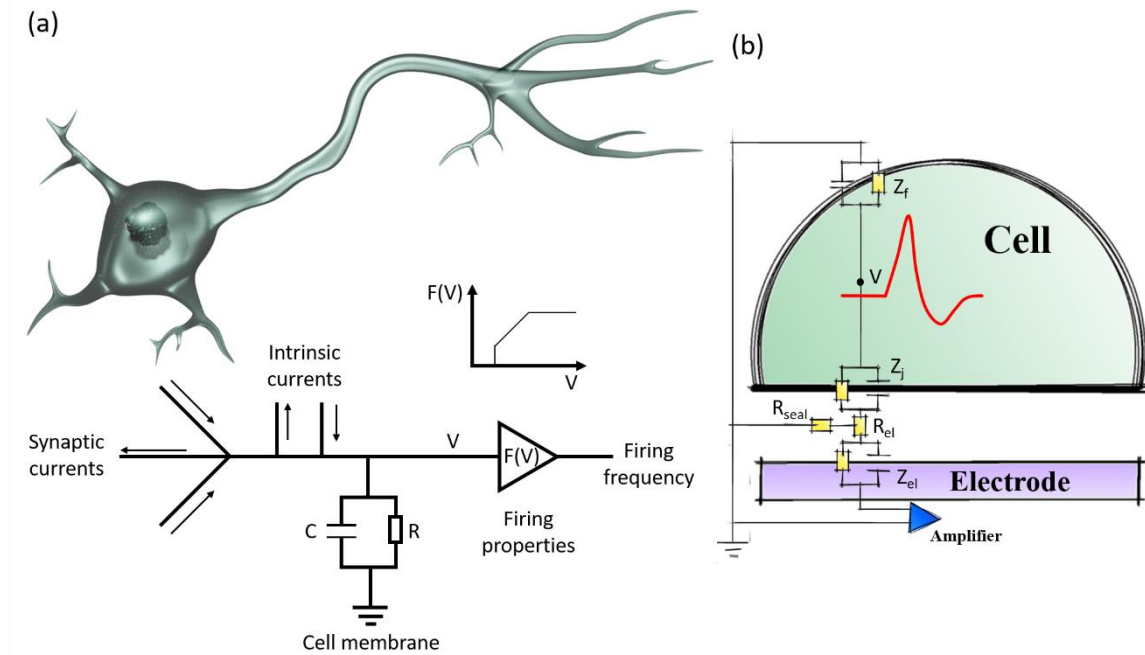


Figure 2-17: Neuronal electronic circuits, with (a) a neuron as an element in an electrical circuit (adapted from Beer (Beer, 1990)) and (b) simplified representation of cell-chip coupling as an electronic circuit.



### 3. Experimental Methods

In this chapter, the experimental methods and sample preparation used in this work are described in detail. Starting with the sample preparation and processing, following the characterization methods, and finally, the cell culture and analysis techniques are sketched.

#### 3.1. Choice of substrates, molecules, and sample preparation

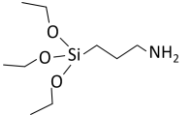
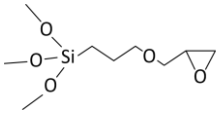
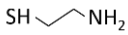
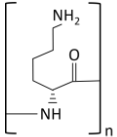
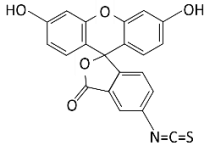
Different samples were prepared for different experiments. These samples, with the corresponding parameters, are listed below.

- For the analysis of APTES on SiO<sub>2</sub>, p-doped (111)-oriented silicon (Si-Mat, 3.6-6.5 Ω-cm) with a 100 nm thick SiO<sub>2</sub> layer was used.
- For the analysis of APTES on Pt, p-doped (111)-oriented silicon (Si-Mat, 3.6-6.5 Ω-cm) with 500 nm thick SiO<sub>2</sub> layer, 10 nm adhesion Ti layer, and a 50 nm Pt top layer via evaporation was used.
- For the SPR analysis for APTES on Pt, special substrates (HIGHINDEX-CG, company Olympus), a type of lanthanum dense flint with a high refractive index and a thickness of 0.1 mm, were used. These substrates were coated with a 6 nm Ti adhesion layer and a 17 nm Pt top layer.
- For impedance and action potential measurements, 0.5 mm thick quartz wafers with 5 nm adhesion Ti layer and a 45 nm Pt top layer via evaporation were used.
- For long term cell cultures, quartz substrates with 5 nm Ti and 5 nm Pt coating were used to ensure transparency for the bottom-up microscopy.

The different organic molecules are listed in Table 4.

The central organic molecule of this work is (3-aminopropyl)triethoxysilanes (APTES) (99%, SigmaAldrich), which was stored in Ar protection gas in a glovebox. For the deposition process, 0.2 ml APTES was filled into a glass container, which is attached to the molecular deposition chamber for our gas-phase deposition (see chapter 3.1.4).

Table 4: Organic molecules used in this work.

<b>Molecule</b>	<b>Structure</b>	<b>Deposition process</b>	<b>Schematic</b>
APTES (3-aminopropyl)triethoxysilanes	$C_9H_{23}NO_3Si$	Gas phase MLD	
GLYMO (3-Glycidyloxypropyl)trimethoxysilane	$C_9H_{20}O_5Si$	Gas phase MLD	
CYS Cysteamine	$C_2H_7NS$	Gas phase MLD	
PLL Poly-L-lysine	$(C_6H_{12}N_2O)_n$	Liquid deposition	
FITC Fluorescein isothiocyanate	$C_{21}H_{11}NO_5S$	Liquid deposition	

### 3.1.1. Chemical cleaning

The quality and formation of SAMs depend strongly on the cleanliness of the surface (Lessel et al., 2015). Therefore, it is essential to carry out thorough cleaning steps. All samples were cleaned at the beginning and intermediate steps in a cleanroom environment (ISO 1-3) in acetone (>99.9 %, Sigma-Aldrich) and propanol (2-propanol, >99.8 %, Sigma-Aldrich) in an ultrasonic bath, for 5 min each at 25 °C, 320 W and a frequency of 37 kHz. After cleaning, the samples were dried under nitrogen flow.

### 3.1.2. Lithography

Two different lithographic methods are used in our institute, e-beam lithography and optical lithography. During the optimizing process of the design of the MEA and the molecule pattern used in this work, high flexibility was required and therefore e-beam lithography was used. Moreover, the resolution of e-beam lithography can reach down to 10 nm (Broers et al., 1996), which helps create precise patterns, e.g. electrodes (in contrast, optical lithography has an approx. 10 – 100 times lower resolution).

Consequently, the different patterns for molecules and electrodes (e.g. MEAs) were obtained via standard e-beam lithography and lift-off technique. For this purpose, special designs are developed (using AutoCAD 2020). The different lithographic steps are sketched in Figure 3-1

(a) and (b) for metallic electrode preparation and the molecule patterns, respectively. Both processes are described in the following and are based on (*Lab Protocol*, n.d.):

- (i) *Resist and chrome layer*: The photoresist poly(methyl-methacrylate) (PMMA AR-P 669.07) is spin-coated on the substrate using 4000 rpm for 60 s (Figure 3-1 (c)). The substrate is completely covered with resist, and the resulting thickness of the PMMA layer is approx. 700 nm. Directly after spin-coating, the sample is placed on a 120 °C hot plate in a closed container and remains there for half an hour. To prevent the sample from sticking to the heating plate, the backside is brushed over a tissue soaked in acetone on the way from the spin coater to the heating plate. In the case of non-conducting substrates, a 10 nm Cr layer is deposited on the PMMA. The Cr layer is necessary to obtain the required conductance for e-beam writing.
- (ii) *E-beam writing*: For the e-beam writing (Figure 3-1 (a & b) (ii)) a mask is designed, typically with design and drafting software, e.g. AutoCAD (here Autodesk AutoCAD 2020). The e-beam writing is done with VISTEC EBPG 5000 plus. The electron beam cracks the polymers in the PMMA at the positions that are exposed to the beam.
- (iii) *Cr etching and development of PMMA*: In case of the use of a chrome layer, the Cr layer has to be etched after e-beam writing. For this, a special solution is used, which consists of water, ceric ammonium nitrate, and perchloric acid. The Cr etching solution has an etching rate of about 80 nm/min (B. Cai, 2016), the appropriate etching time is ~12 s for the 10 nm thick Cr layer. After etching, the sample stays in propanol for 60 s. To develop the PMMA pattern, the sample is dried with nitrogen gas and submerged for 90 s in the developer AR600-55. After the development, the PMMA, which was exposed to the e-beam, is removed, whereas the unexposed areas are still covered with PMMA (see Figure 3-1 (h), dark spots are areas without PMMA). To remove left-overs of PMMA, the samples are placed for 3 s in an oxygen plasma (Figure 3-1 (e)).
- (iv) *Metallization and molecule deposition*: For the metallic structure and electrodes (Figure 3-1 (a) (iv)) first, an adhesion layer of Ti is deposited before the actual electrode material Pt is deposited. Both metals are evaporated on the PMMA and the open areas. Depending on the application, the thickness of the Ti- and Pt-layer are different and range from 5 nm to 10 nm for Ti and 5 nm to 50 nm for Pt (see *Choice of substrates, molecules, and sample preparation*). In the case of molecular patterns, the substrates are transported to our MLD device, and instead of metal deposition, molecules are deposited on the PMMA patterned surface. The detailed steps for the deposition are described below in *Molecular layer deposition*.
- (v) *Lift-off*: To obtain the final structure, the PMMA, together with the Ti/Pt layer or molecule layer on top of the PMMA, is removed (therefore lift-off). The removal of the PMMA is done by placing the sample in acetone in an ultrasonic bath (10 min, 25 °C, 320 W, 37 kHz). In the next step the acetone is removed with propanol (for 1 min in an ultrasonic bath) and dried with nitrogen gas. In the end, only the wanted metal or molecule structure is left over (see Figure 3-1 (a & b) (v-vi) and Figure 3-1 (g)).

*Molecular Layer Functionalized Neuroelectronic Interfaces:  
From Sub-Nanometer Molecular Surface Functionalization to Improved Mechanical  
and Electronic Cell-Chip Coupling*



Figure 3-1: Lithography and lift-off technology for sensor creation (a) and patterned molecule deposition (b) consisting of (i) PMMA and (optional) chrome coating, (ii) e-beam writing, (iii) chrome etching, development and oxygen plasma/ozone cleaning, (iv) metal vaporization/molecule deposition, (v) lift-off; (vi) represents the sample with the resulting electrodes/stripes of molecules. Additional pictures of (c) spin coater, (d) 10 x 10 mm<sup>2</sup> SiO<sub>2</sub> and Pt samples, (e) plasma oven, (f) ozone generator, (g) wafer with 9 sensors, and (h) patterned sample for molecule deposition.

### 3.1.3. Ozone cleaning and ozone activation

When a sample surface comes into contact with the environment, also organic contamination can occur. Therefore, it is important to clean each sample with ozone directly before the deposition of the organic molecules starts. Additionally, to the cleaning, the surface has to be activated, i.e. unsaturated OH bonds form on the surface, which serves as docking points for the organic molecules. All these processes take place in the deposition chamber (see Figure 3-2), which allows us to deposit the molecules directly after cleaning and activation without opening the deposition chamber.

For ozone cleaning and activation, the substrates are placed in the molecular layer deposition (MLD) chamber (see Figure 3-2), which is then evacuated to a pressure of  $\sim 10^{-5}$  hPa. After the

evacuation, the chamber is subsequently flooded with oxygen (99.99 % purity) up to an oxygen pressure of 100 Pa. Using a microwave discharge at a frequency of 2.45 GHz and a power of 700 W, ozone is generated (Figure 3-1 (f)) and directed with the oxygen flow (100 sccm) to the chamber with the substrate (Figure 3-2 (a)). The ozone leads to the removal of residual organic impurities on the surface. Parallel to the cleaning, the ozone might activate the surface, as known for oxides like SiO<sub>2</sub> (Yuan et al., 2019), or might create a thin layer of Pt oxide on the Pt surface. Since the ozone treatment is performed in our MLD chamber (see next section *Molecular layer deposition*), we benefit from the advantage that the molecules can be deposited directly after activation, i.e. without delays and a possible decay of the activation.

#### 3.1.4. Molecular layer deposition

The gas-phase deposition of the molecules took place in our self-made molecular layer deposition (MLD) device, which is shown schematically in Figure 3-2 (a) and as an image in Figure 3-2 (b). During this work, the MLD was constantly developed further. Finally, the MLD device now consists of different components: mixer with the molecular sources, the MLD chamber, and the ozone generator (see Figure 3-3), which are described in more detail below.

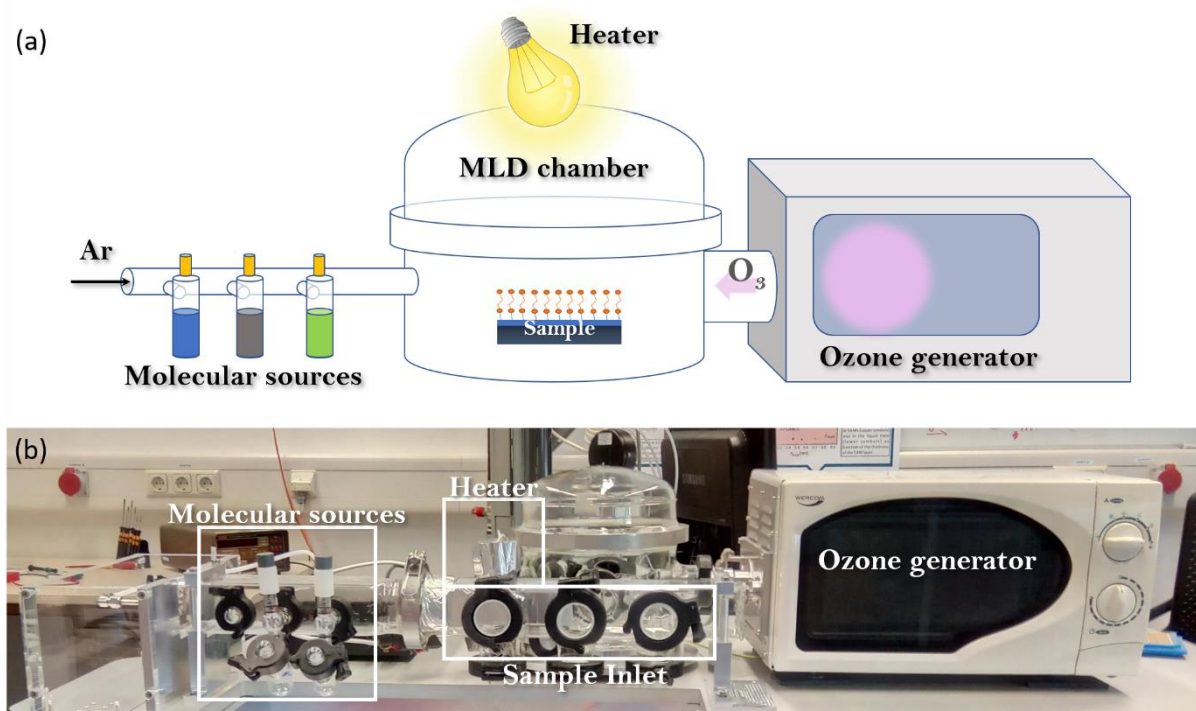


Figure 3-2: MLD chamber for gas-phase deposition of molecules: (a) schematic setup and (b) picture, consisting of (from left to right) the molecular sources, the chamber for deposition, and the ozone generator for cleaning and activating the samples.

**Mixing chamber:** The working gas (Ar or N<sub>2</sub>) flows first into the mixing chamber (Figure 3-3, light blue) to establish the adequate concentration of organic molecules in the gas. The chosen pressure depends on the vapor pressure of the molecules. The gas flow passes the molecule sources. Three different molecule sources can be installed simultaneously (e.g. for multi or mixed layer deposition (Markov et al., 2017)) which can be opened without interrupting the protective atmosphere. Each of these sources can be additionally heated in a water bath to

enhance the vapor pressure. The molecules are transported by the working gas flow towards the three insets for sample stages or sensors. Lamps can be placed above each of the stations to heat the samples radially (Glass, 2020) (see Figure 3-2).

*MLD chamber:* From the mixing chamber, the flow continues into the MLD chamber (Figure 3-3, light green). In the middle is another sample table on which larger samples (wafers) or several samples can be placed. The MLD chamber is the central chamber where the mixing chamber, pump, ozone generator and various control sensors (e.g. pressure sensor, capacitance sensor, and resistive sensor, which are used to monitor the molecular deposition (Markov et al., 2017; Wolf, 2017)) are connected.

*Ozone generator:* The ozone generator (Figure 3-3, light red) is a modified microwave oven (see Figure 3-2 (b)) through which oxygen passes during the cleaning and activation (during this time the working gas Ar or N<sub>2</sub> is switched off). The oxygen converted into a plasma by the microwaves and ozone is generated. This ozone flows into the system and breaks up organic residues (cleaning) and activates the samples. Since this process (cleaning and activation) can be performed without interrupting the protective atmosphere, a perfect cleanliness and degree of activation can be achieved prior to the actual deposition of the molecules.

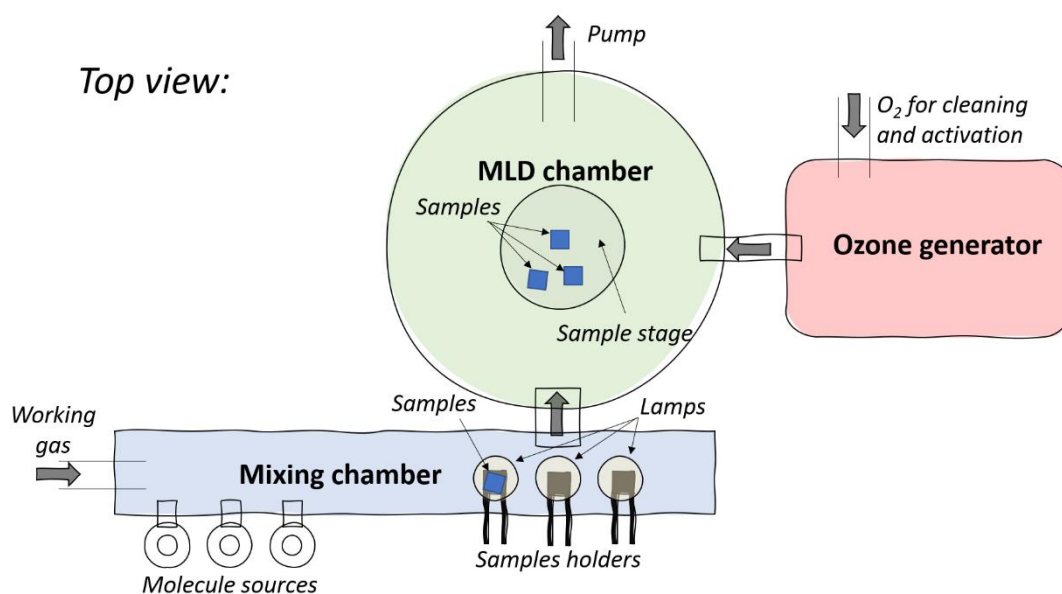


Figure 3-3: Sketch of the MLD chamber (top view), including the three main areas, the mixing chamber with molecular sources (blue), the main MLD chamber (green), and the ozone generator (red). The arrows mark the direction of the gas flow (oxygen and working gas) for different processes.

A typical APTES deposition process starts with inserting the samples and evacuate the system. The pressure of 10 mPa can be reached. Prior to the deposition, the substrates are always cleaned and activated for 3 minutes with ozone in the MLD setup (the procedure is described above in Ozone cleaning and ozone activation). After surface activation, the oxygen supply is turned off, and the process gas is switched to Ar (10 Pa, 27 sccm) for the deposition. The actual deposition of APTES is initiated by opening the valve of the molecule source. After 10 minutes of deposition, the valve of the molecule source is closed again. After the deposition, the samples are kept in the MLD device under vacuum condition for 2.5 days post-deposition treatment,

which is vital for the formation of APTES SAMs for gas-phase deposition at room temperature (Yuan et al., 2019) (see S 5 in *Appendices*).

### 3.2. SAM characterization

After the deposition, measurements are necessary to analyze the molecular layers. In this work ellipsometry, fluorescence microscopy, atomic force microscope (AFM), time of flight secondary ion mass spectrometry (ToF-SIMS), surface plasmon resonance (SPR), streaming potential, and impedance spectrometry were used. In the following chapter, these ex-situ characterization methods are described in more detail.

#### 3.2.1. Ellipsometry

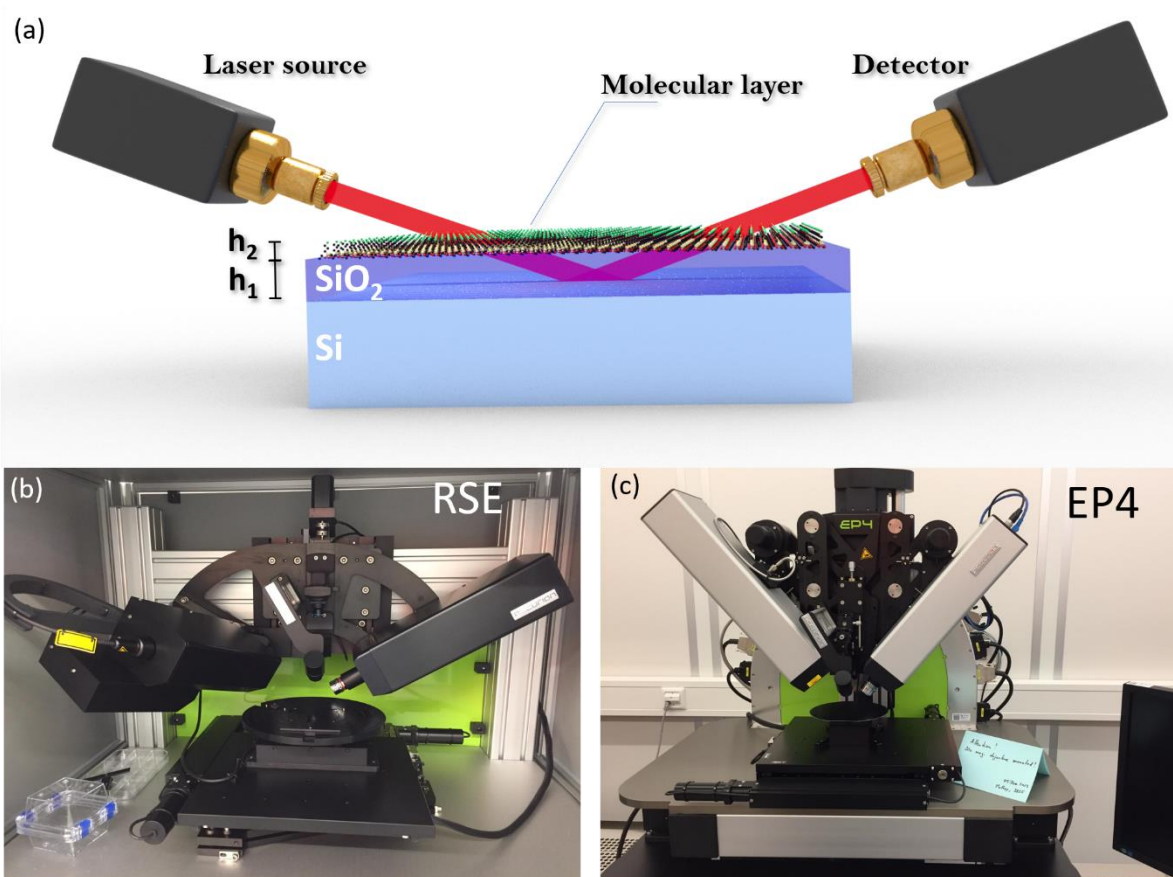


Figure 3-4: Ellipsometry setup, with (a) a sketch of the working principle, and (b) and (c) pictures of the two ellipsometers used in this work (Lab Collection, n.d.).

Ellipsometry is a very sensitive optical method that has been used to analyze surfaces and thin films for about a hundred years. It exploits the fact that the state of polarization of light can change when the light beam is reflected from a surface or interface. If the surface is covered with a thin film, the entire optical system of film and substrate affects the change in polarization. It is, therefore, possible to obtain information about the film properties, in particular the film thickness, via this technique.

Two different ellipsometer setups (RSE (Figure 3-4 (b)) and EP4 (Figure 3-4 (c))) are used in this work. They operate on the same working principle, which is sketched in Figure 3-4 (a) and

in Figure 3-5. The linear polarized white light is first guided to a reference sample where the beam is reflected with an angle of incidence (AOI). This reference sample is rotated by 90° around the central beam axis (Figure 3-5). From the reference probe, the laser beam is directed to the sample to be examined, where it is reflected with the same AOI. The light passes through an analyzer and is detected by a spectrometer, where the final polarization of the beam is analyzed. The final polarization of the laser light is then modeled using the known (or assumed) layer sequence with the corresponding diffraction index to obtain the thickness of a layer. Alternatively, one can also deduce the diffraction index for a layer if its thickness is known.

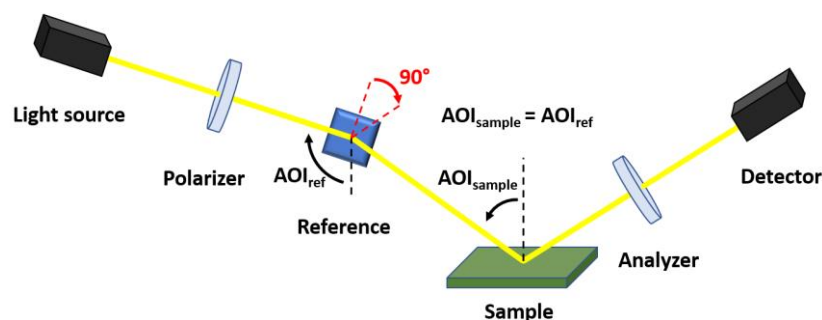


Figure 3-5: Pathway of the laser beam of the RSE (adapted from (Glass, 2020)). The light is first polarized then reflected on a reference sample to the sample to be analyzed, back to an analyzer, and finally to the detector. The reference sample is rotated by 90° with respect to the beam axis.

Most of the measurements were performed with a reference spectroscopic ellipsometer (Accurion nanofilm RSE) (see Figure 3-4 (b)). Since the thin molecular layer can only be detected in the comparison of areas with and without molecules, patterned molecule layers are used in these measurements (see *Lithography*). For reference samples (SiO<sub>2</sub> terminated Si coated with APTES), a three-layer model (SiO<sub>2</sub>-APTES-air) was used, whereas a 2-layer model (APTES-air) was used for Pt coated substrates with APTES. For APTES, a reflective index of  $n = 1.413$  has been chosen (Yameen et al., 2013). The set of material parameters used in this work is given in Table 5.

Table 5: Parameters used for ellipsometry.

Material	Reflection index
Air	1
APTES	1.413
SiO <sub>2</sub>	1.454

### 3.2.2. Fluorescence Microscopy

Fluorescence microscopy was used for the visualization and analysis of:

- molecule layers on Si-based substrate using a fluorescent marker and
- living and dead staining of neuronal cells using fluorescent dyes (see *Neuronal cells*).

The fluorescence microscope is based on the fluorescence of material (e.g., molecules), which absorbs and emits upon illumination. The emission is based on fluorescence, a form of luminescence, and usually has a longer wavelength, and thus, lower energy. The emission happens with a small delay of a few microseconds after the illumination of the material. The



emitted light, which is much weaker than the illumination, is recorded. The detection limit depends on the brightness of the background.

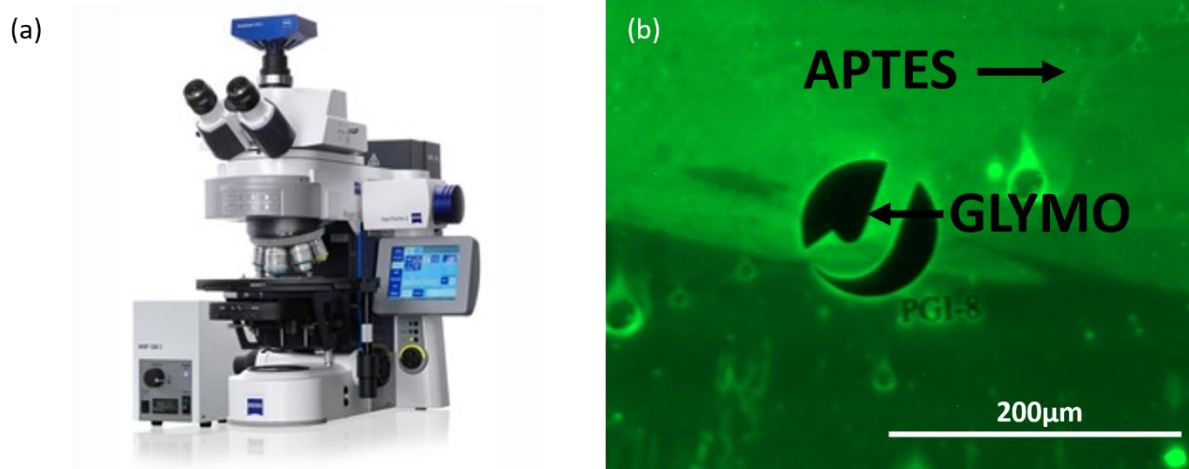


Figure 3-6: Apotome fluorescence microscope (a) (taken from (SelectScience, n.d.)) and example results (b) showing a patterned APTES layer marked by FITC with GLYMO, which doesn't bind FITC, filling the openings.

For fluorescence analyses of the molecular layers and for the cell cultures, a Zeiss Apotom microscope (increased axial resolution) (Figure 3-6 (a)) and the associated Zen microscope software were used. Fluorescein isothiocyanate (FITC) was used as an optical marker for the analysis of the molecular layers. FITC is a fluorescein molecule functionalized with an isothiocyanate-reactive group. This group is reactive with nucleophiles, which includes amine groups. Therefore, FITC binds excellently to APTES (Figure 3-6 (b) and S 2 in *Appendices*).

The preparation steps are performed according to the (*Lab Protocol*, n.d.). FITC was mixed with a concentration of 10 µg/mL with ultrapure water. The sample coating is done via liquid deposition. A drop (100 µL) of the FITC solution is placed on the sample and kept at room temperature for 1 h in a dark room to avoid any exposure to light. The samples were rinsed with ultra-pure water twice, each time for ~ 2 min, to remove all unbound FITC molecules from the surface. After rinsing, the sample was purged in N<sub>2</sub> flow. In the end, only chemisorbed FITC remains on the APTES surface, unbound FITC and physisorbed FITC are removed during the rinsing step (Figure 3-6 (b)).

### 3.2.3. Atomic force microscopy

Atomic force microscope (AFM) represents a mechanical scanning technique of surfaces on a nanometer-scale, which is based on atomic interaction between a scanning tip and the surface of the sample (Figure 3-7). A (fragile) tip on a cantilever is moved above the surface, the motion of the tip depends on the topography of the surface. The topography is measured and recorded via a reflected laser beam on the cantilever (Figure 3-7 (a)), which is detected with 2D position-sensitive photodetector. The vertical motion of the tip is due to the atomic interaction (force) between the tip and the surface. A typical image obtained from a patterned molecular layer on a surface is shown in Figure 3-7 (c). The AFM can measure in different modes. In the contact mode, the topography is scanned, whereas in the tapping mode (phase image) van der Waals force (without contact) or the elasticity (in contact with the surface) are analyzed.

AFM images were recorded using a Nanoscope MultiMode 8 microscope (Bruker) with a piezoelectric scanner (E-series with a scan range of  $8\ \mu\text{m} \times 8\ \mu\text{m}$ ) applied on an area of  $50 \times 50\ \mu\text{m}^2$  in the center of the larger area in the tapping mode (*Lab Protocol*, n.d.). Aluminum back-coated Si cantilevers (Bruker, OTESPA-R3) were used with a nominal tip radius of  $\sim 7\ \text{nm}$  and a typical spring constants of  $k \approx 26\ \text{N/m}$ ,  $f_0 \approx 300\ \text{kHz}$ .

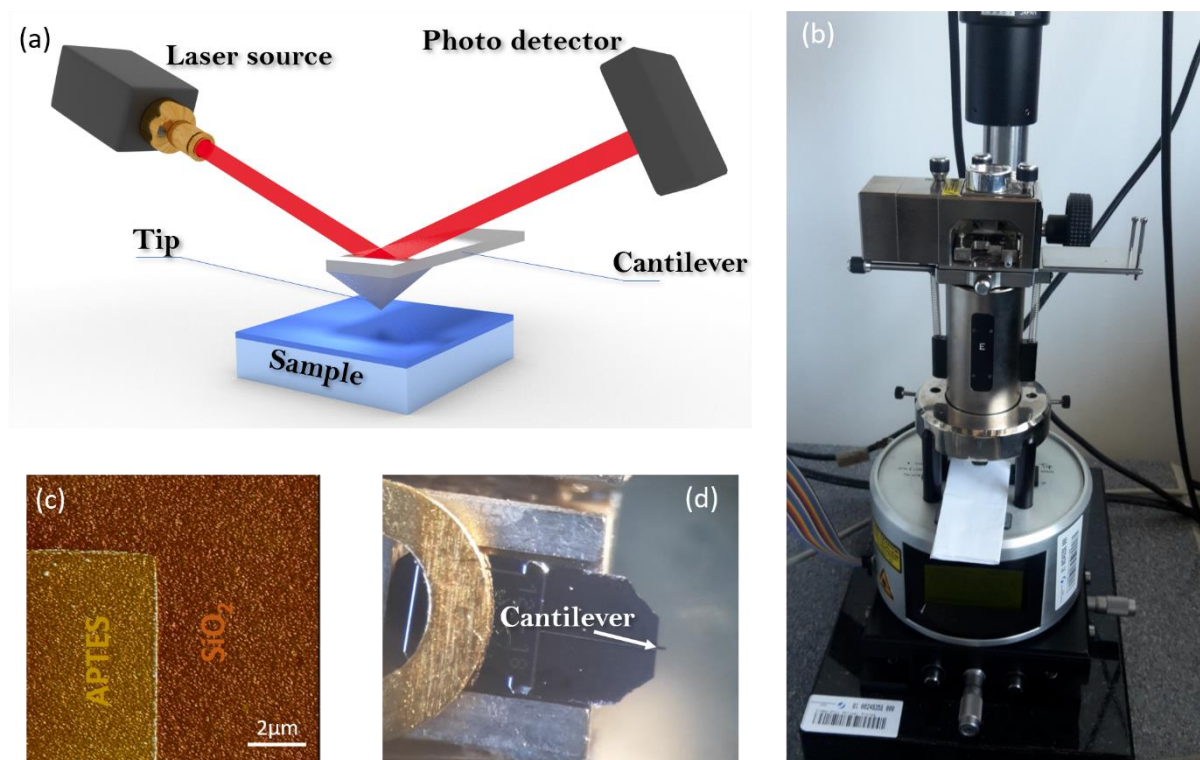


Figure 3-7 AFM setup with (a) a sketch of the working principle, (b) an image of an AFM setup, (c) an example of a typical measurement of a patterned APTES layer on  $\text{SiO}_2$ , and (d) a picture of the cantilever and parts of the holder. In (c), the yellowish part represents the area covered with molecules and the reddish part the pure  $\text{SiO}_2$  substrate.

#### 3.2.4. Time of flight secondary ion mass spectrometry

In time-of-flight secondary ion mass spectrometry (ToF-SIMS), the surface of the object under investigation is bombarded with primary ions (usually noble gas, gallium, or bismuth ions), secondary particles (positive and negative ions as well as neutral particles) are released from the uppermost atomic layers of the sample, which can consist of single atoms, but also of clusters and fragments and the emitted ions (positive or negative) are identified with a time-of-flight mass spectrometer providing information about the chemical composition of the sample surface.

*Molecular Layer Functionalized Neuroelectronic Interfaces:  
From Sub-Nanometer Molecular Surface Functionalization to Improved Mechanical  
and Electronic Cell-Chip Coupling*

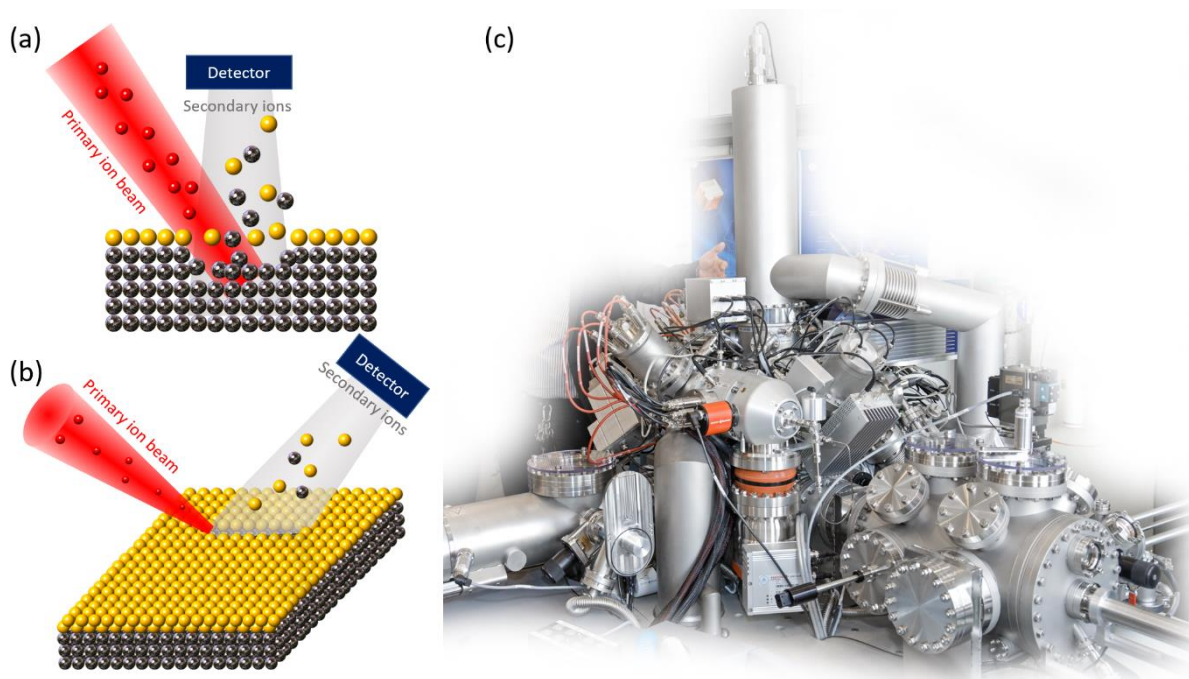


Figure 3-8: Schematic of ToF-SIMS for (a) depth profile and (b) mapping; in (c) an image of the ToF-SIMS IV used in this work is shown [Copyright: Forschungszentrum Jülich / Ralf-Uwe Limbach].

For this type of spectroscopy, the surface is bombarded with an ion beam and the surface species are sputtered off. Mainly neutral ions are produced, but also ions with positive or negative charges, which are then analyzed in a time-of-flight (ToF) tube. The ions are detected by a dual channel plate. Due to the effect of the ion beam on the surface, the material is continuously removed, which means that as the sputtering time progresses, the material is penetrated deeper and deeper. This allows a depth profile of the sample to be analyzed.

With a lower dose of the ion beam, however, it is also possible to scan over the sample to be analyzed, thus obtaining element or distribution maps. With these maps, quantitative statements can be made, e.g., structured surfaces. Depending on the primary source used, resolutions of about one micrometer can be achieved in spectroscopy and mapping.

A ToF-SIMS setup (TOF.SIMS IV.NCS, IONTOF GmbH, Germany) (Figure 3-8 (b)) was used to analyze the molecular layers on Pt. For the analysis of the material's depth profile, a Cs beam (1 keV, 90 nA) was applied to remove material on a layer area of  $300 \times 300 \mu\text{m}^2$  with a sputter ion dose density of  $1.49$  to  $2.15 \cdot 10^{17}$  ions/cm<sup>2</sup>. For the material analysis, a primary ion beam of Bi<sup>+</sup> ions with an energy of 30 keV and a primary ion dose density of  $1.84$  to  $2.59 \cdot 10^{14}$  ions/cm<sup>2</sup> is applied to a smaller area of  $50 \times 50 \mu\text{m}^2$  in the center of the larger area. For the mapping of the elements at the surface, only the primary beam of Bi<sup>+</sup> ions are used.

### 3.2.5. Surface plasmon resonance spectroscopy

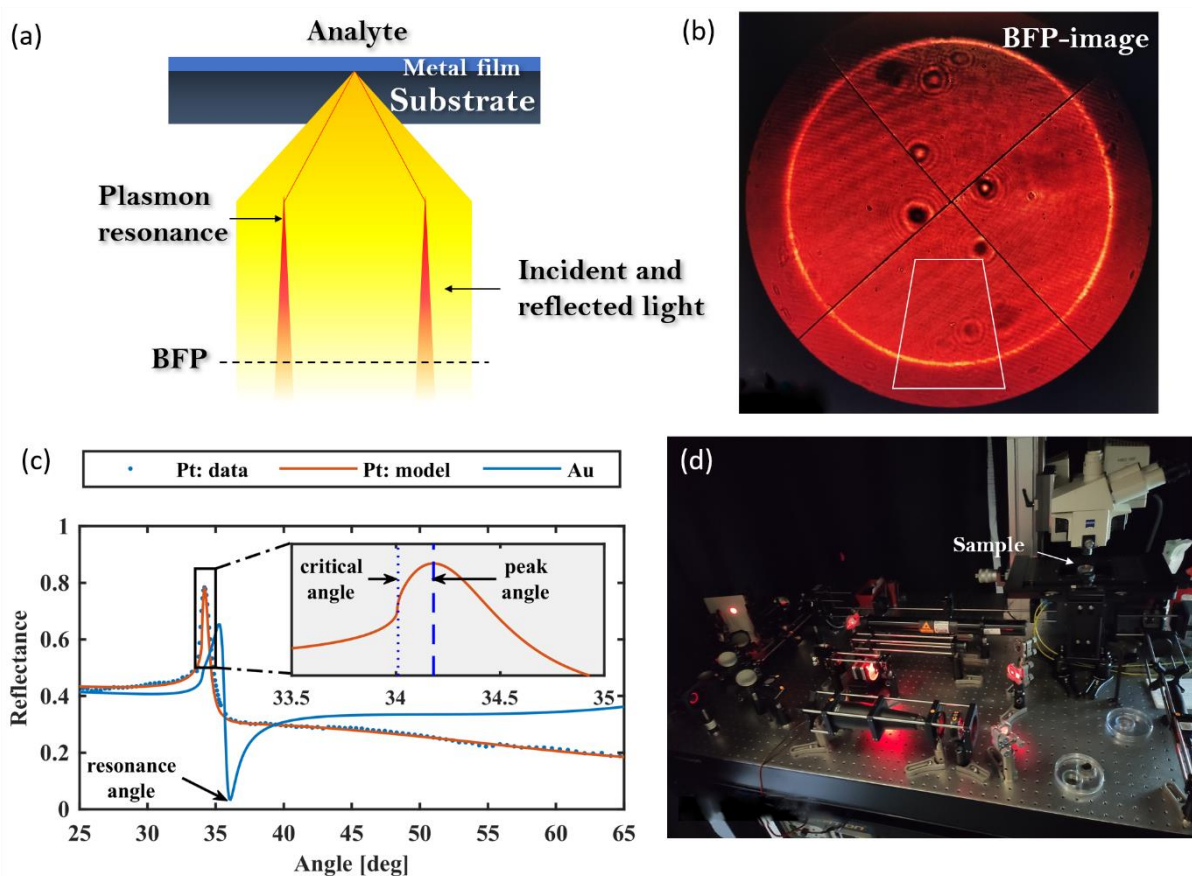


Figure 3-9: SPR-spectroscopy with (a) the sketch of the light path (adapted from (Kreysing et al., 2018)), (b) image of the back focal plane (BFP) with the white marked area used for (c) the resulting measurement including model fits for Pt and Au (taken from (Hassani et al., 2020)) and (d) image of the SPR setup.

Surface plasmon resonance (SPR) spectroscopy represents an analysis method for a fast-quantitative determination of layer thicknesses or gap sizes in the nanometer range. For this purpose, surface plasmons are excited on a thin metal layer on which the analyte is located. For this, the back of the metal, i.e., the other side of the analyte, is examined for total reflection with polarized light using a prism. The refractive index of the analyte significantly influences the excitation conditions and thus the angle.

We used an objective-based SPR microscope setup, which is shown schematically in Figure 3-9. It requires the use of specific samples consisting of high-index coverslips usually coated with a thin gold layer (Hassani & Kreysing, 2019). In this work, we successfully introduced Pt (which represents our electrode material) as a metal layer for surface plasmon (Hassani et al., 2020). These samples were covered with molecular layers and placed on top of a total internal reflection fluorescence (TIRF) objective and illuminated spot-wise using radially polarized He – Ne laser light. The laser light is focused on the backside of the sample and excites surface plasmon waves. Due to the plasmon resonance, the plasmon can be analyzed by imaging the reflected light at the back focal plane (BFP) (Figure 3-9 (a) and (b)). By fitting the reflection (Figure 3-9 (c)), a quantitative statement about the layer thickness of each point or pixel can be obtained, a scan of the sample could even yield the layer profile (Hassani et al., 2020).

### 3.2.6. Streaming potential analysis

The electrokinetic potential measurement is a powerful tool to analyze the electronic properties of a surface. The theoretical background of the surface potential and Helmholtz layer was already described in *Surface potential*. In this work, the streaming current method is chosen for the determination of the  $\zeta$  potential. A schematic of the principle and the setup are shown in Figure 3-10.

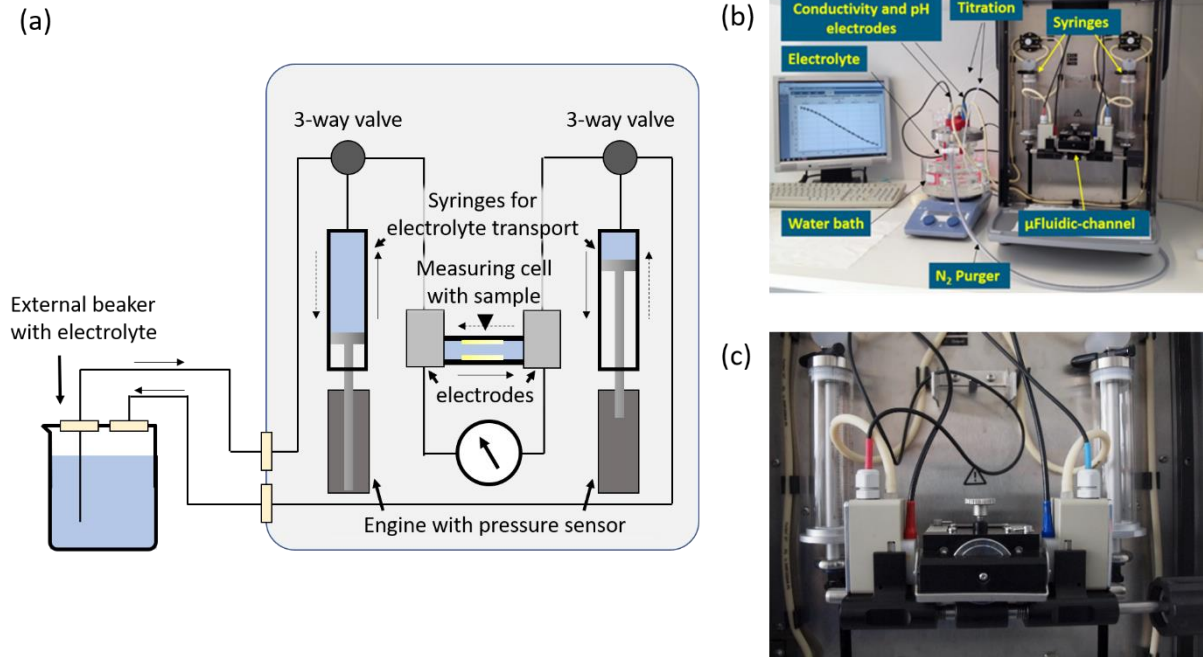


Figure 3-10: Streaming potential measurement with (a) a sketch of the working principle (adapted from (Glass, 2020)), (b) picture of SurPASS electrokinetic analyzer device, and (c) flow channel cell. ((b) and (c) are taken from (Lab Collection, n.d.))

For the surface potential measurement, a modified electrokinetic analyzer (SurPASS, AntonPaar Deutschland GmbH) was used. It is used to determine the surface charge at the shear plane of substrate surfaces, coatings or molecular layers. Two identically prepared samples were mounted with their surfaces facing a flow channel with a gap distance of  $\sim 75 \mu\text{m}$  (Figure 3-10). Using the syringes, electrolyte from the external reservoir is pumped through the microchannel between the samples. Electrodes at both ends of the microchannel allow to determine the  $\zeta$  potential using the Helmholtz-Smoluchowski equation:

$$\zeta = \frac{dI}{dp} \cdot \frac{\eta L}{\epsilon \epsilon_0 A}, \quad (3-1)$$

where  $I$  is the resulting current flowing between the two electrodes,  $p$  is the pressure which is necessary to generate the laminar flow,  $\eta$  and  $\epsilon$  are viscosity and dielectric constant of the electrolyte, and  $L$  and  $A$  are the length and cross-section of the flow channel, respectively. The resulting electrokinetic potential ( $\zeta$ -potential) represents the potential at the shear plane, which separates the mobile layer and the immobile (Helmholtz layer) and is a measure of the surface potential. According to the lab protocol (Yuan et al., 2020), the electrolyte solutions are aqueous solutions based on ultrapure water (Milli-Q) containing potassium chloride (1 mM KCl). During the experiment, the temperature of the medium was kept constant at  $25 \text{ }^\circ\text{C}$ , the pH value was kept at 5.4. Before each experiment, the experimental setup was rinsed with 2 L of ultrapure water and subsequently with the working electrolyte solution.

### 3.2.7. Impedance spectroscopy

The impedance spectroscopy was used to analyze the frequency dependent electronic response of our Pt samples exposed to an electrolyte. In these measurements, the amplitude and the phase are measured as function of the frequencies (spectrum). The theoretical description has already been given in *Electrochemical impedance spectroscopy*. Especially for these measurements, different chips and designs were developed to mimic the situation at the neuroelectronic interface.

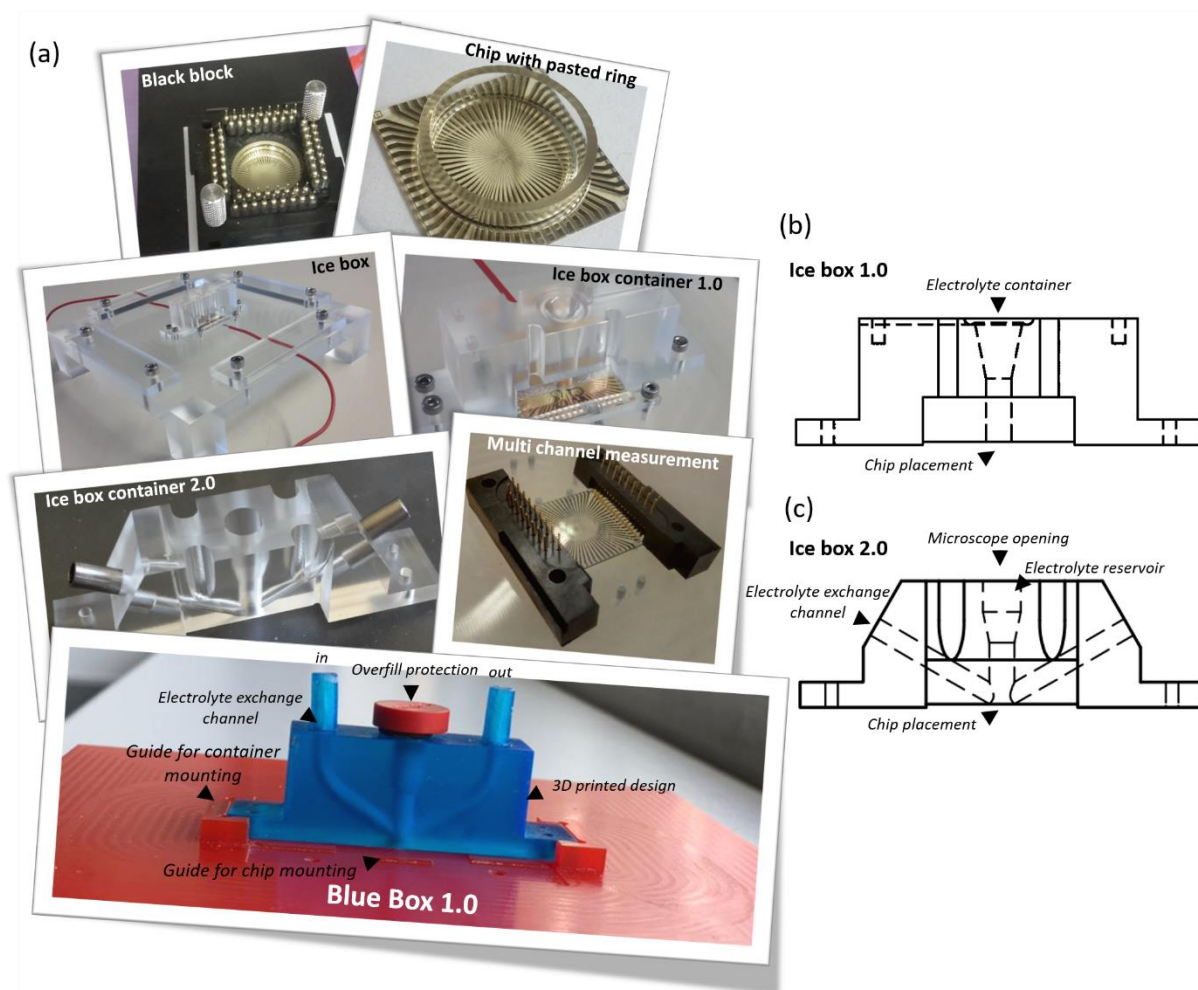


Figure 3-11: Development of measuring setup for the impedance measurements, which are used to mimic the cell-chip behavior, with (a) picture series of the development of the sample design (especially electrodes) and electrolyte container. (b) and (c) represent technical drawings of the container for the EIS measurement in side view (Icebox 1.0 and Icebox 2.0).

For the impedance measurement, a special chip container was developed (Figure 3-11). The standard setup for the electrochemical impedance spectroscopy (EIS) for bioapplications consists of a glass ring glued with polydimethylsiloxane (PDMS) onto the chip. This container is then filled with electrolyte or cell medium for the measurement (Figure 3-11 (a), top). Obviously, this setup can only be used once, since the removal of the ring would destroy the chip.

Since we want to perform a series of experiments with different coatings, we developed a new setup which should be:

- reusable (without damaging the film or electrodes),
- transparent to allow better control of this experiment, and
- with a slow flow of the electrolyte in order to avoid gradients in the electrolyte concentration or formation of crystals on the layer.

For this purpose we developed the system Icebox I to III and the corresponding chip designs (Figure 3-11) with, in the end, the following properties:

- high visibility (transparent),
- long term electrolyte supply (electrolyte exchange channel, see Figure 3-12 (d)),
- plug-and-play principle (easy connection of the tubes for electrolyte),
- mechanical sealing by pressing (no glue or paste),
- flexible in design changes (3D printed),
- transportable and handy (container + table: 150 mm x 150 mm x 50 mm),
- 200  $\mu$ L container for electrolyte reserve (dehydration protection),
- 4 mm in diameter chip-electrolyte contact area,
- hole for microscope analysis (see Figure 3-12 (c)),
- fast mounting and dismounting (guidelines for container and chip, see Figure 3-12 (e)),
- stable and easy multichannel connection (electrode bar, see Figure 3-12 (f)), and
- backside hole for heating and orientation (see Figure 3-12 (e)).

With the above improvements, it is now possible to measure the chips faster and more accurately.

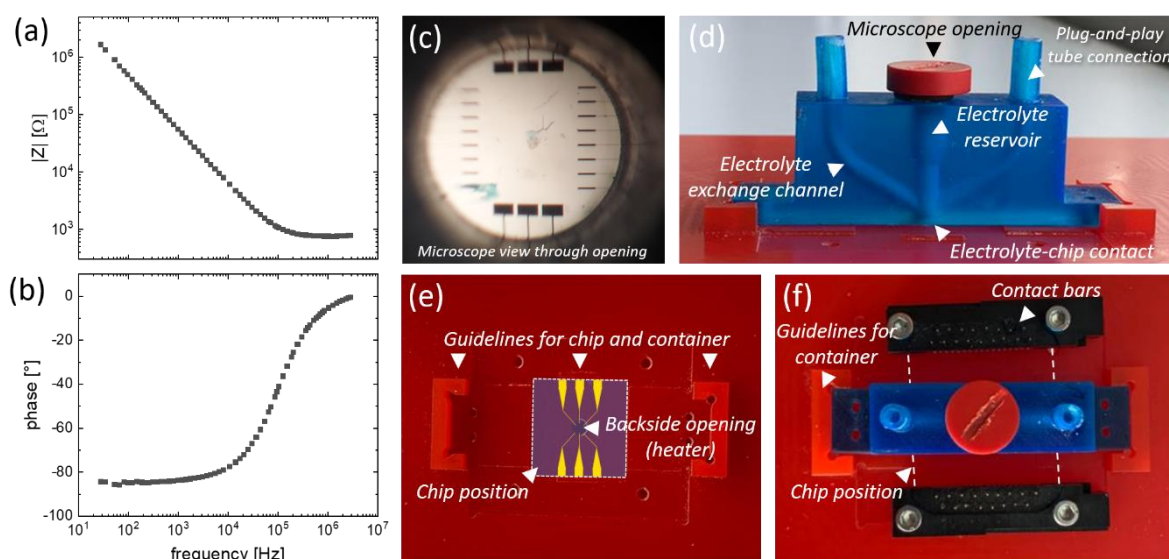


Figure 3-12: Impedance spectroscopy with (a) and (b) typical impedance measurement in Bode representation, (c) microscope image through the opening, and (d) to (f) pictures of the setup. (a) shows the absolute value  $|Z|$  of the impedance and (b) shows the phase of the impedance, both of a  $10\,000\ \mu\text{m}^2$  electrode in a  $1\ \text{M}\ \text{KCl}$  electrolyte. (d) shows the blue electrolyte container in the side view, (e) table in top view, and (f) table, container and contact bars in top view.

In this work, an LCR ST2826 (Sourcetric GmbH, Germany) was used to measure the impedance in a frequency regime of 20 to 5 MHz and a voltage of 100 mV. The size of the different electrodes ranges from  $100\ \mu\text{m}^2$  to  $10\,000\ \mu\text{m}^2$ . A typical measurement of the amplitude of the impedance  $|Z|$  and the phase is shown in Figure 3-12 (a) and (b), respectively.

### 3.3. Neuronal cells

In this chapter, cell culture, life-dead staining, and cell chip communication experiments are described.

#### 3.3.1. Cell culture

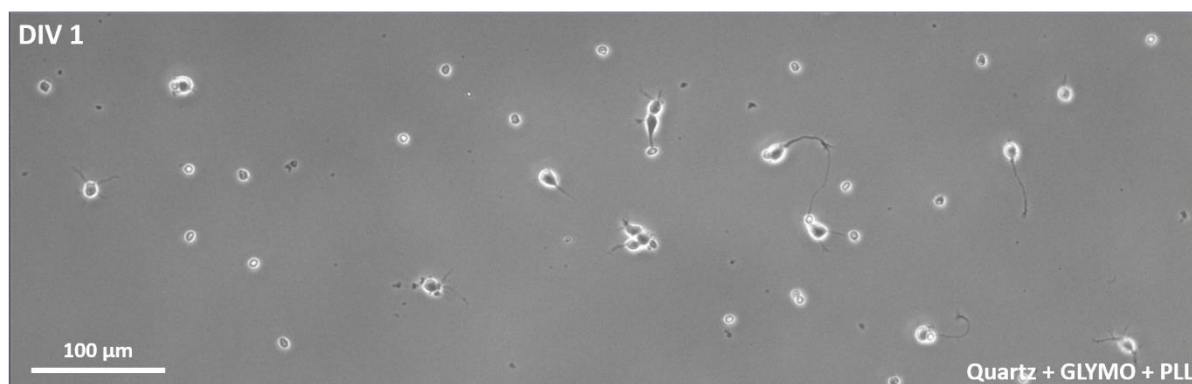


Figure 3-13: Example of a cell culture on quartz (here coated with GLYMO and PLL) at DIV 1, after the first medium change, approx. 5 h after seeding. The white circles represent already dead cells, whereas the larger objects are living cells.

The cells (rat cortical neurons) were cultured according to an existing lab protocol (Yuan et al., 2020). Before starting the actual cell culture, the samples must be sterilized. For this purpose,



the samples are immersed in ethanol and dried in a nitrogen stream. Now, the cells can be seeded. The cortical neurons used here were taken from E18 Wistar rat embryos. The cortex is dissected from the embryonic brain tissue and is digested with trypsin-EDTA at 100 % humidity, 37 °C and 5 % CO<sub>2</sub> atmosphere. In the next step, neurobasal medium (Life Technologies GmbH, Germany) is supplemented with 1 % B27 (Life Technologies, Germany), 50 µg/mL gentamicin and 0.5 mM L-glutamine to remove the trypsin. The sample is washed three times and then carefully dissociated with a 1 µL pipette. To separate glial cells and cell clumps, the sample is left at room temperature for 2 min and then the supernatant is diluted in neurobasal medium. In the case of cell staining, 75 k - 80 k cells per substrate were added to a 12-well culture dish, which corresponds to a cell density of ~200 mm<sup>-2</sup>. For electrical signal measurements, typically 220 k cells are used, which corresponds to a cell density of ~1 000 mm<sup>-2</sup>. After 4 hours the cells have settled and the medium can be carefully exchanged. For the rest of the cell culture time, the half of the medium is changed 2 times a week. A typical cell culture on the first day in vitro (DIV 1) after the first medium change is shown in Figure 3-13. The animal work was carried out with the approval of the Landesumweltamt für Natur, Umwelt und Verbraucherschutz Nordrhein-Westfalen, Recklinghausen, Germany, number 84-02.04.2015.A173 and 81-02.04.2018.A190.

### 3.3.2. Cell staining

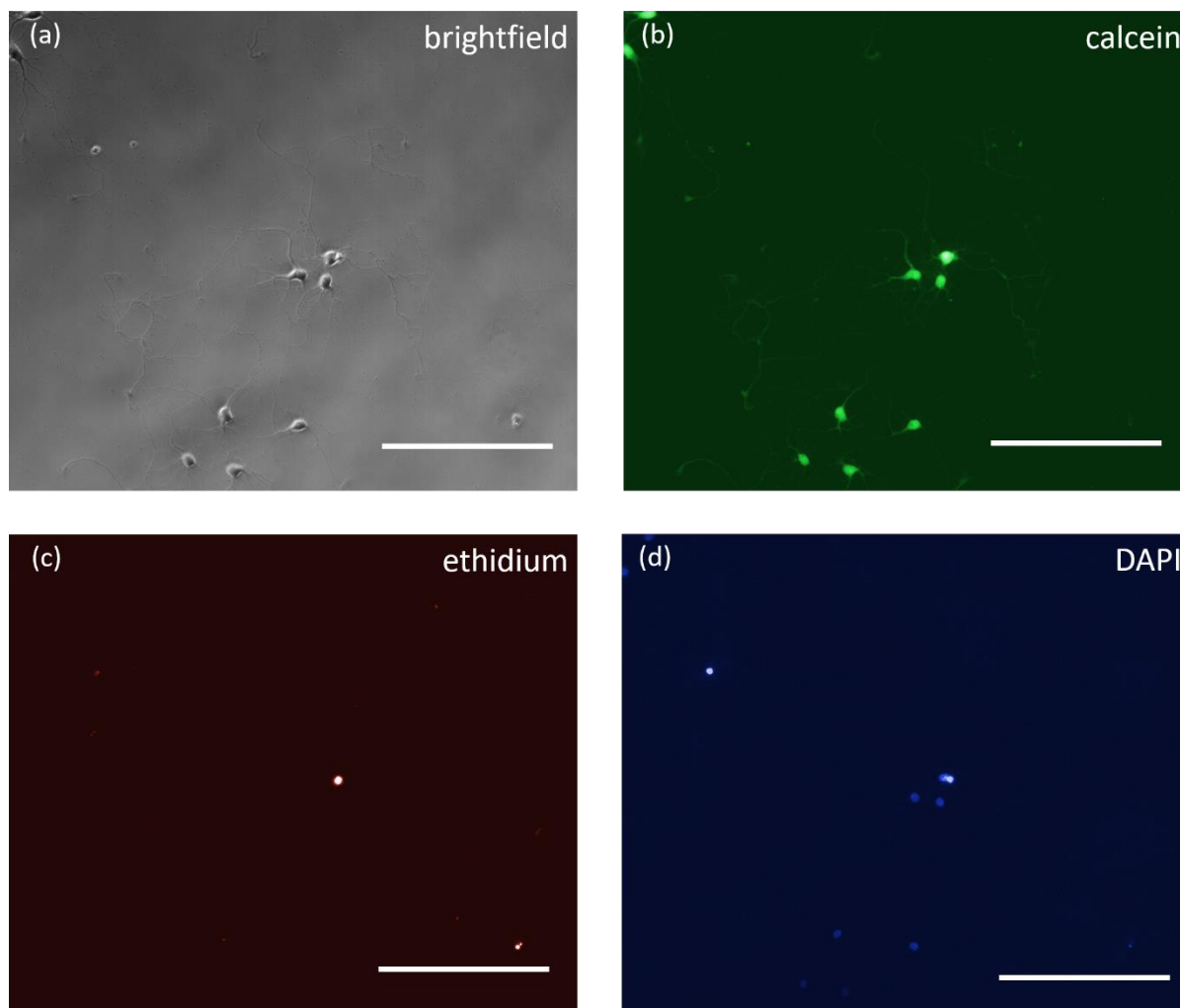


*Figure 3-14: Apotome fluorescence microscope results (a-d). (a) shows a brightfield image of neuron cell culture, where living cells are stained with calcein (b), dead cells with ethidium (c), and DNA stained with DAPI (d). The white scale bars are 200 μm.*

Fluorescence analysis of cell cultures includes different staining (Figure 3-6 (b-d)) and brightfield images (Figure 3-6 (a)). For the cell growth analysis, live/dead staining was performed using 1 μg/mL calcein-AM (Figure 3-6 (b)) and 2 μM ethidium homodimer (Figure 3-6 (c)) (both Life Technologies) in supplemented cell growth medium to stain live and dead cells green and red, respectively. Additionally, DNA staining was performed using 1 μg/mL of 4',6-Diamidin-2-phenylindol (DAPI) (Figure 3-6 (d)), which stains the nucleus of live and dead cells. Cells and dyes were incubated for 15 min at 37 °C.

### 3.3.3. Cell-chip communication

For recording cell signals (action potential), neuron cells were immobilized on specially prepared microelectrode arrays (MEAs). The MEAs were fabricated on quartz wafers and consist of arrays of Pt microelectrodes (size 100 to 10 000 μm<sup>2</sup>) with APTES or, for comparison, PLL coating. The electrodes consist of 5 nm of Ti as an adhesive sublayer and 45 nm Pt top layer. The neuronal signal was measured on DIV 14 using an in-house build amplifier system (BioMAS19).

*Molecular Layer Functionalized Neuroelectronic Interfaces:  
From Sub-Nanometer Molecular Surface Functionalization to Improved Mechanical  
and Electronic Cell-Chip Coupling*

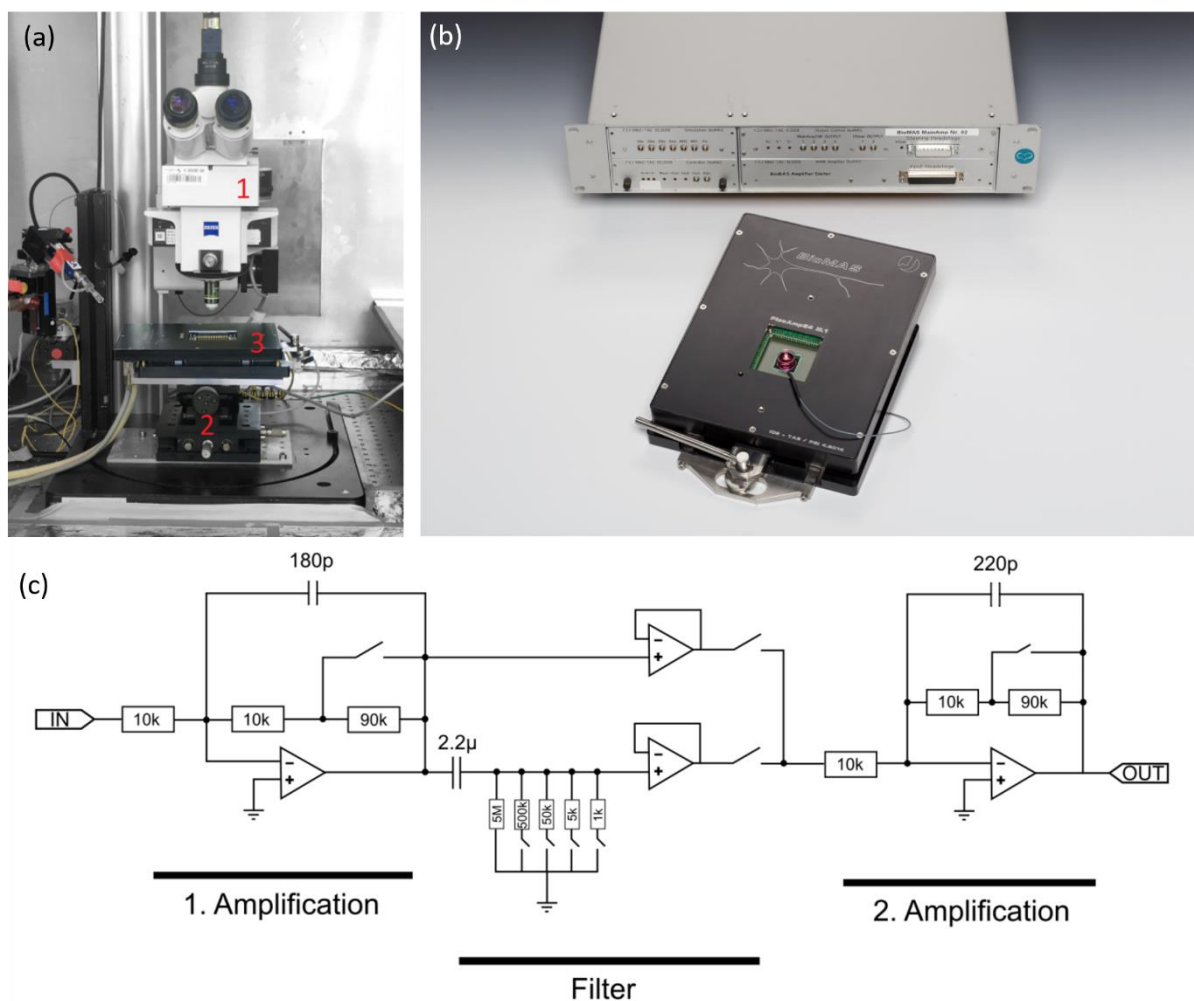


Figure 3-15: BioMAS19 for cell signal measurements, with (a) head stage with a chip in a Faraday cage (taken from (Lewen, 2019)), (b) main- (top) and pre-amplifier (bottom) [Copyright: Forschungszentrum Jülich / Ralf-Uwe Limbach], and (c) simplified schematic of the working principle of the main-amplifier (taken from (Lewen, 2019)). In (a) the microscope (1) is positioned above the pre-amplifier (3) on an x-y stage (2). In (c) the electronic circuit is separated into the two amplification circuits and the filter circuit.

The actual chip is inserted into the chip holder (with 64 spring contacts) in the pre-amplifier (Figure 3-15 (a) number 3 and Figure 3-15 (b), bottom), in which the signal is amplified tenfold. This complete setup is placed in a Faradic cage under an optical microscope, which allows observing the cells during electrical measurements (Figure 3-15 (a)). All up to 64 electrodes are connected and can be read out by the electronic simultaneously. From the pre-amplifier, the amplified signal goes via an optical filter to the main-amplifier (Figure 3-15 (b), top). A simplified working principle of the main amplifier circuit is shown in Figure 3-15 (c). In principle, it consists of the indicated three functional parts, first amplification step, filter, and second amplification step. The combination of both amplifiers offers the choice of further amplifying the already ten times amplified signal (pre-amplifier) up to 1000 times amplification in total. The filter circuit consists of a parallel RC circuit with 2.2 μF. Resistors of either 5 MΩ, 500 kΩ, 50 kΩ, 5 kΩ, or 1 kΩ result in a variable 3 dB high-pass filter from 0.01 to 72 Hz. Since the operational amplifiers built into the BioMAS invert the signal, there is an additional option to reset the input to the original polarization. Two capacitors in parallel to the two amplification stages (180 pF and 220 pF) are implemented to filter out higher frequencies (8.8 kHz and 7.2 kHz, respectively) for edge smoothing. The amplified data is

*Molecular Layer Functionalized Neuroelectronic Interfaces:  
From Sub-Nanometer Molecular Surface Functionalization to Improved Mechanical  
and Electronic Cell-Chip Coupling*

transferred into an analog to digital converter (USB-6255 DAQ - National Instruments, Austin Texas USA). It provides a 16-bit resolution at a maximum sample rate of 1.25 MHz for single-channel operation, and in total 750 kHz for multi-channel operation, applying for example 64 electrodes ending with a sample rate of ~12 kHz (750 kHz/64).

## 4. Results and Discussion

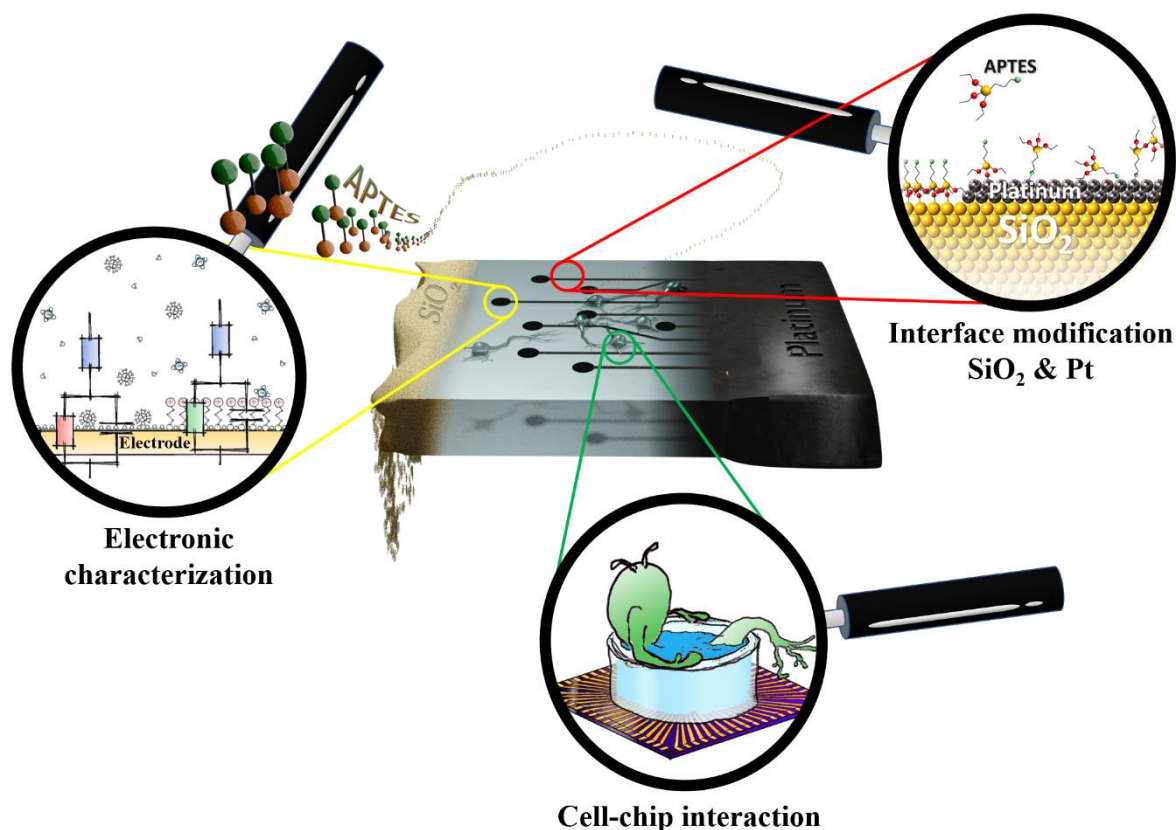


Figure 4-1: The three major tasks for investigations in cell-chip coupling. The interface modifications for tailoring the surface properties, the modified electrode's electrical characterization, and the resulting cell chip interaction.

This work's major aim was to analyze and, if possible, improve the mechanical and electrical cell-chip coupling via the functionalization of the electrodes with organic molecules. The demands of neuroelectronic applications on the cell-electrode interface are high. In the best case, it should be:

- bioaffine, i.e., cells should adhere and grow on it without deterioration,
- it should allow a good electrical coupling, which enables a “communication” between cells (neurons) and electronic, and
- it should be stable without deterioration of neither cells nor electronic.

Furthermore, it would be nice if the process would be simple, robust, and flexible concerning both, substrates and electronics. Considering all these demands, we decided to test an APTES functionalization of the electrodes. The resulting research is therefore divided into three major steps (Figure 4-1), which are discussed in this chapter:

- (i) first, in chapter 4.1 SAM formations on electrodes, we demonstrate and discuss the deposition and SAM formation of APTES on Pt electrodes and compare the layers on Pt with the deposition of APTES on SiO<sub>2</sub> substrates,

- (ii) then, in chapter 4.2, *Electronical characterization of the interface*, we analyze the electronic properties of these electrodes with and without APTES coating in an electrolyte, and
- (iii) finally, in chapter 4.3 *Cell culture*, we demonstrate the positive impact of APTES coating on the cell cultures (cortical neurons) and the electronical and mechanical cell-chip coupling.

Let's start with the investigation of the APTES coated Pt surfaces.

#### 4.1. SAM formations on electrodes

This chapter is based on my publication "Surface Functionalization of Platinum Electrodes with APTES for Bioelectronic Applications" (Wolf et al., 2020).

The interface between the usually inorganic electronic components and biological objects such as neurons plays a crucial role in the success of applications ranging from biosensors to bioelectronics (An et al., 2019; Bardecker et al., 2008; Magar et al., 2020). Modifying the surface of substrates in order to tailor their surface properties (ranging from mechanical or electronic properties to bioaffinity) and thus optimizing them for a given application is a well-known strategy. For example, the functionalization of a conventional inorganic substrate such as SiO<sub>2</sub> via silanization is well understood (Markov et al., 2017; Stevens, 1999; Vandenberg et al., 1991; Yuan et al., 2019). However, bioelectronic components such as electrophysiological sensors are typically composed of several materials like insulating oxides and metals with very different surface properties. So far, there is no general and simple way to modify these materials. While the modification of SiO<sub>2</sub> is done via silanes, metals are typically treated with thiols. The latter works well for Au, but Pt is more involved. Therefore, the question remains of how we can functionalize the substrate, including its electronic components (e.g., in the form of metallic electrodes) in a similar way, if possible, simultaneously and with comparable results.

There are many approaches for surface functionalization, which all have their strengths and weaknesses. They are mainly based on the modification of the existing surface (e.g. morphological modification (J.-H. Kim et al., 2010; Petrossians et al., 2011; S. Weidlich et al., 2017; Wesche et al., 2012)) or on the functionalization of the surface with the help of an additional layer (or multilayer), which then represents the new surface. The conventional path is the coating of the substrate and electronic component with a biocompatible polymer (e.g. polystyrene sulfonate (PEDOT:PSS)) or peptides (e.g. poly-L-lysine (PLL)). The polypeptide PLL provides perfect biocompatibility, whereas PEDOT:PSS, being a conducting polymer, promises improved electronical signal transmission. However, these large molecules are usually only electrostatically bound to the substrate and are easily removed from the surface in high salt culture medium (Y. H. Kim et al., 2011). Therefore, they typically form unstable bioelectronic interfaces. In order to obtain a stable interface, the use of linker molecules covalently binding the large molecules to the substrate is proposed (Balland et al., 2008; Frasconi et al., 2010). However, this automatically increases the thickness of the interface and, thus, the separation between the electronic and the biological objects in bioelectronic applications.

Therefore, the question arises as to whether a thin molecular layer could be used, which binds

to the substrate surface and, at the same time, serves as an interface to the biological object. For the interface between metallic electrodes and neurons, the use of various alkanethiols which form self-assembled monolayers (SAM) on metals such as Au, Ag, or Cu has been suggested and successfully tested (Bryant & Pemberton, 1991; Laibinis et al., 1991; Swalen et al., 1987). However, these thiols typically do not bind to the rest of the substrate surface, which in most cases, consists of oxides (e.g. SiO<sub>2</sub>). It has therefore been discussed whether silanes that bind to oxides could also be used for the functionalization of metallic electrodes (Brito et al., 2002; Moses et al., 1978; Rosario-Castro et al., 2010; Takenaka et al., 2015).

In this chapter, we analyze the binding of (3-aminopropyl)triethoxysilane (APTES) to Pt surfaces. These layers serve as a reference for the APTES layers on Pt. First, we demonstrate that we are able to produce SAMs of APTES on SiO<sub>2</sub> comparable to the literature (Markov et al., 2017; Pasternack et al., 2008). We will show that with adequate oxidation of the Pt surface, we obtain a stable APTES layer on Pt, which is comparable to those on SiO<sub>2</sub>. We demonstrate that APTES is able to bind to Pt via its silane head group and appears to form a stable organic SAM coating.

#### 4.1.1. Detection of monolayer

Since the characterization of extremely thin molecular layers is challenging, APTES was deposited on SiO<sub>2</sub> and Pt in a patterned fashion, forming alternating stripes with and without APTES. For this purpose, SiO<sub>2</sub>- and Pt-coated substrates (see *Choice of substrates, molecules, and sample preparation in Experimental Methods*) were spin-coated with PMMA, and a stripe pattern was generated on the substrate via e-beam lithography and lift-off technique (see *Lithography in Experimental Methods*). Depending on the envisioned analysis technique, different patterns were chosen. The substrate with the PMMA pattern was placed in the MLD device (Figure 3-2 (a)). Prior to APTES deposition, the substrate was exposed to ozone treatment for 3 minutes (see *Ozone cleaning and ozone activation in Experimental Methods*), which leads to a removal of the remaining resist at the open parts of the PMMA pattern and, at the same time, in case of Pt substrates, generates a platinum oxide on the Pt surface (Mom et al., 2019; Saliba et al., 1999). The platinum oxide is stable under ambient conditions and in a buffer medium. Even exposure to ethanol or 30 % H<sub>2</sub>O<sub>2</sub> is not reducing the oxide back to its metallic state (see S 1 in *Appendices*). APTES was deposited onto the patterned surfaces via gas-phase MLD according to the recipe given in *Molecular layer deposition*, including a post-deposition treatment of 24 h for SiO<sub>2</sub> and approx. 2.5 days for Pt substrates. After this treatment, the PMMA was removed in acetone, leaving a sample with APTES in a stripe pattern.

Different analysis techniques were chosen, including AFM, ellipsometry, XPS, fluorescence microscopy, IR-, Raman spectroscopy, UV-vis spectroscopy, ToF-SIMS, and SPR. Due to the limitations in either sensitivity or selectivity and to restrictions imposed by the Pt layer on the different techniques, only a few characterization techniques permit the resulting APTES pattern to be visualized and/or characterized. In the following, we first show the AFM (Figure 4-2) and ellipsometry measurements (Figure 4-3) for APTES on SiO<sub>2</sub> for comparison and then we show the results of AFM, ToF-SIMS, ellipsometry, and SPR (Figure 4-4 to Figure 4-7) for APTES on Pt substrates. Furthermore, the surface potential was analyzed for both types of substrates, SiO<sub>2</sub> and Pt, with and without molecules (Figure 4-8). It should be noted that some of the

experiments were performed or repeated months after deposition in order to demonstrate the stability of the APTES layer.

#### 4.1.2. APTES on SiO<sub>2</sub>

The binding and SAM formation of APTES molecules on SiO<sub>2</sub> is well established. It is just briefly demonstrated to show that our gas-phase MLD process can produce comparable layers of APTES. More experimental results (e.g. fluorescence microscope and XPS) have been performed and can be seen in Appendices S 2 and S 3.

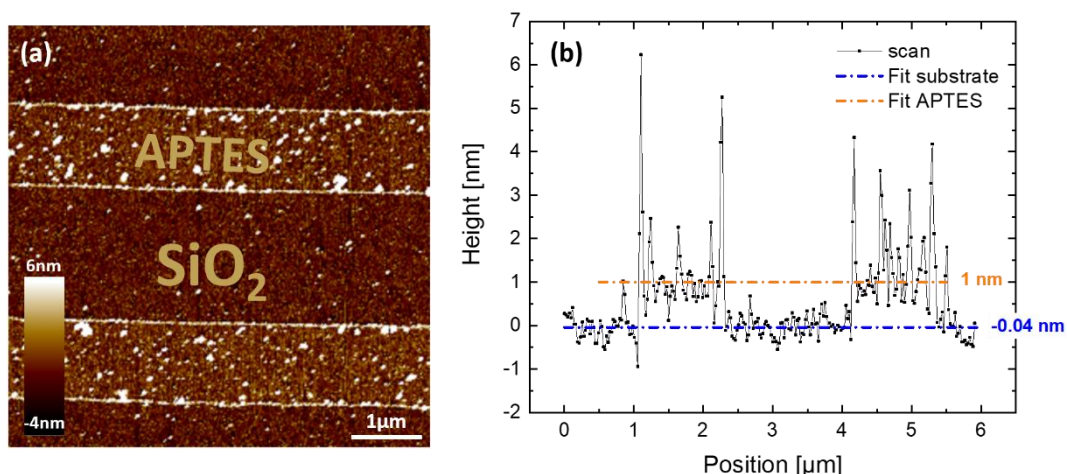


*Figure 4-2: Characterization of patterned APTES layers on SiO<sub>2</sub>, (a) topological mapping and (b) a height line scan from top to bottom. The orange dashed-dotted line is the corresponding fit for the bars of APTES, and the blue dashed-dotted line the fit of the substrate.*

**AFM (Figure 4-2):** In order to directly obtain the thickness of our APTES layers on SiO<sub>2</sub>, we analyzed patterned APTES samples using AFM. A 6 x 6 μm<sup>2</sup> area was scanned. Figure 4-2 (a) shows two APTES strips with a width of 1 μm and a distance of 2 μm. In a typical line scan of the height (Figure 4-2 (b)), the fit of the heights of the stripes and bare substrate are marked with an orange and blue dot-dashed line, respectively. The difference in height is approx. 1 nm. The white dots most likely represent leftovers of the PMMA after development.



*Molecular Layer Functionalized Neuroelectronic Interfaces:  
From Sub-Nanometer Molecular Surface Functionalization to Improved Mechanical  
and Electronic Cell-Chip Coupling*

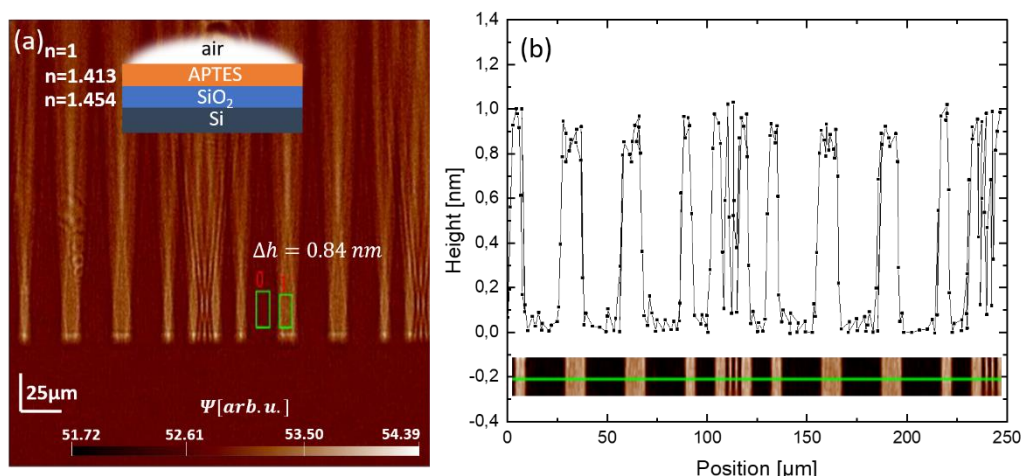


Figure 4-3: Characterization of patterned APTES layers on SiO<sub>2</sub> via ellipsometry. (a) shows the mapping with the 3-layer model.  $\Delta h$  is the difference between the two green squares. (b) shows a height scan from the green line in the picture section in the inset.

**Ellipsometry (Figure 4-3):** Another way to determine the height of the APTES layer is given by ellipsometric analyzes. For the mapping of another APTES pattern (Figure 4-3 (a)) a 3-layer model is used with the layers and reflection indices of SiO<sub>2</sub> ( $n = 1.454$ ), APTES ( $n = 1.413$ ) and air ( $n = 1$ ). A typical height scan provides a step of 0.84 nm, considering all steps across the sample (Figure 4-3 (b)) height of 0.8 to 1 nm is visible.

Both experiments in Figure 4-2 and Figure 4-3 correspond to the thickness of an APTES SAM, which is given by the length of APTES molecules of approximately 0.7 nm (Markov et al., 2017; Pasternack et al., 2008). Further experiments like XPS (S 3), surface potential (Figure 4-8), and fluorescence microscope measurements (S 2) confirmed the presents of APTES SAMs on SiO<sub>2</sub>.

#### 4.1.3. APTES on Pt

Since the electronic cell-chip coupling mainly takes place at the electrodes, the question of whether APTES binds to Pt electrode and whether it forms SAMs might even be more important in neuroelectronics. However, as described above, it is much more tricky to obtain the experimental evidence of the APTES layer on Pt than on SiO<sub>2</sub>. Nevertheless, in the following, we first describe the experiments for analyzing the presence of molecules on Pt and their stability, starting with AFM measurements.

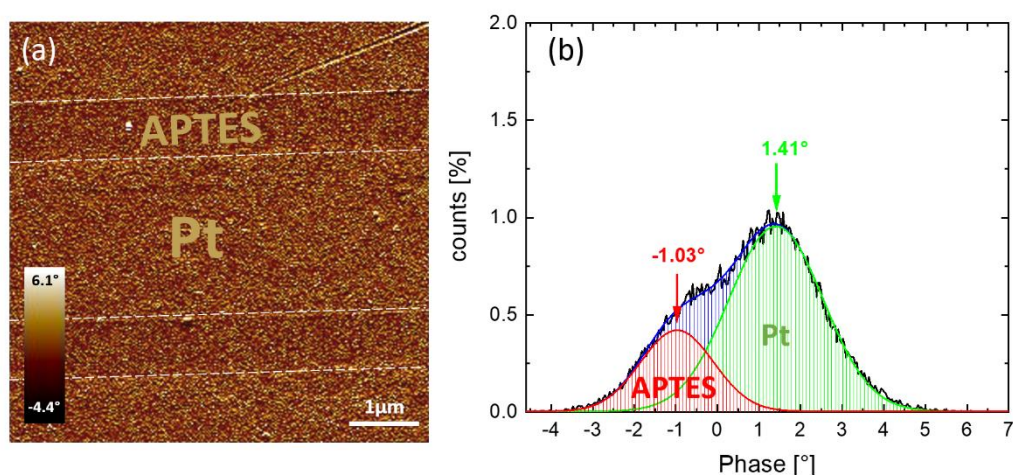


Figure 4-4: Characterization of patterned APTES layers on Pt via AFM. (a) shows the phase mapping of the APTES bars on a Pt substrate and (b) the corresponding phase distribution with Gaussian fits of the peaks of APTES bars in red, Pt in green and resulting curve in blue.

AFM (Figure 4-4): Obviously, the analysis of the surface topography via AFM would be the simplest way to verify the presence of an APTES layer. However, the roughness of the Pt layer and the fact that the patterning (including ozone treatment) itself introduces surface modifications in the order of the expected APTES layer prevents reasonable surface mapping via this technique. Therefore, we produced AFM phase maps that reveal differences in the surface properties of the patterned sample. A typical phase image ( $6 \times 6 \mu\text{m}^2$  area) taken in tapping mode (Figure 4-4 (a)) clearly shows a material contrast.  $1\mu\text{m}$  wide stripes of APTES appear in a horizontal orientation. The phase contrast is a result of the different stiffnesses of the areas with and without molecules (Halper & Ellenbogen, 2006). The phase distribution of the complete mapping is plotted in Figure 4-4 b. The two areas are separated by Gaussian fits, where green represents the substrate and red the molecules. Both phases, the molecules and Pt substrate, show a different stiffness expressed by a phase difference of  $\sim 2^\circ$  in the AFM experiment.

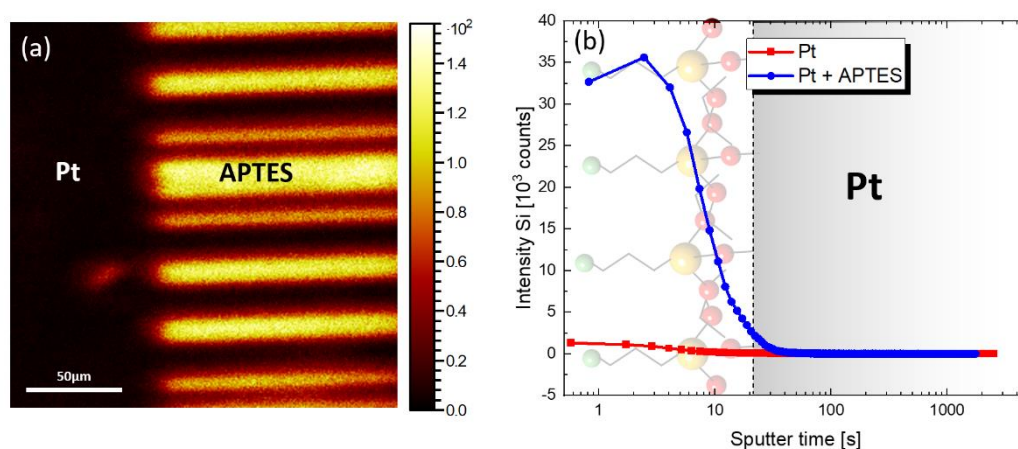
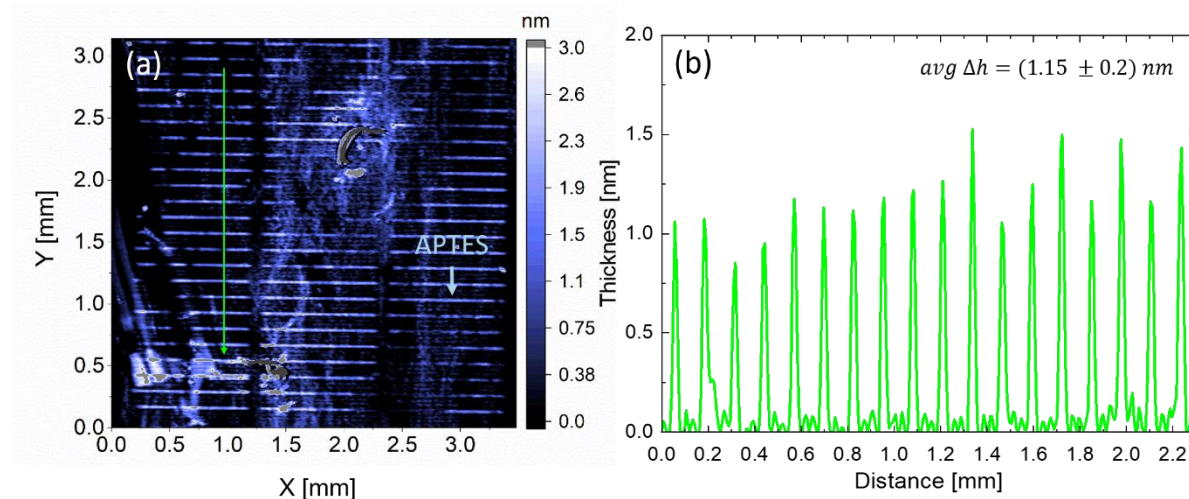


Figure 4-5: Characterization of patterned APTES layers on Pt via ToF-SIMS. (a) shows a ToF-SIMS mapping and (b) a ToF-SIMS depth profile. The dashed line symbolizes the surface. (Measured by Uwe Breuer, ZEA-3, Forschungszentrum Jülich)

*ToF-SIMS (Figure 4-5):* Two different types of ToF-SIMS experiments were performed for our samples. In the first experiment, element mapping employing only the primary ion beam ( $\text{Bi}^+$ ) at low energy was used to scan the surface of a patterned APTES layer on Pt. Setting the analysis to  $^{28}\text{Si}^+$  (for other isotopes see S 4 in *Appendices*), we obtain a map of the areas coated with the silane APTES. Figure 4-5 (a) shows a typical Si map of a sample patterned with APTES stripes of different widths. The APTES stripes (starting halfway at a horizontal position of  $\sim 70\ \mu\text{m}$ ) show up in yellow, which indicates the enhanced amount of Si due to the presence of APTES, whereas the areas protected by PMMA during APTES deposition show no Si (black), indicating the absence of APTES in these areas. Since the mapping in Figure 4-5 (a) was performed 3 months after the deposition of the APTES molecule, this also indicates the stability of the molecular layer on the Pt sample.

The second experiment shows a depth profile of Si recorded on an APTES decorated area and for comparison an area without APTES. In Figure 4-5 (b), the respective intensity of the Si is shown as a function of sputter time, which is equivalent to a depth profile of Si. Although there is a small Si signal at the reference surface without APTES, which probably stems from contaminations, the initial Si signal of the APTES area is by far higher than that of the area without APTES. Moreover, immediately after the initial peak, the Si signal also vanishes for the measurement on the APTES-coated sample, indicating that the ultrathin APTES layer is removed by the Cs ions and the ToF-SIMS analysis penetrates the Pt. This transition of the signal occurred after a few seconds (therefore, the timescale is plotted logarithmically) as indicated by a dashed line in the figure. Both ToF-SIMS experiments demonstrate that our deposition process leads to the formation of a stable and thin APTES layer on Pt.



*Figure 4-6: Characterization of patterned APTES layers on Pt via ellipsometry. (a) shows ellipsometry mapping with (b) the resulting line scan of height taken along the green line in (a).*

*Ellipsometry (Figure 4-6 (a)):* In order to obtain an idea of the thickness of the APTES layers, we analyzed the patterned APTES samples using ellipsometry. Figure 4-6 (a) shows a typical height mapping of an APTES pattern. The bars (3 groups of bars with a length of 1 mm) are clearly visible in the color plot. In order to perform a quantitative analysis, line scans across the bar structure are extracted from the experiment. Figure 4-6 (b) shows a typical height profile taken along the line indicated in Figure 4-6 (a). It shows the expected pattern consisting of

extended areas (width 110  $\mu\text{m}$ ) without APTES and smaller areas (width 18  $\mu\text{m}$ ) with APTES. On average, the difference in height between the two types of areas is  $\Delta h \approx (1.15 \pm 0.2)$  nm.

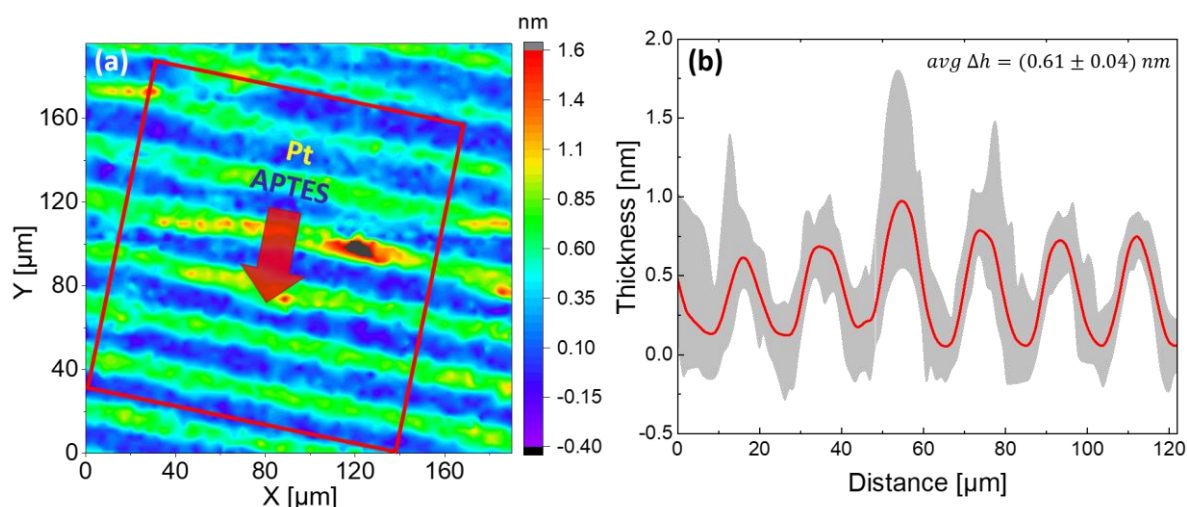


Figure 4-7: Characterization of patterned APTES layers on Pt via SPR. (a) shows SPR mapping; and (g) SPR line scan (red) showing the average height profile (red) and the background range (gray) of all lines in the marked red square in (f). (Measured by Hossein Hassani, IBI-3, Forschungszentrum Jülich)

**SPR (Figure 4-7):** Another way to analyze the height of the APTES layer is given by the SPR experiment. The scanning mode of our custom-built SPR microscopy setup (see chapter 3.2.5) was employed to acquire the angular spectrum of reflectance at each point at a wavelength of 632.8 nm for the APTES-coated Pt samples (see *Choice of substrates, molecules, and sample preparation*). The subnanometer thickness of the APTES layer was calculated based on the shift in the peak of the reflectance spectrum in the close proximity of the critical angle using the Fresnel equations (Hassani et al., 2020). The measurement was performed in air, and the reflectance indices glass ( $n_{\text{glass}} = 1.788$ ), Ti ( $n_{\text{Ti}} = 3.3 + i3.8$ ), Pt ( $n_{\text{Pt}} = 2.8 + i5.6$ ), air ( $n_{\text{air}} = 1.000$ ) and APTES ( $n_{\text{APTES}} = 1.429$ ) were used to evaluate the APTES film thickness.

Figure 4-7 (a) shows a mapping of the APTES height of a patterned sample obtained by SPR (Hassani et al., 2020). The mapping was performed on a 190 x 190  $\mu\text{m}^2$  area, the red square marks the areas of line scans used for the evaluation of the height profile (Figure 4-7 (b)). The distance between the peaks agrees with the periodicity of the structure, and the resulting average height of  $0.61 \pm 0.1$  nm. Additionally, this experiment was repeated after 1.5 years with the same result, which again indicates the stability of our APTES layer on Pt surfaces.

In conclusion of these first measurements shown in Figure 4-4 to Figure 4-7, we demonstrated the presence of APTES on Pt and showed that the resulting layer has a thickness which corresponds to the length of APTES molecules of approximately 0.7 nm in the literature (Markov et al., 2017; Pasternack et al., 2008) and to the layer thickness of APTES SAMs on  $\text{SiO}_2$  (see Figure 4-2 and Figure 4-3).

#### 4.1.4. APTES monolayer properties

*Surface potential analysis (Figure 4-8):* Measurements of the kinetic potential ( $\zeta$  potential) were performed to obtain information on the different functionalization of the surface due to the ozone treatment (activation) and APTES coating. For this purpose, the results obtained for our Pt sample are compared to data recorded for  $\text{SiO}_2$ , a system that is well understood (Stevens, 1999; Yuan et al., 2019). For the  $\zeta$  potential analysis, two identical  $10 \times 10 \text{ mm}^2$  samples were mounted with the surfaces to be analyzed facing each other, forming a  $75 \mu\text{m}$  gap for the electrolyte flow (see *Streaming potential analysis*). By measuring the electrolyte flow and the corresponding drop of the electrical potential in the flow channel, the  $\zeta$ -potential can be evaluated using the Helmholtz-Smoluchowski equation:

$$\zeta = \frac{dI}{dp} \cdot \frac{\eta L}{\epsilon \epsilon_0 A} \quad (4-1)$$

where  $p$  is the pressure necessary to generate the laminar flow,  $\eta$  and  $\epsilon$  are the viscosity and dielectric constant of the electrolyte,  $L$  and  $A$  represent the length and cross-section of the flow channel, respectively, and  $I$  is the resulting current measured between two electrodes placed at each side of the measuring cell. Moreover, recording the  $\zeta$ -potential for a prolonged period allows additional information to be obtained about the stability and possible changes of the surface exposed to the electrolyte.

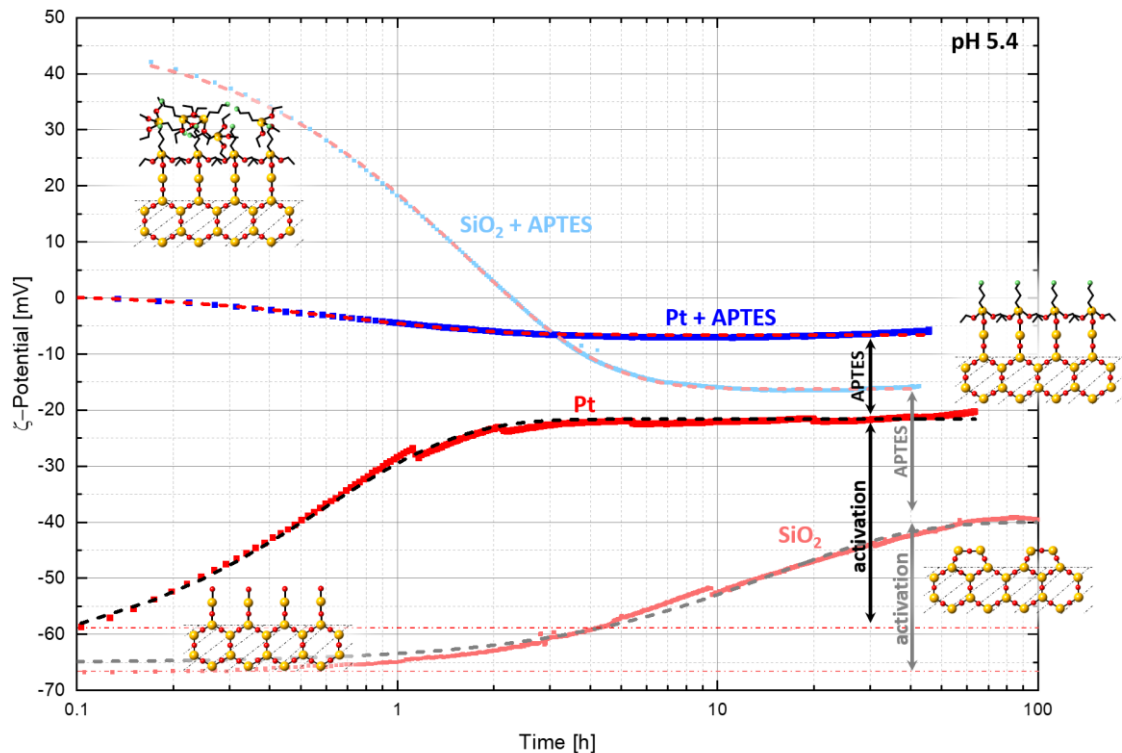


Figure 4-8: Development over time of the  $\zeta$  potential measurement of Pt and  $\text{SiO}_2$  after ozone activation (red) and APTES coating (blue) in a 1 mM KCl electrolyte at pH 5.4. The dashed lines are exponential fits of the experimental data (points) according to  $\zeta = A \cdot \exp(t/\tau) + \zeta_0$  with decay time  $\tau$ , the dashed-dotted line represents the initial potential of the activated samples.

Figure 4-8 shows the development of the surface potentials of SiO<sub>2</sub> and Pt after activation with ozone (see *Ozone cleaning and ozone activation*) and after coating with APTES (see *Molecular layer deposition*). Zero time (t = 0) refers to the first exposure of the surface to the electrolyte. Continuous measurements were performed in 1 mM KCl at pH 5.4 and a constant temperature of 25 °C. Since the behavior of the surface potential of SiO<sub>2</sub> after activation and APTES coating is well understood (Stevens, 1999; Yuan et al., 2019), the comparison of the two systems proved to be very helpful.

Figure 4-8 shows that both systems, SiO<sub>2</sub> and Pt behave very similarly and therefore:

- (i) it seems to be possible to activate Pt in a similar manner to SiO<sub>2</sub>,
- (ii) Pt and SiO<sub>2</sub> lose their activation, although this process is much faster for Pt,
- (iii) physisorbed APTES seems to be removed in the electrolyte for both systems, whereas
- (iv) at the same time, a stable (i.e. chemically bound) APTES layer can be formed on both substrates with
- (v) most likely the amino group of APTES representing the functional group which defines the new surface on both systems.

The different surface states of the systems will first be described in detail.

*Activated state:* At the beginning (t = 0) of the measurement, the bare samples (Pt and SiO<sub>2</sub>) are in the activated state. As a result of the ozone treatment of the surface, a strongly negative  $\zeta$  potential is established. This phenomenon is well known (Stevens, 1999; Yuan et al., 2019). It results from the formation of OH<sup>-</sup> groups at the SiO<sub>2</sub> surface (see *Silanes*). By activating the sample, open silanol bonds form at the surface and upon exposure to the electrolyte, the surface potential of SiO<sub>2</sub> decreased to approx. -67 mV. The behavior of Pt is comparable to that of SiO<sub>2</sub>. Due to the ozone treatment, a highly negative  $\zeta$  potential of approx. -59 mV is established.

*Transition to the non-activated state:* For SiO<sub>2</sub>, we know that activation vanishes with time and the silanol groups return to their more stable Si-O-Si siloxane configuration (Yuan et al., 2019). After 2-3 days of exposure to the electrolyte, the activation of SiO<sub>2</sub> has vanished and the  $\zeta$  potential reaches a stable value of approx. -40 mV, which corresponds to the non-activated state of a cleaned SiO<sub>2</sub> surface for the chosen experimental conditions (see Figure 4-8). The Pt samples behave very similarly. They also lose their activation over time. However, this process is much faster for Pt compared to SiO<sub>2</sub> and the change of the  $\zeta$  potential is much greater. We obtain an exponential decay with a time constant  $\tau_{SiO_2} = 15.2$  h for SiO<sub>2</sub> and  $\tau_{Pt} = 0.6$  h for Pt indicating that the activated state is less stable or the surface is more reactive in the electrolyte for Pt compared to SiO<sub>2</sub>. The change of the surface potential depends among other things on the density of the -OH groups, which can be activated by the ozone treatment. The SiO<sub>2</sub> ( $\beta$ -cristobalite structure) most likely forms a hexagonal structure of oxygen positioned on Si, which can be activated (see Figure 4-10). The distance between adjacent oxygen atoms can be approximated by:

$$x_{NN} = \frac{a\sqrt{2}}{2} = 5.06 \text{ \AA}, \quad (4-2)$$

( $a = 7.16 \text{ \AA}$  is the lattice parameter of the cubic unit cell of  $\text{SiO}_2$ ) and leads to a maximum density of OH groups of  $n_{\text{SiO}_2} = 4.55 \text{ nm}^{-2}$ , which agrees with experimental data of  $4.9 \text{ nm}^{-2}$  (Pelmenschikov et al., 2000).

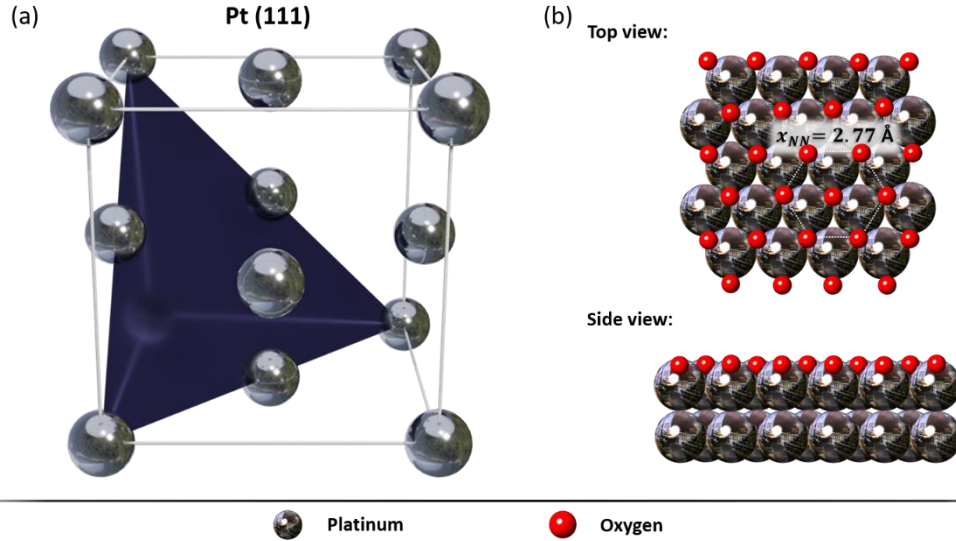


Figure 4-9: Platin face-centered cubic crystal structure as (a) unit cell including the (111) plane (blue), and (b) the top and side view of the oxidized (111) surface, including (white) the resulting hexagonal structure of the oxygen atoms (red points) with the next-neighbor distance  $x_{NN} = 2.77 \text{ \AA}$ .

In comparison, Pt is expected to grow in a face-centered cubic structure with a lattice constant of  $a = 3.92 \text{ \AA}$  (see Figure 4-9 (a)). The expected binding of oxygen with 3 Pt atoms results in a hexagonal arrangement of oxygen on the Pt surface (here we assume Pt (111)) with an oxygen spacing of

$$x_{NN} = a\sqrt{2}/2 = 2.77 \text{ \AA}, \quad (4-3)$$

(see Figure 4-9 (b)). In this case, the resulting maximum density of OH groups would be  $n_{\text{Pt}} = 15 \text{ nm}^{-2}$  and thus  $\sim 3$  times larger than  $n_{\text{SiO}_2}$ . This could be one reason for the greater charge of the  $\zeta$  potential induced by the activation of Pt ( $\Delta\zeta \approx -43 \text{ mV}$ ) compared to  $\text{SiO}_2$  with a reduction of the  $\zeta$  potential of  $\Delta\zeta \approx -26 \text{ mV}$ .

**APTES-coated samples:** The APTES coating generally leads to a significant increase in the surface potential, which is due to the APTES amino group that reacts with the electrolyte and forms  $-\text{NH}_3^+$  (ammonium cation) (K. Cai et al., 2006). In both systems, the initially strong increase (for APTES on  $\text{SiO}_2$  we observe a  $\zeta$  potential of  $\sim 40 \text{ mV}$  at  $t = 0$ ) decreases within a few hours ( $\tau \approx 1.7 \text{ h}$  and  $0.8 \text{ h}$  for  $\text{SiO}_2$  and Pt, respectively) to a stable value which, however, is still clearly higher than the  $\zeta$  potential of the surface without APTES (see arrows in Figure 4-8). For  $\text{SiO}_2$  it is known that this decrease in the  $\zeta$  potential is a result of the removal of weakly physisorbed APTES from the surface (Greiben et al., 2015; Yuan et al., 2019). The stable  $\zeta$  potential observed after a few hours of exposure to the electrolyte represents the electrokinetic potential of the  $\text{SiO}_2$  surface coated with a chemically bound monolayer of APTES, a self-assembled monolayer (SAM) (Yuan et al., 2019). We believe that the behavior of APTES on Pt is very similar. The initial decrease of the  $\zeta$  potential of the APTES-coated Pt surface stems from the removal of physisorbed APTES. After  $\sim 2$  hours ( $\tau \approx 0.8 \text{ h}$ ) a stable  $\zeta$  potential of approximately  $-6.5 \text{ mV}$  is obtained, which is still significantly higher than the potential of the

Pt layer without APTES (see Figure 4-8). Long-term measurements showed that these layers seem to be stable even over several months.

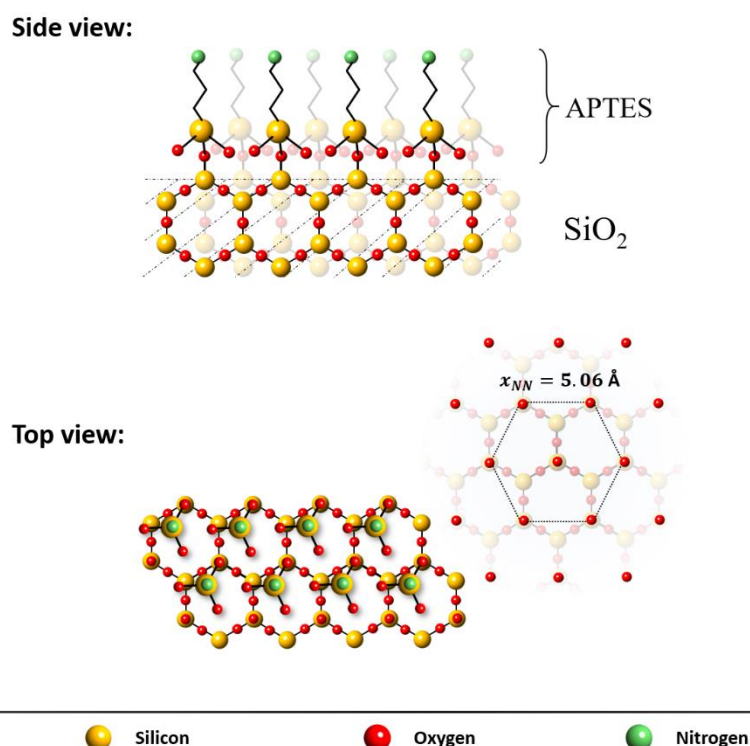


Figure 4-10: Schematics of APTES binding onto  $\text{SiO}_2$  surfaces consisting of side and top views of covalently bound APTES on  $\text{SiO}_2$  ( $\beta$ -cristobalite structure) including (right) the resulting hexagonal structure of the oxygen atoms (red points) with the next-neighbor distance  $x_{NN} = 5.06 \text{ \AA}$ .

To conclude this part of the work, we will discuss and compare the possible options of the binding of gas-phase deposited APTES on  $\text{SiO}_2$  and Pt. For APTES on  $\text{SiO}_2$ , it is known that the ethoxy group ( $\text{OC}_2\text{H}_5$ ) of the molecule can covalently bind to the activated silanol surface bonds ( $\text{Si-OH}$ ) (Figure 4-10). Since the distance between adjacent silanol bonds on the  $\text{SiO}_2$  surface is typically much larger than the extension of the APTES ethoxy groups, APTES is expected to bind with only one arm onto  $\text{SiO}_2$  (Stevens, 1999; M. Zhang et al., 2015). As a result, APTES can form SAMs on  $\text{SiO}_2$  with a maximum molecule density equal to the density of silanol groups, i.e.  $n_{\text{APTES},\text{SiO}_2} = 4.55 \text{ nm}^{-2}$  for the  $\beta$ -cristobalite structure with an oxygen next-neighbor distance of  $x_{NN} = 5.06 \text{ \AA}$  (equation (4-2)). The formation of APTES SAMs on  $\text{SiO}_2$  has already been demonstrated for our gas-phase MLD process (Yuan et al., 2019).

In contrast, much less is known about the binding of APTES on Pt. Although it has been reported that APTES layers can be deposited on Pt surfaces (Brito et al., 2002; Moses et al., 1978; Rosario-Castro et al., 2010; Takenaka et al., 2015), there are mostly speculations about the binding and SAM formation of APTES on Pt.

The possible bonds that are suggested for APTES molecules on platinum surfaces are shown in Figure 4-11. The bonds are ordered by strength, starting with the Van der Waals bond (Figure 4-11 (a)) up to the strongest covalent bond (Figure 4-11 (d)).

The van der Waals bond (Figure 4-11 (a)) is based solely on the force between the carbon chain and the surface. This force is generated by fluctuations in the electron shells. These fluctuations



introduce a dipole moment in the neighboring surface, which leads to the bonding of the molecules at the surface. Typically, the force is in the order of 0.4 – 4.0 kJ/mol (Gross & Marx, 2018, p. 102).

The second possibility is the binding between the amino group of APTES and the platinum surface (Figure 4-11 (b & c)). Generally, a covalent bond between amino and platinum is possible, however, it can only be achieved in complicated synthetization processes (e.g. cisplatin (Jeschonek et al., 2011)). More likely would be an electrostatic bond or hydrogen bond between the amino group and the platinum surface. In this case, the hydrogen loses its electrons almost completely. As a result, a positively charged area is created to which a second electronegative atom can bind ionically. Due to the size of a proton, only two atoms can be connected via one hydrogen bond (Gross & Marx, 2018, p. 140). The strength of the hydrogen bond is approx. 12-30 kJ/mol. The bond can be stronger by crosslinked molecules with multiple hydrogen bonds (Figure 4-11 (c)).

The last and strongest option would be the covalent bond via an oxygen atom with the silane group. Due to shared electrons between atom cores, their positive charge obscured by them, and an attractive force is created (>60 kJ/mol) (Gross & Marx, 2018, Chapter 3.4).

In the literature, the discussion is mainly focused on amino-Pt (Brito et al., 2002; Lenhard & Murray, 1977; Takenaka et al., 2015) and Si-Pt bonding (Kuo et al., 1979; Lenhard & Murray, 1977; Moses et al., 1978). Brito et al. for example performed X-ray and infrared spectroscopy on aminopropyltrimethoxysilane and found out, that all atoms (Pt, C, Si, and N) atoms can be found on the surface, but in the infrared spectroscopy, the band for stretched N-H vanishes. They conclude that this is due to amino – Pt bonds. Takenaka et al. investigated the connection between carbon nano tubes and platinum nanoparticles via APTES molecules and presumed that the amino group is connected to both sides, the platinum and the carbon nanotubes, and are interconnected by crosslinks between the silane group (Figure 4-11 (c)). Lenhard & Murray did volumetric analyses and measured Electron Spectroscopy for Chemical Analysis (ESCA) spectra. They concluded that it's a complex mixture of bindings and both, the amino and silane group, could bind to Pt/PtO surfaces. Moses et al. and Kuo et al. analyzed amine silanes on different surfaces (among others also on platinum) via X-ray photoelectron spectroscopy, infrared spectroscopy, and electrochemical methods. They stated that silanes bind stably via anhydrous reaction media to metal oxide electrodes.

The different possible types of binding suggested for this system in the literature, which is illustrated schematically in Figure 4-11, will therefore be discussed in the light of our experimental results.

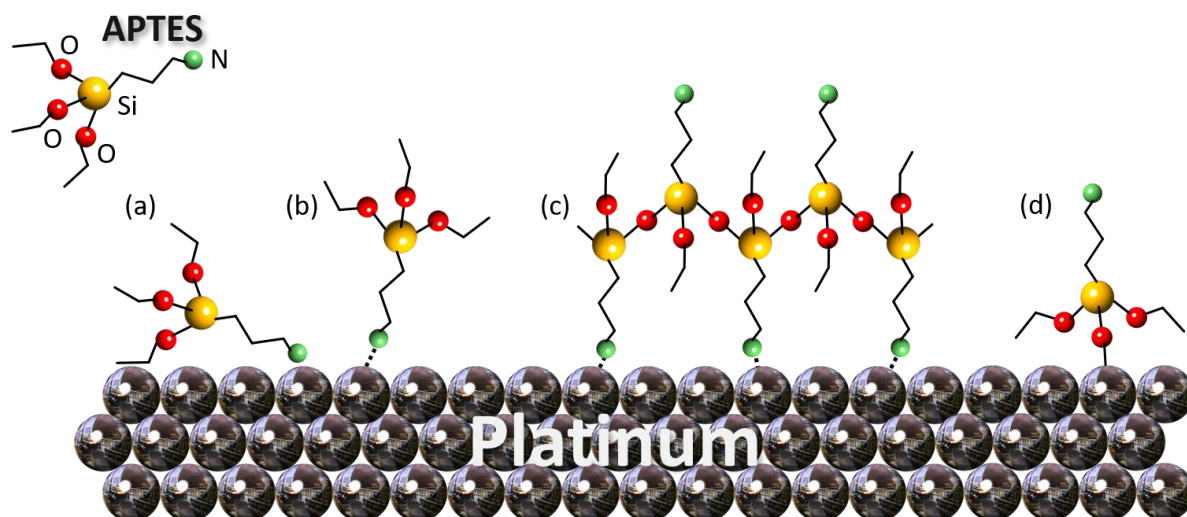


Figure 4-11: Possible types of binding of APTES on Pt surfaces ordered by binding strength: (a) van der Waals bond, (b) hydrogen bonding via the amino group, (c) polymerized APTES layer again with amino group binding, and (d) covalent bond via the ethoxy head group.

The probably weakest binding is expected for a *van der Waals interaction* (Figure 4-11 (a)) of molecules and Pt layer. Such physical binding is most likely present directly after the deposition of the molecules. However, our surface potential analysis (Figure 4-8), as well as reports in the literature (Geben et al., 2015; Yuan et al., 2019), demonstrated that physisorbed molecules are easily removed from the Pt surface. During our streaming potential measurements, an exposure of the surface to the electrolyte led to a removal of the physisorbed molecules, although the remaining APTES layer was stable for months (Figure 4-8). Therefore, we can exclude a van der Waals bond for the stable APTES layer.

Another weak interaction is given by an *amino-platinum bond* (Figure 4-11 (b)) of APTES on Pt (Brito et al., 2002; Takenaka et al., 2015). This bond consists of either a hydrogen bond between the molecule amino group and the oxidized Pt or a covalent bond between the amino group and Pt. Both options are sketched in Figure 4-11 (b). Since the hydrogen bond is quite weak, it can be excluded for the formation of a stable APTES layer. Moreover, since we demonstrated that the Pt can be functionalized with APTES showing a significant increase in the surface potential due to the impact of the amino functional group (see Figure 4-8), this type of binding is also not likely to be responsible for our stable APTES layer. However, *polymerization* of amino-bound APTES (Figure 4-11 (c)) could enhance the overall binding of an interlinked molecule and would also permit functionalization (Takenaka et al., 2015). However, in this case, we would expect thicker APTES layers than those measured in our case via ellipsometry and SPR (see Figure 4-6 and Figure 4-7).

*Molecular Layer Functionalized Neuroelectronic Interfaces:  
From Sub-Nanometer Molecular Surface Functionalization to Improved Mechanical  
and Electronic Cell-Chip Coupling*

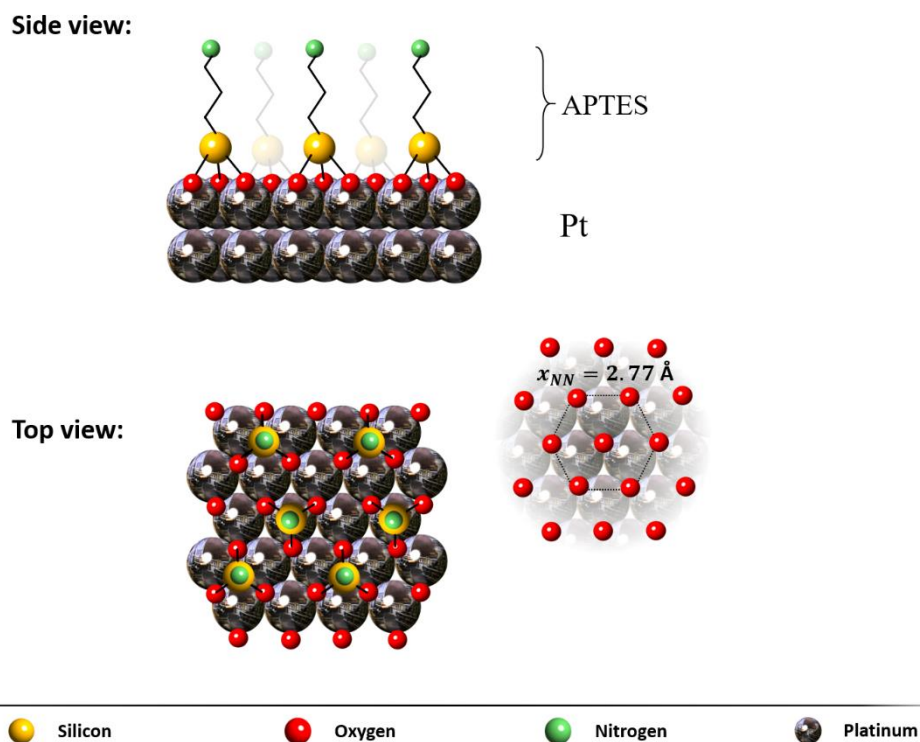


Figure 4-12: Schematics of APTES binding onto Pt surfaces consisting of side and top view of APTES SAM formation with triple covalent binding on Pt(111) including (right) the hexagonal structure of the oxygen atoms (red points) at distance  $x_{NN} = 2.77 \text{ \AA}$ .

There are good reasons to believe that our gas-phase deposition leads to *covalent binding* of the ethoxy group of APTES to the oxidized Pt (Figure 4-11 (d) and Figure 4-12):

- (i) First, after the removal of the physisorbed APTES, the remaining layer proves to be extremely stable. Repeated measurements demonstrated the presence of the APTES layer even after several months and repeated exposure to the electrolyte. This requires a strong binding such as the covalent binding between the ethoxy group and Pt.
- (ii) Second, the thickness of the APTES layer was found to be 0.61 - 1.15 nm (see Figure 4-6 and Figure 4-7). This value agrees very well with literature values reported for APTES SAMs on SiO<sub>2</sub> (Markov et al., 2017; Pasternack et al., 2008) and with our measurements on SiO<sub>2</sub> (see Figure 4-2 and Figure 4-3).
- (iii) Third, we not only observe a significant increase in the surface potential due to the functionalization with APTES (see Figure 4-8), but this increase is even comparable to the impact of APTES SAM on SiO<sub>2</sub> on the electrokinetic potential. Considering the face-centered cubic structure ( $a = 3.92 \text{ \AA}$ ) of Pt again with the binding of oxygen to 3 Pt atoms, the resulting hexagonal arrangement of oxygen on the Pt surface with an oxygen spacing of  $x_{NN} = 2.77 \text{ \AA}$  (Figure 4-12) and a maximum density of -OH groups of  $n_{Pt} = 15 \text{ nm}^{-2}$  would be too dense to allow the covalent binding of one APTES molecule per oxygen atom (Stevens, 1999). Therefore, in contrast to the situation for SiO<sub>2</sub>, binding of all 3 ethoxy groups of each APTES molecule to the adjacent oxygen atoms of the oxidized Pt surface would be possible (Eslamibidgoli & Eikerling, 2016). The resulting binding of APTES would be very stable and would

lead to the formation of a SAM, as illustrated in Figure 4-12. The resulting optimum density of APTES molecules would be  $n_{\text{APTES,Pt}} \approx 5 \text{ nm}^{-2}$ , which is similar to the value of  $n_{\text{APTES,SiO}_2} = 4.55 \text{ nm}^{-2}$  obtained for APTES SAMs on SiO<sub>2</sub>.

- (iv) Finally, the electrokinetic potential of the surfaces with APTES SAMs is given by:

$$\zeta_{\text{tot}} = (1 - g) \cdot \zeta_{\text{sub}} + g \cdot \zeta_{\text{APTES}}, \quad (4-4)$$

where  $\zeta_{\text{sub}}$  and  $\zeta_{\text{APTES}}$  represent the individual  $\zeta$  potential of the substrate and APTES, respectively, and  $g$  characterizes the coverage of the surface with APTES. Since the coverage seems to be similar for both systems,  $g$  and  $\zeta_{\text{APTES}}$  can be evaluated from the comparison of the electrokinetic data of both systems by:

$$g = 1 - \frac{\zeta_{\text{tot,Pt}} - \zeta_{\text{tot,SiO}_2}}{\zeta_{\text{Pt}} - \zeta_{\text{SiO}_2}}, \quad (4-5)$$

$$\zeta_{\text{APTES}} = \frac{\zeta_{\text{tot}} - (1 - g) \cdot \zeta_{\text{sub}}}{g}. \quad (4-6)$$

Inserting the data obtained for the stable surfaces (SiO<sub>2</sub> and Pt) with and without APTES shown in Figure 4-8, we obtain reasonable values of  $g \approx 0.54$  for the coverage with APTES for both systems and a slightly positive  $\zeta$  potential of 3 mV for APTES at pH 5.4.

In conclusion, all evidence showed that APTES is present in the intended areas, stable for months, and has a layer thickness of 0.61 – 1.15 nm. Additionally, we have shown that both systems, SiO<sub>2</sub> and Pt, show similar behavior patterns and both surfaces can be functionalized. Also, the coverage of the molecules on the surface is as expected. This series of experimental results convinced us that we deal with an APTES SAM on Pt, which is comparable to the one on SiO<sub>2</sub>.

## 4.2. Electronical characterization of the interface

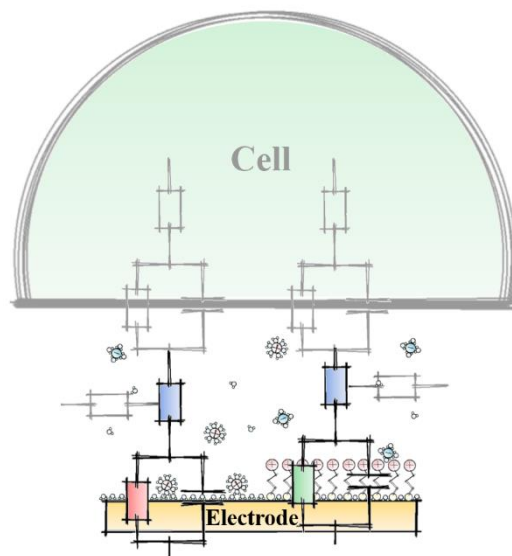


*Figure 4-13: Electronical characteristics of electrode-cell coupling with the emphasis on the electrode-electrolyte interface.*

After demonstrating the binding and monolayer formation of APTES on Pt, the material of electrodes for the neuroelectronic interface, we have to examine the impact of the molecule layer on the electrode impedance. In order to do this, an impedance spectroscopy experiment has been developed, which consists of a setup (see *Impedance spectroscopy*) and chip design, which simulates the situation of a cell-chip contact (see Figure 4-13). The construction of the measuring device explained in detail in chapter 3.2.7, had to allow long-term measurement without contamination in a flow of a stable electrolyte. Moreover, the definition and design of the electrodes exposed to the electrolyte turned out to be quite tricky. In this chapter, the development of the impedance spectroscopy, especially the design and preparation of the chip and the subsequent characterization of the electrodes with and without APTES functionalization, are discussed.

#### 4.2.1. Chip design

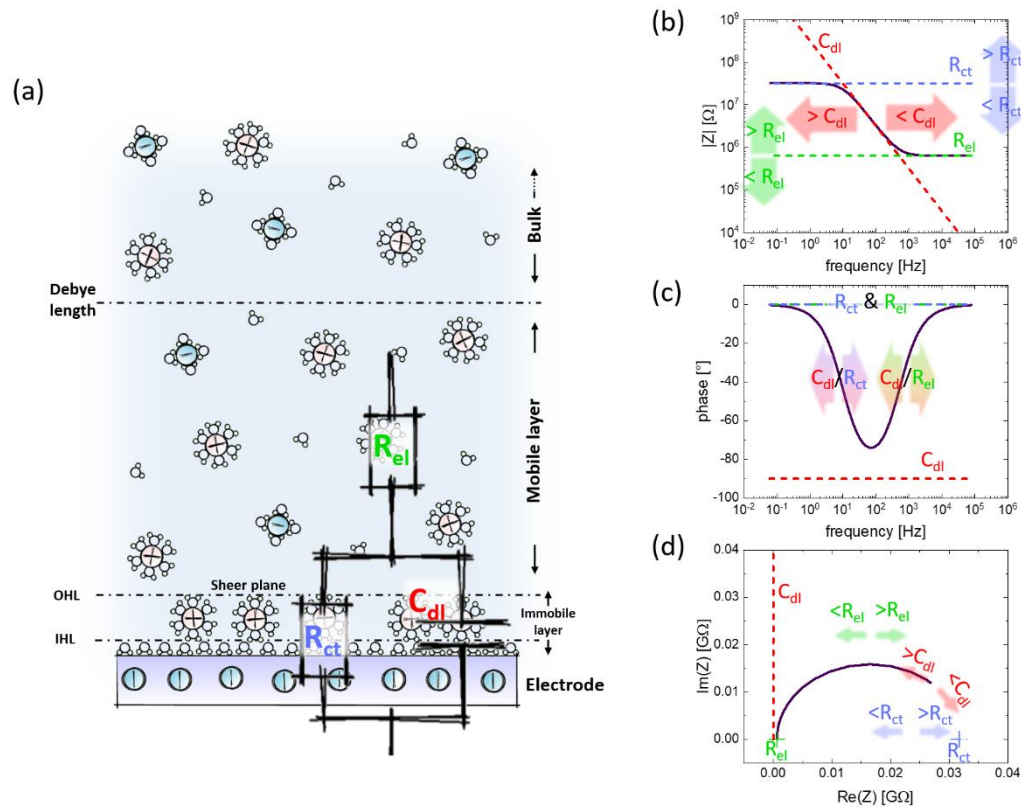


Figure 4-14: General understanding of impedance with (a) sketch of an electrode in an electrolyte including Helmholtz layer and the corresponding model of the electric circuit and (b-d) the impedance representations of a Randles circuit (black) and in colors the different elements themselves (i.e. charge transfer resistance  $R_{ct}$ , double layer capacitance  $C_{dl}$ , and electrolyte resistance  $R_{el}$ ) including the symbolized shift of the curves by changing the parameter of the elements.

In order to optimize the chip and electrode design, let's first take a brief look at what we want to measure. The impedance of a metallic electrode in an electrolyte is typically described by the Randles circuit (Randles, 1947) (see Figure 4-14 (a)). The Randles circuit consists of an (electrolyte) resistor  $R_{el}$  connected in series with a capacitor  $C_{dl}$  in parallel to a resistor  $R_{ct}$ . In the Randles circuit, the capacitor describes the capacitance that is formed on the water layer on the surface by the ions in the electrolyte. The parallel resistor is called the charge transfer resistor and describes the leakage of the capacitor. Figure 4-14 (b)-(c) describe the impact of the individual components in the Randles circuit on the impedance spectra to be measured. Figure 4-14 (b) and (c) show the Bode representation (see *Representation of complex impedance*) of the amplitude of phase of the impedance. Figure 4-14 (c) shows the impact of the elements of the Randles circuit on the Nyquist representation of impedance (see *Representation of complex impedance*).

For the analysis of the interface, the relevant experimental regime has to be adapted to the situation in neuroelectronic experiments, which means the typical electrolyte (e.g. the cell medium) can be simulated by 1 mol KCl solution, and the relevant frequency regime is several Hz to several kHz. We chose a frequency regime of 20 Hz to 2 MHz for our impedance spectroscopy. In order to identify and analyze the different elements of the Randles circuit, i.e.  $R_{ct}$ ,  $C_{dl}$ , and  $R_{el}$ , we had to choose an adequate design of the electrodes. Let's discuss the different issues separately.

*Electrolyte resistance:* The role of the electrolyte in the impedance of the Randles circuit is the simplest and least interesting one.  $R_{el}$  affects the impedance at high frequencies. It causes a plateau in the  $|Z|$  and a return of the phase to  $0^\circ$  (Figure 4-14 (b) and (c)). The actual frequency regime of the transition to the plateau and zero phases basically depends on the ratio  $C_{dl}/R_{el}$ . In the Nyquist plot (Figure 4-14 (d))  $R_{el}$  shifts the entire semicircle only slightly to the right. The electrolyte resistance can be changed by the concentration of the electrolyte, by the distance between the electrodes, and by the electrode sizes. Since the electrolyte resistance is not interesting for our analysis, we try to minimize the resistance  $R_{el}$  by choosing the high molarity of our electrolyte, i.e. 1M KCl, and a small distance between the electrodes.

*Double-layer capacitance:* The double-layer capacitance  $C_{dl}$  has the largest impact on the impedance. It dominates the central frequency regime of the spectrum and, as we will see later, also the cell-chip coupling. An increase of  $C_{dl}$  leads to a decrease in  $|Z|$ . It also broadens and deepens the U-shaped minimum in the phase plot (Figure 4-14 (c)). Similar to  $R_{el}$ , the capacitance does not change the general shape of the Nyquist plot, but it determines how far the circle extends into the frequency regime (Figure 4-14 (d)), i.e., if the capacitance increases, a smaller part of the semicircle can be measured in an experiment with a lower frequency limit (or the frequency range has to be extended). For example, only a quarter of the circle may be drawn. The double-layer capacitance depends on the type of ions, the thickness of the Helmholtz layer, and the area of the electrode. It is typically given as  $0.1 - 0.6 \text{ F/m}^2$  (Lvovich, 2012, p. 69).

*Charge transfer resistance:* The charge transfer resistance  $R_{ct}$  describes the charge transfer of the Helmholtz layer. It is responsible for the low-frequency plateau in the Bode plot (Figure 4-14 (b)). The height of the plateau is given by the sum of  $R_{ct}$  and  $R_{el}$ . Together with  $C_{dl}$ ,  $R_{ct}$  determines when  $|Z|$  and  $\varphi$  deviate from the plateau and the zero-phase, respectively. In the Nyquist plot, the charge transfer resistance represents the diameter of the semicircle. The semicircle itself is zero at  $R_{el}$  and the sum of  $R_{el}$  and  $R_{ct}$ . There exists no reliable literature values for the charge transfer resistance, but it is known that  $R_{ct}$  depends on the area of the electrodes, the electrolyte concentration, electron activity, electric field, temperature, and pressure (Lvovich, 2012, p. 74).

*Design optimization:* Obviously, it would be desirable to see the complete set of features, as shown in Figure 4-14 (b) – (d). However, this is not possible. Therefore, an adequate design of the electrodes had to be developed. This was done in 4 steps (see Figure 4-15):

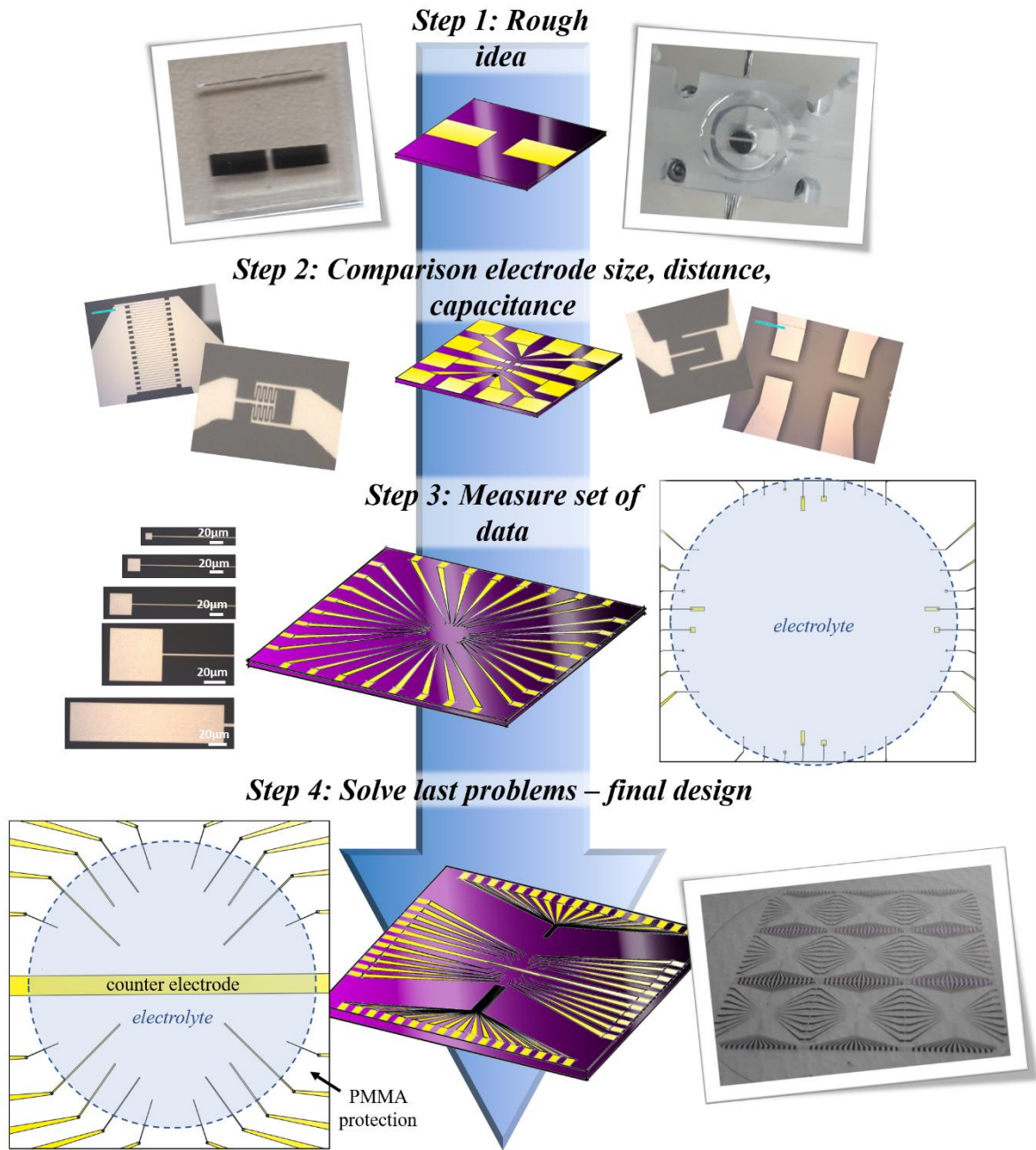


Figure 4-15: Development of chips for impedance spectroscopy from top to bottom, separated in 4 steps: step 1: most straightforward design with two large sputtered Pt electrodes on a 10 x 10 mm<sup>2</sup> borosilicate substrate; step 2: multi-electrode array with different capacitance, electrode size, and electrode-electrode distances; step 3: different sized electrodes (100 μm<sup>2</sup> - 20 000 μm<sup>2</sup>) in a symmetric arrangement; and step 4: electrode bars with a large electrode bar, serving as 2<sup>nd</sup> electrode for all measurements in the middle. The blue, dashed circuit is the contact area for the electrolyte in the measurement setup (see chapter 3.2.7), and the yellow lines are the electrodes. Furthermore, in the 4<sup>th</sup> step the non-exposed area is protected by a ~700 nm thick PMMA layer.

- (i) In a first test, two large Pt electrodes were sputtered onto a 10 x 10 mm<sup>2</sup> borosilicate substrate (Figure 4-15, step 1) and measured in the electrolyte (1 mM KCl). The two electrodes connected in series via an electrolyte, possess a total impedance:

$$Z_{tot} = \left( \frac{1}{Z_{R_{ct,1}}} + \frac{1}{Z_{C_{dl,1}}} \right)^{-1} + Z_{Rel} + \left( \frac{1}{Z_{R_{ct,2}}} + \frac{1}{Z_{C_{dl,2}}} \right)^{-1}, \quad (4-7)$$



with  $Z_{R_{ct,n}}$  the impedance of the respective charge transfer resistance,  $Z_{C_{dl,n}}$  the impedance of the respective double-layer capacitance and  $Z_{R_{el}}$  the electrolyte impedance. The resulting capacitances turned out to be too large to provide a reasonable impedance spectrum that would allow us to derive the characteristic features of the Helmholtz layer.

- (ii) In a second step, different types of designs were tested. The designs differ in the electrode sizes, electrode-electrode distance, and in the capacitance. Microscopic images of the different electrodes are shown in Figure 4-15. Unfortunately, it turned out that the feedlines strongly contribute to the measurement and made it impossible to interpret the data.
- (iii) In a third step, a symmetric design was chosen (Figure 4-15). In this design, always electrodes of the same size can be measured against each other. The symmetrical arrangement simplifies the analysis since:

$$Z_{tot} = \left( \frac{1}{2 \cdot Z_{R_{ct}}} + \frac{1}{2 \cdot Z_{C_{dl}}} \right)^{-1} + Z_{R_{el}} \quad (4-8)$$

Since we learned from step 2 that the electrolyte container cannot be placed with adequate precision, extended electrodes with extremely thin feedlines were used. For example, electrodes with a size of  $10 \times 10 \mu\text{m}^2$  had  $100 \mu\text{m}$  long feedlines with a width of  $1 \mu\text{m}$ , of which  $100 \mu\text{m}$  should be in contact with the electrolyte. Therefore, even if the chip is perfectly installed, the feedlines still contribute 50 % to the total surface. This means that already small displacements can lead to a significant change in the impedance spectrum. Additional problems are:

- the complex lithography, necessary for the  $1 \mu\text{m}$  feedlines can lead to misproductions,
  - the changing of the electrodes via the tiny lines might be problematic, especially at high frequencies, and
  - the fact that the electrical lines cannot be modeled as a simple plate capacitor, but rather like a 2D to 3D line.
- (iv) In order to avoid all these effects and to get reliable data, the design has been fundamentally changed:
- most noticeable is the large counter electrode in the center of the chip (Figure 4-15). The capacitance of the counter electrode was chosen such that its features lie outside our frequency range and do not affect the spectrum (see Table 6).
  - The electrode pads with feedlines were replaced by a uniform electrode bar. For statistics and control, there are 4 electrodes of each size on each side. This time, however, not to be measured against each other, but to be measured against the counter electrode.
  - In order to avoid problems with the displacement of the chip and the resulting variation of the exposed area, a  $\sim 700 \text{ nm}$  thick PMMA film was spin-coated on

the chip leaving only the central part open, which is supported to be exposed to the electrolyte. As a result, we obtained perfect and reproducible data. Figure 4-16 shows the impedance  $|Z|$  and phase of four electrodes of the same size (in this case  $10\,000\ \mu\text{m}^2$ ) in the Bode representation. The data perfectly overlap indicating that there is no difference in the properties of the electrodes, i.e. exposed area, resulting Helmholtz layer, etc. That means our measurement is extremely stable and reliable. Only such extremely stable measurements ultimately allow a reliable statement about the impact of the subnanometer molecules on the electronic properties of the Helmholtz layer.

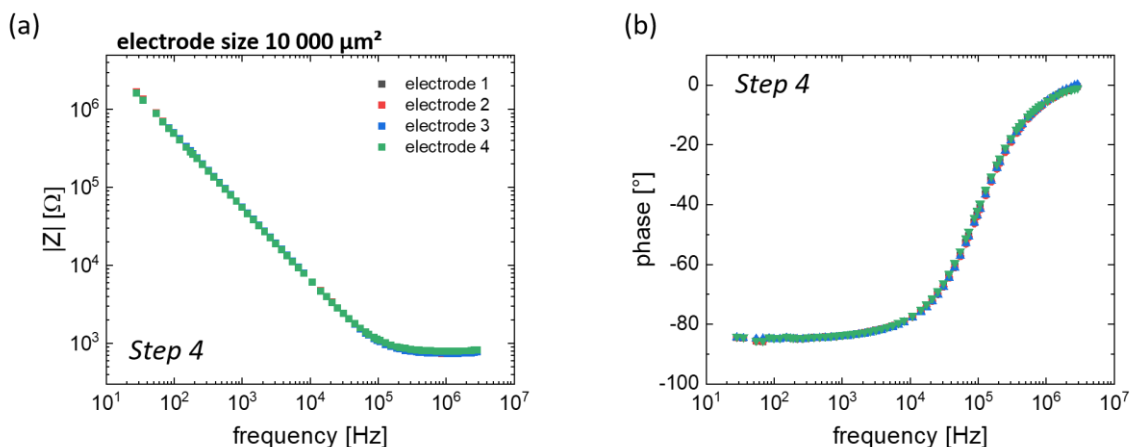


Figure 4-16: Bode representation of the impedance spectrum of 4 different electrodes with the same size with (a) the absolute value of the impedance and (b) the phase angle vs. the frequency of all 4 electrodes. The electrode for the final design (step 4) ( $10\,000\ \mu\text{m}^2$ ) was measured against the large counter electrode (see Figure 4-15 (c)), the data lie exactly on top of each other. (Measurement together with Pratika Rai, IBI-3, Forschungszentrum Jülich)

The typical size of the electrodes in neuroelectronics has to match the size of the neuronal structures and, therefore, should be smaller than  $\sim 400\ \mu\text{m}^2$ . In order to prevent the small electrodes from having geometric effects, i.e., that they behave like electrodes between 2D and 3D due to their small size, much larger electrodes (up to  $20\,000\ \mu\text{m}^2$ ) were examined in addition to electrodes  $< 400\ \mu\text{m}^2$ . Only in this way is it possible to analyze the different characteristics geometrically independent. The resulting design parameters of the electrodes are listed in Table 6.

Table 6: Important sizes for final design (step 4). The distance represents the shortest distance between the electrode and counter electrode.

Electrodes	Sizes [ $\mu\text{m}^2$ ]	Length [ $\mu\text{m}$ ]	Width [ $\mu\text{m}$ ]	Distance [ $\mu\text{m}$ ]
1	200	40	5	738
2	1000	200	5	1624
3	6000	500	12	1275
4	10000	500	20	1062
5	20000	1000	20	448
Counter electrode	1200000	4000	300	

#### 4.2.2. Electronic model for the interface

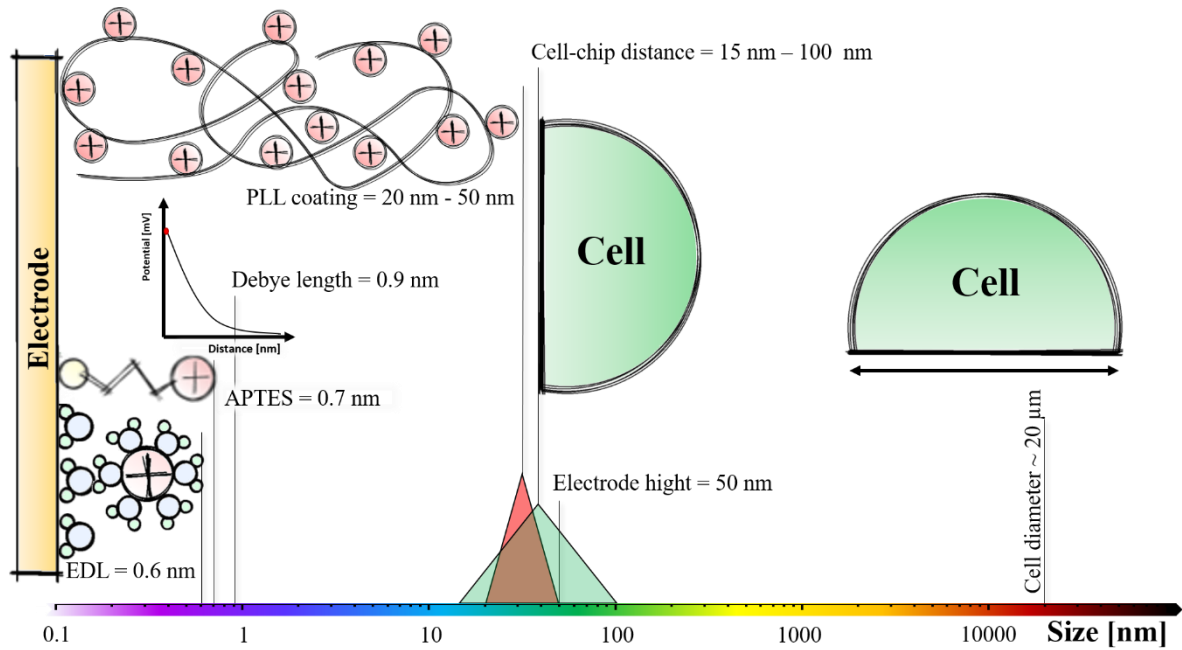


Figure 4-17: Different important sizes for the surface analysis, including from small to large: EDL (Brown et al., 2016), APTES molecule (Pasternack et al., 2008), Debye length (see eq. (4-9)), PLL (Colville et al., 2010), electrode height (chapter 3.1.2), typical cell-chip distance for typical coatings (Khalili & Ahmad, 2015; Zaidel-Bar et al., 2004), and the cell diameter.

Before we start modeling the surface, we should consider the different sizes in order to be able to make statements, comparisons, and estimates of our parameters. For this purpose, the different sizes of characteristic features and components in a neuroelectronic interface are shown in Figure 4-17. The thickness of the electronic double layer (EDL) is given by the height of an adhered water molecule and the diameter of a hydrated  $K^+$  ion (Brown et al., 2016). The thickness of APTES SAM is given by the length of the APTES molecule (see chapter 4.1), and the Debye length is calculated with:

$$\lambda_D = \sqrt{\frac{\epsilon_0 \epsilon_r k_B T}{2 N_A e^2 I}}, \quad (4-9)$$

where  $\epsilon_0$  is the field constant,  $\epsilon_r$  is the permittivity of water ( $\sim 80$ ),  $k_B$  is the Boltzmann constant,  $N_A$  is the Avogadro constant,  $e$  is the elementary charge, and  $I$  is the ionic strength, which is

$$I = \frac{1}{2} \sum c_i \cdot z_i^2, \quad (4-10)$$

with the molar concentration  $c_i$  and the charge number  $z_i$  of ion type  $i$ . For our single charged ions,  $I$  is simply given by to the concentration. Additionally, Figure 4-17 shows the thickness of a PLL layer, which typically ranges between 20 nm and 30 nm if the sample is rinsed after liquid deposition and 40 nm to 50 nm if PLL is air-dried (Colville et al., 2010). The cell-chip distance lies typically between 15 nm and 100 nm (Khalili & Ahmad, 2015; Zaidel-Bar et al., 2004), and depends on the coating and the attraction of the substrate.

Using the thickness of the EDL, we can estimate the capacitance of the Helmholtz layer simply by:

$$\frac{C}{A} = \epsilon_0 \epsilon_r \frac{1}{d} = 0.138 \frac{\text{F}}{\text{m}^2}, \quad (4-11)$$

with  $d = 0.6 \text{ nm}$  of the thickness of the Helmholtz layer and  $\epsilon_r = 9.34$  of the permittivity for  $0.1 \text{ M KCl}$  at a distance of  $0.6 \text{ nm}$  from the surface (Teschke et al., 2001).

Let's now apply the standard electrochemical model, the Randles circuit, to our data. Figure 4-18 shows the Bode and Nyquist representations of our data obtained for the  $10\,000 \mu\text{m}^2$  electrodes in  $1 \text{ M KCl}$  solution. Furthermore, it shows the best fit using the Randles approach with  $C_{dl} = 2.1 \text{ nF}$ ,  $R_{ct} = 20 \text{ M}\Omega$ , and  $R_{el} = 740 \Omega$ . It is quite obvious that the Randles fit can only roughly explain the measured data. For example,  $|Z|$  fits only at high frequencies, whereas it is incorrect at low frequencies. Also, the phase is correct in the high-frequency range. The fit is particularly bad in the Nyquist representation (Figure 4-18 (c)), where it doesn't fit at all.

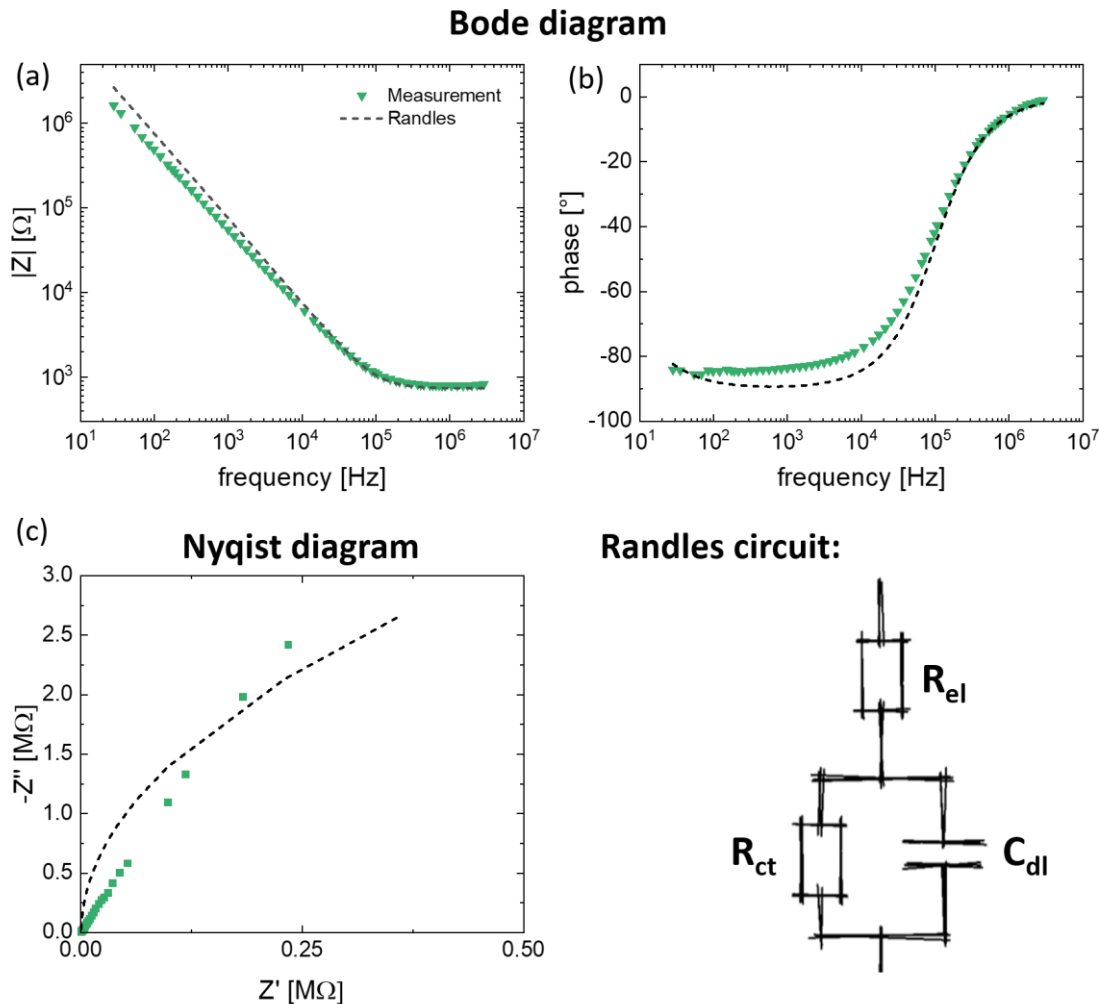


Figure 4-18: Experimental data for  $10\,000 \mu\text{m}^2$  Pt electrodes and best Randles fit in Bode representation (a) and (b) and Nyquist representation (c). For the Randles circuit  $R_{ct} = 20 \text{ M}\Omega$ ,  $R_{el} = 740 \Omega$ , and  $C_{dl} = 2.1 \text{ nF}$  are chosen. (Measurement together with Pratika Rai, IBI-3, Forschungszentrum Jülich)

This shows that it is impossible to apply the simple Randles circuit with fixed (i.e. frequency independent) values for  $C_{dl}$ ,  $R_{ct}$ , and  $R_{el}$  to explain the electrode-electrolyte interface. Only the

high frequency regime might be explained reasonably well, which indicates that we might be able to obtain reasonable statements about the electrolyte resistance. Experiments on the resistance of the electrolyte (not shown here) actually demonstrated that  $R_{el}$  is nearly frequency independent and can be associated with the impedance at high frequencies. This allows us to separate the problem and simplify the system to  $R_{ct}$  and  $C_{dl}$  in parallel.

For this, we have to calculate from the impedance for a Randles circuit allowing frequency dependent values for  $R_{ct}$  and  $C_{dl}$ :

$$Z = Z' + iZ'' = \left( \frac{1}{R_{ct}} - i \frac{1}{D} \right)^{-1} + R_{el}, \quad (4-12)$$

with

$$D = \frac{1}{\omega C_{dl}}, \quad (4-13)$$

$$Z'' = |Z| \cdot \sin \varphi, \quad (4-14)$$

$$Z' = |Z| \cdot \cos \varphi. \quad (4-15)$$

The imaginary and real parts of the impedance is then:

$$Z'' = |Z| \cdot \sin \varphi = - \frac{R_{ct}^2 D}{R_{ct}^2 + D^2}, \quad (4-16)$$

$$Z' - R_{el} = |Z| \cdot \cos \varphi - R_{el} = \frac{R_{ct}}{\left( \frac{R_{ct}}{D} \right)^2 + 1}. \quad (4-17)$$

By using the ratio of equation (4-16) and (4-17):

$$\frac{Z''}{Z' - R_{el}} = - \frac{R_{ct}}{D} \quad (4-18)$$

and insert it in equation (4-17) we obtain values for the charge transfer resistance and the double layer capacitance:

$$R_{ct} = (|Z| \cdot \cos \varphi - R_{el}) \cdot \left( \left( \frac{|Z| \cdot \sin \varphi}{|Z| \cdot \cos \varphi - R_{el}} \right)^2 + 1 \right) \quad (4-19)$$

$$C_{dl} = - \frac{\left( \frac{|Z| \cdot \sin \varphi}{|Z| \cdot \cos \varphi - R_{el}} \right)}{\omega R_{ct}} \quad (4-20)$$

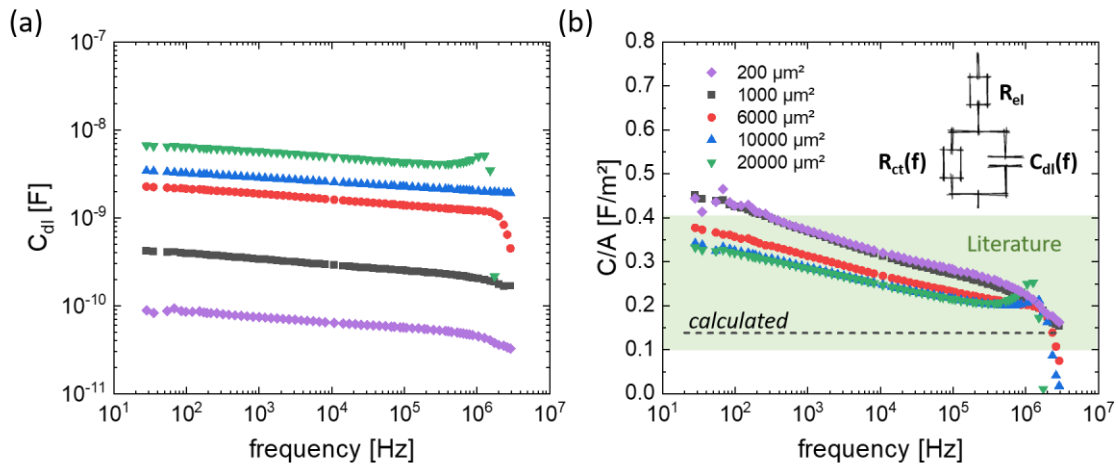


Figure 4-19: Double-layer capacitance (a) and normalized double-layer capacitance (b) for different Pt electrode sizes obtained from the experimental data using eq. (4-19) and (4-20). The green area indicates the regime of literature values, the dashed line represents the theoretical capacitance (eq. (4-11)), and the inset shows the modified Randles model with frequency dependent parameters  $C_{dl}$  and  $R_{ct}$ . (Measurement together with Pratika Rai, IBI-3, Forschungszentrum Jülich)

Figure 4-19 summarizes the resulting frequency dependence of the capacitor  $C_{dl}$  for the electrodes of different sizes (200  $\mu\text{m}^2$  - 20 000  $\mu\text{m}^2$ ). The electrolyte resistance (see equation (4-20)) is assumed to be constant and taken from the high-frequency part of the impedance spectrum. The main observations are:

- As expected, the larger the area, the greater the capacitance.
- Most striking is that the capacitance is linear in the double logarithmic plot for all different electrode sizes. This suggests that we “isolated” the capacitance from the circuit.
- It is also noticeable that the capacitance is frequency-dependent and decreases with increasing frequency. This decrease speaks for a frequency-dependent diffusion for charges (ions) into the insulator (Maxwell-Wagner mechanism), which affects the capacitance. If the capacitance is normalized with the electrode area, Figure 4-19 (b), this decrease with increasing frequency becomes even more apparent. This also explains why different values for the capacitance of a double layer in KCl electrolyte are given in the literature (Halper & Ellenbogen, 2006; Namisnyk, 2003; Rocha et al., 2016; Srinivasan, 2006).
- The theoretical value of the EDL capacitance (equation (4-11)) is marked by the dashed line in Figure 4-19 (b). It represents the capacitance of the ideal EDL, i.e. without diffusion of ions into the Helmholtz layer and, as such, agrees well with the experimental value obtained for the highest frequencies.
- Finally, it is noticeable that the electrodes with the same width (see Table 6) lie directly above each other. The electrodes with the widths 5  $\mu\text{m}$  (200  $\mu\text{m}^2$  and 1 000  $\mu\text{m}^2$ ), 12  $\mu\text{m}$  (6 000  $\mu\text{m}^2$ ), and 20  $\mu\text{m}$  (10 000  $\mu\text{m}^2$  and 20 000  $\mu\text{m}^2$ ) show 3 individual, slightly different frequency dependencies, which indicate that the small dimension (width) plays a role. Our results are in accordance with the literature (Halper & Ellenbogen, 2006; Namisnyk, 2003; Rocha et al., 2016; Srinivasan, 2006).

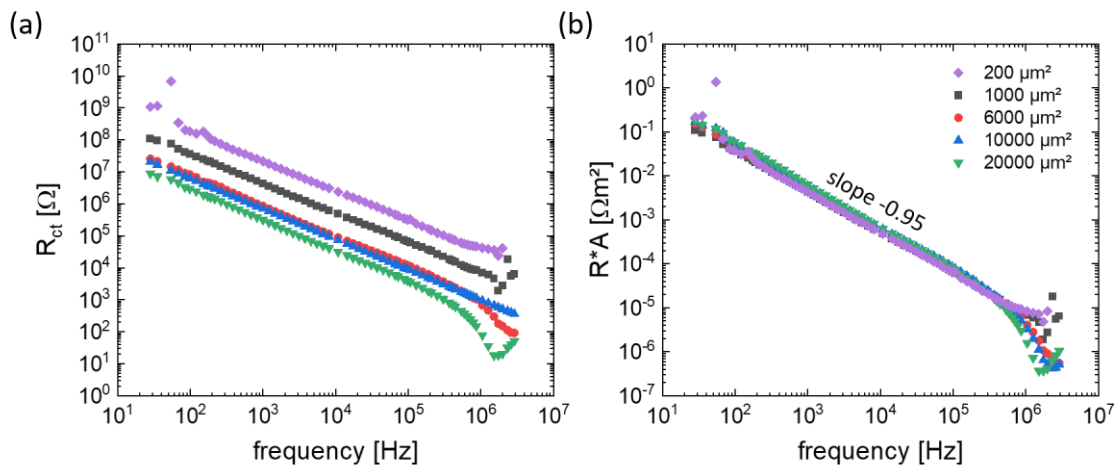


Figure 4-20: Charge transfer resistance (a) and normalized charge transfer resistance (b) for different Pt electrode sizes obtained for experimental values using eq. (4-19). (Measurement together with Pratika Rai, IBI-3, Forschungszentrum Jülich)

Let's look at the corresponding charge transfer resistance determined with to equation (4-19), which is plotted in Figure 4-20 (a):

- As expected, the largest contact (20 000  $\mu\text{m}^2$ ) has the lowest resistance and the smallest contact (200  $\mu\text{m}^2$ ) the highest resistance.
- Similar to the capacitance, the resistance decreases with increasing frequency. This indicates that the leakage current (probably a displacement current) increases with increasing frequency. Since the charge transfer resistance is composed of tunneling effects of electrons and ion movement near the Helmholtz layer in the electrolyte, this decrease in resistance at higher frequencies can be explained by the inertia of the ions in the electrolyte during diffusion into the Helmholtz layer. The slope of  $R_{ct}$  vs  $f$  in the double logarithmic plot is approx -1, which suggests a power law dependence of  $R_{ct} \propto f^{-1}$ . This is actually not the exponential behavior, which is characteristic for a diffusive behavior. It rather indicates the connection of  $R_{ct}$  to the capacitive component and motivates the interpretation of the system with a parallel circuit of a frequency independent resistor  $R_{ct}$  and a constant phase element (CPE), which is used in the following.
- In contrast to the capacitance (Figure 4-19 (b)), no geometric effect of the electrodes can be observed here. Literature values for the charge transfer resistance are not found, which is probably due to the strong frequency dependence.

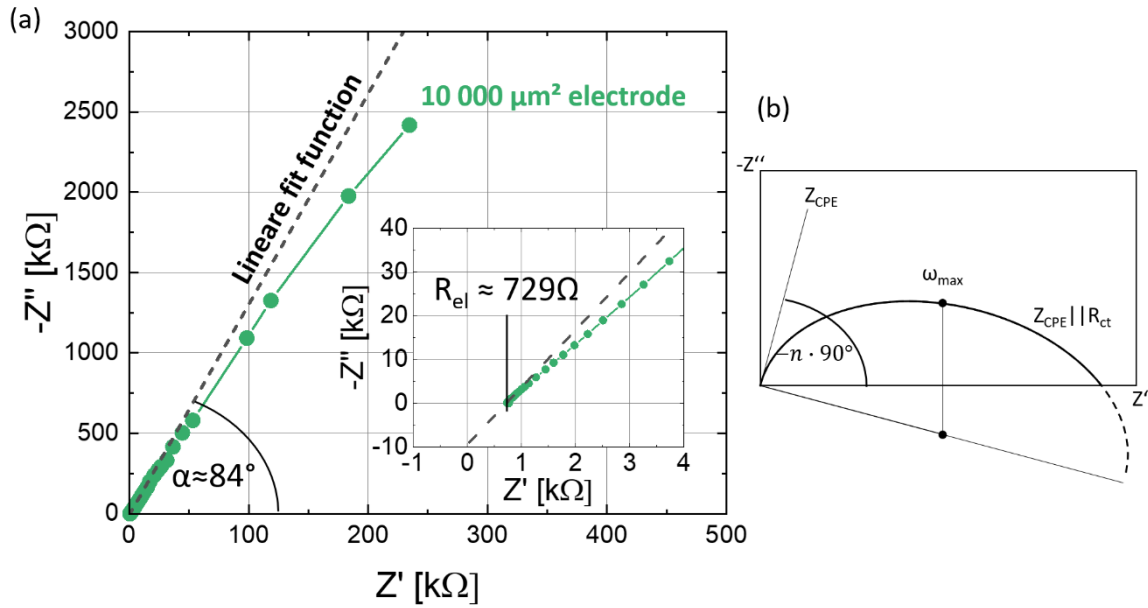


Figure 4-21: Nyquist representation of the impedance of a 10 000  $\mu\text{m}^2$  Pt electrode in an electrolyte (1 M, KCl), including a the linear fit of the first 15 points, and the angle of the resulting fit in (a), the inset zoom-in shows the measured electrolyte resistance  $R_{el}$ . In (b) a sketch of the Nyquist plot of Randles circuit with a CPE replacing the capacitor is shown (Lvovich, 2012, p. 40,41). The linear fit in (a) is  $f(x) = -13.1 \cdot x + 9457$ . (Measurement together with Pratika Rai, IBI-3, Forschungszentrum Jülich)

In order to further improve the model, we replaced the modified Randles model by substituting the dominating capacitance by a CPE (see chapter 2.3.2). Mathematically seen, the CPE acts similar to an arbitrarily long string of parallel-connected resistors and capacitors. For us, it describes the local variation of capacitance and resistance on real electrode as well as the diffusion of ions. A significant advantage of the CPE is that we can separate the systemic parameters, i.e., the capacitance of the Helmholtz layer and the charge transfer resistance, from the diffusion and consider them as frequency-independent parameters. For this purpose, we first have to take a closer look at the different parameters.

To get a first idea of the modified electric circuit, we look at the Nyquist representation of the impedance (Figure 4-21 (a)). The onset of the expected semicircle in the Nyquist plot provides:

- The value of the electrolyte resistance (here  $R_{el} \approx 729 \Omega$ ) and
- the initial slope  $n = \alpha/90^\circ$ , which should be 1 ( $\alpha = 90^\circ$ ) for a perfect capacitor.

In our measurement, the angle is clearly smaller than  $90^\circ$  (here  $84^\circ$ ), which indicates that the capacitor should be replaced by a constant phase element  $Z_{CPE}$  (see chapter 2.3.2). The impedance of a constant phase element is given by the formula (Table 2):

$$Z_{CPE} = \frac{1}{Q(j\omega)^n} \quad (4-21)$$

where  $Q$  and  $n = \alpha/90^\circ$  are frequency-independent variables. The value of the fractional exponent  $n$  must lie between -1 and 1.  $Q$  is a phenomenological parameter, which describes a perfect capacitor at  $n = 1$ , a perfect inductor at  $n = -1$ , and an inverse resistor at  $n = 0$ .



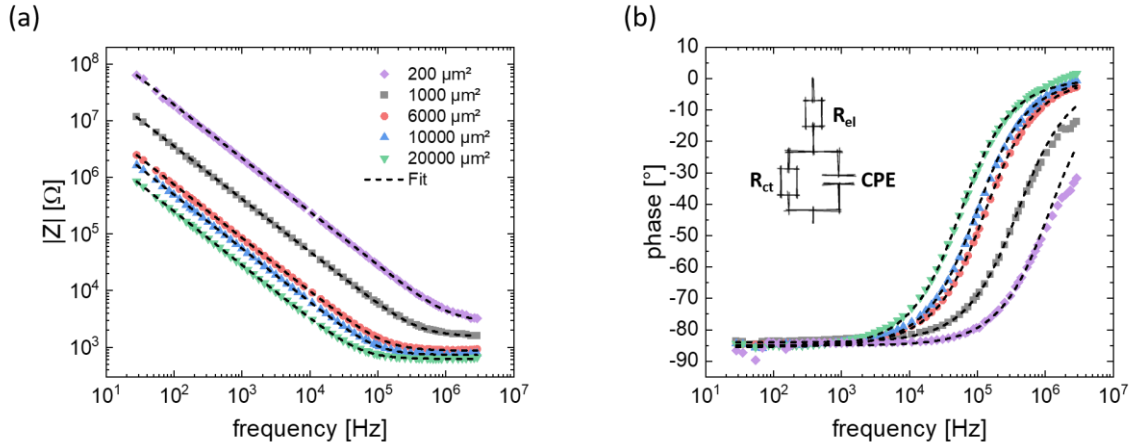


Figure 4-22: Bode representation of the impedance of ozone cleaned Pt electrodes of different sizes with (a) the absolute value of the impedance and (b) the phase. The dashed line represents the Randles fits replacing the capacitor by a constant phase element (inset in (b)). The electrode sizes are ranging from 200  $\mu\text{m}^2$  to 20 000  $\mu\text{m}^2$ . (Measurement together with Pratika Rai, IBI-3, Forschungszentrum Jülich)

For the new fit, the Randles model (Figure 4-22 (b), inset) with a constant phase element was chosen. Representative measurement curves for the different electrodes are plotted in the form of the Bode representation with the corresponding fits (dashed lines) in Figure 4-22. The fits describe the experimental data perfectly. So we can assume that our modified Randles model describes the system well. The values of the different parameters are summarized in Table 7. The self-written script for analyzing the impedance data is given in the appendix (see *Script for impedance*). The major component of the script is a fit vector, which ensures that the absolute impedance, phase, and imaginary part are fitted in parallel. The charge transfer resistance  $R_{ct}$  should be considered with special caution, since only a few (Figure 4-21 (a)) to no (Figure 4-22 (a and b)) data points at low frequency provide features for the evaluation of  $R_{ct}$ . Since  $R_{ct}$  is extremely large, we only see a small part of the beginning of the semicircle in our plots, which leads to large errors. All other fit parameters seem to be trustworthy.

Table 7: Fit parameters averaged over 4 electrodes of the same size and their standard deviation for our ozone cleaned Pt electrodes using the modified Randles circuit with a constant phase element.

Electrode size [ $\mu\text{m}^2$ ]	$R_{el}$ [ $\Omega$ ]	$Q$ [ $10^{-9} \cdot \Omega \text{s}^n$ ]	$n$	$R_{ct}$ [ $10^{15} \cdot \Omega$ ]
200	$2783 \pm 116$	$0.140 \pm 0.023$	$0.942 \pm 0.003$	$21.2 \pm 29.5$
1000	$1583 \pm 24$	$0.633 \pm 0.046$	$0.938 \pm 0.003$	$7.46 \pm 9.97$
6000	$871 \pm 21$	$2.79 \pm 0.68$	$0.946 \pm 0.002$	$2.97 \pm 4.66$
10000	$739 \pm 30$	$4.17 \pm 0.68$	$0.949 \pm 0.002$	$1.44 \pm 1.09$
20000	$624 \pm 4.9$	$8.68 \pm 0.65$	$0.950 \pm 0.002$	$0.85 \pm 0.41$

The parameters of Table 7 are plotted in Figure 4-23 as function of electrode size. The fractional exponent is similar for all electrodes indicating that:

- All electrodes behave similar with respect to their homogeneity and their electronic character and
- with a value of  $n \approx 0.94$  the CPE behaves very similar to a perfect capacitor with  $n = 1$ .

All other parameters,  $Q$ ,  $R_{ct}$ , and  $R_s$  depend on the electrode size and will be discussed separately in the following.

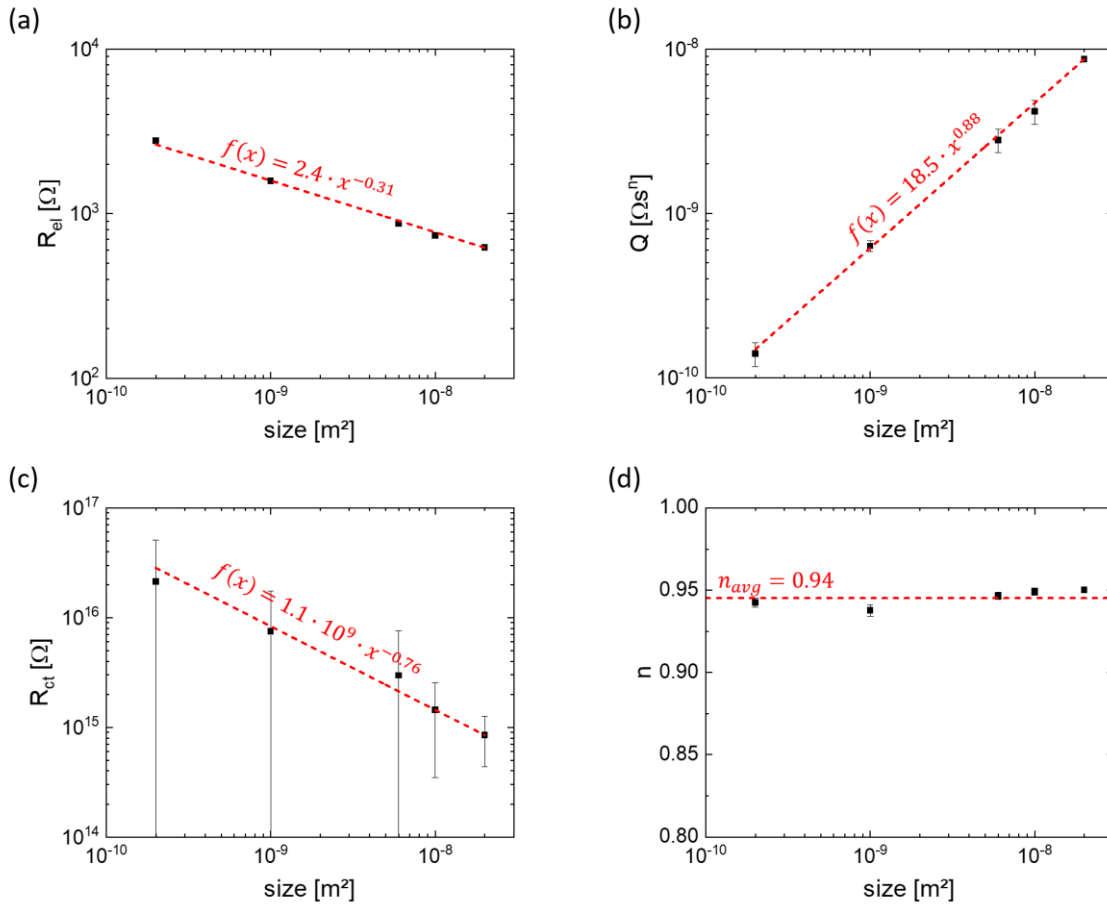


Figure 4-23: Fitted parameters of ozone cleaned Pt electrodes of different sizes with (a) the electrolyte resistance  $R_{el}$ , (b) the phenomenological parameter  $Q$  of the CPE (equation (4-21)), (c) the charge transfer resistance  $R_{ct}$ , and (d) the fractional exponent  $n$  of the CPE. Fits are shown as a dashed line, including the fit results in red. The electrode size is ranging from 200  $\mu\text{m}^2$  to 20 000  $\mu\text{m}^2$ . (Measurement together with Pratika Rai, IBI-3, Forschungszentrum Jülich)

#### 4.2.3. Electrolyte resistance

Via the Randles fit, where the capacitance is replaced by a CPE, the electrolyte resistance can be verified. To compare the resistance with literature values, one can calculate the resistivity by using the spreading resistance of a rectangular electrode (Kristiansson et al., 2007). With the approximation of the electrode by an ellipse with sizes (see Figure 4-24 (a)):

$$a = L/\sqrt{\pi}, \quad b = W/\sqrt{\pi} \quad (4-22)$$

and the use of the elliptical integral  $K(m)$ :

$$K(m) = \int_0^{\pi/2} \frac{dx}{\sqrt{1 - m \cdot \sin^2(x)}}, \quad (4-23)$$

where  $L$  is the electrode length and  $W$  is the electrode width, we obtain a specific resistance of the electrolyte of:

$$\rho_{el} = \frac{R_{el} \cdot 2\pi a}{K \left(1 - \frac{b^2}{a^2}\right)}. \quad (4-24)$$

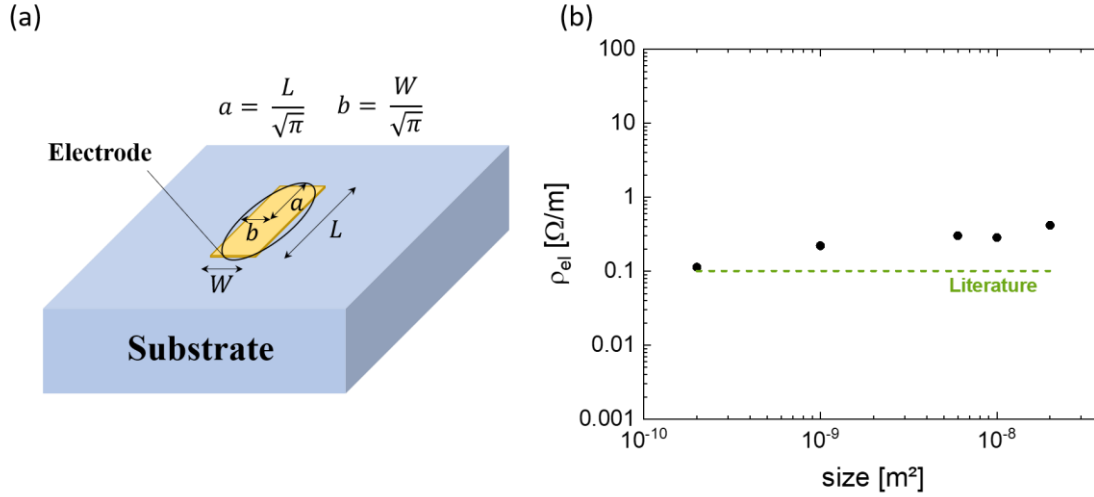


Figure 4-24: (a) schematic of the elliptical approximation to a rectangle electrode used for the definition of the spreading resistance of an electrode (adapted from (Kristiansson et al., 2007)) and (b) resulting electrolyte resistance for our electrodes of different sizes in 1 M KCl. Literature values (green dashed line) are for 20 °C and a KCl concentration of 1 M. (Measurement together with Pratika Rai, IBI-3, Forschungszentrum Jülich)

Figure 4-24 (b) shows the resulting specific resistance of the electrolyte obtained for the different electrodes using equation (4-24). The specific resistance of the electrolyte  $\rho_{el}$  is more or less constant and of the correct order of magnitude. The small deviations from the literature values (Handbook of Chemistry & Physics, 2001) can be ascribed to the rough approximation of the rectangular electrode by an ellipse.

#### 4.2.4. Double-layer capacitance

According to Brug et al. (Brug et al., 1984; Hirschorn et al., 2010) and as shown in equation (2-12), the effective capacity can be determined for our model according to:

$$C_{eff} = \left[ \frac{QR_{el}R_{ct}}{R_{el} + R_{ct}} \right]^{1/n} \frac{R_{el} + R_{ct}}{R_{el}R_{ct}}. \quad (4-25)$$

The effective capacitances for the different electrode sizes are plotted in Figure 4-25 (a), a sketch of the modified Randles model is added in the inset.

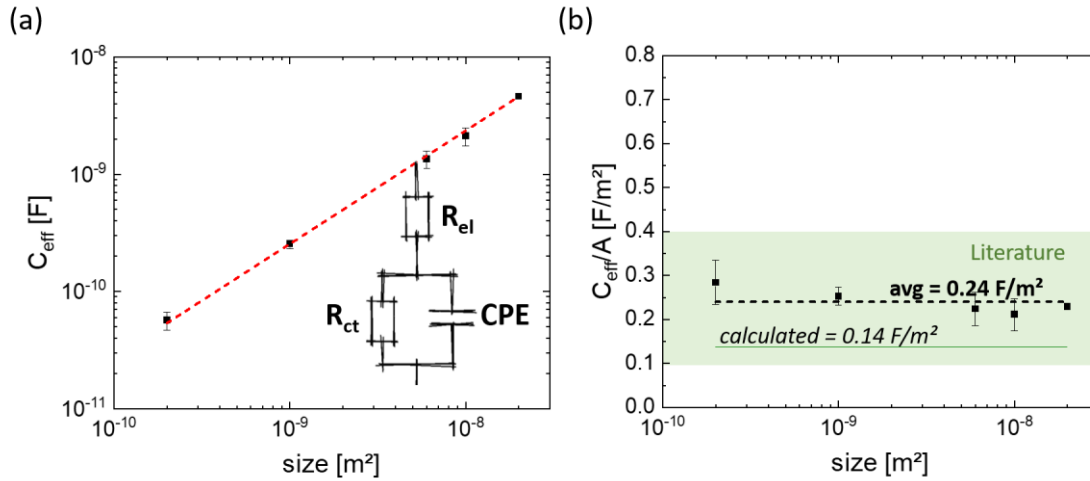


Figure 4-25: Effective capacitance (a) and normalized effective capacitance (b) from the fit parameters in Table 7, as function of electrode size. The green range is correlated to the different values found for  $C_{dl}$  in the literature (Halper & Ellenbogen, 2006; Namisnyk, 2003; Rocha et al., 2016; Srinivasan, 2006), the line is the theoretical value of an ideal Helmholtz layer calculate for 0.1M according to equation (4-11). The error is calculated via the propagation of uncertainty. The modified Randles model is shown in the inset. (Measurement together with Pratika Rai, IBI-3, Forschungszentrum Jülich)

Figure 4-25 (a) shows the expected increase of the effective capacitance with increasing electrode size. The calculated values are summarized in Table 8. In order to be able to compare the values of the effective capacitance or the double layer capacitance with the values given for KCl in literature, Figure 4-25 (b) shows the normalized capacitance  $C/A$ , which is more or less constant and thus independent of the area. The literature values for a double layer capacitance usually vary between 0.1 and 0.4  $F/m^2$  (Halper & Ellenbogen, 2006; Namisnyk, 2003; Rocha et al., 2016; Srinivasan, 2006) in one literature even 0.63  $F/m^2$  is reported (Brown et al., 2016). Theoretically (equation (4-11)), we estimated a capacitance of 0.14  $F/m^2$ . Even though our determined values are in perfect agreement with the literature values, it should be noted that the CPE method is a mathematical approach that provides an effective, frequency-independent value that describes a frequency-dependent parameter.

Table 8: Calculated effective capacitance for fit values in Table 7 with the help of equation (4-25).

Size [ $\mu m^2$ ]	$C_{eff}$ [pF]
200	$56.8 \pm 10.1$
1000	$252.9 \pm 20.4$
6000	$1344.2 \pm 229.3$
10000	$2112.1 \pm 364.3$
20000	$4593.0 \pm 604.8$

In a last step, we can try to analyze the permittivity of the Helmholtz layer. Using the data in Figure 4-25 (b) and assuming a distance of 0.6 nm, we obtain a permittivity:

$$\epsilon_r = \frac{C_{eff} \cdot d}{A \cdot \epsilon_0} = 16.3. \quad (4-26)$$

This permittivity is larger than the value of 7.5 (Teschke et al., 2001) reported for a distance of 0.6 nm to a surface. There might be two main reasons for this discrepancy:

- Teschke et al. used a smaller concentration of 0.1 M KCl in their experiment and
- the effective size of the Helmholtz layer might be smaller than 0.6 nm, which represents the bare size of the molecules.

Another way to obtain the permittivity is given by a conversion of the impedance into a “modulus” according to (Lvovich, 2012, Chapter 1):

$$M^* = M' + jM'' = j\omega C_0 Z^* = \frac{1}{\varepsilon_r^*}, \quad (4-27)$$

where  $j$  is the imaginary number,  $C_0$  the vacuum capacitance,  $Z^*$  the complex impedance, and  $\varepsilon_r$  the permittivity. This way large  $R_{ct}$ 's do not play a role. We can calculate the real and imaginary part of the modulus according to:

$$M'' = -\frac{\omega\varepsilon_0 Z' A}{d}, \quad (4-28)$$

$$M' = \frac{\omega\varepsilon_0 Z'' A}{d}. \quad (4-29)$$

The permittivity is the inverse modulus (equation (4-27)):

$$\varepsilon'' = \frac{M''}{M'^2 + M''^2}, \quad (4-30)$$

$$\varepsilon' = \frac{M'}{M'^2 + M''^2}. \quad (4-31)$$

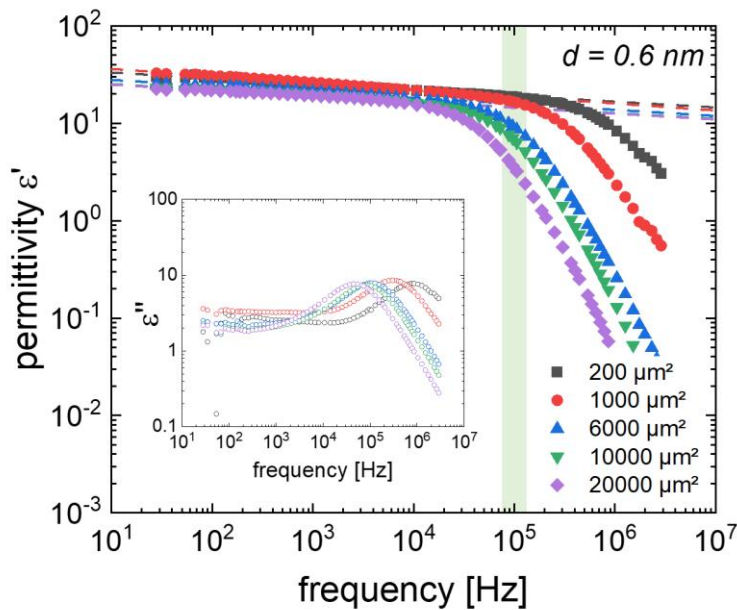


Figure 4-26: Complex dielectric constant according to equations (4-30) and (4-31) for our different sized electrodes separated in real and imaginary (inset) part of the permittivity. The green marked area is the frequency range where typically the permittivity is determined. The dashed lines are the fits to the low frequencies. (Measurement together with Pratika Rai, IBI-3, Forschungszentrum Jülich)

Using again a thickness of the Helmholtz layer of  $d = 0.6$  nm, we obtain the complex permittivity of the Helmholtz layer for our electrodes (Figure 4-26).

- First, the permittivity  $\epsilon_r$  is typically taken at high frequencies (i.e. where  $C_{dl}$  dominates  $R_{ct}$ ) and in the linear regime (i.e. where  $R_{el}$  doesn't play a role). Typically a frequency of 100 kHz is chosen, which results in a permittivity of  $\epsilon_r \approx 18.4$ . This is in perfect agreement with the permittivity calculated above (equation (4-26)).
- Second, the peak in the imaginary part of  $\epsilon''$  (inset Figure 4-26) are indications of Maxwell-Wagner interfacial polarisation or the Maxwell-Wagner relaxation frequency. At this frequency, the system losses energy and the molecules in the Helmholtz layer start to relax.

#### 4.2.5. Charge transfer resistance

As already mentioned, the charge transfer resistance  $R_{ct}$  is burdened with large errors, since only a small part of the semicircles can be seen in the Nyquist plot (see Figure 4-21 (a)). However, we can obtain values for  $R_{ct}$  from the fit.

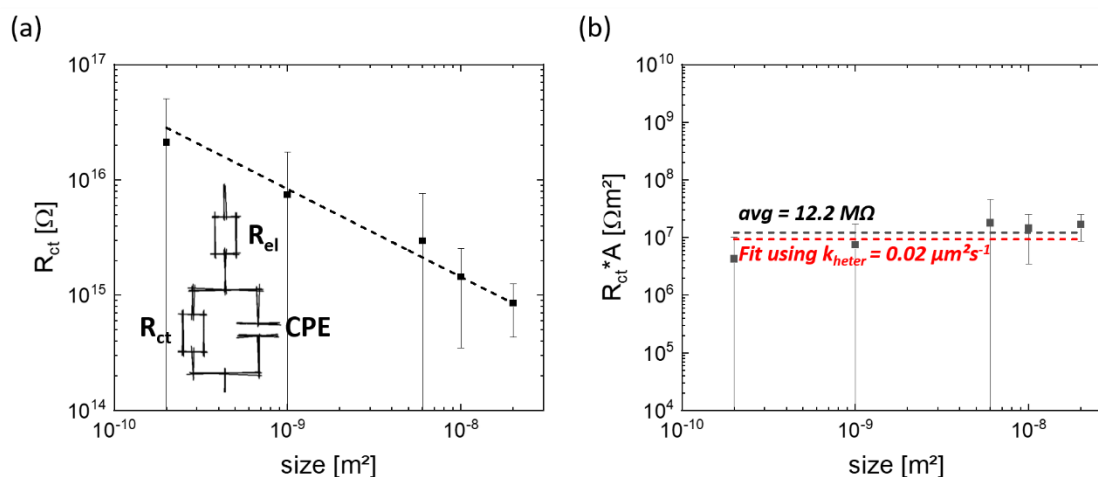


Figure 4-27: Charge transfer resistance  $R_{ct}$  (a) and normalized charge transfer resistance (b) according to the fit parameters in Table 7 as a function of electrode size. The black dashed line in (b) is the averaged value of  $R_{ct}$  and the red dashed line the fit of the heterogeneous kinetic rate constant  $k_{heter}$ . The error is calculated via error propagation, the modified Randles model is shown in the inset. (Measurement together with Pratika Rai, IBI-3, Forschungszentrum Jülich)

Figure 4-27 shows the behavior of the charge transfer resistance  $R_{ct}$  plotted against the electrode size, in (b) the resistance is normalized with the electrode size. It can be seen that:

- $R_{ct}$  decreases as expected with increasing electrode size,
- it is extremely high ( $10^{15} - 10^{17} \Omega$ ),
- it becomes more accurate with larger electrode size, i.e. the error bars become smaller, and
- $R_{ct} \cdot A$  is constant.

Both, the high charge transfer resistance and its constancy when normalized with the area indicates that we have successfully separated the resistance from the diffusion part, i.e. the

frequency-dependent charge displacement. We can, therefore, assume, that the charge transfer resistance mainly describes chemical reactions on the electrode surface and tunnel effects. Moreover, since the voltage is very low (100 mV), we are in a regime where water reactions should not be expected. Even tunnel effects over a distance of 0.6 nm have to be still relatively small, leading to the high resistances.

In addition, we can fit a modified form of the Butler-Volmer equation to determine the heterogeneous kinetic rate constant  $k_{heter}$  (Figure 4-27 (b), dashed red line), which is a measure of the speed of chemical reactions in the nearer equilibrium potential (Lvovich, 2012, p. 75):

$$R_{ct} = \frac{R_G T}{F^2 A \cdot k_{heter} \sum z_i C_i} \quad (4-32)$$

with the gas constant  $R_G$ , the absolute temperature  $T$ , the Faraday constant  $F$ , the electrode area  $A$ , and the valence  $z$  and concentration  $C$  of the ion species  $i$ . This results in a  $k_{heter}$  of:

$$k_{heter} = 0.028 \frac{\mu m^2}{s} \quad (4-33)$$

From this, it becomes obvious that very few reactions take place on the surface.

#### 4.2.6. Impact of molecules

Now that we have understood the basic properties and behavior of electrodes in the electrolyte, we can look at the impact of APTES molecule on the electronic properties of the interface.

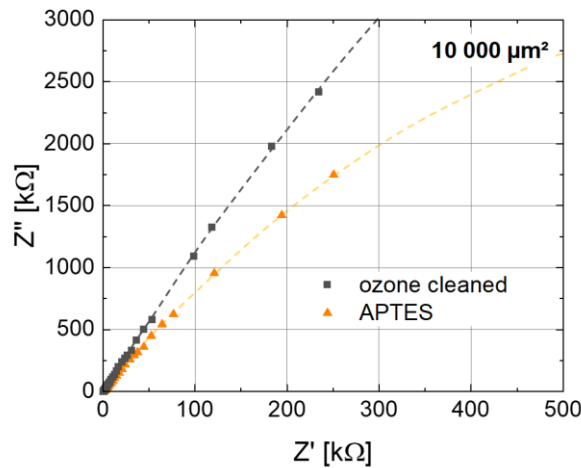


Figure 4-28: Comparison of the impedance of a 10 000  $\mu m^2$  Pt electrode with (orange) and without (black) APTES coating in an electrolyte (1 M, KCl) in Nyquist representation. The dashed lines are the sketched semicircles. (Measurement together with Pratika Rai, IBI-3, Forschungszentrum Jülich)

Figure 4-8 shows the Nyquist representation of the impedance of an APTES coated Pt electrode compared to the bare Pt electrode. Due to the linear form of the Nyquist plot, the small changes caused by the APTES layer are clearly visible. Obviously, the semicircle has changed due to the coating, which can be explained by either:

- A reduced radius, and thus a smaller charge transfer resistance, which would speak for an increased conductivity of the electrode-electrolyte interface or
- a further "tilting" of the circle and thus a smaller fractional exponent, which would indicate a change in the surface conditions.

Let's first look at the electrode properties that should not change, such as the electrolyte resistance  $R_{el}$ .

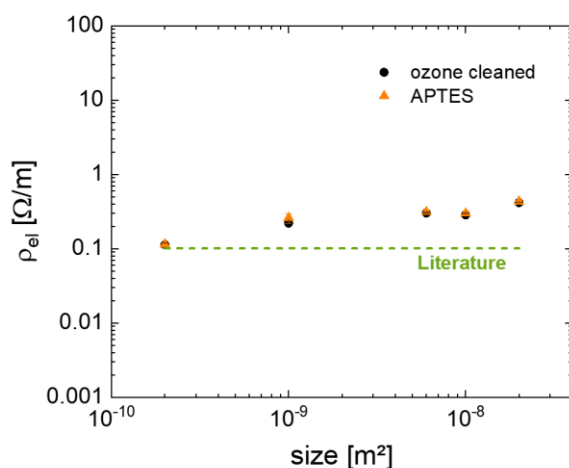


Figure 4-29: Comparison of electrolyte resistance for ozone cleaned electrodes and APTES coated electrodes. The resistivity of the electrolyte is calculated via the spreading resistance using equation (4-24). (Measurement together with Pratika Rai, IBI-3, Forschungszentrum Jülich)

Figure 4-29 shows the resistivity of the electrolyte. This resistivity is calculated from the measurement data for bare Pt electrodes (black) and APTES coated electrodes (orange) using the spreading resistance from equation (4-24). Additionally, the literature value (dashed green line) for a 1 M KCl solution at 20 °C is plotted. The electrolyte resistance is exactly the same for both electrodes (APTES coated and ozone cleaned) and is slightly higher than the literature value (Handbook of Chemistry & Physics, 2001). That simply means the conditions are the same in both experiments.

In order to analyze the surface condition, we take a closer look at the fractional exponent  $n$  of the CPE for both cases (with and without APTES coated Pt electrode). The values were determined using the fit as described in chapter 4.2.2 for the Randles model with a constant phase element (Figure 4-30, inset).



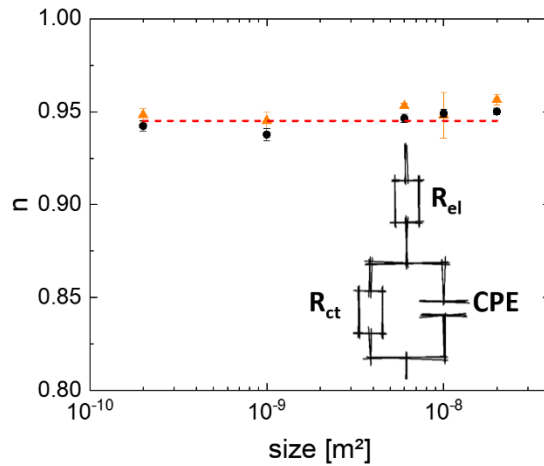


Figure 4-30: Comparison of the fractional exponent of the CPE (see equation (4-21)) for ozone cleaned electrodes (black) and APTES coated electrodes (orange), including the model for the fitting (inset). (Measurement together with Pratika Rai, IBI-3, Forschungszentrum Jülich)

Also, the values of the fractional exponent are almost identical. The same or a slightly smaller exponent has been expected for APTES since the coating with molecules should yield slightly rougher electrode with more defects. However, the  $n$ -values of the APTES coated electrodes lie slightly above the ozone-cleaned reference samples, which means that APTES seems to even improve the homogeneity of the capacitor. However, this increase is small and maybe not significant enough to make a statement about a positive impact of the molecules on the  $n$ -value. Nevertheless, we can state that the molecules do not have a negative influence on the capacitor behavior.

To see the impact of the molecules, let's look at the charge transfer resistance and the effective capacitance, both directly describe the double layer. If there are changes in the interface, we would expect to see it at the Helmholtz layer.

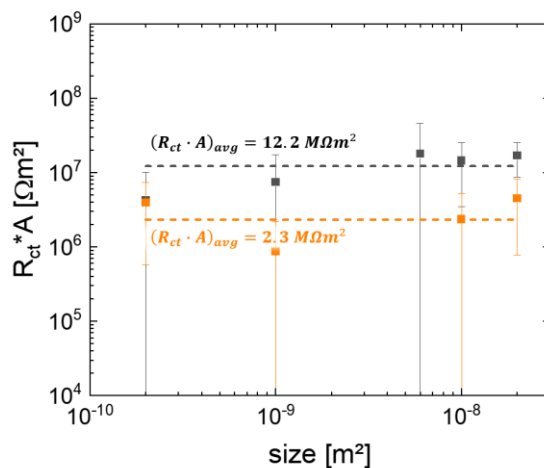


Figure 4-31: Comparison of the charge transfer resistance  $R_{ct}$  normalized by the area for ozone cleaned reference electrode (black) and APTES coated electrodes (orange). The dashed lines represent the average values of  $R_{ct} \cdot A$ . (Measurement together with Pratika Rai, IBI-3, Forschungszentrum Jülich)

Figure 4-31 shows the charge transfer resistance normalized by the electrode area of the cleaned bare reference sample and the APTES-coated sample. The dashed lines represent the average value of  $R_{ct} \cdot A$ .

In general,  $R_{ct}$  is difficult to be determined (see chapter 4.2.2), since in the given frequency range hardly any features of the charge transfer resistor are visible. Therefore, the values should only be considered with caution. Nevertheless, we can state that in both cases (with and without APTES) the charge transfer resistors are approximately constant. Overall, all values for  $R_{ct}$  and thus for the normalized resistance of the APTES-coated sample range below the reference sample. The average values for the normalized charge transfer resistance for the APTES sample are  $\sim 2.3 \text{ M}\Omega\text{m}^2$  and, thus,  $\sim 5$  times smaller than that of the reference sample with  $\sim 12.2 \text{ M}\Omega\text{m}^2$ .

However,  $R_{ct}$  is basically only relevant in the low-frequency range from Hz to  $\mu\text{Hz}$  (Lvovich, 2012, p. 74) and is therefore not really relevant for the measurement of the action potentials of the neurons with a typical frequency spectrum (of  $\sim 20 \text{ Hz} - 10 \text{ kHz}$ ). More important is the capacitive coupling.

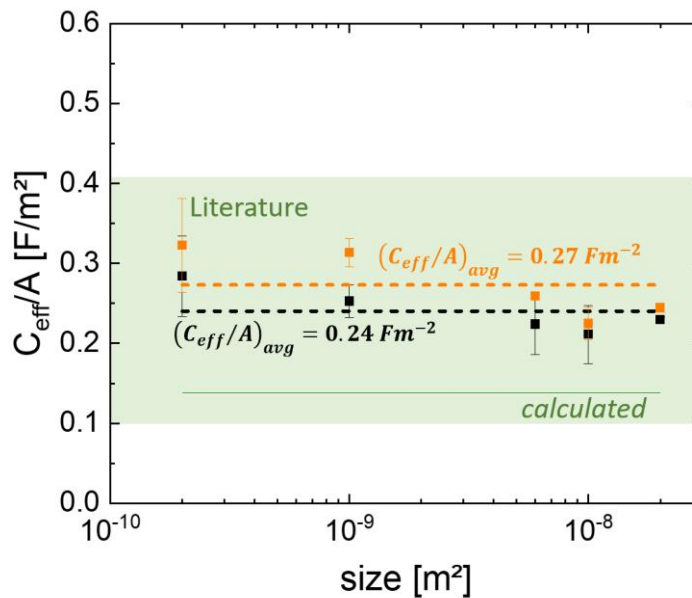


Figure 4-32: Comparison of the effective capacitance  $C_{eff}$  normalized by the electrode area for ozone cleaned reference electrodes (black) and APTES coated electrodes (orange). The dashed lines are the average values of  $C_{eff}$  color-coded to the corresponding coating. The green range marks the literature values for the double layer capacitance in a KCl solution (Halper & Ellenbogen, 2006; Namisnyk, 2003; Rocha et al., 2016; Srinivasan, 2006), and the green line is the calculated plate capacitor (see equation (4-11)). (Measurement together with Pratika Rai, IBI-3, Forschungszentrum Jülich)

Consequently, we now look at the electrode size normalized effective capacitance in Figure 4-32. The capacitance is calculated from the constant phase element according to equation (4-25). The error bars are determined with error propagation. The dashed lines indicate the respective mean value of the capacitances of the different electrode sizes. The area marked in green indicates the range for which literature values for the double layer capacitance in KCl solution are found (Halper & Ellenbogen, 2006; Namisnyk, 2003; Rocha et al., 2016; Srinivasan, 2006), and the green solid line represents the capacitance estimated from the sizes of the EDL (Figure 4-17). We observe:

- All values (APTES coated (orange) and reference sample (black)) lie within the range of the literature values.
- The normalized capacitance values seem to be independent of the electrode sizes.
- All capacitances obtained for the APTES coated electrodes lie slightly above the value for the reference sample.

The averaged normalized capacitance of the APTES coated electrodes is  $\sim 0.27 \text{ Fm}^{-2}$ , and that of the reference sample is  $\sim 0.24 \text{ Fm}^{-2}$ . Assuming an EDL thickness of 0.6 nm we obtain a reasonable permittivity of the inner Helmholtz layer for APTES coated electrodes of  $\epsilon_{r, \text{APTES}} = 18.3$  ( $\epsilon_{r, \text{ref}} = 16.3$ ). Using the size of the APTES molecule of 0.7 nm, we obtain even  $\epsilon_{r, \text{APTES}} = 21.3$ .

Although it is obvious that the molecule can change the properties of the electronic double layer, the mechanism behind it is not fully understood. It is possible that

- the molecule changes the effective electrode size and thus its capacitance and resistance.
- Another explanation could be a modification of the Helmholtz layer by the molecule, allowing more defects and, therefore, a lower charge transfer resistance. This could also decrease the effective distance between the capacitor electrodes due to the increased number of defects on the surface.
- Additionally, the molecules could shift the surface charge of the electrode closer to a neutral potential (see Figure 4-8), which increases the mobility and thus the polarizability of the water molecules. As a result the higher permittivity of the water layer would result in a higher capacitance.

In conclusion of this chapter:

- (i) We developed a setup and a chip design which mimics the situation of the electrode-electrolyte contact in neuroelectronic experiments and delivers reliable and trustworthy impedance measurements.
- (ii) We successfully developed a model to analyze the impedance data, separate the diffusion from the static circuit elements and provide the characteristic coupling parameters such as n-value,  $R_{ct}$ ,  $C_{dl}$ , and  $R_{el}$ .
- (iii) Finally, we demonstrated that a subnanometer thick APTES molecule layer has a positive impact on the electrical coupling. This improvement can be characterized by:

$$n_{C_{dl}} = \frac{C_{APTES} - C_{ref}}{C_{ref}}, \quad (4-34)$$

showing an improvement of 13.25 % for the electrode-electrolyte coupling obtained via APTES coating (Figure 4-33).

*Molecular Layer Functionalized Neuroelectronic Interfaces:  
From Sub-Nanometer Molecular Surface Functionalization to Improved Mechanical  
and Electronic Cell-Chip Coupling*

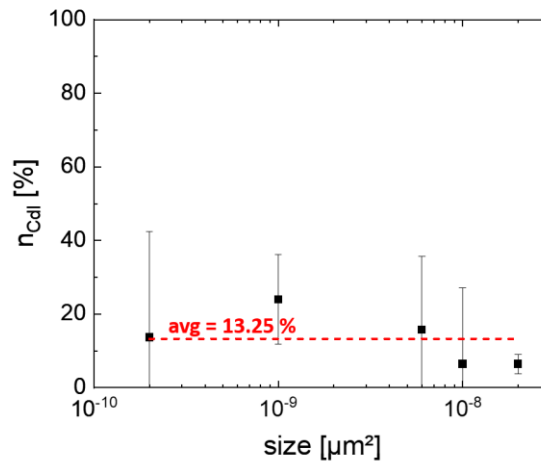


Figure 4-33: Improvement  $n_{\text{Cdl}}$  of the electrode-electrolyte coupling obtained by APTES coating of the Pt electrodes according to eq.(4-34). The ratio of the energies in the capacitor is shown, including the average increase of 13.2% as a dashed line. (Measurement together with Pratika Rai, IBI-3, Forschungszentrum Jülich)

Although on first sight this increase seems to be small, it might represent a first step to a larger improvement. Since the APTES layer is only 0.7 nm thick compared to 20 – 30 nm thick PLL layers (see Figure 4-17) (Colville et al., 2010), we expect that the cell-electrode distance is also reduced for APTES coating. This would increase the sealing resistance, i.e. the resistance responsible for signal loss, and thereby could further increase the signal transmission.

### 4.3. Cell culture and cell-chip coupling on functionalized electrodes

This chapter is partial based on my publication “Surface Functionalization of Platinum Electrodes with APTES for Bioelectronic Applications” (Wolf et al., 2020).

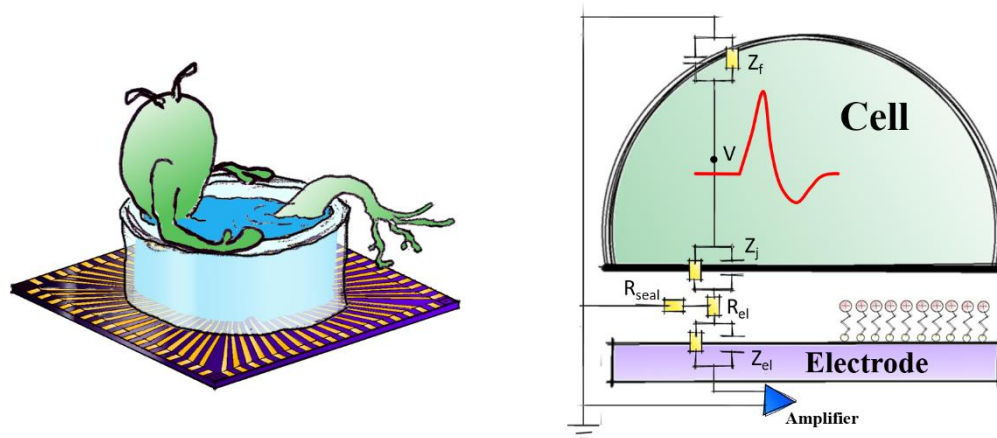


Figure 4-34: Artistic sketch of cell cultures on a chip (left) and electrical cell-chip coupling (right), including the corresponding electrical circuit.

In the last part of this work, we discuss the impact of the APTES coating on neuronal cell growth and the resulting electronic signal transfer between neuronal cells and electrodes. It is known that the surface potential has a huge impact on the initial cell adhesion on surfaces (Gilles et al., 2012; Hao et al., 2016; Yuan et al., 2019). However, it is also important to know whether cells mature on a given surface and, in the case of electronic cell interfacing, whether the interface allows reasonable electronic signal communication (Figure 4-34). In order to analyze the impact of the APTES coating on cell growth and cell-chip communication and to confirm first experiments on HL-1 cells of Markov et al. (Markov et al., 2018), cortical neurons were seeded on  $\text{SiO}_2$  substrates, and Pt coated surfaces with PLL coating as reference. In this part of the thesis, we will first

- (i) analyze the bio affinity (chapter 4.3.1, *Bio affinity of  $\text{SiO}_2$  and Pt surface*) by observing the initial adhesion of cells on Pt and  $\text{SiO}_2$  substrates with different coatings, and compare it to the respective surface potential.
- (ii) In the second step (chapter 4.3.2, *Growth behavior and dynamic*) we will analyze the growth behavior during the complete culture to study the development and maturation of the cells.
- (iii) In chapter 4.3.3, *Mechanical cell chip coupling*, we compare the mechanical cell chip coupling, by analyzing the development of adhesiveness and resulting gap formation of the cells on the substrate, and
- (iv) finally, in chapter 4.3.4, *Electronic cell-chip coupling*, we will show the improved electronic coupling between cells and the electrode.

Let's start with the bioaffinity of the different substrates and different coatings.

#### 4.3.1. Bio affinity of SiO<sub>2</sub> and Pt surface

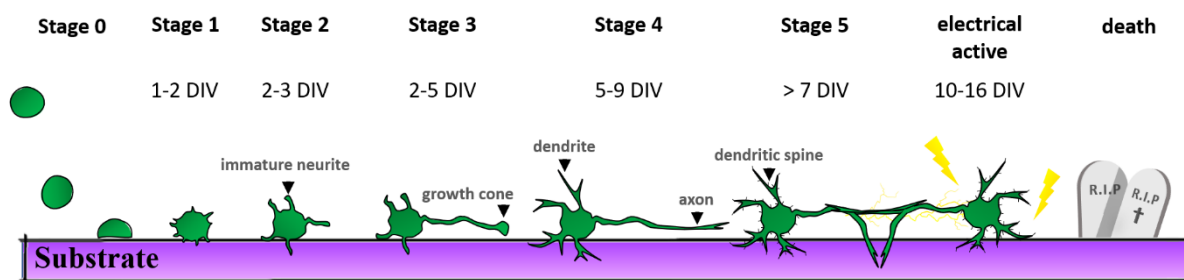


Figure 4-35: Cell growth, according to Arimura et al. (Arimura & Kaibuchi, 2007): stage 0: cells sink to the ground (i.e. substrate); stage 1 and 2: development of the neurites; stage 3: evolution of a growth cone; stage 4: development of axon and dendrites; stage 5: full matured cell and interconnection of neighboring cells to neighbors; after a developed network the cells start to be electronically active and die after some time.

The mechanical adhesion of cells on a surface can be divided into different phases (Figure 4-35; see also chapter 2.4.3). It starts with a sedimentation phase in which gravity and the electrostatic interaction between cell and substrate are the dominant forces. After then the actual cell attachment the first bonds are formed by membrane proteins with the surface. Finally, the cell starts to spread resulting in a permanent, stable bond with the help of focal adhesion, i.e. anchoring cell bonds that mechanically bind the actin cytoskeleton of a cell to the substrate and can bring the cell up to 15 nm close to the substrate (Khalili & Ahmad, 2015; Zaidel-Bar et al., 2004).

At the same time, the cells start to grow and form dendrites and axons. According to Arimura et al. (Arimura & Kaibuchi, 2007), cell growth on a substrate can be divided into 5 stages (Figure 4-35):

- In stage 1 short lamellipodia and filopodia are formed around the soma.
- After about 2 days in vitro (DIV), in stage 2, the cell develops first the immature neurites.
- At 2-5 DIV, a growth cone is formed on one of the neurites (stage 3), which is then assigned to become the axon of the cell. This neurite develops faster than the others. This choice of the neurite does not have to be final, it can change.
- The longest neurite undergoes a molecular change in stage 4 that transforms it into the axion of the cell, whereas all other neurites change to dendrites in stage 4. This process happens on about 5 – 9 DIV.
- From DIV 7 on, the cells begin to develop into fully developed neurons and establish connections to neighboring cells, i.e. formation of first synapses.
- Typically, the cell becomes electronically active between DIV 10 and DIV 16.
- Obviously, the last stage is the cell's death, which depends on the conditions imposed on the cell by the environment.

In this context, not only electrostatic cell-substrate interaction, but also physical (e.g. mechanical or topological) and chemical interactions between cell and substrate play an important role for cell adhesion, growth, formation of a network, electronic activity, and,

finally, death of a cell on a substrate. Deviations from the “standard” behavior of cell culture (e.g. cell density, growth features, death rate, and life time) are indications for the neuroaffinity of a given environment or substrate. It is therefore important to first analyze the affinity and growth of cells on our APTES functionalized Pt in comparison to standard systems like PLL coated on SiO<sub>2</sub>.

First of all, we compare the different substrates. As reference substrate, we take SiO<sub>2</sub> with PLL and APTES coatings and compare it with Pt samples with and without APTES.

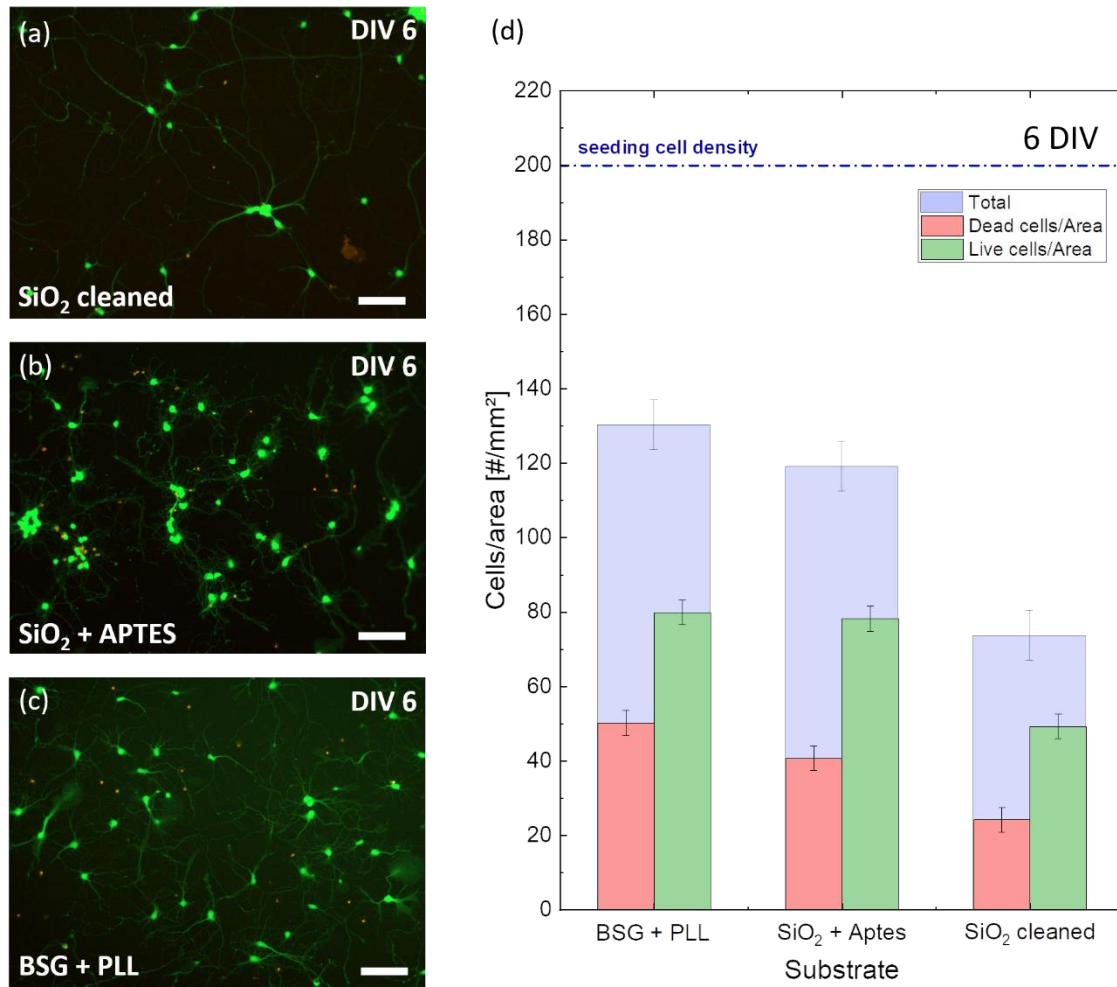


Figure 4-36: Neuronal cell culture experiments on SiO<sub>2</sub> surfaces with different coatings consisting of: (a)-(c) comparison of fluorescent microscope images of live/dead staining of neurons on ozone cleaned SiO<sub>2</sub> samples without (a) and with the coating with APTES (b) and borosilicate sample coated with PLL (c) as the reference sample. The cell cultures are taken at DIV 6, the scaling bar corresponds to 100 μm, (d) resulting statistics of neurons after DIV 6 showing the total number of live neurons (green bars), dead neurons (red bars), the total number of neurons (blue bar), and the nominal seeding neuron density (dashed line) For the statistics 6-14 representative areas of 895.26 x 670.80 μm<sup>2</sup> were investigated. (Cell culture preparation Frano Milos and Bettina Breuer, IBI-3, Forschungszentrum Jülich)

Figure 4-36 shows a comparison of cortical neuron cell distributions (a-c) and the resulting densities (d) for cleaned SiO<sub>2</sub>, SiO<sub>2</sub> surfaces coated with APTES, and a PLL-coated BSG (borosilicate glass) as references. The culture was stained at the 6<sup>th</sup> day in vitro (DIV) with calcein-AM for the living cells and ethidium homodimer for the dead cells (see chapter 3.2.2). The main observations without any coating are:

- That on ozone cleaned SiO<sub>2</sub> are much fewer cells than on the APTES coated or the reference sample coated with PLL.
- The ozone cleaned SiO<sub>2</sub> sample (Figure 4-36 (a)) has the lowest amount of living cells (green) and also fewer dead cells (red). Thus, the total number of cells (Figure 4-36 (d), blue) is also much lower compared to the other samples, and the seeded cell density (blue dashed line). This is in accordance with the literature (Yuan et al., 2020). Also, the network seems to be much less developed, the typical high dendrite density is missing. This shows that an attractive coating is necessary for cell culture to achieve a healthy cell culture.
- The samples coated with APTES or PLL show similar behavior, with a high density of cells of ~40 % of the seeding cell density. Also, the network development seems to be on the same level.
- On all 3 samples, the ratio between living and dead cells is almost the same. The APTES coated sample shows 52.1 % dead cells compared to the living, PLL 49.2 %, and the uncoated SiO<sub>2</sub> surface 62.9 %. From this, it can be concluded that the death rate is about the same and that the problem lies in the sedimentation phase, i.e. the electrostatic attraction between cells and substrates at the beginning of the cell culture. This is in accordance with the surface potential of SiO<sub>2</sub> and APTES coated samples (Figure 4-8 and Figure 4-38). The higher the surface potential, the more cells adhere to settle on it in the earliest phase of the cell culture (Hong et al., 2006; Khalili & Ahmad, 2015). PLL also has amino groups, which suggests that the surface potential of PLL coated SiO<sub>2</sub> is even slightly higher than the APTES coated SiO<sub>2</sub>.

The cell culture seems to confirm our assumptions and the results of Markov et al. (Markov et al., 2018) that an amino layer like an APTES SAM transforms the surface into a more attractive surface for neurons.



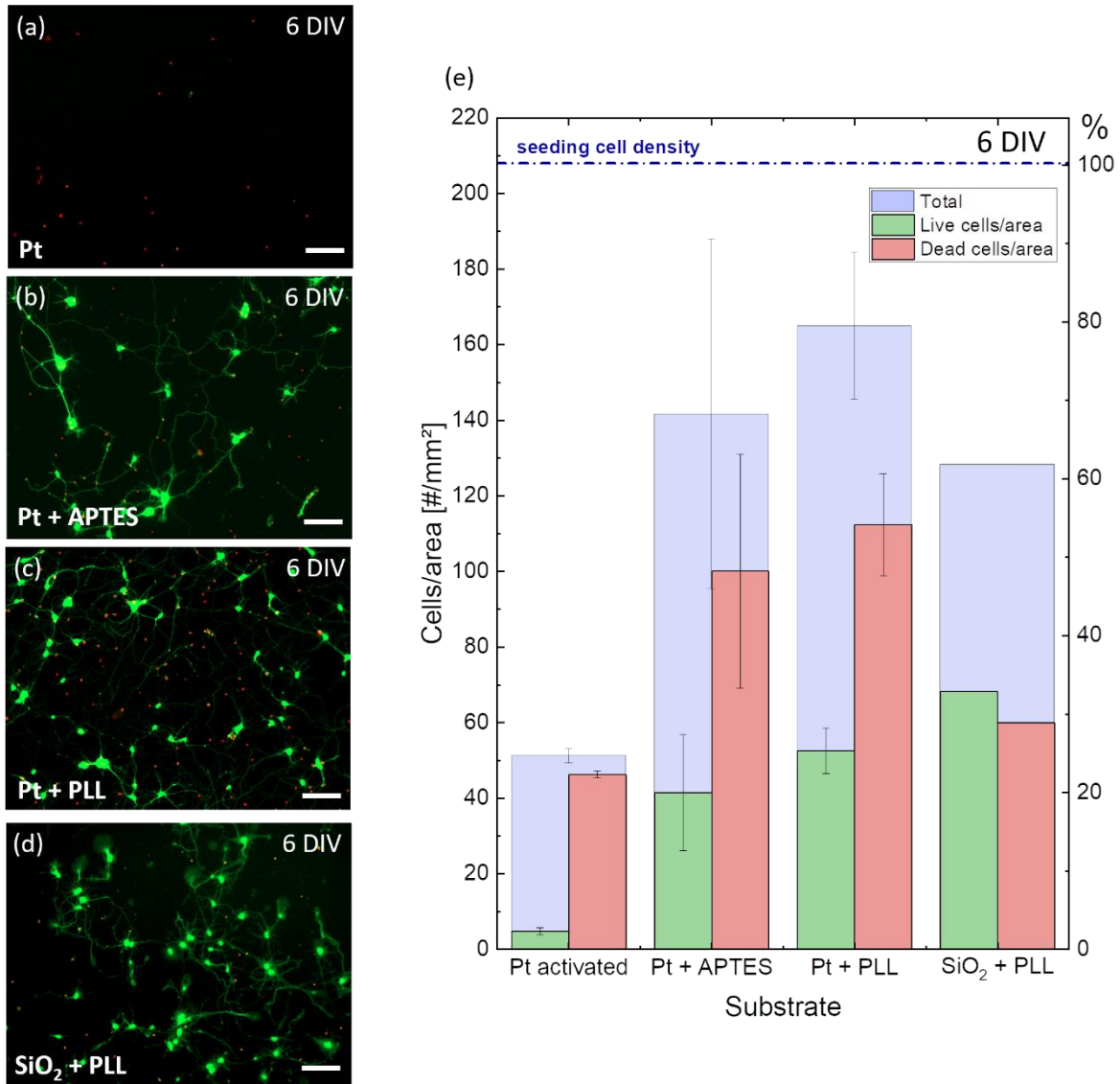


Figure 4-37: Neuronal cell culture experiments on Pt surfaces with different coatings consisting of: (a)-(d) comparison of fluorescent microscope images of live/dead staining of neurons on Pt samples without (a) and with the coating with APTES (b) or PLL (c, d), (c) shows a BSG reference sample with PLL, the cell cultures are taken at DIV 6, the scaling bar corresponds to 100  $\mu\text{m}$ ; (e) resulting statistics of neurons after DIV 6 showing the total number of live neurons (green bars), dead neurons (red bars), the total number of neurons (blue bar), and the nominal seeding neuron density (dashed line), for the statistics 11-40 representative areas of  $895.26 \times 670.80 \mu\text{m}^2$  were investigated. (Cell culture preparation Frano Milos and Bettina Brewer, IBI-3, Forschungszentrum Jülich)

Figure 4-37 shows a comparison of cortical neuron cell distributions (a-d) and the resulting densities (e) for cleaned Pt, Pt surfaces coated with APTES or PLL, and a PLL-coated BSG as reference. The main observations of this comparison are:

- Neurons don't mature on pure (cleaned) Pt surfaces. In detail, there are hardly any living neurons (green) on the cleaned Pt sample. Only a few dead neurons (red dots) are visible. Furthermore, living neurons are not at all mature. They possess a spherical shape without neurites in contrast to the other images. Since dead neurons are easily detached from the surface, the total density of neurons is extremely low in this case (see Figure 4-37 (e)).

- In the case of PLL- or APTES-coated Pt (Figure 4-37 b, d), the neuron cell densities (alive, dead, total) is similar to that of the reference sample (Figure 4-37 e), and the living neurons are in a mature state.

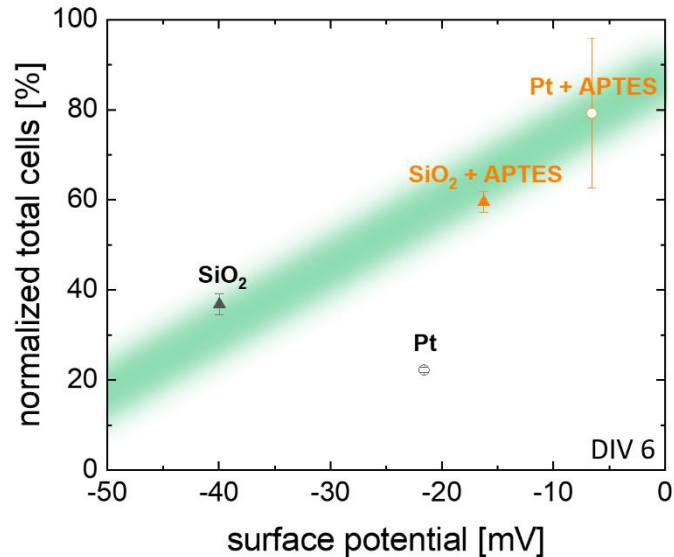


Figure 4-38: Total (live and dead) number of cells normalized by the seeding cell density as a function of the surface potential of the substrate at pH 5.4 taken from Figure 4-8, Figure 4-36, and Figure 4-37 for SiO<sub>2</sub> substrates (solid points) and Pt substrates (open points), both with (orange) and without (black) APTES coating. (Cell culture preparation Frano Milos and Bettina Breuer, IBI-3, Forschungszentrum Jülich)

- Different from the SiO<sub>2</sub> (Figure 4-36) on all Pt samples, the number of dead cells is higher than that of living cells. At the same time, the surface potential of pure Pt is higher compared to SiO<sub>2</sub>. Figure 4-38 shows a comparison of the surface potential and the total number of adhered cells, the values of the surface potential are taken from Figure 4-8. It should be noted that this value represents the  $\zeta$  potential at a pH value of 5.4 and not the physiological conditions. Nevertheless, it can be taken as a measure for the surface potential at physiological conditions. Except for bare Pt, we observe a clear trend, the higher the surface potential, the more cells adhere on the surface. This agrees with the literature (Markov et al., 2018; Yuan et al., 2020). The only exception is the cleaned Pt sample, where hardly any cell adheres. This indicates that in the case of cleaned platinum, there are other reasons for the low cell adhesiveness. Moreover, more or less, only dead cells adhere.

All these results show that bare Pt is an unfriendly environment for cells. Therefore, and especially for Pt electrodes indicating that a coating with PLL or APTES is required to enhance the neuron viability and to obtain a network of matured neurons comparable to that of the reference sample consisting of PLL-coated SiO<sub>2</sub>.

### 4.3.2. Growth behavior and dynamic

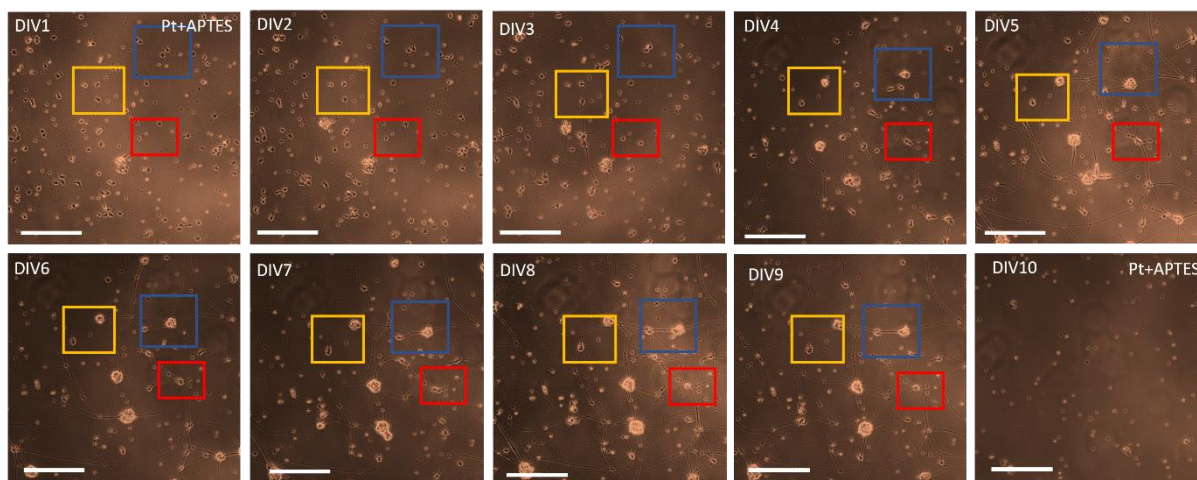


Figure 4-39: Time series of microscope brightfield pictures of typical growth behavior neuron cells for Pt plus APTES as an example. The white bars represent 200  $\mu\text{m}$ . The zoom-in in the colored rectangles are shown in Figure 4-40 – Figure 4-42. (Cell culture preparation Frano Milos and Bettina Breuer, IBI-3, Forschungszentrum Jülich)

Cells need their time to become electronically active. Usually, this takes 10 – 14 days. Therefore, it is important not only to look at the cells at DIV 6 but to pay special attention to their development over time. Figure 2-1 shows microscope pictures of a typical neuron growth on Pt coated with APTES for the first 10 days in vitro (DIV). For the platinum sample, special 5 nm thick Pt layers had to be deposited to ensure a sufficient transparency for the bottom-up microscopy. Unfortunately, the cells on the APTES coated 5 nm Pt films didn't adhere well and were removed on DIV 9 during medium change. However, we can nicely observe the growth of the cells, the development of the network, and the formation of neurospheres (clusters of neurons). Examples for all three cases are discussed in the following.

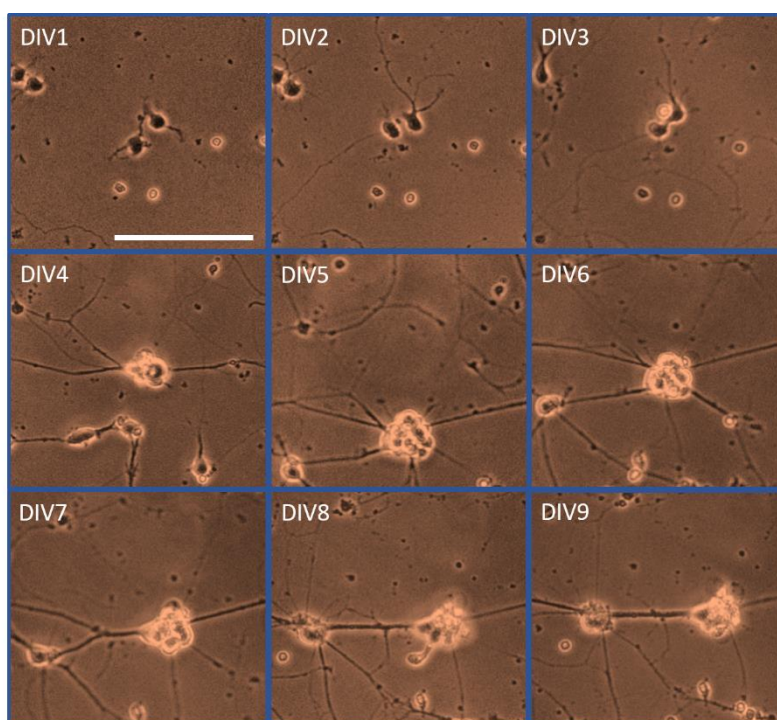
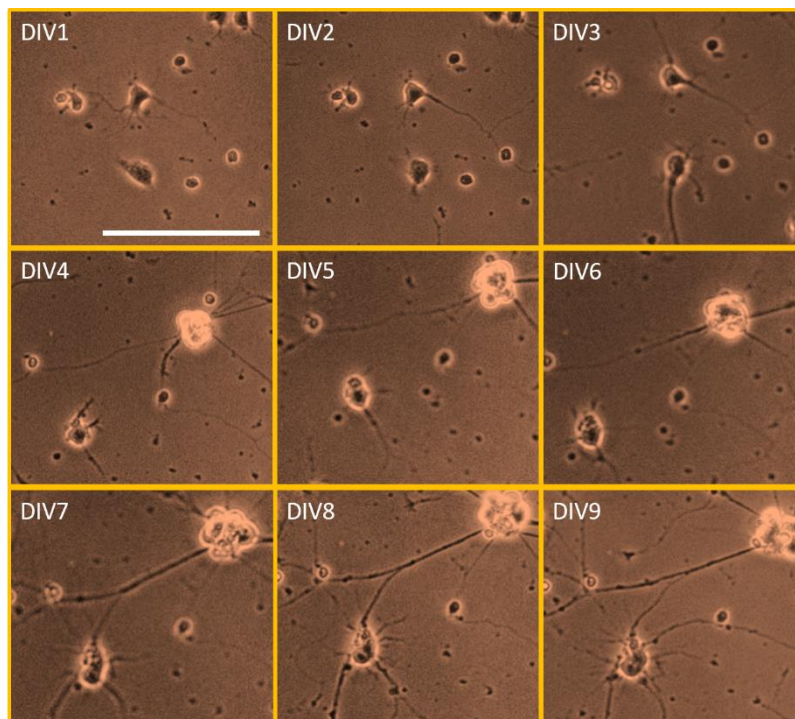


Figure 4-40: Neurosphere formation over time on APTES coated Pt samples. Zoom of blue rectangles in Figure 4-39. The white bar represents 100  $\mu\text{m}$ . (Cell culture preparation Frano Milos and Bettina Breuer, IBI-3, Forschungszentrum Jülich)

*Molecular Layer Functionalized Neuroelectronic Interfaces:  
From Sub-Nanometer Molecular Surface Functionalization to Improved Mechanical  
and Electronic Cell-Chip Coupling*

First, we look at the formation of neurospheres. An example from Figure 4-39 is selected (blue rectangle) in Figure 4-40. At DIV 1, it starts with two single cells that join at DIV 3 on top of a dead cell or contamination. Then this part migrates over the surface of the substrate and collects cells (DIV 4-6). Thereby links to other cells are continuously forming. From DIV 8 on, it looks as if the inner cells are dead and only the outer ones are still alive. After day nine, the neurosphere has disappeared.



*Figure 4-41: Cell growth over time on APTES coated Pt samples. Zoom of yellow rectangles in Figure 4-39. The white bar represents 100  $\mu\text{m}$ . (Cell culture preparation Frano Milos and Bettina Breuer, IBI-3, Forschungszentrum Jülich)*

Figure 4-41 shows an example of cell growth over time (bottom right of the image). The yellow rectangles in the cell time-series in Figure 4-39 are expanded. It visualizes how the cell body is getting bigger and more dendrites grow on the cell body. A neurosphere is formed from the remaining cells.

*Molecular Layer Functionalized Neuroelectronic Interfaces:  
From Sub-Nanometer Molecular Surface Functionalization to Improved Mechanical  
and Electronic Cell-Chip Coupling*

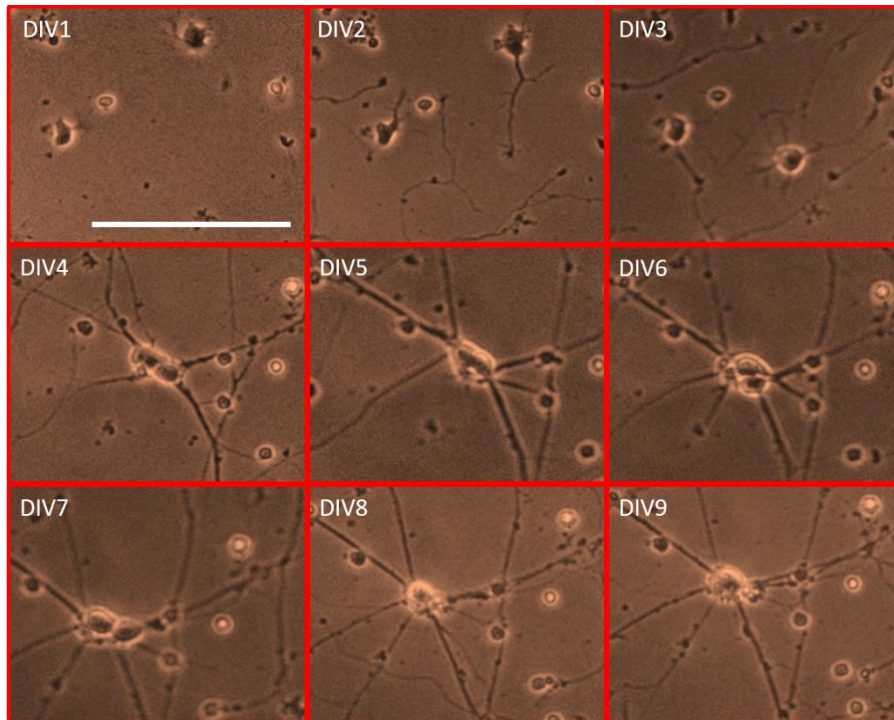


Figure 4-42: Network formation over time on APTES coated Pt samples. Zoom of red rectangles in Figure 4-39. The white bar represents 100  $\mu\text{m}$ . (Cell culture preparation Frano Milos and Bettina Breuer, IBI-3, Forschungszentrum Jülich)

Figure 4-42 shows the formation of a network of cells. The red rectangle in the cell time-series in Figure 4-39 are shown. First, the cells orbit each other while they are still mobile (DIV 1-3). At DIV 4, two cells move together and form stronger and more diverse connections to the neighboring cells.

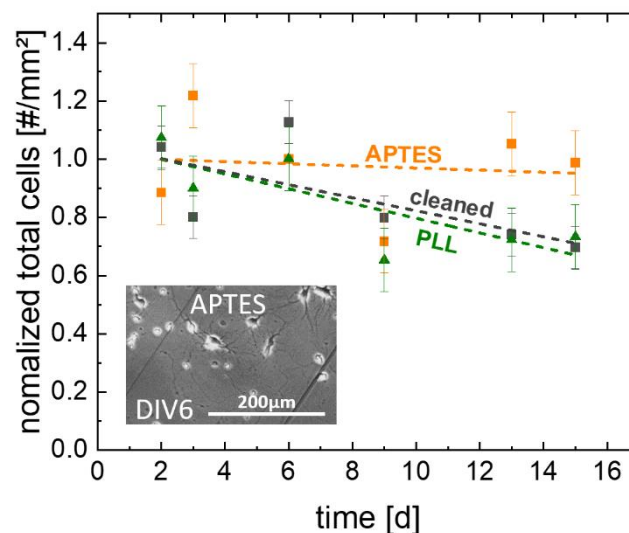


Figure 4-43: Neuron density (live and dead) vs. time of culturing on  $\text{SiO}_2$  without (black), with APTES (orange) and PLL (green) coating. The inset represents an excerpt from a typical brightfield microscope image used for this analysis. The dashed lines represent a linear fit for the different cultures. (Cell culture preparation Frano Milos and Bettina Breuer, IBI-3, Forschungszentrum Jülich)

A first analysis of the cell culture development can be obtained by the statistics of the cell density for the different systems.

Figure 4-43 shows the development of the total cell density (dead and live, however without neuronspheres) on the different functionalized SiO<sub>2</sub> surfaces, cleaned, APTES coating, and PLL coated. Since live-death staining, used for instance in Figure 4-36 and Figure 4-37, has a toxic effect on the cells, brightfield microscope images (Figure 4-43, inset) had to be used for the statistics. This makes it difficult to identify cells at an earlier age than DIV 2, where the first cell signatures become visible (e.g. dendrite growth). The scattering of the data is due to the fact that the cell cultures are stored in an incubator and were only taken out for the images. Therefore, it is not possible to photograph the same positions, instead, representative places on the samples were chosen and evaluated. The linear fits, therefore, represent the best indications for the development of the respective cell culture. Moreover, since slightly different starting populations and especially after the first change of the medium 4 h after preparation are not uncommon, we normalized the cell density by the value obtained by the linear fit for DIV 2.

From the course of the linear fit, it can be seen that the neuron density decreases over time for bare SiO<sub>2</sub> and PLL coated SiO<sub>2</sub>, whereas it is constant for the APTES coated SiO<sub>2</sub>. As described in chapter 3.3.1, the medium is changed twice a week. During this process, cells (especially dead cells) that adhere to the surface are rinsed away. This explains the reduction in the total number of cells for the bare and the PLL coated sample. The APTES coated sample, on the other hand, shows no reduction in the cell density, which indicates a higher adhesiveness of neurons on the APTES-coated sample, i.e. a stronger bond between cells and APTES-coated surface.

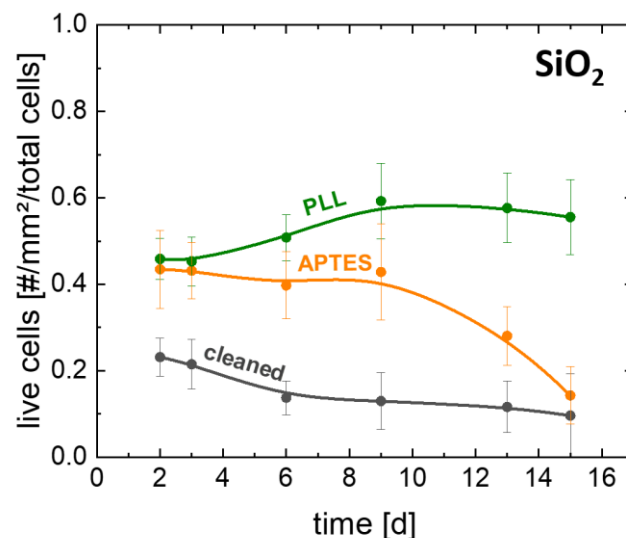


Figure 4-44: Living cells during the cell culture, on SiO<sub>2</sub> without (black), with APTES (orange), and PLL (green) coating. Living cells are normalized by the area and the total number of cells. (Cell culture preparation Frano Milos and Bettina Breuer, IBI-3, Forschungszentrum Jülich)

In a second step we consider the survival rate of the cells on different substrates. Figure 4-44 shows the density of living cells normalized by the total density of cells. The percentage of living cells on bare SiO<sub>2</sub> is very low from the beginning, which means that most cells are dead but still adhere to the surface. This confirms the result of Figure 4-36 (d) that bare SiO<sub>2</sub> isn't suitable for cell growth, it needs an adequate functionalization. The sample coated with PLL starts (DIV 2) with about 50 % living cells and increases slightly to ~60 %. The latter can be explained by the washing away of the dead cells, which indicates a worse adhesion of dead cells

on PLL coated SiO<sub>2</sub> and agrees with the decrease of the total cell density shown in Figure 4-43. The APTES coated sample starts with a similar ratio of ~50 % as the PLL coated sample, but unlike PLL, this ratio remains constant until day 9 (better cell adhesion of dead cells), before the living cells density rapidly decreases. This also agrees with observations shown in Figure 4-43, which demonstrated the better cell adhesiveness also for dead cells for APTES coated SiO<sub>2</sub>.

The decrease in the density of living cells starting at day 9 on APTES-coated SiO<sub>2</sub> is also reported in literature (Gilles, 2010). But it has been suspected that the molecules detach from the SiO<sub>2</sub> and thus the cell adhesion decreases. However, in chapter 4.1 we already demonstrated that APTES binds strongly to SiO<sub>2</sub>, especially stronger than PLL, which can easily be detached from the surface by cells (Y. H. Kim et al., 2011).

The explanation for the reduction of living cells is probably rather given by the (too) strong adhesion of neurons to the substrate. Cells have to be supplied with food from the medium. If the cells are attached too close to the substrate, the food supply of the cells hampered, as a result, the cells can no longer be properly supplied with food. According to Hong et al (Hong et al., 2006; Khalili & Ahmad, 2015) the flattening of the cell, i.e. the strong mechanical interaction with the surface, occurs in phase III of the cell connection (see chapter 2.4.3) and thus shortly before the cell becomes electronically active. Thus, the development over time of the living cell density coincides with this explanation and indicates one shortcoming of the functionalization with APTES, i.e. the too strong mechanical coupling of the cell to the substrate.

#### 4.3.3. Mechanical cell chip coupling

Common techniques to analyze the cell-chip distance are for example focused ion beam or electron microscope investigations (F. Santoro et al., 2017; Seyock et al., 2017; Wrobel et al., 2008) or plasmon resonance experiments (Kreysing et al., 2018). However, these methods require complex preparation steps like a fixation process that kill the cells and could change the cell-chip distance. Moreover, it provides only a value for the cell-chip distance but not the development of the cell-chip coupling over time. However, by using the correlation between the flattening of the cells and the cell-chip distance (chapter 4.3.2), we are able to monitor the cell-chip coupling by recording the cell diameter.

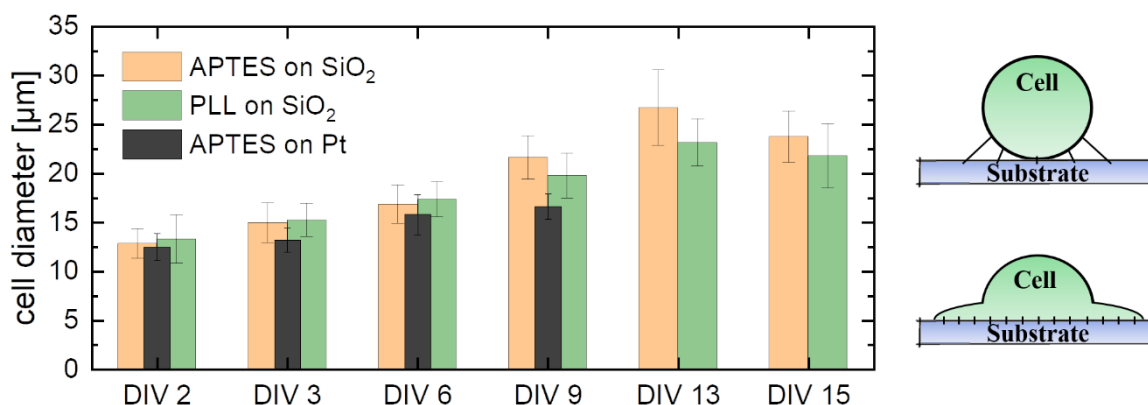


Figure 4-45: Averaged cell diameter of living cells on APTES coated (orange) and PLL coated (green) SiO<sub>2</sub> samples, and for comparison on APTES coated Pt (black) as function of the days of culturing. On the right side, the impact of the cell-chip interaction on the lateral cell diameter is sketched. (Cell culture preparation Frano Milos and Bettina Breuer, IBI-3, Forschungszentrum Jülich)

Figure 4-45 shows the resulting cell diameter of isolated cells on the APTES and PLL coated SiO<sub>2</sub> samples and for APTES coated Pt.

Generally, the diameter of the cells increases with days of culturing and have a maximum at day 13 before they apparently start to shrink again. This increase of the diameter is caused by the growth of the cells on the surface. In the beginning, the diameter of the cell on APTES and PLL coated SiO<sub>2</sub> samples are similar or even a bit smaller on APTES in comparison to PLL. However, around day 9, this behavior is reversed, the cells on the APTES coated SiO<sub>2</sub> sample start to have a larger diameter in comparison to the cells on PLL coated samples. This is exactly the time when the cells are completing their adherence. As a result, the cell is pressed to the surface and the diameter increases. The stronger increase of the diameter of the APTES coated SiO<sub>2</sub> indicates that the cell-chip interaction is larger in this case compared to the PLL coated SiO<sub>2</sub>. The decrease of the diameter, in the end, could be taken as an indication of maturation (PLL) or even the onset of dying of the cells (APTES). The fact that the diameter of the cells on the extremely thin Pt layer with APTES are smaller than those on SiO<sub>2</sub> (with PLL or APTES) might be an indication for the smaller cell-chip interaction of APTES coated Pt. However, we can not exclude that it is an artifact of the extreme thin layer, since cells didn't really adhere to this system.



#### 4.3.4. Electronic cell-chip coupling

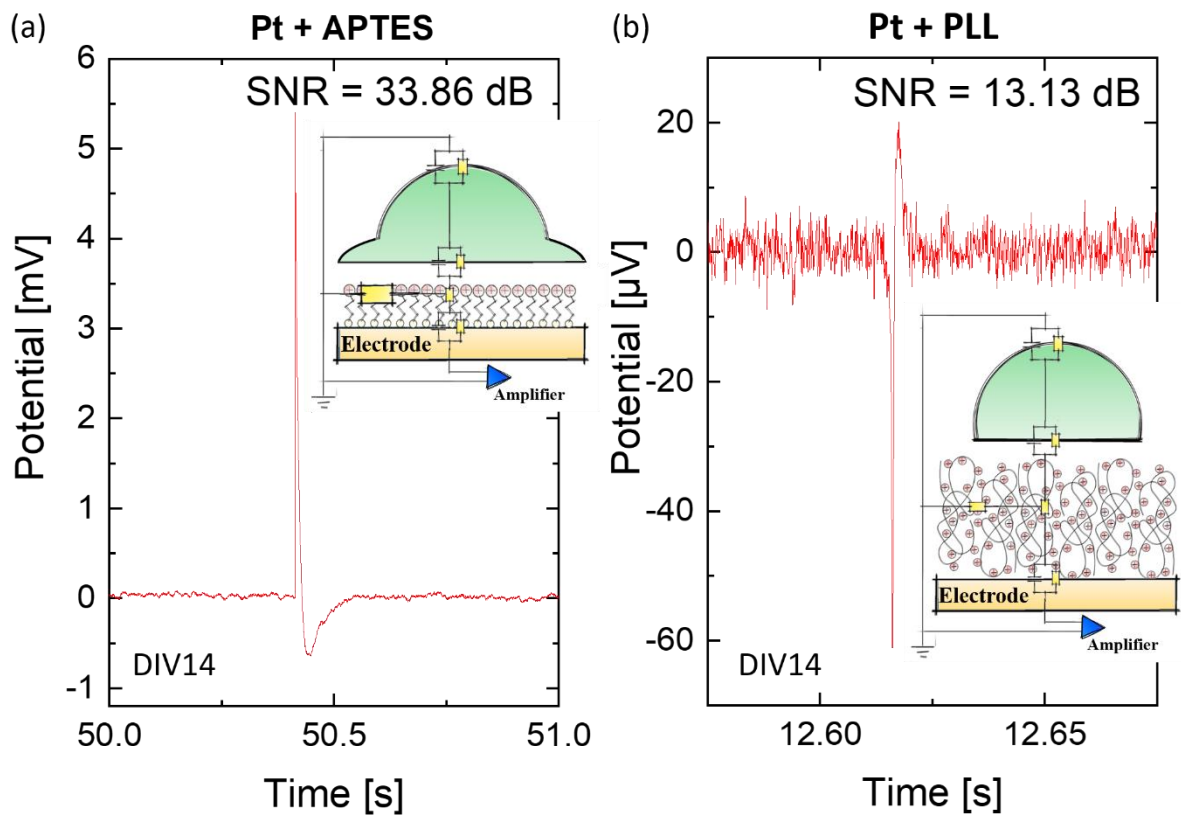


Figure 4-46: Action potential of neuronal cells on Pt electrodes with APTES (a) and PLL (b) coating at DIV 14. The insets show the schematics of the respective cell-chip contacts including the corresponding electronic circuitry. (Cell culture preparation Frano Milos and Bettina Breuer, IBI-3, Forschungszentrum Jülich)

Finally, we characterized the impact of the APTES coating on the cell-chip communication of Pt multielectrode arrays (MEA). For this purpose, we compared action potential (AP) signals of rat cortical neurons that were seeded on quartz wafers equipped with APTES- or PLL-coated Pt MEAs. We used a seeding cell density of 881 neurons/mm<sup>2</sup> and recorded the neuronal signals after maturation of the neurons (DIV14) using a custom-built amplifier system (BioMAS) (see chapter 3.3.3) with an Ag/AgCl reference electrode in the cell culture medium.

Typical AP signals recorded for the neuron cell culture on APTES- and PLL-coated chips and the corresponding signal-to-noise ratio (SNR) are shown in Figure 4-46 (a) and (b). Whereas the PLL-coated Pt electrode shows an AP signal of  $\sim 60 \mu\text{V}$ , the APTES coating leads to a much larger AP signal of  $\sim 5.5 \text{ mV}$ . This agrees with the literature, where publications typically report AP signals  $< 500 \mu\text{V}$  for extracellular measured signals via MEAs (Spanu et al., 2020; Wu et al., 2020), whereas AP signals of up to 10 mV are demonstrated for a different type of neurons (HL-1 cells) on APTES-coated MEAs (Markov et al., 2018). Moreover, considering the typical noise level of  $\sim 5 \mu\text{V}$ , our observation leads to a significantly higher SNR  $\approx 34 \text{ dB}$  for APTES-coated MEAs compared to an SNR  $\approx 13 \text{ dB}$  for PLL-coated MEAs. This vast improvement of the SNR again agrees with the observation of HL-1 cells on APTES-coated MEAs reported in the literature (Markov et al., 2018).

There are two possible explanations for the vast improvement of the AP signal and resulting SNR caused by the APTES coating:

- On the one hand, the signal transfer between neurons and electrodes is improved by the reduction of the electronic double layer impedance  $Z_{el}$  at the Pt-electrolyte interface, (Figure 4-46, inset). This impedance is defined by the electronic properties of the Helmholtz layer, which forms at this interface and which is affected by the APTES layer or the alternative PLL coating. In chapter 4.2.6 we demonstrated the positive impact of the APTES on the capacitance and charge transfer resistance and, thus, the impedance of the interface. The peptide PLL is much larger (Colville et al., 2010) than the APTES molecules and doesn't adhere (bind) at the surface, which indicates that we do not expect a stable improvement of the electronic cell-chip coupling by a PLL coating.
- On the other hand, the spacing between the Pt electrode and the neuron is reduced due to the mechanical cell-chip interaction with the APTES layer. This has been demonstrated in chapter 4.3.3. This automatically increases the seal resistance  $R_s$  and, thus, improves the signal transfer.

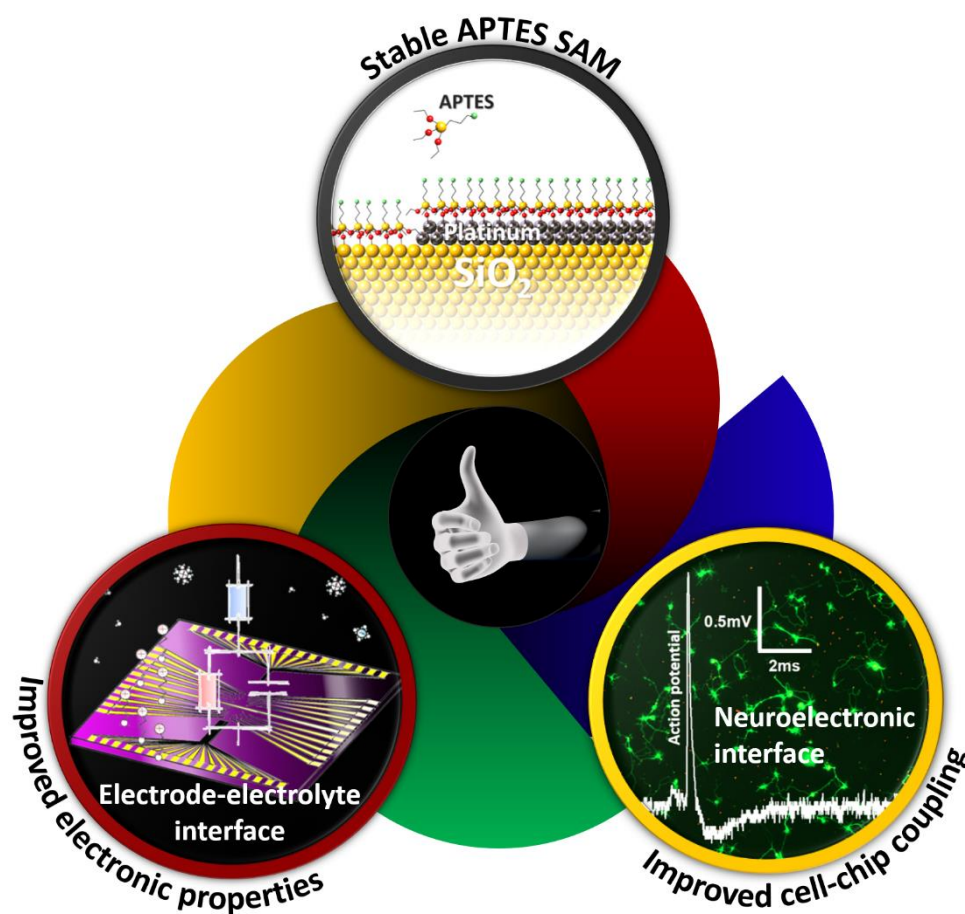
The increase of the signal transfer between neurons and the Pt electrodes for APTES coating and the resulting vast improvement of the SNR, most likely results from a combination of both, the reduction of the interface impedance and the increase of the sealing resistance.

In conclusion, we showed in this chapter:

- that a coating of the substrate ( $\text{SiO}_2$ ) and the electrode (Pt) is necessary for cell growth. Without a suitable coating, the network cannot develop properly, and the cells die.
- Furthermore, APTES coating and PLL coating seem to be nearly equally ideal for cell growth itself. However, the adhesion of cells on APTES is stronger than that on PLL.
- On the other hand, cells on PLL survive longer, which may be due to the "softer" surface of the thicker PLL coating or the stronger adhesion of APTES and the resulting lack of nutrition.
- Nevertheless, and most important, we showed that APTES coating results in much higher signal transmission (in the mV regime) and a much larger signal-to-noise ratio (~13 dB).

## 5. Conclusion and Outlook

In this thesis, we demonstrated that electronic chips with surfaces consisting of an insulating oxide ( $\text{SiO}_2$ ) with integrated metallic electrodes (Pt) can be functionalized with APTES and, thus, improved for neuroelectronic applications. The APTES molecules form a SAM layer on  $\text{SiO}_2$  and Pt, which is stable (at least for a year), and, due to their amino group, generate a biocompatible surface, facilitating the growth of neurons on  $\text{SiO}_2$  and Pt electrodes. Moreover, this stable APTES SAM improves the electronic and mechanical cell-chip coupling between electrodes and neurons.



APTES was deposited via gas-phase-based MLD, which allowed to perform the complete preparation consisting of cleaning and activation of the chip, APTES deposition, and post-deposition treatment in a perfectly controlled way in one recipient without breaking the vacuum.

The presence of APTES layers on Pt has been demonstrated by various ex-situ methods such as AFM, ToF-SIMS, ellipsometry, SPR, and surface potential experiments. We showed that the APTES layer on Pt grows and behaves similarly to that on  $\text{SiO}_2$ . The Pt surface can be activated and the resulting difference in the electrokinetic potential is consistent with the calculations and density of possible docking bonds for molecules on the surface. APTES forms stable layers on Pt after the removal of physisorbed molecules. The resulting functionalization of the surface

shows a clear impact of the amino group on the surface potential ( $\zeta \approx 3$  mV at 5.4 pH and 1 mM KCl). The coverage of the molecules on SiO<sub>2</sub> and Pt surfaces seems to be similar (~50 %) and the thickness of the APTES layer on Pt (0.6 – 1 nm) is comparable to the values of 0.7 – 0.8 nm measured and reported for APTES SAMs on SiO<sub>2</sub> (Markov et al., 2017; Pasternack et al., 2008). The analyses indicate that the gas-phase deposited APTES most likely binds covalently with their silane group on Pt and forms a stable SAM.

In a second step, we demonstrated a successful chip development, enabling reproducible electronic measurements via impedance spectroscopy in electrolyte conditions and mimicking the cell-chip interface. These measurements made it possible to visualize and analyze even the smallest changes in the impedance caused by surface modifications. With the help of a specially developed model, we successfully separated the impact of the diffusion from characteristic static properties of the electronic double layer. We were able to demonstrate an improvement of the double layer capacitance from 2.4 F/m<sup>2</sup> to 2.7 F/m<sup>2</sup> and a reduction of the charge transfer resistance caused by the APTES coating resulting in an improvement of the electrode-electrolyte coupling by ~13 %.

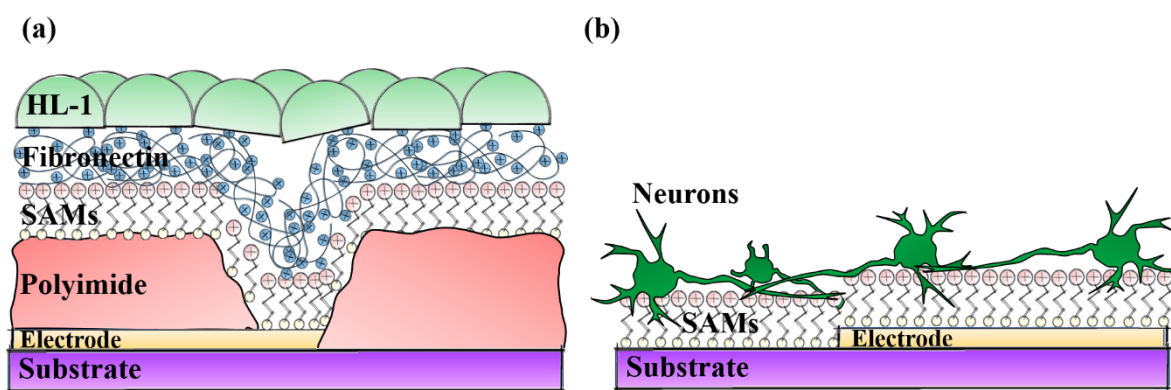


Figure 5-1: *Electronical cell-chip coupling experiments according to A. Markov et al. (Markov et al., 2018) using standard PI passivated MEAs functionalized with APTES and fibronectin and tested with HL-1 cells forming a confluent layer yielding AP signal up to ~10 mV (a) and our approach using MEAs without passivation and APTES functionalization tested with cortical rat neurons yielding signals up to ~6mV.*

In the last step, we showed that both, SiO<sub>2</sub> substrates and Pt electrodes became biocompatible if they are coated with APTES. In contrast to a conventional coating, for example with PLL, the APTES coating also improves the mechanical coupling between chip and cells. This seems to lead to a smaller gap between electrodes and cells and, thus, a higher sealing resistance. This sealing resistance together with the electrode-electrolyte coupling are responsible for the signal transfer between cell and electrode. Since both, sealing resistance and electrode-electrolyte coupling, are improved by the APTES coating, we obtained a strong improvement of the cell signals (action potential) to several mV (typically 4-6 mV, SNR ~34 dB) compared to typical signals of 200 – 400  $\mu$ V (SNR ~ 13 dB) obtained for PLL coated chip. This confirms the first and at that time surprising observations of A. Markov obtained for conventional chips and HL-1 cells (Markov et al., 2018) that the functionalization with APTES improves the electronic cell-chip coupling significantly, here by ~1 500 %.

In contrast to our work, Aleksandr Markov (Markov et al., 2018) used standard MEAs passivated with 1  $\mu$ m polyimide (PI), which were coated with organic molecules (APTES and GLYMO) and fibronectin (a glycoprotein) (Figure 5-1 (a)). Due to the special features of HL-1

cells (cardiac muscle cell derived from AT-1 mouse artial cardiomyocyte tumor lineage (Claycomb et al., 1998)), which form a confluent layer, it was argued that the complex molecular layer or sealing between the confluent cell layer and the functionalized PI passivation could have been responsible for the large signal transfer of ~10 mV for the extracellular action potential. Our measurements are performed on bare MEAs without passivation and for neuronal cells, which grow sporadically and form networks (Figure 5-1 (b)). This system is obviously closer and more relevant for neuroelectronic applications. Moreover, it allowed to analyze the signal transfer in detail.

In this work, we demonstrated that APTES SAMs represent an exceptional tool for surface functionalization for neuroelectronic applications. The APTES SAMs create stable, patternable, and biofriendly coatings that increase the cell-chip coupling (mechanically and electronically) and lead to fantastic signal-to-noise ratios. This technology might, therefore, not only be suitable for tomorrow's prosthetics but could also be used in a variety of biosensors. By simply exchanging the functional group of the organic molecule, surfaces could be tailored for specific purposes or used as linker (receptor) for other bio-objects such as proteins or DNA. As a next step, the issue of the cell stability (in our case, cells died typically on DIV 9) should be solved. One solution might be to combine molecules with a monolayer of the peptide PLL. Another option could be the use of flexible substrates like PDMS or porous substrates to solve the nutrition problem.

In the end, the APTES functionalization of the electrodes represents an outstanding and exciting possibility to boost the cell-chip coupling. It might represent an important tool to improve neuroelectronic sensor and actuator devices.

## I. References

- Alibart, F., Pieutin, S., Guérin, D., Novembre, C., Lenfant, S., Lmimouni, K., Gamrat, C., & Vuillaume, D. (2010). An organic nanoparticle transistor behaving as a biological spiking synapse. *Advanced Functional Materials*, 20(2), 330–337. <https://doi.org/10.1002/adfm.200901335>
- An, D., Liu, H., Wang, S., & Li, X. (2019). Modification of ITO anodes with self-assembled monolayers for enhancing hole injection in OLEDs. *Applied Physics Letters*, 114(15), 153301. <https://doi.org/10.1063/1.5086800>
- Arimura, N., & Kaibuchi, K. (2007). Neuronal polarity: From extracellular signals to intracellular mechanisms. *Nature Reviews Neuroscience*, 8(3), 194–205. <https://doi.org/10.1038/nrn2056>
- Asadi, K., Gholamrezaie, F., Smits, E. C. P., Blom, P. W. M., & Boer, B. de. (2007). Manipulation of charge carrier injection into organic field-effect transistors by self-assembled monolayers of alkanethiols. *Journal of Materials Chemistry*, 17(19), 1947. <https://doi.org/10.1039/b617995a>
- Balland, V., Hureau, C., Cusano, A. M., Liu, Y., Tron, T., & Limoges, B. (2008). Oriented immobilization of a fully active monolayer of histidine-tagged recombinant laccase on modified gold electrodes. *Chemistry - A European Journal*, 14(24), 7186–7192. <https://doi.org/10.1002/chem.200800368>
- Bardavid, Y., Ghabboun, J., Porath, D., Kotylar, A. B., & Yitzchaik, S. (2008). Formation of polyaniline layer on DNA by electrochemical polymerization. *Polymer*, 49(9), 2217–2222. <https://doi.org/10.1016/j.polymer.2008.03.014>
- Bardecker, J. A., Ma, H., Kim, T., Huang, F., Liu, M. S., Cheng, Y. J., Ting, G., & Jen, A. K. Y. (2008). Self-assembled electroactive phosphonic acids on ITO: Maximizing hole-injection in polymer light-emitting diodes. *Advanced Functional Materials*, 18(24), 3964–3971. <https://doi.org/10.1002/adfm.200800033>
- Barron, W., Murray, B. S., Scales, P. J., Healy, T. W., Dixon, D. R., & Pascoe, M. (1994). The streaming current detector: A comparison with conventional electrokinetic techniques. *Colloids and Surfaces A: Physicochemical and Engineering Aspects*, 88(2–3), 129–139. [https://doi.org/10.1016/0927-7757\(94\)02824-9](https://doi.org/10.1016/0927-7757(94)02824-9)
- Bazant, M. Z. (2019). Editorial Overview: Fundamental and Theoretical Electrochemistry Advances in the theory of electrochemical interfaces. *Current Opinion in Electrochemistry*, 13, A1–A4. <https://doi.org/10.1016/j.coelec.2019.02.008>
- Beer, R. D. (1990). *Intelligence as adaptive behavior: an experiment in computational neuroethology*. Academic Press Professional, Inc.
- Berggren, C., Bjarnason, B., & Johansson, G. (2001). Capacitive Biosensors. *Electroanalysis*, 13(3), 173–180. [https://doi.org/10.1002/1521-4109\(200103\)13:3<173::AID-ELAN173>3.0.CO;2-B](https://doi.org/10.1002/1521-4109(200103)13:3<173::AID-ELAN173>3.0.CO;2-B)
- Bockris, J. O. (1998). *Modern Electrochemistry 2B: Electrodicts in Chemistry, Engineering, Biology and Environmental Science, Band 2*. Springer Science & Business Media.
- Breuls, R. G. M., Jiya, T. U., & Smit, T. H. (2008). Scaffold Stiffness Influences Cell Behavior: Opportunities for Skeletal Tissue Engineering. *The Open Orthopaedics Journal*, 2(1), 103–109. <https://doi.org/10.2174/1874325000802010103>
- Brito, R., Rodríguez, V. A., Figueroa, J., & Cabrera, C. R. (2002). Adsorption of 3-mercaptopropyltrimethoxysilane and 3-aminopropyltrimethoxysilane at platinum electrodes. *Journal of Electroanalytical Chemistry*, 520(1–2), 47–52. [https://doi.org/10.1016/S0022-0728\(01\)00718-5](https://doi.org/10.1016/S0022-0728(01)00718-5)
- Broers, A. N., Hoole Andrew, A. C. F., & Ryan, J. M. (1996). Electron beam lithography - Resolution limits. *Microelectronic Engineering*, 32(1-4 SPEC. ISS.), 131–142. [i](https://doi.org/10.1016/0167-</a></p></div><div data-bbox=)

9317(95)00368-1

- Brown, M. A., Abbas, Z., Kleibert, A., Green, R. G., Goel, A., May, S., & Squires, T. M. (2016). Determination of surface potential and electrical double-layer structure at the aqueous electrolyte-nanoparticle interface. *Physical Review X*, 6(1), 1–12. <https://doi.org/10.1103/PhysRevX.6.011007>
- Brug, G. J., van den Eeden, A. L. G., Sluyters-Rehbach, M., & Sluyters, J. H. (1984). The analysis of electrode impedances complicated by the presence of a constant phase element. *J. Electroanal. Chem.*, 176, 275–295.
- Bryant, M. A., & Pemberton, J. E. (1991). Surface Raman Scattering of Self-Assembled Monolayers Formed from 1-Alkanethiols: Behavior of Films at Au and Comparison to Films at Ag. *Journal of the American Chemical Society*, 113(22), 8284–8293. <https://doi.org/10.1021/ja00022a014>
- Byun, S., Oh, J., Lee, B. Y., & Lee, S. (2005). Improvement of coagulation efficiency using instantaneous flash mixer (IFM) for water treatment. *Colloids and Surfaces A: Physicochemical and Engineering Aspects*, 268(1–3), 104–110. <https://doi.org/10.1016/j.colsurfa.2005.06.027>
- Cai, B. (2016). *Manipulating the Structural and Electronic Properties of Epitaxial NaNbO<sub>3</sub> Films via Strain and Stoichiometry* Biya Cai. <http://kups.ub.uni-koeln.de/id/eprint/7070>
- Cai, K., Frant, M., Bossert, J., Hildebrand, G., Liefelth, K., & Jandt, K. D. (2006). Surface functionalized titanium thin films: Zeta-potential, protein adsorption and cell proliferation. *Colloids and Surfaces B: Biointerfaces*, 50(1), 1–8. <https://doi.org/10.1016/j.colsurfb.2006.03.016>
- Chaudhary, U., Mrachacz-Kersting, N., & Birbaumer, N. (2020). Neuropsychological and neurophysiological aspects of brain-computer-interface (BCI)-control in paralysis. *The Journal of Physiology*, 0, JP278775. <https://doi.org/10.1113/JP278775>
- Claycomb, W. C., Lanson, N. A., Stallworth, B. S., Egeland, D. B., Delcarpio, J. B., Bahinski, A., & Izzo, N. J. (1998). HL-1 cells: A cardiac muscle cell line that contracts and retains phenotypic characteristics of the adult cardiomyocyte. *Proceedings of the National Academy of Sciences*, 95(6), 2979–2984. <https://doi.org/10.1073/pnas.95.6.2979>
- Colville, K., Tompkins, N., Rutenberg, A. D., & Jericho, M. H. (2010). Effects of Poly(L-lysine) Substrates on Attached Escherichia coli Bacteria. *Langmuir*, 26(4), 2639–2644. <https://doi.org/10.1021/la902826n>
- Danzer, M. A., & Hofer, E. P. (2009). Analysis of the electrochemical behaviour of polymer electrolyte fuel cells using simple impedance models. *Journal of Power Sources*, 190(1), 25–33. <https://doi.org/10.1016/j.jpowsour.2008.10.003>
- Dowling, D. P., Miller, I. S., Ardhaoui, M., & Gallagher, W. M. (2011). Effect of surface wettability and topography on the adhesion of osteosarcoma cells on plasma-modified polystyrene. *Journal of Biomaterials Applications*, 26(3), 327–347. <https://doi.org/10.1177/0885328210372148>
- Dreier, L. B., Nagata, Y., Lutz, H., Gonella, G., Hunger, J., Backus, E. H. G., & Bonn, M. (2018). Saturation of charge-induced water alignment at model membrane surfaces. *Science Advances*, 4(3), 1–9. <https://doi.org/10.1126/sciadv.aap7415>
- Dudel, J. (1998). *Innerneurale Homeostase und Kommunikation, Erregung* (pp. 31–58). [https://doi.org/10.1007/978-3-662-22216-4\\_2](https://doi.org/10.1007/978-3-662-22216-4_2)
- ElKoura, G., & Singh, K. (2003). Handrix: Animating the human hand. *Proceedings of the 2003 ACM SIGGRAPH/Eurographics Symposium on Computer Animation, SCA 2003*, 11. <https://doi.org/10.2312/SCA03/110-119>
- Eslamibidgoli, M. J., & Eikerling, M. H. (2016). Atomistic Mechanism of Pt Extraction at Oxidized Surfaces: Insights from DFT. *Electrocatalysis*, 7(4), 345–354. <https://doi.org/10.1007/s12678->

016-0313-2

- Fattahi, P., Yang, G., Kim, G., & Abidian, M. R. (2014). A review of organic and inorganic biomaterials for neural interfaces. *Advanced Materials*, 26(12), 1846–1885. <https://doi.org/10.1002/adma.201304496>
- Fiore, V., Battiato, P., Abdinia, S., Jacobs, S., Chartier, I., Coppard, R., Klink, G., Cantatore, E., Ragonese, E., & Palmisano, G. (2015). An Integrated 13.56-MHz RFID Tag in a Printed Organic Complementary TFT Technology on Flexible Substrate. *IEEE Transactions on Circuits and Systems I: Regular Papers*, 62(6), 1668–1677. <https://doi.org/10.1109/TCSI.2015.2415175>
- Fourneret, É. (2020). The Hybridization of the Human with Brain Implants: The Neuralink Project. *Cambridge Quarterly of Healthcare Ethics*, 29(4), 668–672. <https://doi.org/10.1017/S0963180120000419>
- Frasconi, M., Mazzei, F., & Ferri, T. (2010). Protein immobilization at gold–thiol surfaces and potential for biosensing. *Analytical and Bioanalytical Chemistry*, 398(4), 1545–1564. <https://doi.org/10.1007/s00216-010-3708-6>
- Fromherz, P., Offenhäusser, A., Vetter, T., & Weis, J. (1991). A neuron-silicon junction: a Retzius cell of the leech on an insulated-gate field-effect transistor. *Science*, 252(5010), 1290–1293. <https://doi.org/10.1126/science.1925540>
- Garcia, M. C. T., Utsunomiya, T., Ichii, T., & Sugimura, H. (2020). Surface potential contrasts between 1-alkene, 1-thiol and 1-alcohol self-assembled monolayers on silicon (111) substrate. *Japanese Journal of Applied Physics*, 59(SD). <https://doi.org/10.7567/1347-4065/ab5925>
- Gilles, S. (2010). *Nanoimprint Lithographie als Methode zur chemischen Oberflächenstrukturierung für Anwendungen in der Bioelektronik*. RWTH Aachen University.
- Gilles, S., Winter, S., Michael, K. E., Meffert, S. H., Li, P., Greben, K., Simon, U., Offenhäusser, A., & Mayer, D. (2012). Control of cell adhesion and neurite outgrowth by patterned gold nanoparticles with tunable attractive or repulsive surface properties. *Small*, 8(21), 3357–3367. <https://doi.org/10.1002/sml.201200465>
- Glass, M. (2020). *Molecular layer deposition and protein interface patterning for guided cell growth* (Vol. 215). Forschungszentrum Jülich GmbH, Zentralbibliothek, Verlag.
- Greben, K. (2015). *Modification and characterization of potential bioelectronic interfaces* [Universität zu Köln]. [https://kups.ub.uni-koeln.de/6057/1/K.\\_Greben\\_-\\_Dissertation\\_-\\_Modification\\_and\\_Characterization\\_of\\_Potential\\_Bioelectronic\\_Interfaces.pdf](https://kups.ub.uni-koeln.de/6057/1/K._Greben_-_Dissertation_-_Modification_and_Characterization_of_Potential_Bioelectronic_Interfaces.pdf)
- Greben, K., Li, P., Mayer, D., Offenhäusser, A., & Wördenweber, R. (2015). Immobilization and surface functionalization of gold nanoparticles monitored via streaming current/potential measurements. *Journal of Physical Chemistry B*, 119(19), 5988–5994. <https://doi.org/10.1021/acs.jpbc.5b02615>
- Gross, R., & Marx, A. (2018). Festkörperphysik. In *Festkörperphysik*. De Gruyter. <https://doi.org/10.1515/9783110559187>
- Halper, M. S., & Ellenbogen, J. C. (2006). Supercapacitors : A Brief Overview. *MITRE - McLean, March*. <tp://www.mitre.org/tech/nanotech>
- Han, L., Koide, N., Chiba, Y., & Mitate, T. (2004). Modeling of an equivalent circuit for dye-sensitized solar cells. *Applied Physics Letters*, 84(13), 2433–2435. <https://doi.org/10.1063/1.1690495>
- Handbook of Chemistry & Physics. (2001). Standard KCl solutions for calibrating conductivity cells. *CRC Handbook of Chemistry & Physics*-, 2001–2001.
- Hao, L., Fu, X., Li, T., Zhao, N., Shi, X., Cui, F., Du, C., & Wang, Y. (2016). Surface chemistry from wettability and charge for the control of mesenchymal stem cell fate through self-assembled monolayers. *Colloids and Surfaces B: Biointerfaces*, 148, 549–556.



<https://doi.org/10.1016/j.colsurfb.2016.09.027>

- Hassani, H., & Kreysing, E. (2019). Noninvasive measurement of the refractive index of cell organelles using surface plasmon resonance microscopy. *Optics Letters*, *44*(6), 1359. <https://doi.org/10.1364/ol.44.001359>
- Hassani, H., Wolf, N., Yuan, X., Wördenweber, R., & Offenhäusser, A. (2020). *Platinum substrate for surface plasmon microscopy at small angles*. 2019 Optical Society of America. <https://doi.org/10.1364/OL.99.099999>
- He, C., Zheng, Z., Tang, H., Zhao, L., & Lu, F. (2009). Electrochemical impedance spectroscopy characterization of electron transport and recombination in ZnO nanorod dye-sensitized solar cells. *Journal of Physical Chemistry C*, *113*(24), 10322–10325. <https://doi.org/10.1021/jp902523c>
- Hejazi, M. A., Tong, W., Stacey, A., Soto-Breceda, A., Ibbotson, M. R., Yunzab, M., Maturana, M. I., Almasi, A., Jung, Y. J., Sun, S., Meffin, H., Fang, J., Stamp, M. E. M., Ganesan, K., Fox, K., Rifai, A., Nadarajah, A., Falahatdoost, S., Prawer, S., ... Garrett, D. J. (2020). Hybrid diamond/ carbon fiber microelectrodes enable multimodal electrical/chemical neural interfacing. *Biomaterials*, *230*, 119648. <https://doi.org/10.1016/j.biomaterials.2019.119648>
- Heuschkel, M. O., Fejtl, M., Raggenbass, M., Bertrand, D., & Renaud, P. (2002). A three-dimensional multi-electrode array for multi-site stimulation and recording in acute brain slices. *Journal of Neuroscience Methods*, *114*(2), 135–148. [https://doi.org/10.1016/S0165-0270\(01\)00514-3](https://doi.org/10.1016/S0165-0270(01)00514-3)
- Hirschorn, B., Orazem, M. E., Tribollet, B., Vivier, V., Frateur, I., & Musiani, M. (2010). Determination of effective capacitance and film thickness from constant-phase-element parameters. *Electrochimica Acta*, *55*(21), 6218–6227. <https://doi.org/10.1016/j.electacta.2009.10.065>
- Hodgkin, A. L., & Huxley, A. F. (1952). A quantitative description of membrane current and its application to conduction and excitation in nerve. *The Journal of Physiology*, *117*(4), 500–544. <https://doi.org/10.1113/jphysiol.1952.sp004764>
- Hong, S., Ergezen, E., Lec, R., & Barbee, K. A. (2006). Real-time analysis of cell-surface adhesive interactions using thickness shear mode resonator. *Biomaterials*, *27*(34), 5813–5820. <https://doi.org/10.1016/j.biomaterials.2006.07.031>
- Hotze, E. M., Louie, S. M., Lin, S., Wiesner, M. R., & Lowry, G. V. (2014). Nanoparticle core properties affect attachment of macromolecule-coated nanoparticles to silica surfaces. *Environmental Chemistry*, *11*(3), 257–267. <https://doi.org/10.1071/EN13191>
- Hsu, C. H., & Mansfeld, F. (2001). Technical Note: Concerning the Conversion of the Constant Phase Element Parameter  $Y_0$  into a Capacitance. *CORROSION*, *57*(9), 747–748. <https://doi.org/10.5006/1.3280607>
- Huang, W., Anvari, B., Torres, J. H., Lebaron, R. G., & Athanasiou, K. A. (2003). Temporal effects of cell adhesion on mechanical characteristics of the single chondrocyte. *Journal of Orthopaedic Research*, *21*(1), 88–95. [https://doi.org/10.1016/S0736-0266\(02\)00130-4](https://doi.org/10.1016/S0736-0266(02)00130-4)
- Hunter, R. J. (1981). *Zeta potential in colloid science : principles and applications*. London : Academic press. <http://lib.ugent.be/catalog/rug01:000130545>
- Ingebrandt, S., Yeung, C.-K., Krause, M., & Offenhäusser, A. (2005). Neuron-transistor coupling: interpretation of individual extracellular recorded signals. *European Biophysics Journal*, *34*(2), 144–154. <https://doi.org/10.1007/s00249-004-0437-9>
- Jacobasch, H. J. (1989). Characterization of solid surfaces by electrokinetic measurements. *Progress in Organic Coatings*, *17*(2), 115–133. [https://doi.org/10.1016/0033-0655\(89\)80018-4](https://doi.org/10.1016/0033-0655(89)80018-4)
- Jeschonek, K., Hanlon, A., Nolzen, A., & Knoche, S. (2011). Cisplatin. In *TU Darmstadt*. [https://www.chemie.tu-darmstadt.de/media/ak\\_fessner/damocles\\_pdf/2011\\_1/Cisplatin.pdf](https://www.chemie.tu-darmstadt.de/media/ak_fessner/damocles_pdf/2011_1/Cisplatin.pdf)

- Johnson, B. J., & Park, S. M. (1996). Electrochemistry of conductive polymer: XIX. Oxidation of aniline at bare and polyaniline-modified platinum electrodes studied by electrochemical impedance spectroscopy. *Journal of the Electrochemical Society*, 143(4), 1269–1276. <https://doi.org/10.1149/1.1836628>
- Kandel, E. R., Schwartz, J. H., & Jessel, T. M. (2000). *Principles of neural science* (4th ed.). McGraw-Hill.
- Kato, T., Nozaki, K., Negishi, A., Kato, K., Monma, A., Kaga, Y., Nagata, S., Takano, K., Inagaki, T., Yoshida, H., Hosoi, K., Hoshino, K., Akbay, T., & Akikusa, J. (2004). Impedance analysis of a disk-type SOFC using doped lanthanum gallate under power generation. *Journal of Power Sources*, 133(2), 169–174. <https://doi.org/10.1016/j.jpowsour.2004.02.010>
- Khalili, A. A., & Ahmad, M. R. (2015). A Review of cell adhesion studies for biomedical and biological applications. *International Journal of Molecular Sciences*, 16(8), 18149–18184. <https://doi.org/10.3390/ijms160818149>
- Kibler, A. B., Jamieson, B. G., & Durand, D. M. (2012). A high aspect ratio microelectrode array for mapping neural activity in vitro. *Journal of Neuroscience Methods*, 204(2), 296–305. <https://doi.org/10.1016/j.jneumeth.2011.11.027>
- Kim, J.-H., Kang, G., Nam, Y., & Choi, Y.-K. (2010). Surface-modified microelectrode array with flake nanostructure for neural recording and stimulation. *Nanotechnology*, 21(8), 085303. <https://doi.org/10.1088/0957-4484/21/8/085303>
- Kim, Y. H., Baek, N. S., Han, Y. H., Chung, M. A., & Jung, S. D. (2011). Enhancement of neuronal cell adhesion by covalent binding of poly-d-lysine. *Journal of Neuroscience Methods*, 202(1), 38–44. <https://doi.org/10.1016/j.jneumeth.2011.08.036>
- Kirchhoff, S. (1845). Ueber den Durchgang eines elektrischen Stromes durch eine Ebene, insbesondere durch eine kreisförmige. *Annalen Der Physik Und Chemie*, 140(4), 497–514. <https://doi.org/10.1002/andp.18451400402>
- Kreysing, E., Hassani, H., Hampe, N., & Offenhäusser, A. (2018). Nanometer-Resolved Mapping of Cell-Substrate Distances of Contracting Cardiomyocytes Using Surface Plasmon Resonance Microscopy. *ACS Nano*, 12(9), 8934–8942. <https://doi.org/10.1021/acsnano.8b01396>
- Kristiansson, S., Ingvarson, F., & Jeppson, K. O. (2007). Compact Spreading Resistance Model for Rectangular Contacts on Uniform and Epitaxial Substrates. *IEEE Transactions on Electron Devices*, 54(9), 2531–2536. <https://doi.org/10.1109/TED.2007.902689>
- Ku, C. H., & Wu, J. J. (2007). Electron transport properties in ZnO nanowire array/nanoparticle composite dye-sensitized solar cells. *Applied Physics Letters*, 91(9), 2005–2008. <https://doi.org/10.1063/1.2778454>
- Kulka, M. (2011). Current Trends in X-Ray Crystallography. In A. Chandrasekaran (Ed.), *Springer* (Vol. 1, Issue December). InTech. <https://doi.org/10.5772/1421>
- Kundu, B., Eltohamy, M., Yadavalli, V. K., Kundu, S. C., & Kim, H. W. (2016). Biomimetic Designing of Functional Silk Nanotopography Using Self-assembly. *ACS Applied Materials and Interfaces*, 8(42), 28458–28467. <https://doi.org/10.1021/acsnano.8b01396>
- Kuo, K. nan, Moses, P. R., Lenhard, J. R., Green, D. C., & Murray, R. W. (1979). Immobilization, Electrochemistry, and Surface Interactions of Tetrathiafulvalene on Chemically Modified Ruthenium and Platinum Oxide Electrodes. *Analytical Chemistry*, 51(6), 745–748. <https://doi.org/10.1021/ac50042a038>

*Lab collection.* (n.d.).

*Lab protocol.* (n.d.).

- Laibinis, P. E., Whitesides, G. M., Aliara, D. L., Tao, Y. T., Parikh, A. N., & Nuzzo, R. G. (1991). Comparison of the Structures and Wetting Properties of Self-Assembled Monolayers of n-Alkanethiols on the Coinage Metal Surfaces, Cu, Ag, Au. *Journal of the American Chemical Society*, 113(19), 7152–7167. <https://doi.org/10.1021/ja00019a011>
- Lee, Y. J., Wang, J., Cheng, S. R., & Hsu, J. W. P. (2013). Solution processed ZnO hybrid nanocomposite with tailored work function for improved electron transport layer in organic photovoltaic devices. *ACS Applied Materials and Interfaces*, 5(18), 9128–9133. <https://doi.org/10.1021/am402511t>
- Lenhard, J. R., & Murray, R. W. (1977). Chemically modified electrodes. *Journal of Electroanalytical Chemistry and Interfacial Electrochemistry*, 78(1), 195–201. [https://doi.org/10.1016/S0022-0728\(77\)80442-7](https://doi.org/10.1016/S0022-0728(77)80442-7)
- Lessel, M., Bäumchen, O., Klos, M., Hähl, H., Fetzer, R., Paulus, M., Seemann, R., & Jacobs, K. (2015). Self-assembled silane monolayers: An efficient step-by-step recipe for high-quality, low energy surfaces. *Surface and Interface Analysis*, 47(5), 557–564. <https://doi.org/10.1002/sia.5729>
- Lewen, J. (2019). *Quantification and Improvement of the Electric Coupling between Electrogenic Cells and Microelectrode Arrays by Nanocavities and Nanostructures*. RWTH Aachen University.
- Loeb, G. E. (2018). Neural Prosthetics: A Review of Empirical vs. Systems Engineering Strategies. *Applied Bionics and Biomechanics*, 2018(Figure 1), 1–17. <https://doi.org/10.1155/2018/1435030>
- Lowry, G. V., Hill, R. J., Harper, S., Rawle, A. F., Hendren, C. O., Klaessig, F., Nobbmann, U., Sayre, P., & Rumble, J. (2016). Guidance to improve the scientific value of zeta-potential measurements in nanoEHS. *Environmental Science: Nano*, 3(5), 953–965. <https://doi.org/10.1039/c6en00136j>
- Lu, D., Li, W., Zuo, X., Yuan, Z., & Huang, Q. (2007). Study on electrode kinetics of Li<sup>+</sup> insertion in Li<sub>x</sub>Mn<sub>2</sub>O<sub>4</sub> (0 ≤ x ≤ 1) by electrochemical impedance spectroscopy. *Journal of Physical Chemistry C*, 111(32), 12067–12074. <https://doi.org/10.1021/jp0732920>
- Lvovich, V. F. (2012). *Impedance Spectroscopy*. John Wiley & Sons, Inc. <https://doi.org/10.1002/9781118164075>
- Lyklema, J. (2011). Surface charges and electrokinetic charges: Distinctions and juxtapositionings. *Colloids and Surfaces A: Physicochemical and Engineering Aspects*, 376(1–3), 2–8. <https://doi.org/10.1016/j.colsurfa.2010.09.021>
- MacDonald, D. D. (2006). Reflections on the history of electrochemical impedance spectroscopy. *Electrochimica Acta*, 51(8–9), 1376–1388. <https://doi.org/10.1016/j.electacta.2005.02.107>
- Magar, H. S., Abbas, M. N., Ali, M. Ben, & Ahmed, M. A. (2020). Picomolar-sensitive impedimetric sensor for salivary calcium analysis at POC based on SAM of Schiff base–modified gold electrode. *Journal of Solid State Electrochemistry*, 24(3), 723–737. <https://doi.org/10.1007/s10008-020-04500-w>
- Mahbuburrahman, M., Chandradebnath, N., & Lee, J. J. (2015). Electrochemical Impedance Spectroscopic Analysis of Sensitization-Based Solar Cells. *Israel Journal of Chemistry*, 55(9), 990–1001. <https://doi.org/10.1002/ijch.201500007>
- Malevich, D., Halliop, E., Peppley, B. A., Pharoah, J. G., & Karan, K. (2009). Investigation of Charge-Transfer and Mass-Transport Resistances in PEMFCs with Microporous Layer Using Electrochemical Impedance Spectroscopy. *Journal of The Electrochemical Society*, 156(2), B216. <https://doi.org/10.1149/1.3033408>
- Mansfeld, F. (1995). Use of electrochemical impedance spectroscopy for the study of corrosion protection by polymer coatings. *Journal of Applied Electrochemistry*, 25(3), 187–202. <https://doi.org/10.1007/BF00262955>

- Markov, A., Maybeck, V., Wolf, N., Mayer, D., Offenhäusser, A., & Wördenweber, R. (2018). Engineering of Neuron Growth and Enhancing Cell-Chip Communication via Mixed SAMs. *ACS Applied Materials & Interfaces*, *10*(22), 18507–18514. <https://doi.org/10.1021/acsami.8b02948>
- Markov, A., Wolf, N., Yuan, X., Mayer, D., Maybeck, V., Offenhäusser, A., & Wördenweber, R. (2017). Controlled Engineering of Oxide Surfaces for Bioelectronics Applications Using Organic Mixed Monolayers. *ACS Applied Materials & Interfaces*, *9*(34), 29265–29272. <https://doi.org/10.1021/acsami.7b08481>
- Martin, F. A., Marconi, D., Neamtu, S., Radu, T., Florescu, M., Turcu, R., Lar, C., Hädade, N. D., Grosu, I., & Turcu, I. (2017). “Click” access to multilayer functionalized Au surface: A terpyridine patterning example. *Materials Science and Engineering C*, *75*, 1343–1350. <https://doi.org/10.1016/j.msec.2017.03.033>
- Mathijssen, S. G. J., Kemerink, M., Sharma, A., Cölle, M., Bobbert, P. A., Janssen, R. A. J., & De Leeuw, D. M. (2008). Charge trapping at the dielectric of organic transistors visualized in real time and space. *Advanced Materials*, *20*(5), 975–979. <https://doi.org/10.1002/adma.200702688>
- McEver, R. P., & Zhu, C. (2010). Rolling Cell Adhesion. *Annual Review of Cell and Developmental Biology*, *26*(1), 363–396. <https://doi.org/10.1146/annurev.cellbio.042308.113238>
- Metwally, S., & Stachewicz, U. (2019). Surface potential and charges impact on cell responses on biomaterials interfaces for medical applications. *Materials Science and Engineering: C*, *104*(May), 109883. <https://doi.org/10.1016/j.msec.2019.109883>
- Metz, S., Heuschkel, M. O., Valencia Avila, B., Holzer, R., Bertrand, D., & Renaud, P. (2001). Microelectrodes with three-dimensional structures for improved neural interfacing. *2001 Conference Proceedings of the 23rd Annual International Conference of the IEEE Engineering in Medicine and Biology Society*, *1*, 765–768. <https://doi.org/10.1109/IEMBS.2001.1019053>
- Mom, R., Frevel, L., Velasco-Vélez, J. J., Plodinec, M., Knop-Gericke, A., & Schlögl, R. (2019). The Oxidation of Platinum under Wet Conditions Observed by Electrochemical X-ray Photoelectron Spectroscopy. *Journal of the American Chemical Society*, *141*(16), 6537–6544. <https://doi.org/10.1021/jacs.8b12284>
- Moses, P. R., Wier, L. M., Lennox, J. C., Finklea, H. O., Lenhard, J. R., & Murray, R. W. (1978). X-ray photoelectron spectroscopy of alkylaminesilanes bound to metal oxide electrodes. *Analytical Chemistry*, *50*(4), 576–585. <https://doi.org/10.1021/ac50026a010>
- Namisnyk, A. M. (2003). A survey of electrochemical supercapacitor technology. *Electrical Engineering*, *June*, 122.
- Novembre, C., Guérin, D., Lmimouni, K., Gamrat, C., & Vuillaume, D. (2008). Gold nanoparticle-pentacene memory transistors. *Applied Physics Letters*, *92*(10), 14–17. <https://doi.org/10.1063/1.2896602>
- Nyquist, H. (1932). Regeneration Theory. *Bell System Technical Journal*, *11*(1), 126–147. <https://doi.org/10.1002/j.1538-7305.1932.tb02344.x>
- Park, S. M., & Yoo, J. S. (2003). Electrochemical impedance spectroscopy for better electrochemical measurements. *Analytical Chemistry*, *75*(21), 455–461.
- Pasternack, R. M., Amy, S. R., & Chabal, Y. J. (2008). Attachment of 3-(aminopropyl)triethoxysilane on silicon oxide surfaces: Dependence on solution temperature. *Langmuir*, *24*(22), 12963–12971. <https://doi.org/10.1021/la8024827>
- Paulsson, H., Kloo, L., Hagfeldt, A., & Boschloo, G. (2006). Electron transport and recombination in dye-sensitized solar cells with ionic liquid electrolytes. *Journal of Electroanalytical Chemistry*, *586*(1), 56–61. <https://doi.org/10.1016/j.jelechem.2005.09.011>

- Pelmenschikov, A., Strandh, H., Pettersson, L. G. M., & Leszczynski, J. (2000). Lattice Resistance to Hydrolysis of Si–O–Si Bonds of Silicate Minerals: Ab Initio Calculations of a Single Water Attack onto the (001) and (111)  $\beta$ -Cristobalite Surfaces. *The Journal of Physical Chemistry B*, 104(24), 5779–5783. <https://doi.org/10.1021/jp994097r>
- Pennisi, C. P., Zachar, V., Gurevich, L., Patriciu, A., & Struijk, J. J. (2010). The influence of surface properties of plasma-etched polydimethylsiloxane (PDMS) on cell growth and morphology. *2010 Annual International Conference of the IEEE Engineering in Medicine and Biology*, 3804–3807. <https://doi.org/10.1109/IEMBS.2010.5627602>
- Petrossians, A., Whalen, J. J., Weiland, J. D., & Mansfeld, F. (2011). Surface modification of neural stimulating/recording electrodes with high surface area platinum-iridium alloy coatings. *Proceedings of the Annual International Conference of the IEEE Engineering in Medicine and Biology Society, EMBS*, 3001–3004. <https://doi.org/10.1109/IEMBS.2011.6090823>
- Piao, T. (1999). Intercalation of Lithium Ions into Graphite Electrodes Studied by AC Impedance Measurements. *Journal of The Electrochemical Society*, 146(8), 2794. <https://doi.org/10.1149/1.1392010>
- Plank, J., & Sachsenhauser, B. (2006). Impact of molecular structure on zeta potential and adsorbed conformation of  $\alpha$ -Allyl- $\omega$ -methoxypolyethylene glycol - Maleic anhydride superplasticizers. *Journal of Advanced Concrete Technology*, 4(2), 233–239. <https://doi.org/10.3151/jact.4.233>
- Pylatiuk, C., & Döderlein, L. (2006). „Bionische“ Armprothesen. *Der Orthopäde*, 35(11), 1169–1175. <https://doi.org/10.1007/s00132-006-1002-2>
- R. Lioutikov. (2012). *WP1210 Armkinematik*. Technische Universität Darmstadt. <http://wiki.ifs-tud.de/biomechanik/projekte/ws2012/armkinematik>
- Randles, J. E. B. (1947). KINETICS OF RAPID ELECTRODE REACTIONS. *Department of Chemistry, University of Birmingham*, 11–19.
- Rocha, P. R. F., Schlett, P., Kintzel, U., Mailänder, V., Vandamme, L. K. J., Zeck, G., Gomes, H. L., Biscarini, F., & de Leeuw, D. M. (2016). Electrochemical noise and impedance of Au electrode/electrolyte interfaces enabling extracellular detection of glioma cell populations. *Scientific Reports*, 6(1), 34843. <https://doi.org/10.1038/srep34843>
- Rosario-Castro, B. I., Contés-De-Jesús, E. J., Lebrón-Colón, M., Meador, M. A., Scibioh, M. A., & Cabrera, C. R. (2010). Single-wall carbon nanotube chemical attachment at platinum electrodes. *Applied Surface Science*, 257(2), 340–353. <https://doi.org/10.1016/j.apsusc.2010.06.072>
- Russell, C., Roche, A. D., & Chakrabarty, S. (2019). Peripheral nerve bionic interface: a review of electrodes. *International Journal of Intelligent Robotics and Applications*, 3(1), 11–18. <https://doi.org/10.1007/s41315-019-00086-3>
- Sachsenhauser, B. (2009). Kolloidchemische und thermodynamische Untersuchungen zur Wechselwirkung von alpha-Allyl- omega-Copolymeren mit CaCO<sub>3</sub> und Portlandzement [Technical University Munich]. In *Doktorarbeit*. <https://mediatum.ub.tum.de/doc/685221/685221.pdf>
- Saliba, N. A., Tsai, Y. L., Panja, C., & Koel, B. E. (1999). Oxidation of Pt (111) by ozone (O<sub>3</sub>) under UHV conditions. *Surface Science*, 419(2–3), 79–88. [https://doi.org/10.1016/S0039-6028\(98\)00667-0](https://doi.org/10.1016/S0039-6028(98)00667-0)
- Santoro, C., Babanova, S., Artyushkova, K., Cornejo, J. A., Ista, L., Bretschger, O., Marsili, E., Atanassov, P., & Schuler, A. J. (2015). Influence of anode surface chemistry on microbial fuel cell operation. *Bioelectrochemistry*, 106, 141–149. <https://doi.org/10.1016/j.bioelechem.2015.05.002>
- Santoro, F., Zhao, W., Joubert, L.-M., Duan, L., Schnitker, J., van de Burgt, Y., Lou, H.-Y., Liu, B., Salleo, A., Cui, L., Cui, Y., & Cui, B. (2017). Revealing the Cell–Material Interface with

- Nanometer Resolution by Focused Ion Beam/Scanning Electron Microscopy. *ACS Nano*, 11(8), 8320–8328. <https://doi.org/10.1021/acsnano.7b03494>
- Sanz-Herrera, J. A., & Reina-Romo, E. (2011). Cell-biomaterial mechanical interaction in the framework of tissue engineering: Insights, computational modeling and perspectives. *International Journal of Molecular Sciences*, 12(11), 8217–8244. <https://doi.org/10.3390/ijms12118217>
- Sarac, A. S., Ates, M., & Kilic, B. (2008). Electrochemical impedance spectroscopic study of polyaniline on platinum, glassy carbon and carbon fiber microelectrodes. *International Journal of Electrochemical Science*, 3(7), 777–786.
- Schmaltz, T., Sforazzini, G., Reichert, T., & Frauenrath, H. (2017). Self-Assembled Monolayers as Patterning Tool for Organic Electronic Devices. *Advanced Materials*, 29(18). <https://doi.org/10.1002/adma.201605286>
- Schweiss, R., Welzel, P. B., Werner, C., & Knoll, W. (2001). Dissociation of surface functional groups and preferential adsorption of ions on self-assembled monolayers assessed by streaming potential and streaming current measurements. *Langmuir*, 17(14), 4304–4311. <https://doi.org/10.1021/la001741g>
- Scully, J. R. (2000). Polarization resistance method for determination of instantaneous corrosion rates. *Corrosion*, 56(2), 199–217. <https://doi.org/10.5006/1.3280536>
- SelectScience. (n.d.). ZEISS ApoTome.2 by ZEISS Research Microscopy Solutions. Retrieved November 2, 2020, from <https://www.selectscience.net/products/zeiss-apotome2?prodID=10512>
- Seyock, S., Maybeck, V., Scorsone, E., Rousseau, L., Hébert, C., Lissorgues, G., Bergonzo, P., & Offenhäusser, A. (2017). Interfacing neurons on carbon nanotubes covered with diamond. *RSC Advances*, 7(1), 153–160. <https://doi.org/10.1039/C6RA20207A>
- Sherif, E. M., & Park, S. M. (2006a). Effects of 1,4-naphthoquinone on aluminum corrosion in 0.50 M sodium chloride solutions. *Electrochimica Acta*, 51(7), 1313–1321. <https://doi.org/10.1016/j.electacta.2005.06.018>
- Sherif, E. M., & Park, S. M. (2006b). Inhibition of copper corrosion in acidic pickling solutions by N-phenyl-1,4-phenylenediamine. *Electrochimica Acta*, 51(22), 4665–4673. <https://doi.org/10.1016/j.electacta.2006.01.007>
- Sizov, A. S., Agina, E. V., & Ponomarenko, S. A. (2019). Self-assembled interface monolayers for organic and hybrid electronics. *Russian Chemical Reviews*, 88(12), 1220–1247. <https://doi.org/10.1070/RCR4897>
- Søndergaard, R. R., Hösel, M., & Krebs, F. C. (2013). Roll-to-Roll fabrication of large area functional organic materials. *Journal of Polymer Science Part B: Polymer Physics*, 51(1), 16–34. <https://doi.org/10.1002/polb.23192>
- Spanu, A., Colistra, N., Farisello, P., Friz, A., Arellano, N., Rettner, C. T., Bonfiglio, A., Bozano, L., & Martinoia, S. (2020). A three-dimensional micro-electrode array for in-vitro neuronal interfacing. *Journal of Neural Engineering*, 17(3), 036033. <https://doi.org/10.1088/1741-2552/ab9844>
- Srinivasan, S. (2006). From Fundamentals to Applications. In *Fuel Cells*. Springer eBooks.
- Stevens, M. J. (1999). *Thoughts on the Structure of Alkylsilane Monolayers*. 13, 2773–2778. <https://doi.org/10.1021/la981064e>
- Swalen, J. D., Allara, D. L., Andrade, J. D., Chandross, E. A., Garoff, S., Israelachvili, J., McCarthy, T. J., Murray, R., Pease, R. F., Rabolt, J. F., Wynne, K. J., & Yu, H. (1987). Molecular monolayers and films. *Langmuir*, 3(6), 932–950. <https://doi.org/10.1021/la00078a011>
- Takenaka, S., Mikami, D., Tanabe, E., Matsune, H., & Kishida, M. (2015). Modification of carbon nanotube surfaces with precious metal and transition metal oxide nanoparticles using thin silica

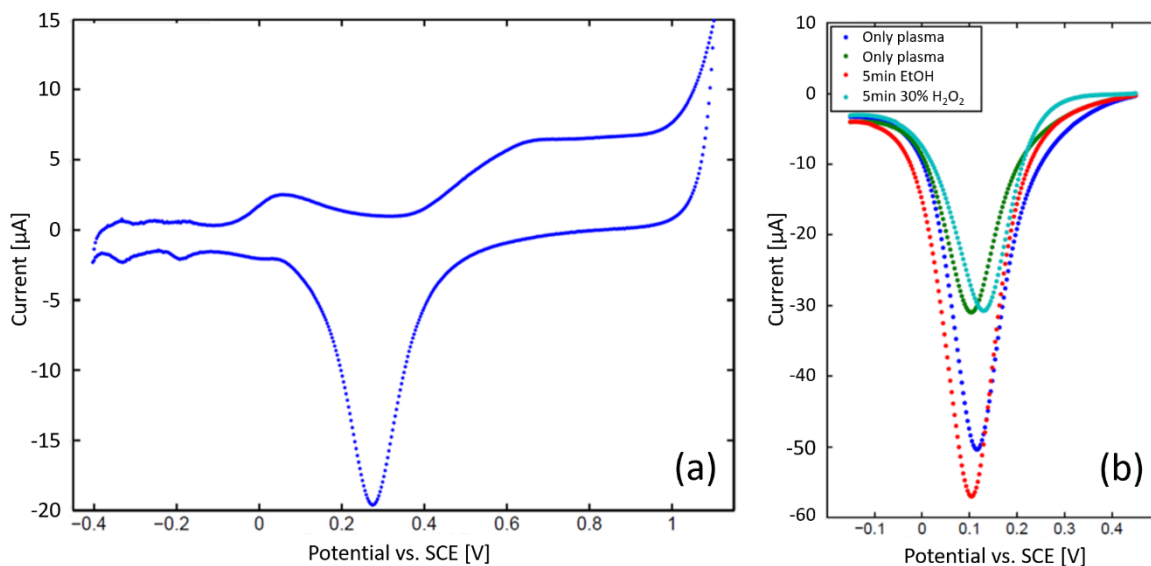
- layers. *Applied Catalysis A: General*, 492, 60–67. <https://doi.org/https://doi.org/10.1016/j.apcata.2014.12.025>
- Tang, L., Thevenot, P., & Hu, W. (2008). Surface Chemistry Influences Implant Biocompatibility. *Current Topics in Medicinal Chemistry*, 8(4), 270–280. <https://doi.org/10.2174/156802608783790901>
- Teschke, O., Ceotto, G., & de Souza, E. F. (2001). Interfacial water dielectric-permittivity-profile measurements using atomic force microscopy. *Physical Review E - Statistical Physics, Plasmas, Fluids, and Related Interdisciplinary Topics*, 64(1), 10. <https://doi.org/10.1103/PhysRevE.64.011605>
- Thiebaud, P., de Rooij, N. F., Koudelka-Hep, M., & Stoppini, L. (1997). Microelectrode arrays for electrophysiological monitoring of hippocampal organotypic slice cultures. *IEEE Transactions on Biomedical Engineering*, 44(11), 1159–1163. <https://doi.org/10.1109/10.641344>
- Thomas-Alyea, K. E., & Newman, J. (2012). *Electrochemical Systems*. John Wiley & Sons.
- Thompson, C. H., Zoratti, M. J., Langhals, N. B., & Purcell, E. K. (2016). Regenerative Electrode Interfaces for Neural Prostheses. In *Tissue Engineering - Part B: Reviews* (Vol. 22, Issue 2). <https://doi.org/10.1089/ten.teb.2015.0279>
- Vandenberg, E. T., Bertilsson, L., Liedberg, B., Uvdal, K., Erlandsson, R., Elwing, H., & Lundström, I. (1991). Structure of 3-aminopropyl triethoxy silane on silicon oxide. *Journal of Colloid and Interface Science*, 147(1), 103–118. [https://doi.org/https://doi.org/10.1016/0021-9797\(91\)90139-Y](https://doi.org/https://doi.org/10.1016/0021-9797(91)90139-Y)
- Viswanathan, P., Ondeck, M. G., Chirasatitsin, S., Ngamkham, K., Reilly, G. C., Engler, A. J., & Battaglia, G. (2015). 3D surface topology guides stem cell adhesion and differentiation. *Biomaterials*, 52(1), 140–147. <https://doi.org/10.1016/j.biomaterials.2015.01.034>
- Wall, S. (2010). The history of electrokinetic phenomena. *Current Opinion in Colloid and Interface Science*, 15(3), 119–124. <https://doi.org/10.1016/j.cocis.2009.12.005>
- Wang, J., Friedman, C. R., Cabrera, W., Tan, K., Lee, Y. J., Chabal, Y. J., & Hsu, J. W. P. (2014). Effect of metal/bulk-heterojunction interfacial properties on organic photovoltaic device performance. *Journal of Materials Chemistry A*, 2(37), 15288–15293. <https://doi.org/10.1039/c4ta02519a>
- Weidlich, S. D. (2017). Nanoscale 3D structures towards improved cell-chip coupling on microelectrode arrays. *Schriften Des Forschungszentrums Jülich. Reihe Schlüsseltechnologien*, 156, 1 Online-Ressource (II, 154 Seiten) : Illustration. <https://doi.org/10.18154/RWTH-2017-10442>
- Weidlich, S., Krause, K. J., Schnitker, J., Wolfrum, B., & Offenhäusser, A. (2017). MEAs and 3D nanoelectrodes: electrodeposition as tool for a precisely controlled nanofabrication. *Nanotechnology*, 28(9), 095302. <https://doi.org/10.1088/1361-6528/aa57b5>
- Weiland, J. D., & Humayun, M. S. (2014). Retinal Prosthesis. *IEEE Transactions on Biomedical Engineering*, 61(5), 1412–1424. <https://doi.org/10.1109/TBME.2014.2314733>
- Wesche, M., Hüske, M., Yakushenko, A., Brüggemann, D., Mayer, D., Offenhäusser, A., & Wolfrum, B. (2012). A nanoporous alumina microelectrode array for functional cell-chip coupling. *Nanotechnology*, 23(49), 495303. <https://doi.org/10.1088/0957-4484/23/49/495303>
- Whitesides, G. M., & Grzybowski, B. (2002). Self-assembly at all scales. *Science*, 295(5564), 2418–2421. <https://doi.org/10.1126/science.1070821>
- Wolf, N. R. (2017). *In-situ Monitoring and Controlling the Growth of Organic Molecular Monolayers Using a Resistive Sensor* [University cologne]. <https://doi.org/FZJ-2017-05092>
- Wolf, N. R., Yuan, X., Hassani, H., Milos, F., Mayer, D., Breuer, U., Offenhäusser, A., & Wördenweber, R. (2020). Surface Functionalization of Platinum Electrodes with APTES for Bioelectronic

- Applications. *ACS Applied Bio Materials*, 3(10), 7113–7121. <https://doi.org/10.1021/acsabm.0c00936>
- Wrobel, G., Höller, M., Ingebrandt, S., Dieluweit, S., Sommerhage, F., Bochem, H. P., & Offenhäusser, A. (2008). Transmission electron microscopy study of the cell–sensor interface. *Journal of The Royal Society Interface*, 5(19), 213–222. <https://doi.org/10.1098/rsif.2007.1094>
- Wu, Y., Chen, H., & Guo, L. (2020). Opportunities and dilemmas of in vitro nano neural electrodes. *RSC Advances*, 10(1), 187–200. <https://doi.org/10.1039/C9RA08917A>
- Yameen, B., Rodriguez-Emmenegger, C., Preuss, C. M., Pop-Georgievski, O., Verveniotis, E., Trouillet, V., Rezek, B., & Barner-Kowollik, C. (2013). SI: A facile avenue to conductive polymer brushes via cyclopentadiene–maleimide Diels–Alder ligation. *Chemical Communications*, 49(77), 8623–8625. <https://doi.org/10.1039/c3cc44683b>
- Yarlagadda, R. K. R. (2010). *Analog and Digital Signals and Systems*. Springer US. <https://doi.org/10.1007/978-1-4419-0034-0>
- Yip, H. L., Hau, S. K., Baek, N. S., Ma, H., & Jen, A. K. Y. (2008). Polymer solar cells that use self-assembled-monolayer-modified ZnO/metals as cathodes. *Advanced Materials*, 20(12), 2376–2382. <https://doi.org/10.1002/adma.200703050>
- Yuan, X., Wolf, N., Hondrich, T. J. J., Shokooimehr, P., Milos, F., Glass, M., Mayer, D., Maybeck, V., Prömpers, M., Offenhäusser, A., & Wördenweber, R. (2020). Engineering Biocompatible Interfaces via Combinations of Oxide Films and Organic Self-Assembled Monolayers. *ACS Applied Materials & Interfaces*, 12(14), 17121–17129. <https://doi.org/10.1021/acsami.0c02141>
- Yuan, X., Wolf, N., Mayer, D., Offenhäusser, A., & Wördenweber, R. (2019). Vapor-Phase Deposition and Electronic Characterization of 3-Aminopropyltriethoxysilane Self-Assembled Monolayers on Silicon Dioxide. *Langmuir*, 35(25), 8183–8190. <https://doi.org/10.1021/acs.langmuir.8b03832>
- Zaidel-Bar, R., Cohen, M., Addadi, L., & Geiger, B. (2004). Hierarchical assembly of cell–matrix adhesion complexes. *Biochemical Society Transactions*, 32(3), 416–420. <https://doi.org/10.1042/bst0320416>
- Zettsu, N., Kida, S., Uchida, S., & Teshima, K. (2016). Sub-2 nm Thick Fluoroalkylsilane Self-Assembled Monolayer-Coated High Voltage Spinel Crystals as Promising Cathode Materials for Lithium Ion Batteries. *Scientific Reports*, 6(May), 1–8. <https://doi.org/10.1038/srep31999>
- Zhang, F. Y., Advani, S. G., & Prasad, A. K. (2008). Performance of a metallic gas diffusion layer for PEM fuel cells. *Journal of Power Sources*, 176(1), 293–298. <https://doi.org/10.1016/j.jpowsour.2007.10.055>
- Zhang, M., Gao, M., Chen, J., & Yu, Y. (2015). Study on key step of 1,3-butadiene formation from ethanol on MgO/SiO<sub>2</sub>. *RSC Advances*, 5(33), 25959–25966. <https://doi.org/10.1039/c4ra17070a>
- Zhang, S. (2003). Fabrication of novel biomaterials through molecular self-assembly. *Nature Biotechnology*, 21(10), 1171–1178. <https://doi.org/10.1038/nbt874>

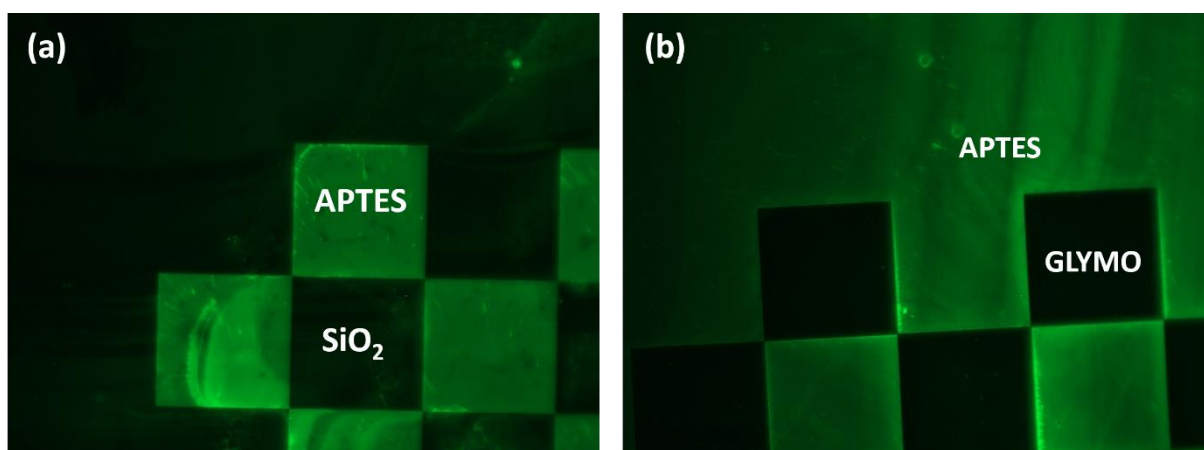


## II. Appendices

### Figures

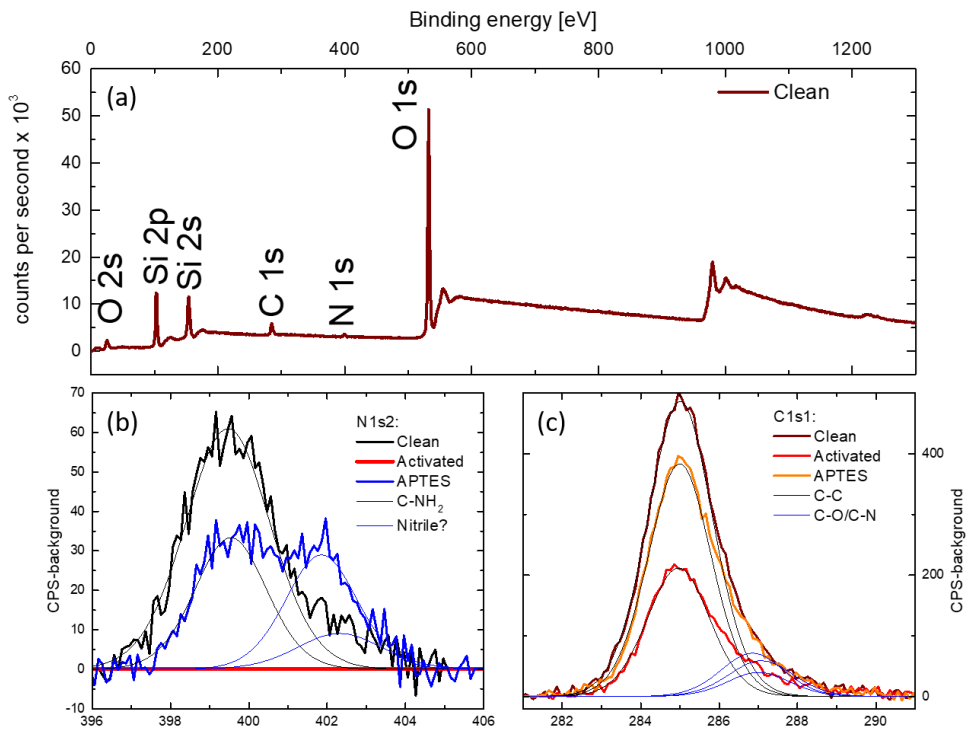


S 1: (a) Cyclic voltammogram of a platinum wire in 1M  $\text{KH}_2\text{POH}_3$  at pH 4.2. Pt oxidation (0.6 V onwards) and reduction (at 0.27 V) peaks are clearly visible. (b) Linear sweep voltammetry of a platinum wire after oxidation in an oxygen plasma oven and after storage of the sample in ethanol or  $\text{H}_2\text{O}_2$  for five minutes. In all voltammograms, a clear reduction peak is present indicating that a Platinum surface oxide was electrochemically reduces and neither previous chemical treatments nor sample storage under ambient conditions could reduce the formed oxide. The peak height is arbitrary and varies from sample to sample due to varying insertion depths of the wire in the electrolyte. SCE is the abbreviation for Standard Calomel Electrode, an electrode with Hg/HgCl as reference system. (Measured by Stefanie Karpinski, IBI-3 Forschungszentrum Jülich)

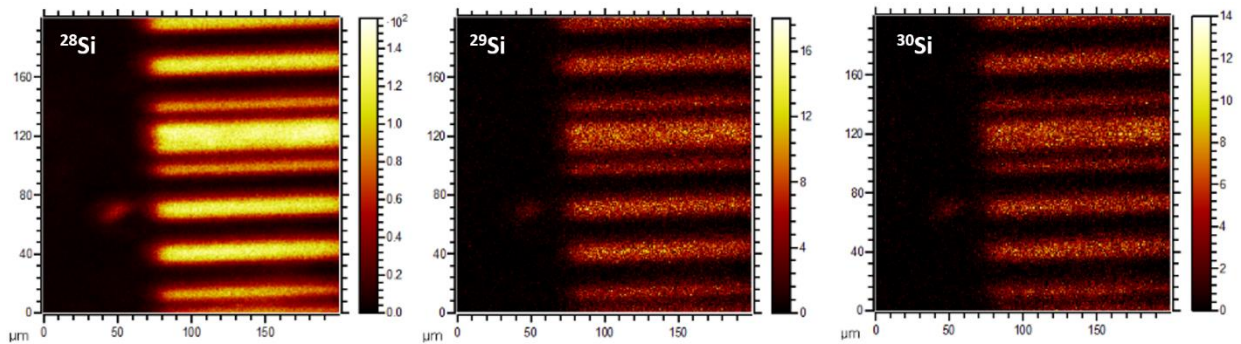


S 2: Fluorescence microscope picture of APTES molecules on  $\text{SiO}_2$  stained with FITC. (a) with  $\text{SiO}_2$  background and (b) with second deposition of GLYMO.

*Molecular Layer Functionalized Neuroelectronic Interfaces:  
From Sub-Nanometer Molecular Surface Functionalization to Improved Mechanical  
and Electronic Cell-Chip Coupling*

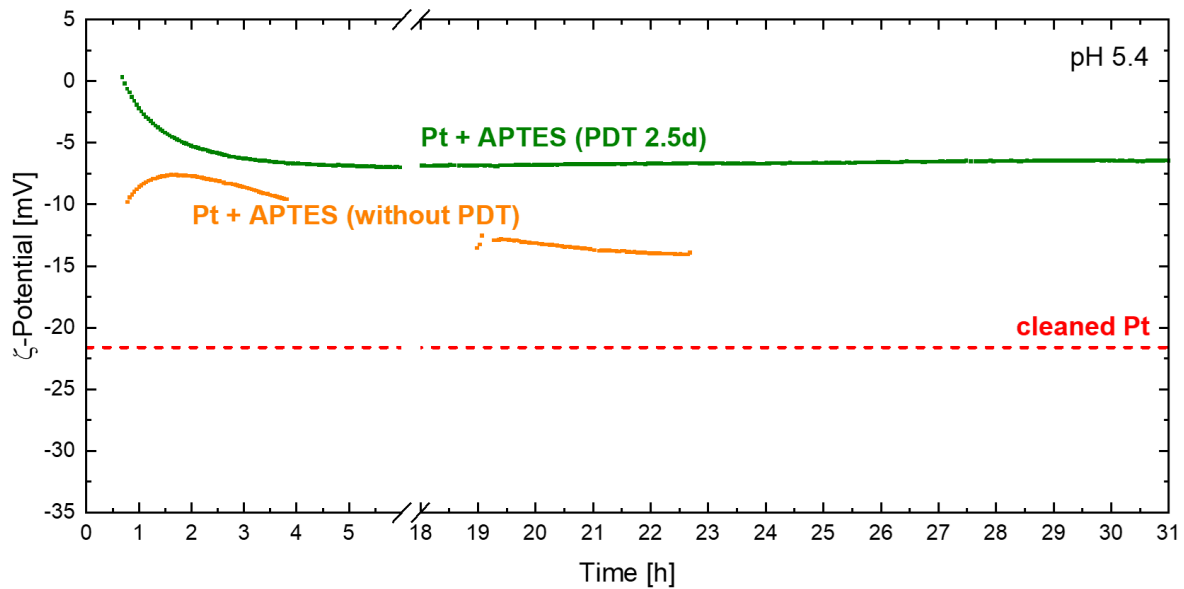


S 3: XPS analysis of the molecular deposition at 3 different states, i. e. after “cleaning” the virgin SiO<sub>2</sub>/Si substrate with acetone and propanol, after “activation” with ozone, and after deposition of APTES. (a) shows a complete spectrum of the cleaned substrate, (b) and (c) show the C-peaks and N-peaks for all 3 states, respectively. (Measured by Heinrich Hartmann, ZEA-3 Forschungszentrum Jülich)



S 4: ToF-SIMS measurement of APTES stripes on Pt substrate, showing (from left to right) the signal of the isotopes <sup>28</sup>Si, <sup>29</sup>Si, and <sup>30</sup>Si. The yellow bars represent the APTES deposited areas. (Measured by Uwe Breuer, ZEA-3 Forschungszentrum Jülich)

*Molecular Layer Functionalized Neuroelectronic Interfaces:  
From Sub-Nanometer Molecular Surface Functionalization to Improved Mechanical  
and Electronic Cell-Chip Coupling*



S 5: Development of the electrokinetic potential of APTES coated Pt samples (MLD) without (orange symbols) and with (green symbols) post-deposition treatment (PDT) measured in 1mM KCl at pH 5.4. During PDT the sample is kept under vacuum condition in the deposition chamber for 3 days; the red dashed line represents the electrokinetic potential of a cleaned Pt sample.

### Script for impedance

```
"""
Created on Wed Aug 5 11:30:02 2020
@author: Niko
"""

### packages
import numpy as np
import matplotlib.pyplot as plt
import pandas as pd
import tkinter as tk
from tkinter import filedialog
import os, os.path
from scipy.optimize import curve_fit
import scipy.integrate as integrate
import ntpath
import glob
from tqdm import tqdm

### constants
epsilon_0 = 8.8541878128e-12

def s(a = 0, b = 0, c = 0):
    serial = a + b + c
    return serial

def p(a, b):
    parallel = (a**(-1)+b**(-1))**(-1)
```

```
return parallel

def getFile(addNum=4):
    ### import dataset and add necessary columns. Here "channel" + channel number + "_" + electrode size
    in  $\mu\text{m}^2$  + ".txt" (e.g. channel1_1000.txt) file with frequency, Z', and Z''
    if file_extension == '.txt':
        print("Ending is: " + file_extension)
        # read data
        data_raw = pd.read_table(file_path, sep="\t")

        #rename columns
        data_raw.rename(columns={str(list(data_raw)[0]):"frequency"}, inplace=True)
        data_raw.rename(columns={str(list(data_raw)[1]):"Re"}, inplace=True)
        data_raw.rename(columns={str(list(data_raw)[2]):"Im"}, inplace=True)

        df = pd.DataFrame(data_raw)

        ### Add columnne
        betragZ = []
        phi = []
        size = []

        for i in range(len(df["Im"])):

            betragZ.append(np.sqrt(data_raw.Re[i]**2+data_raw.Im[i]**2))
            phi.append(np.arctan(data_raw.Im[i]/data_raw.Re[i])*180/np.pi)
            size.append(int(tail_1.split("_")[1])*1e-12)

        df["Z"] = betragZ
        df["Phi"] = phi
        df["Electrode_size"] = size

    else: print("don't know file format")

    return df

def linearFit():
    ### Fit to Nyquist plot linear, for estimate electrolyte resistance Rel and fractional exp. n
    coef1 = np.polyfit(raw.Re[-30:-5],raw.Im[-30:-5],1)
    poly1d_Rel = np.poly1d(coef1)
    Rel = -coef1[1]/coef1[0]
    n = -1*np.arctan(coef1[0])*180/np.pi /90

    return Rel, n, poly1d_Rel

def funcx(x, Rel, Q, n, Rct):
    ### Function for fitting. s(...,...) is serial and p(...,...) is parallel
    w = (2 * np.pi * x)
    ZRct = Rct*1e8
    ZRel = Rel
    ZQ = 1/(Q*1e-11*(1j*w)**n)
    model_test = s(ZRel, p(ZQ, ZRct))
    return model_test

def fit_Randles(Rel, n):
```

*Molecular Layer Functionalized Neuroelectronic Interfaces:  
From Sub-Nanometer Molecular Surface Functionalization to Improved Mechanical  
and Electronic Cell-Chip Coupling*

```

### Fit of funcx to |Z|, phi, and Z''
Q=0.5
Rct=1

fit_parameter = (Rel, Q, n, Rct) #fit parameter
param_bounds=( [Rel*0.99, 0, n*0.9, 0], [Rel*1.01, 1000, n*1.001, 1e15] ) #parameter borders

def fmodel(x, Rel, Q, n, Rct):
    return np.vstack([np.abs(funcx(x, Rel, Q, n, Rct)), np.angle(funcx(x, Rel, Q, n, Rct), deg=True),
    np.abs(funcx(x, Rel, Q, n, Rct))*np.sin(np.angle(funcx(x, Rel, Q, n, Rct)))]

x = raw.frequency.to_numpy()
y1 = raw.Z.to_numpy()
y2 = raw.Phi.to_numpy()
y3 = raw.Im.to_numpy()

y_data = np.vstack([y1,y2, y3])

def fmodel_flat(x, Rel, Q, n, Rct):
    return fmodel(x[0:int(len(x)/3)], Rel, Q, n, Rct).flatten()

popt, pcov = curve_fit(f=fmodel_flat, xdata=np.tile(x, 3), ydata=y_data.flatten(), p0=fit_parameter,
bounds=param_bounds, maxfev=100000)

print("Rel = " + str(popt[0]) + "\n" +
      "Q = " + str(popt[1]*1e-11) + "\n" +
      "n = " + str(popt[2]) + "\n" +
      "Rct = " + str(popt[3]*1e8))

return popt, pcov

def cir_3D(x, Z, phi, Rel):

    ### frequency dependent Rct, Cdl, and loss

    Rct_f = (Z*np.cos(phi*np.pi/180)-popt[0])*((Z*np.sin(phi*np.pi/180)/(Z*np.cos(phi*np.pi/180)-
    Rel))*2+1)
    Cdl_f = -(Z*np.sin(phi*np.pi/180)/(Z*np.cos(phi*np.pi/180)-Rel))/(2*np.pi*x*Rct_f)

    return Rct_f, Cdl_f, Loss

def plotOverview():

    ### Graphen plotten

    fig = plt.figure(dpi=90, facecolor='w', edgecolor='k', figsize = (20,20))#13.5
    fig.suptitle(tail + '\n' + 'rho = ' + str(rho_el))
    ax1 = fig.add_subplot(331)

    ax1.plot(raw.Re, -1*raw.Im, 'o--', raw.Re[0:-1], (-1)*poly1d_Rel(raw.Re[0:-1]), '--k')
    ax1.grid(True)
    ax1.set_xlabel("Z' [$\Omega$]")

```

*Molecular Layer Functionalized Neuroelectronic Interfaces:  
From Sub-Nanometer Molecular Surface Functionalization to Improved Mechanical  
and Electronic Cell-Chip Coupling*

```
ax1.set_ylabel("-Z" [\$Omega\$])
ax1.set_title("Nyquist"+ '\n' + "R$_{el}$=" + str(np.format_float_scientific(Rel,2)) + ",
n="+str(np.format_float_scientific(n,2)))

ax2 = fig.add_subplot(332)
ax2.loglog(raw.frequency, raw.Z, 'o--', label="data")
ax2.loglog(raw.frequency, raw.Z/raw.Z*Rel, '--k', label="Rel from Nyquist = " + str(Rel))
ax2.set_xlabel("Frequency [Hz]")
ax2.set_ylabel("|Z| [\$Omega\$]")
ax2.set_title("Bode |Z|" + "\n" + "R$_{el}$=" + str(np.format_float_scientific(popt[0],2)) + ", Q=" +
str(np.format_float_scientific(popt[1]*1e-11,2)) + "\n" + "n=" +
str(np.format_float_scientific(popt[2],2)) + ", R$_{ct}$=" +
str(np.format_float_scientific(popt[3]*1e8,2)))
ax2.loglog(raw.frequency, np.abs(funcx(raw.frequency, *popt)), linestyle='--', color='orange',
label="Fitted Curve")
ax2.grid(True)

ax3 = fig.add_subplot(333)
ax3.semilogx(raw.frequency, raw.Phi, 'o--')
ax3.plot(raw.frequency, np.arctan((funcx(raw.frequency, *popt).imag/funcx(raw.frequency,
*popt).real))*180/np.pi, color="orange")
ax3.set_xlabel("Frequency [Hz]")
ax3.set_ylabel("Phase [°]")
ax3.set_title("Bode Phase")
ax3.grid(True)

ax4 = fig.add_subplot(334)
ax4.loglog(raw.frequency, Rct_f, 'o--', label="data")
ax4.set_xlabel("Frequency [Hz]")
ax4.set_ylabel("R$_{ct}$ [\$Omega\$]")
ax4.set_title("parallel Resistance")
ax4.grid(True)
ax4.legend()

ax5 = fig.add_subplot(335)
ax5.loglog(raw.frequency, Cdl_f, 'o--', label="data")
ax5.set_xlabel("Frequency [Hz]")
ax5.set_ylabel("C$_{dl}$ [F]")
ax5.set_title("parallel Capacitor")
ax5.grid(True)
ax5.legend()

def R_Spread(Rel):
    ### calculate spreading resistance
    if raw.Electrode_size[1] == 200*1e-12:
        a = 40e-6/(np.pi)**0.5
        b = 5e-6/(np.pi)**0.5
    elif raw.Electrode_size[1] == 1000*1e-12:
        a = 200e-6/(np.pi)**0.5
        b = 5e-6/(np.pi)**0.5
    elif raw.Electrode_size[1] == 6000*1e-12:
        a = 500e-6/(np.pi)**0.5
        b = 12e-6/(np.pi)**0.5
    elif raw.Electrode_size[1] == 10000*1e-12:
        a = 500e-6/(np.pi)**0.5
        b = 20e-6/(np.pi)**0.5
```

```
elif raw.Electrode_size[1] == 20000*1e-12:
    a = 1000e-6/(np.pi)**0.5
    b = 20e-6/(np.pi)**0.5
else:
    print("size is not defined")

def integrand(x):
    return 1/(1-(1-b**2/a**2)*(np.sin(x))**2)**0.5

K = integrate.quad(integrand, 0, np.pi/2)

rho = Rel*2*np.pi*a/K[0]
return rho

def save():
    ### save all parameter (*.csv) and the overview figure (*.jpg)

    panda = pd.DataFrame(raw)
    panda["rho"] = rho_el
    panda["R_ct"] = Rct_f
    panda["C_dl"] = Cdl_f
    panda["Real_cal"] = funcx(raw.frequency, *popt).real
    panda["Imag_cal"] = funcx(raw.frequency, *popt).imag
    panda["|Z|_cal"] = np.abs(funcx(raw.frequency, *popt))
    panda["Phase_cal"] = np.angle(funcx(raw.frequency, *popt), deg=True)
    panda["R_ct*A"] = Rct_f*raw.Electrode_size
    panda["C_dl/A"] = Cdl_f/raw.Electrode_size

    panda.to_csv(head + '/' + os.path.basename(file_path) + '_data.csv', index = False)
    picture_path = head + '/' + os.path.basename(file_path) + '_fit_' + 'data.jpg'
    plt.savefig(picture_path, format='jpg', dpi=100)

    if test == True:
        pass
    else:
        plt.close()

if __name__ == '__main__':
    ### Program order
    # if test is 1 or True, just one file will be analyzed, if test is 0 or False, all files in the folder will be
    analyzed
    test = 1

    root = tk.Tk()
    root.withdraw()

    if test==True:
        # fetch and print file
        file_paths = []
        file_path_1 = filedialog.askopenfilename()
        file_paths.append(file_path_1)
        print(file_paths[0])

    else:
        file_dir = filedialog.askdirectory()
```

```
print(file_dir)
file_paths = glob.glob(file_dir + '*.*txt')

for i in tqdm(range(len(file_paths))):

    file_path = file_paths[i]
    head, tail = ntpath.split(file_path)
    filename, file_extension = os.path.splitext(file_path)
    head_1, tail_1 = ntpath.split(filename)

    raw = getFile()

    Rel, n, poly1d_Rel = linearFit()

    popt, pcov = fit_Randles(Rel, n)

    rho_el = R_Spread(popt[0])

    Rct_f, Cdl_f = cir_3D(raw.frequency, raw.Z, raw.Phi, popt[0])
    x_log = np.logspace(1, 7, 1000, endpoint=True)

    plotOverview()

    if test==True:
        pass
    else:
        save()
```



### III. Acknowledgments

Zum Schluss möchte ich noch meinen Dank an das gesamte Institut IBI-3 aussprechen, für die Kooperation, die Atmosphäre und das großartige miteinander. Ich habe die Zeit während meines Doktors sehr genossen. Im Folgenden möchte ich ein paar Personen besonders hervorheben.

Als aller erstes möchte ich meinem Doktorvater Prof. Dr. Roger Wördenweber danken. Es war immer inspirieren mit dir zu diskutieren, egal ob über fachliche Themen oder über Gott und die Welt. Zusammen waren wir bei den Team Events nicht selten die letzten beiden die noch durchgehalten haben. Auch möchte ich dir besonders für die fantastische Unterstützung danken. Danke für die tolle Zeit!

Außerdem möchte ich natürlich auch dem Institutsleiter Prof. Dr. Andreas Offenhäusser danken. Nicht nur für die Chance in dem Forschungszentrum meinen Doktor zu machen, sondern auch für das Miteinander und die Möglichkeit an Projekten wie dem Festvortrag mitzuwirken.

Als nächstes möchte ich meiner Arbeitsgruppe danken. Nicht nur die verbliebenen Sijia Liang, Xiaobo Yuan und Pratika Rai, sondern auch meinem Masterbetreuer Aleksandr Markov, meinem Langjährigen Büro Kollegen Yang Dai, meinem Masterstudenten Manuel Glass, unserem kleinen Bachelor Marc Neis und natürlich auch Dennis Finke. Mit euch hat das Leben im Forschungszentrum viel mehr Spaß gemacht und jeder hatte immer Zeit für spannende Diskussionen. Danke euch allen.

Natürlich war es mit dem gesamten Institut eine Freude, aber einige möchte ich hier nochmal besonders hervorheben. Ich danke Dirk Mayer für das offene Ohr was Chemiefragen angeht, aber auch für die Spaß Gespräche. Ich danke Vanessa Maybeck für die Hilfe bei Experimenten und bei Fragen zur Biologie, Tina Breuer für die Präparation der Zellkulturen, Timm Hondrich für die Hilfe bei Experimenten und die Diskussionen über machine learning, Frano Milos (meinem Lab-buddy) für die Feierabendbierchen und die gemeinsame Arbeit, Hussein Hassani aka Erfan für die SPR Messungen zusammen, Stefanie Karpinski für die Voltammogrammmessungen und Rolf Kutzner für den technischen Support und die Scherze auf dem Flur.

Des Weiteren möchte ich Uwe Breuer aus dem ZEA-3 danke für die Zeit, die er sich genommen hat bei den ToF-SIMS Messungen und die guten Gespräche, Heinrich Hartmann aus dem ZEA-3 für die XPS Messungen, Guillermo Beltramo aus dem IBI-2 für die versuchte Ramanmessung, Jenia Jitsev aus dem JSC für die machine learning Diskussionen, dem Team aus dem HNF, für die Unterstützung und die Diskussionen im Reinraum und der mechanischen Werkstatt und elektrische Werkstatt für die Beratung und Unterstützung bei all meinen vielen Anliegen.

Ganz zum Schluss möchte ich mich noch bei meinem Team von jNM<sup>2</sup> - Jens Schreiber, Markus Strehlau und Mathis Ernst bedanken, dass sie immer für Diskussionen und Unterstützung zur Stelle waren und meiner Freundin Zhiyi Yin, die mich während der Doktorarbeit ertragen musste.

Vielen Dank für die fantastische Zeit!

## Erklärung

Ich versichere, dass ich die von mir vorgelegte Dissertation selbständig angefertigt, die benutzten Quellen und Hilfsmittel vollständig angegeben und die Stellen der Arbeit - einschließlich Tabellen, Karten und Abbildungen -, die anderen Werken im Wortlaut oder dem Sinn nach entnommen sind, in jedem Einzelfall als Entlehnung kenntlich gemacht habe; dass diese Dissertation noch keiner anderen Fakultät oder Universität zur Prüfung vorgelegen hat; dass sie - abgesehen von unten angegebenen Teilpublikationen - noch nicht veröffentlicht worden ist, sowie, dass ich eine solche Veröffentlichung vor Abschluss des Promotionsverfahrens nicht vornehmen werde.

Die Bestimmungen der Promotionsordnung sind mir bekannt. Die von mir vorgelegte Dissertation ist von Prof. Dr. Roger Wördenweber betreut worden.

### Teilpublikationen:

*2020 ACS Appl. Bio  
Materials*


**“Surface Functionalization of Platinum Electrodes with APTES for Bioelectronic Applications”** Nikolaus R. Wolf, Xiaobo Yuan, Hossein Hassani, Frano Milos, Dirk Mayer, Uwe Breuer, Andreas Offenhäusser, Roger Wördenweber

*2020 Optical Society of  
America*

**“Platinum substrate for surface plasmon microscopy at small angles.”** Hossein Hassani, Nikolaus Radja Wolf, Xiaobo Yuan, Roger Wördenweber, Andreas Offenhäusser

Datum / Unterschrift

02.11.2020



# Nikolaus R. Wolf

Genoveastr. 48 • 51063 Köln • Tel.: 01781569636 • E-Mail: n.r.wolf@jnm2.de

---

## Lebenslauf

### ■ Persönliche Daten

Name: Nikolaus Radja Wolf  
Adresse: Genoveastr. 48,  
51063 Köln  
Telefonnummer: 01781569636  
E-Mail: n.r.wolf@web.de  
Geburtstag: 24.08.1986  
Geburtsort: Fritzlar  
Zivilstand: Ledig, keine Kinder



### ■ Schulbildung

2007 – 2013 Bachelor Physik (Note: 2,4) an der Universität zu Köln, Abschlussarbeit: „*Thermodynamische Eigenschaften von  $(\text{NH}_4)_2[\text{InCl}_5(\text{H}_2\text{O})]$ ,  $\text{CuBr}_2$  und  $\text{Cs}_2\text{CuCl}_2\text{Br}_2$* “ (Note: 1,0)  
2014 – 2017 Masterstudiengang Physik (auf Englisch, Note: 1.7) an der Universität zu Köln, Abschlussarbeit Forschungszentrum Jülich PGI-8: „*In-situ Monitoring and Controlling the Growth of Organic Molecular Monolayers Using a Resistive Sensor*“ (Note: 1.3)  
2017 – 2020 PHD Forschungszentrum Jülich: *IBI-3 Bioelectronics*

### ■ Sprachen:

- Deutsch Muttersprache
- Englisch Verhandlungssicher

### ■ Nebenberufliche Selbständigkeit:

08/2019 Gründung GbR: jNM<sup>2</sup>  
Schwerpunkt:  
- Machine Learning  
- Visualisierung  
- Mixed Reality  
- Sensorik

### ■ Geräte:

Reinraum	ISO 1-3
Interface Analysen	AFM, DekTak, Ellipsometer
Elektrische Charakterisierung	Impedanzspektroskopie, LCR, IVC
Nanoelektronik	Lithografie, Mikroverkablung
Moleküldeposition	Gasphase MLD SAMs
Tieftemperatur Kryostat	N <sub>2</sub> , He <sub>4</sub> , He <sub>3</sub>

# Nikolaus R. Wolf

Genoveastr. 48 • 51063 Köln • Tel.: 01781569636 • E-Mail: n.r.wolf@jnm2.de

---

## ■ EDV-Kenntnisse:

---

<i>Textverarbeitung:</i>	LaTeX, Microsoft Word, LibreOffice Writer (sehr gute Kenntnisse)
<i>Präsentationsprogramme:</i>	Microsoft PowerPoint, LibreOffice Impress, Prezi (sehr gute Kenntnisse)
<i>Tabellenkalkulation:</i>	Microsoft Excel, LibreOffice Calc (sehr gute Kenntnisse)
<i>Konstruktionsprogramme:</i>	AutoCAD, Inventor (sehr gute Kenntnisse)
<i>Analyse und Darstellung:</i>	ORIGIN Lab, QtiPlot (sehr gute Kenntnisse), gnuplot (gute Kenntnisse)
<i>Grafik-/Bildbearbeitung:</i>	Inkscape, GIMP (sehr gute Kenntnisse), Cinema 4D (gute Kenntnisse), Blender (sehr gute Kenntnisse)
<i>Visualisierungsprogramme:</i>	Diamond (Grundkenntnisse), Agros2D (gute Kenntnisse)
<i>Videobearbeitungsprogramme:</i>	Adobe Premiere Pro CC, DaVinci Resolve 16 (gute Kenntnisse)
<i>Sprachen:</i>	C#, Python (gute Kenntnisse), C++, HTML, Java (Grundkenntnisse)
<i>KI:</i>	Mask-RCNN (gute Kenntnisse)
<i>Entwicklungsumgebungen:</i>	Android Studio, Arduino IDE, Unity (sehr gute Kenntnisse)

## ■ Talks:

---

06/2016	<b>Magnetical, Electrical, Chemical and Biological Sensors</b> ( <i>International summer school: "New Challenges in Bioelectronics"</i> )
03/2018	<b>from EEG to BCI</b> ( <i>International winter school: "Neurotechnology: Fundamentals &amp; Applications"</i> )
07/2019	<b>Introduction in Deep Learning</b> ( <i>International summer school "Bioelectronics: from In Vitro to In Vivo Applications"</i> )

## ■ Paper:

---

2020 ACS Appl. Bio Materials	<b>"Surface Functionalization of Platinum Electrodes with APTES for Bioelectronic Applications"</b> Nikolaus R. Wolf, Xiaobo Yuan, Hossein Hassani, Frano Milos, Dirk Mayer, Uwe Breuer, Andreas Offenhäusser, Roger Wördenweber
2020 Optical Society of America	<b>"Platinum substrate for surface plasmon microscopy at small angles."</b> Hossein Hassani, Nikolaus Radja Wolf, Xiaobo Yuan, Roger Wördenweber, Andreas Offenhäusser
2020 ACS Appl. Mater. Interfaces	<b>"Engineering Biocompatible Interfaces via Combinations of Oxide Films and Organic Self-Assembled Monolayers."</b> Xiaobo Yuan, Nikolaus Wolf, Timm J. J. Hondrich, Pegah Shokooimehr, Frano Milos, Manuel Glass, Dirk Mayer, Vanessa Maybeck, Michael Prömpers, Andreas Offenhäusser, Roger Wördenweber
2019 Langmuir	<b>"Vapor-Phase Deposition and Electronic Characterization of 3-Aminopropyltriethoxysilane Self-Assembled Monolayers on Silicon Dioxide."</b> Xiaobo Yuan, Nikolaus Wolf, Dirk Mayer, Andreas Offenhäusser, Roger Wördenweber
2018 ACS Appl. Mater. Interfaces	<b>"Engineering of Neuron Growth and Enhancing Cell-Chip Communication via Mixed SAMs."</b> Aleksandr Markov, Vanessa Maybeck, Nikolaus Wolf, Dirk Mayer, Andreas Offenhäusser, Roger Wördenweber
2017 ACS Appl. Mater. Interfaces	<b>"Controlled Engineering of Oxide Surfaces for Bioelectronics Applications Using Organic Mixed Monolayers"</b> Aleksandr Markov, Nikolaus Wolf, Xiaobo Yuan, Dirk Mayer, Vanessa Maybeck, Andreas Offenhäusser, Roger Wördenweber